DISSERTATION

Long-term topographic evolution of the African plate, causes and consequences for surrounding lithospheric plates

Submitted to the
Combined Faculties of Nature Sciences and Mathematics
Heidelberg University,
Germany

As Requirement for the Degree of
Doctor of Natural Sciences (Dr. rer. nat.)

Presented by

Sherif Elshahat Elsayed Mansour
born in Kalyobiya, Egypt

M.Sc. Geology
Kanazawa University
Japan, 2010

Oral examination: December 18th, 2015

INAUGURAL-DISSERTATION

Long-term topographic evolution
of the African plate, causes and consequences for
surrounding lithospheric plates
zur
Erlangung der Doktorwürde
der
Naturwissenschaftlich-Mathematischen Gesamtfakultät
der
Ruprecht-Karls-Universität Heidelberg

vorgelegt von

M.Sc. Sherif Elshahat Elsayed Mansour
aus Kalyobiya, Ägypten

2015

Tag der mündlichen Prüfung: 18.12.2015

Gutachter: apl. Prof. Dr. Ulrich A. Glasmacher
Prof. Dr. Peter A. Kukla

“The best among you are those who learn the science and teach it” - prophet Muhammad

“There will come a time when you believe everything is finished; that will be the beginning” - louis l’amour

“We must learn to live together as brothers or perish together as fools” - Martin Luther King

Acknowledgements

In the beginning I would like to mention that every success I have been gotten was, before and after others, by the donation and support of the **GOD** where no words can express my appreciation and gratitude to HIS generous giving

Efforts were done and results were achieved during this research are production of a team work attempts which had participated either direct or indirect way. It is of my great pleasure to find a chance here to express my appreciation and gratefully thanks to all of them:

apl. Prof. Dr. Ulrich A. Glasmacher
Who gave me the chance to conduct my dissertation in the University of Heidelberg and facilitated for this research in all possible ways.

My Family
In hard times and weakness points I got help from many, whose help is appreciated, but no support was equal or even close to theirs especially my wife and my mother.

Prof. Dr. Heinz F. Schöler
I also want to thank the expertise he contributed, time he spent and the discussions on the annual project reports.

Heidelberg ThermoArcheo research group
All group members especially **Dr. Sebastian Kollenz** and **Dr. Manuel Sehrt** whom helped me a lot in both scientific and living matters to participate in removing many obstacles.

Mrs. Margit Brückner
For her help, advices and cooperation during the laboratory work.

Friends
Many friends who were always beside me, those who are in Egypt, Japan, USA and Germany especially **Dr. Mohamed Ahmed** (Western Michigan University) and **Dr. Mohamed El Sherif Badr** (RIKEN Center for Integrative Medical Sciences, Japan)

- THANK YOU

Funding

Of course I owe thanks for the financial support from the Egyptian Ministry of Higher Education and State for Scientific Research (MHESR) and the German Academic Exchange Service (DAAD) through the German-Egyptian Research Long-Term Scholarship (GERLS).

Abstract

The African lithospheric continent has an extended history over 3.8 Ga and is tectonically active since more than 2.9 Ga. Ever since the topography of that continent was changing under influences of a series of endogenic (tectonic) and exogenic (surface) processes. Generally the earth's topography has major influences on the planet, examples include but are not limited to species distribution, forest succession, erosion, sedimentation, fluvial systems and climate. The topographic changes are accompanied by rock exhumations in either way of endogenic forces or as response to exogenic processes. These exhumation events could be traced by low temperature thermochronology (LTT) techniques. The LTT techniques date the rock passing through a certain isotherm (closure temperature) and are used to quantify the cooling rates. The closure temperature is function of the applied LTT technique and mineral type. Combining these cooling ages and LTT data with the time-temperature (t-T) modelling enables visualizing and quantifying the rock movement through the upper crust. Therefore, these combinations were used to compare and reconstruct the topographic changes in key areas dominated by various geologic environments as response to different magnitudes from multiple landscaping processes in the African continent. Furthermore, the ability of LTT to answer difficult questions related to landscaping processes (e.g., landslide detection and quantifying and the endogenic-exogenic processes relationship) was also tested.

Comparing and reconstructing rift flanks uplifted areas (the Albertine Rift; the Rwenzori Mountains and the Gulf of Suez; the Samra Mountain area) on an old craton revealed a relatively long cycle of life. The non-uniform uplift through fault-bounded blocks was the dominant mechanism of response for all the induced far-field continental scale tectonics and surface processes. Only a uniform uplift was demonstrative during the rifting event. The thermochronological record of the Samra area has started earlier with the East African Orogeny (EAO) plutonism and accretion. Afterwards, both areas (the Rwenzoris and the Samra) were affected by the post orogenic erosional event. Shortly after, each area of them was affected differentially by a series of far-field tectonic events. Then, the rift started to activate affecting the whole areas with corresponding uplift. While the Gulf of Suez was nearly deactivated by the movement along the Dead Sea transform

fault at mid-Miocene. The movement along the footwall of Bwamba fault caused additional uplift to the Rwenzoris at the Pliocene.

On the other hand, comparing and reconstructing volcanic islands (Fuerteventura and La Gomera; Canary Islands) on passive margin revealed a relatively short cycle of life. That cycle started by emerging, followed by formation of the shield stage with adding a huge amount of magmatic materials forming a highly topographic island (Fuerteventura; ~20 Ma, La Gomera; ~10 Ma). Afterwards, the topography destruction starts with landsliding (Fuerteventura; ≤20 Ma, La Gomera; ~7 Ma) when suitable topographic and climatic conditions, among others, were dominated. Then the volcanic island experience other cycle, starting with constructing high topography by feeding with new magmatic materials till the hot spot related magmatic activities transfer to other regions. That activity shift was recorded by a lateral movement of the Canary plume materials beneath northwest Africa to west the Mediterranean Sea produced a track of intraplate volcanism through its course.

Furthermore, LTT techniques were able to detect, differentiate, and quantify different landscaping events (including landslides) with various magnitudes in different geologic environments.

- In rifted regions; the Rwenzori Mountains have experienced 4 rapid cooling/exhumation events. 1) the Silurian-Devonian (420-390 Ma) event associated with ~3.5 (1.5) km of rock uplift as response to the post Pan-African orogeny deep erosional event. 2) The Triassic (240-220 Ma) event that caused ~3.0 km of rock uplift associated with rapid cooling and a major erosional event at the end of the Karoo sedimentary regime. 3) The Eocene-Miocene (52-10 Ma) event resulted in an average rock uplift of ~3.0 (0.2) km, the Early Eocene tectonic events were associated with India drifting afterwards the Eastern Rift activity was started. 4) The Pliocene-Pleistocene event (3-2.5 Ma) caused ~≤2.0 km of rock uplift along the footwall of Bwamba fault.

The last two exhumation events with ~5 km of corresponding rock uplift produced the exceptionally high Rwenzori Mountains in the EARS extensional regime as a rift flank within two stages. The latter movement caused the tilt uplifting in the western flank of the mountains.

While, the Samra Mountain area has experienced 5 rapid cooling/exhumation events. 1) The Neoproterozoic (775-640 Ma) event caused ~5.8 (0.1) km of rock uplift as a response to the accretion and plutonism during the EAO. 2) The Cambrian-Devonian (507-457 Ma) event causing ~5.6 (0.2) km of rock uplift as response to the post-EAO erosional event. 3) The Carboniferous-Permian (390-230 Ma) event resulted in ~4.2 (1.6) km of rock uplift as response to the Hercynian tectonic event. 4) The Jurassic-Cretaceous (170-70 Ma) event resulted in ~2.9 (0.5) km of rock uplift as a response to the Gondwana breakup. 5) The Oligocene-Miocene (27-22 Ma) event causing rock uplift of ~1.3 (0.3) km as response to the rift initiation. Additional reheating event was reported in the time span extending between the uplift associated with the Gulf of Suez and the prior cooling event causing an average subsidence of ~0.6 (0.3) km.

- The Albertine rift flanks uplift is double the Gulf of Suez related flanks uplift which suggests an additional heat component during the Albertine rift formation. That heat component resulted from being the corresponding mantle plume directly beneath the EARS and more than 2000 Km away from the Gulf of Suez (Afar plume).

- In volcanic islands; Fuerteventura Island has experienced two rapid cooling/exhumation events; one has started ~20 Ma with ~2.7 (0.5) km of corresponding rock uplift that caused the onset of the Fuerteventura landslide. The other has been initiated ~7 Ma with ~2.3 (0.2) km of corresponding rock uplift forming the doming stage on the western part of Fuerteventura ~5 Ma. Finally, these domes were eroded to nowadays surfaces. La Gomera Island also has experienced two rapid cooling/exhumation events; the first event has started between ~10 and 7 Ma with corresponding ~2.7 (0.2) km of rock uplift causing the onset of the La Gomera landslide. The second rapid cooling event occurred by ~4 Ma resulting in ~2 km of rock uplift. Finally, this topography was eroded to reduce elevation to nowadays surfaces.

Zusammenfassung

Die afrikanische Lithosphäre hat eine Geschichte von mehr als 3,8 Mrd. Jahren und zeigt seit mehr als 2,9 Mrd. Jahren tektonische Aktivität. Seit jeher verändert sich sich die Topographie durch die Einflüsse von endogenen (tektonischen) und exogenen (Oberfläche) Prozessen. Die Erdoberfläche wird vor Allem durch die Verteilung von Lebewesen, das Auftreten von Wäldern, Erosion, Sedimentation, fluvialtile Systeme und Klima beeinflusst. Die Veränderungen der Topographie geht einher mit der Exhumierung von Gesteinen durch endogene oder exogene Kräfte. Diese Exhumierung kann durch Methoden der Niedrig-Temperatur-Thermochronologie quantifiziert werden. Bei der Niedrig-Temperatur-Thermochronologie werden Gesteine mit Hilfe von spezifischen Schließtemperaturen datiert, die abhängig von der Methode und dem jeweiligen Mineral sind, so dass man unterschiedliche Abkühlalter erhält. Die Mehoden der LTT datieren das Gestein beim Durchlaufen einer bestimmten Isotherme und nimmt die so ermittelten Abkühlalter als Grundlage für die Berechnung von Abkühlraten. Die Schließtemperatur ist abhängig von der Methode und dem genutzten Mineral. Durch die Kombination der Abkühlalter, dem ermittelten LTT-Datensatz und den Zeit-Temperaturmodellierungen erhält man einen möglichen Einblick wie das Gestein sich durch die Erdkruste bewegte. Hierfür wurde diese Kombinationen der Methodik benutzt um die topographische Entwicklung der Schlüsselgebiete, welche von unterschiedlichen geologischen Eigenschaften als Rückkopplung veschiedener Magnituden differenzierter Landschaftsprozesse des Afrikanischen Kontinents geprägt sind, zu rekonstruieren und zu vergleichen. Zusätzlich wurde mit den Methoden der LTT die Beantwortung von Fragestellungen zu verschiedenen Prozessen der Topographieveränderungen getestet.

Hierbei zeigten vulkanische Inseln (Fuerteventura und La Gomera; Kanarische Inseln) am passiven Kontinentalrand einen relativ kurzen Lebenszyklus. Der Zyklus beginnt mit der Bildung der Insel, gefolgt von der shield stage, die durch die Ansammlung eines großen Volumens an magmatischem Material charakterisiert ist. Dieses magmatische Material führt zu einer Insel mit einer ausgeprägten Topographie (Fuerteventura; ~20 Ma, La Gomera; ~10 Ma). Hangrutsche führen im weiteren Verlauf, bei günstigen klimatischen Bedingungen zur Zerstörung der Topographie (Fuerteventura; ~20 Ma, La

Gomera; ~7 Ma). Der Beginn eines neuen Zyklus führt zur erneuten Bildung von Topographie, durch frisches magamtisches Material. Dieser Prozess hält so lange an bis die magmatische Aktivität des hot-spots sich auf eine andere Region konzentriert und dort eine weitere Vulkan-Insel bildet.

Im Gegensatz dazu zeigen herausgehobene Gebiete an den Riftflanken eines alten Kratons (das Albertine Rift; die Rwenzori-Gebirge und der Golf von Suez; der Samra-Berg) einen relativ langen Lebenszyklus. Vor dem initialen Rifting führten Oberflächenprozesse und tektonische Prozesse zu einer heterogenen Heraushebung des Gebiets entlang von Störungen. Das Rifting selbst führte zu einer homogenen Heraushebung des ganzen Gebietes. Die thermochronologischen Daten des Samra-Gebiets sind alle älter als das eigentliche Rifting-event und verweisen auf plutonische Aktivität der EAO. Danach wurden beiden Gebiete von der post-orogenen Erosion beeinflusst. Kurz darauf wurden beide Gebiete von mehreren unterschiedlichen tektonischen far-field events beeinflusst. Die Aktivierung des Riftings führt zur Heraushebung weiter Gebiete, während der Golf von Suez im mittleren Miozän entlang der Totes Meer Transform-Störung deaktiviert wurde. Eine Bewegung entlang des Gleithangs der Bwamba-Störung führte zu einer zusätzlichen Heraushebung der Rwenzoris im Pliozän.

Des Weiteren waren LTT-Techniken in der Lage diverse landschaftsbildende Ereignisse (einschließlich Erdrutsche) mit unterschiedlicher Größenordnung in verschiedenen geologischen Umgebungen zu erkennen, zu unterscheiden, und zu quantifizieren.

In Rift-Regionen hat das Rwenzori Gebirge hat vier schnelle Abkühlungs-/Exhumierungs-Ereignisse erlebt. 1) Das Silur-Devon-Ereignis (420-390 Ma) im Zusammenhang mit ~ 3,5 (1,5) km Krustenhebung als Reaktion auf das tiefe Erosionsereignis nach der Panafrikanischen Orogenese. 2) Das Trias-Ereignis (240-220 Ma), das eine Krustenhebung von ~3.0 km verursachte, verbunden mit schneller Abkühlung und einem großen Erosionsereignis am Ende des Karoo-Sedimentregimes. 3) Das Eozän-Miozän-Ereignis (52-10 Ma) führte zu einer durchschnittlichen Krustenhebung von ~ 3,0 (0,2) km. Die tektonischen Ereignisse aus dem frühen Eozän werden mit der Drift Indiens nach dem Beginn der östlichen Rift Aktivität assoziiert. 4) Das Pliozän-Pleistozän-Ereignis (3-2,5 Ma) verursacht ~ ≤2.0 km Krustenhebung entlang des Liegenden der Bwamba-Störung.

Das Gebiet um den Berg Samra hingegen hat fünf schnelle Abkühlung-/Exhumierungs-Ereignisse erlebt. 1) Das Neoproterozoische-Ereignis (775-640 Ma) verursachte ~ 5,8 (0,1) km an Krustenhebung als Reaktion auf die Akkretion und den Plutonismus während der EAO. 2) Das Kambrium-Devon-Ereignis (507-457 Ma) verursachte ~ 5,6 (0,2) km Krustenhebung in Folge des Post-EAO-Erosionsereignisses. 3) Das Karbon-Perm-Ereignis (390-230 Ma) führte zu ~ 4,2 (1,6) km Krustenhebung als Reaktion auf das herzynische tektonische Ereignis. 4) Das Jura-Kreide-Ereignis (170 bis 70 Ma) führte zu ~ 2,9 (0,5) km Krustenhebung als Folge des Auseinanderbrechens Gondwanas. 5) Das Oligozän-Miozän-Ereignis (27-22 Ma) verursachte Krustenhebung von ~ 1,3 (0,3) km als Reaktion auf das beginnende Rifting. Es wird zudem von einem weiteren Wiederaufheizungsereignis im Zeitraum der, mit dem Golf von Suez und dem vorhergehenden Abkühlungsereignis assoziierten, Anhebung berichtet, die eine durchschnittliche Absenkung von ~ 0,6 (0,3) km verursachte.

Das außergewöhnlich hohe Ruwenzori-Gebirge wurde in dem EARS Extensionsregime als Rift-Flanke in letzte zwei Stufen gebildet. Die letztere Bewegung verursachte das geneigte Anheben in der westlichen Flanke des Gebirges.

Die Anhebung der Albertine Riftflanken ist doppelt so hoch wie Anhebung der auf den Golf von Suez bezogenen Flanken, die auf eine zusätzliche Wärmekomponente während der Bildung des EARS hindeutet.

In vulkanischen Inseln; Fuerteventura hat zwei schnelle Abkühlungs-/Exhumierungsereignisse erlebt; eines begann vor ~ 20 Ma mit ~ 2,7 (0,5) km entsprechendem Gesteinshebungen, welches den Beginn des Fuerteventura Erdrutsches verursachte. Das andere wurde vor ~ 7 Ma eingeleitet mit entsprechend ~ 2,3 (0,2) km an Gesteinshebung, welches die Aufdomungsphase auf dem westlichen Teil von Fuerteventura ~ 5 Ma bildete. Letztendlich wurden diese Aufdomungen zur rezenten Oberfläche erodiert. Die Insel La Gomera erlebte ebenfalls zwei schnelle Abkühlungs-/Exhumierungsereignisse; das erste Ereignis zwischen ~ 10 und 7 Ma mit ~ 2,7 (0,2) km Gesteinshebung löste den La Gomera-Erdrutsch aus. Die zweite schnelle Abkühlung trat vor ~ 4 Ma ein, was zu ~ 2 km von Gesteinshebung führte. Schließlich führte die Abtragung der Topographie zur heutigen Landoberfläche.

Keywords: Low-temperature thermochronology; Long-term landscape evolution; Canary Islands; Landslide Dating; East African Rift System; Albertine Rift; Rwenzori Mountains; Gulf of Suez; ; Arabian-Nubian Shield; Rift initiation; Rift Flanks Uplift; zircon; apatite; fission-track; (U-Th-Sm)/He; t-T Modelling

TABLE OF CONTENTS

LIST OF FIGURES

LIST OF TABLES

1

INTRODUCTION

Topography is a dynamic state which changes continuously due to interaction between endogenic (tectonic) and exogenic (surface) processes over time (e.g., Beaumont et al., 1992; Willett, 1999; Zeitler et al., 2001). The endogenic activities can be as slow as hundreds of millions of years as in the case of orogenic belts or as fast as human lifetimes as in the case of volcanic island construction or destruction. The exogenic processes, on the other hand, can be as slow as the mechanical denudation rate in non-mountainous areas or as fast as sudden landslides or cliff falls. These endogenic and exogenic processes are significantly related to each other; tectonically uplifted areas affected intensely by surface processes (e.g., erosion and landslides). This intense effect, in turn, causes rock exhumation and cooling through lithospheric isostatic rebound (Molnar and England, 1990; Montgomery, 1994; Braun, 2002b; Braun and Robert, 2005).

The major endogenic and exogenic progresses were accounted for by the recent enhancement in low temperature thermochronology (LTT) techniques (e.g., Ketcham et al., 2007; 2009; Flowers et al., 2009; Shuster and Farley, 2009; Herman et al., 2010b; Gautheron et al., 2013) that lead to great improvements in quantifying and visualization of timing, trends and rates of the rock exhumation through the upper crust (Braun et al., 2012). The LTT-derived information, in turn, could be used to reconstruct the temporal and spatial development of topography (Brown et al., 1994; Gunnell, 2000; Braun, 2002b; Ehlers and Farley, 2003).

The LTT recent progresses have raised questions about the ability of these techniques to detect and quantify the earth's landscaping behaviour as a response to multiple processes of different magnitudes in various geologic environments. Moreover, other questions such as:

- Could LTT distinguish between landscaping behaviour as response to endogenic or exogenic event(s)?,
- Could a rapid exogenic event (e.g., landslide) be thermochronologically detected?, and
- How fast does the landscape changes in a particular region (e.g., volcanic island or continental rift)? were also raised.

The African continent (Fig. 1.1) has experienced a geological history of 3.8 Ga covering ~75% of the total history of the earth. It comprises seven main Archean cratons: the Nile, the Reguibat Shield, the Man Shield, the Congo, the Tanzania, the Zimbabwe and the Kaapvaal cratons, which were merged, covered and/or reworked later (Thomas et al., 1993). These cratons have experienced a series of major tectono-metamorphic cycles namely; Archean (>2.9 Ga), Ubendian (~2.0–1.8 Ga), and Kibaran (~1,200–900 Ma) (Leggo, 1974; Theunissen et al., 1996; Appel et al., 2005; Fritz et al., 2005). Afterwards, the African continent was formed by accretion of island arcs and microcontinental fragments into these Archean cratons during the Pan-African Orogeny (PAO) (~900-550 Ma; Kennedy, 1964). By end of the PAO, the supercontinent Gondwana was created with Africa in the centre of it. In the Jurassic-Cretaceous time Gondwana broke apart and initiated the opening of the Atlantic and Indian oceans, shaping the African continent (van Hinsbergen et al., 2011). Later on, the African tectonic regime was dominated by extensional forces, rifting and basin filling processes (Baker and Wohlenberg, 1971;Shackleton, 1978; Delvaux, 1991).

In order to answer the preceding questions, key areas (initiated rifts on old craton and volcanic islands on passive margin) from the African continent were chosen to represent important geologic environments that characterised by long-term dynamic topography.

Furthermore, these areas represent different processes, mechanisms, and rates of topographic changes. The selected key areas are:

1- The continental rifts; the Rwenzori Mountains from the eastern flank of the Albertine Rift and The Samra Mountain area from the eastern flank from the Gulf of Suez were chosen. The Rwenzoris are exceptionally high elevated (>5 km a.s.l) non-volcanic mountains within an extensional regime of the Western branch of the East African Rift System (EARS). While, the Samra mountain area is a low elevated (<0.7 km a.s.l) rift flank within the Red Sea/Gulf of Suez rifting system.

2- Volcanic islands; the islands Fuerteventura and La Gomera of the Canary islands were selected to study their basal complex (BC). The BC have experienced the entire history since transition from normal ocean-floor sedimentation to building up a discrete oceanic island, followed by island destruction. Such destruction expressed by several events of landslides and intense mass wasting which stripped the BC on Fuerteventura and La Gomera.

Examination of the nature of these key areas developed more question:

- How can exceptionally high mountains such as the Rwenzoris form in an extensional regime such as the EARS?
- What is the nature of the Rwenzoris' exhumation?
- Were the thermochronological ages reset during the rift initiation in either the Albertine Rift or the Gulf of Suez? If not, could the rift initiation be detected thermochronologically?

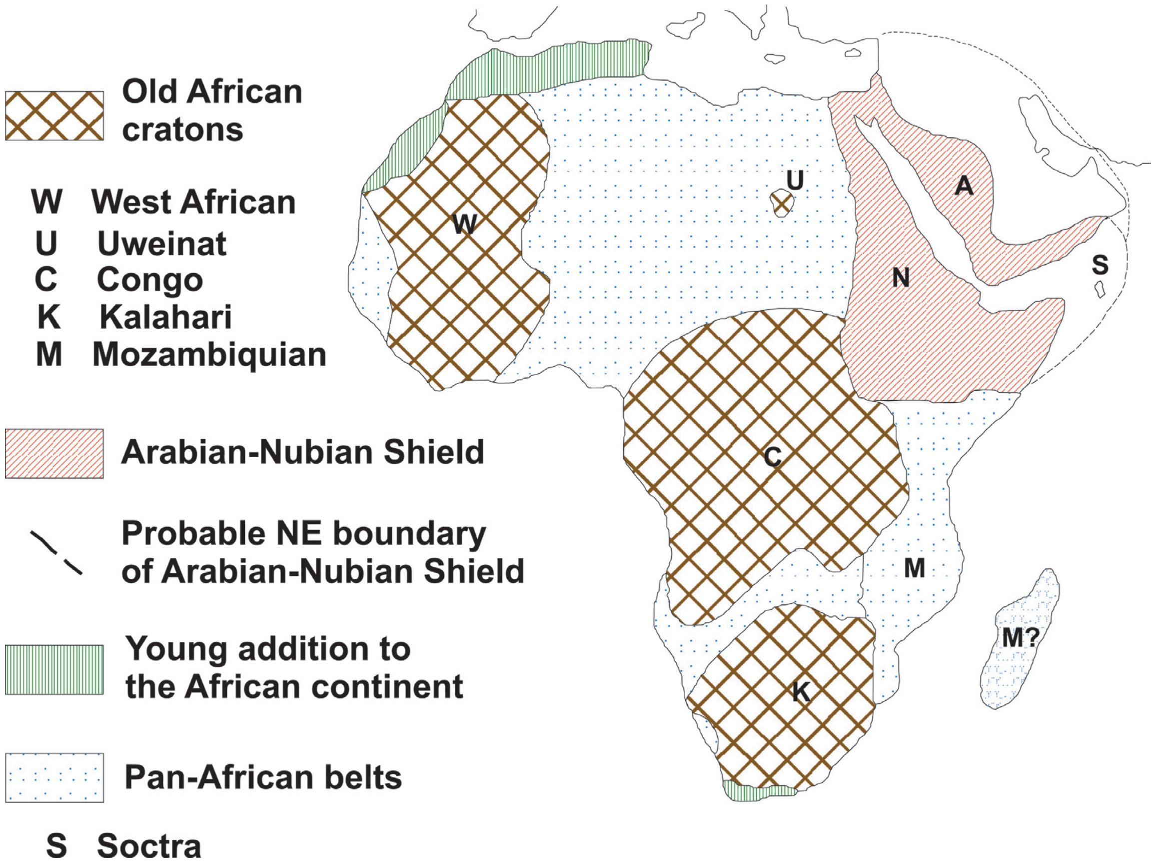

Fig. 1.1: Tectonic Map for African and Arabian plates (after Bentor, 1985 and Kennedy, 1964).

- Did the rift initiation overprint the preceding events of topographic changes or is it still in the thermochronological record?
- Did the Gulf of Suez flanks ever reach high elevations?
- Is there any clear difference between the thermo-tectonic history of the Albertine Rift and the Gulf of Suez that explains the difference in corresponding flank elevations?
- Is there a difference between the tectonic and erosional history of Fuerteventura and La Gomera or is it one cycle of events for a volcanic island?

The LTT techniques have been proven to be an efficient tool for these purposes in a variety of geological environments and settings (e.g., Hurford, 1986; Moore et al., 1986; Gleadow and Fitzgerald, 1987; Omar et al., 1989; Foster and Gleadow, 1992, 1996; Gallagher et al., 1994; Van der Beek et al., 1994; Cliff et al., 1996; , Van der Beek et al., 1998; Spiegel et al., 2007; Wipf et al., 2010; Bauer et al., 2013). The LTT techniques were used to reconstruct the thermal history by providing cooling ages of the rock through certain isotherms (Batt and Brandon, 2002; Reiners and Ehlers, 2005; Lisker et al. 2009). Furthermore, combining the LTT data with the time-temperature (t-T) models enables to predict both cooling and exhumation rates which in turn provides information about the coupled tectonic-erosion system behaviour over geologic time. Hence, a combination of LTT techniques; zircon and apatite fission track (ZFT, AFT), zircon and apatite (U-Th)/He (ZHe, AHe), was performed with t-T modelling during this study.

2

PLATE TECTONICS

CONTENTS

Plate tectonics is a unified theory explaining the main features of the Earth's surface. Plate tectonics was born by merging the sea floor spreading theory with the transform fault hypothesis (Kearey et al., 2009). Hess (1962) suggested a concept of "sea floor spreading" that explains the continental drift as a response to extension of oceanic basins. Oceanic basins extend by supplying new materials from the mantle through volcanic submarine swells in mid-ocean ridges (Menard, 1958; 1959; Heezen, 1960).The continental plates, on the other hand, are passive, less dense, and drift apart or together by the lateral movement of the oceanic crust. This lateral movement is believed to be produced by convection currents in the upper mantle (Fig. 2.1). Hess (1962) further proposed trenches at certain oceanic margins where the oceanic crust thrusts back into the mantle. These oceanic trenches are zones of volcanic activities and epicentres of high intensity earthquakes. The hypothesis of the "sea floor spreading" successfully explained the lithospheric behaviour in two directions between the mid-oceanic ridge and the oceanic trench but failed to provide any clues regarding timing and location at which this process could be terminated. To overcome that problem, Wilson (1965) proposed the concept of "transform fault" at which these features (the mid-oceanic ridges and the oceanic trenches) terminate without construction or destruction of the lithosphere instead the faulted bodies laterally slide past one another.

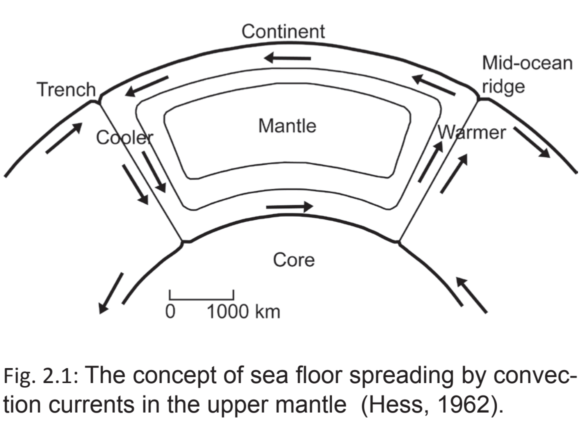

Fig. 2.1: The concept of sea floor spreading by convection currents in the upper mantle (Hess, 1962).

2.1 Wilson Cycle

Wilson (1966) develops a cycle that illustrates the progression of ocean construction (opening phase) and destruction (closing phase); also known as Wilson cycle. Wilson cycle describes the plate tectonics periodicity (Fig. 2.2). The opening phase begins with initial lithosphere thinning and breakup of a stable continental craton followed by the development of a thinned and rifted continental margin. These segments extend to sea floor spreading and eventually convert to a full oceanic basin while the two continents are drifting apart. The closing phase starts when a subduction zone develops, where the oceanic basin is thrusted into the mantle. Consequently, the continental plates drift together and eventually collide forming mountainous ranges. These mountains start to erode and develop to peneplain surfaces with time circling back to a stable cratonic stage.

2.2 Hotspot and Mantle Plume

From a plate tectonic point of view, volcanoes can be divided into two basic types; plate margins volcanoes (e.g., in mid-oceanic ridges and subduction zones) and intraplate volcanoes (Zhao, 2015). Although the majority of volcanic activities on the Earth occur at the plate boundaries, inraplate volcanoes represent an important fraction of it. Both the intraplate volcanic activities and the extraordinary huge ones at plate boundaries are generally identified as hotspot zones (Zhao, 2015). The hotspot creates upwelling and rifting in the continent (e.g., East African Rift System, Gulf of Aden/The Red Sea Rift System) or linear chains of islands and

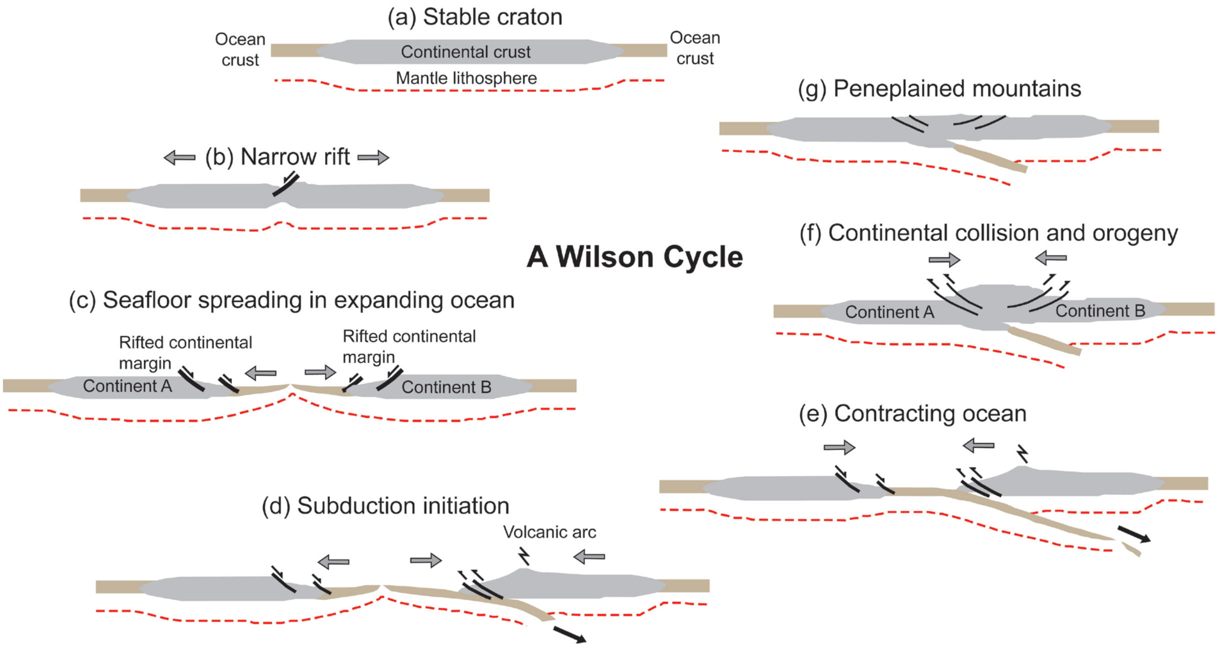

Fig. 2.2: The Wilson Cycle presenting: (a) continental craton; (b) rift initiation; (c) seafloor spreading onset develops to rifted continental margin in an expanding ocean basin; (d) subduction zone initiation; (e) a closing ocean basin; (f) continental collision and orogeny (Kearey et al., 2009).

seamounts in the ocean (e.g., Canary Islands).

Morgan (1971; 1972) considered the plume hypothesis as a source for the hotspots and the related volcanic activities where, the hotspot is a surface expression of the mantle plume. Therefore, it is characterized by zones of elevated heat flow, melts, active volcanism and high topography (e.g., Condie, 2001; Sleep, 2006; Ernst, 2007; Ito and van KeKen, 2007; Zhao, 2007).

The theory of plume mechanism consider a thermal layer deep in the Earth (Fig. 2.3) producing a plume of hot floating substances, where its conduit (100–300 km in diameter) rises rapidly through the viscous mantle. This fast pump up usually causes additional push on the plume head upward causing partial melting and fracturing in the lithosphere and 1-2 km of surface uplift. Afterwards, the magma rises through the fractures forming a large igneous province(s), basalt floods, and eruptions. The basalt floods can move for extended distances within the lithosphere as long as the plume conduit supplies. At this point the plume head diameter could extends to 500-3000 km providing magmatic materials for a series of magmatic activities along hotspot tracks that form with time (Sleep, 2006; Humphreys and Schmandt 2011; Zhao, 2015).

2.3 Rift Initiation

Rifts are regions characterised by restricted extension and thinning of the Earth's lithosphere representing an initial phase of continental breakup (Kearey et al., 2009). They are usually accompanied by collapsing through faulted blocks, accumulation of syn-rift sediments in their axis and uplifting in their flanks (Ziegler, 1992; Allen and Allen, 2005; Sachau and Koehn, 2010). These initiated rifts convert to a passive or a continental rifted margin if it extended to allow ruptures from the lithosphere to form a new oceanic crust.

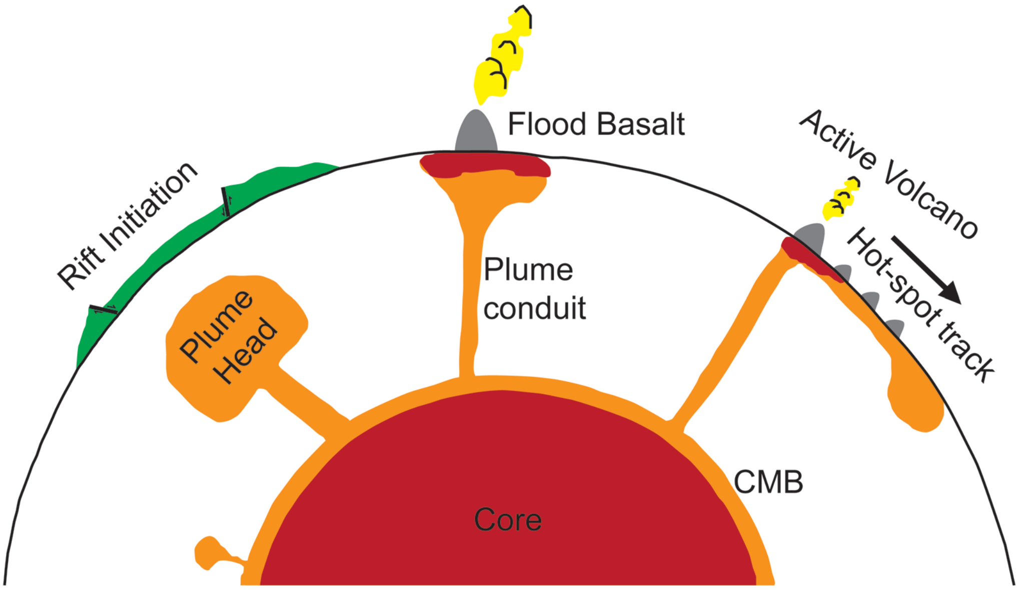

Fig. 2.3: The mantle plume and its phases of development (Humphreys and Schmandt, 2011).

Rifts-producing extensions are effective when the lithospheric horizontal tensional stresses are sufficient enough to break the lithosphere. These stresses could be inherited from earlier tectonics or just caused by the extension (Kearey et al., 2009). A combination of factors could produce such stresses, among them; the relative plate motions, upwelling of the asthenosphere and gravitational forces produced by differentiation in crustal thickness (Husimans et al., 2001; Kearey et al., 2009).

Rift flank uplift is a common phenomenon produced by isostatic rebound to the rifting disturbance of the isostatic equilibrium between densities of the crust and the sub-crustal lithosphere (McKenzie, 1978). This isostatic rebound could be produced by crustal stretching through faulting that reduces the load from the top of the lithosphere (Karner et al., 2000), crustal bending due to footwall uplifting and hanging-wall subsidence in normal faults (Kusznir and Ziegler, 1992), or depth-related lithospheric stretching where the mantle lithosphere extends beneath rift flanks (Royden and Keen, 1980; Rowley and Sahagian, 1986; Sachau and Koehn, 2010). The topography deform till the balance between the crust and the sub-crustal lithospheric densities achieved (McKenzie, 1978). Therefore, subsidence in ridges and uplifting in flanks of a rift are usually related (e.g., subsidence to uplift ratio in EARS is about 2:1 to 3:1) (Sachau and Koehn, 2010).

The East African hotspots are underlain by significant seismic low-velocity features (Fig. 2.54) in the mantle (Zhao, 2015). These features are associated with the African superplume (Maruyama, 1994; Ritsema et al., 1999; Zhao, 2001b; 2004; Montelli et al., 2006; Chang and Van der Lee, 2011; Davies et al., 2012; Hansen et al., 2012; Brandt, 2013; Mulibo and Nyblade, 2013; Zhao et al., 2013). The African superplume extends from the core-mantle boundary to the lithosphere providing the driving forces in eastern Africa for the Cenozoic rifting, volcanic activities and plateau construction (Mulibo and Nyblade, 2013; Zhao, 2015).

The plume head is located under the Tanzanian craton's lithosphere (Nyblade et al., 2000; Huerta et al., 2009). While, the hotspots are situated beneath the Afar, the northern Ethiopian rift, the Eastern and the

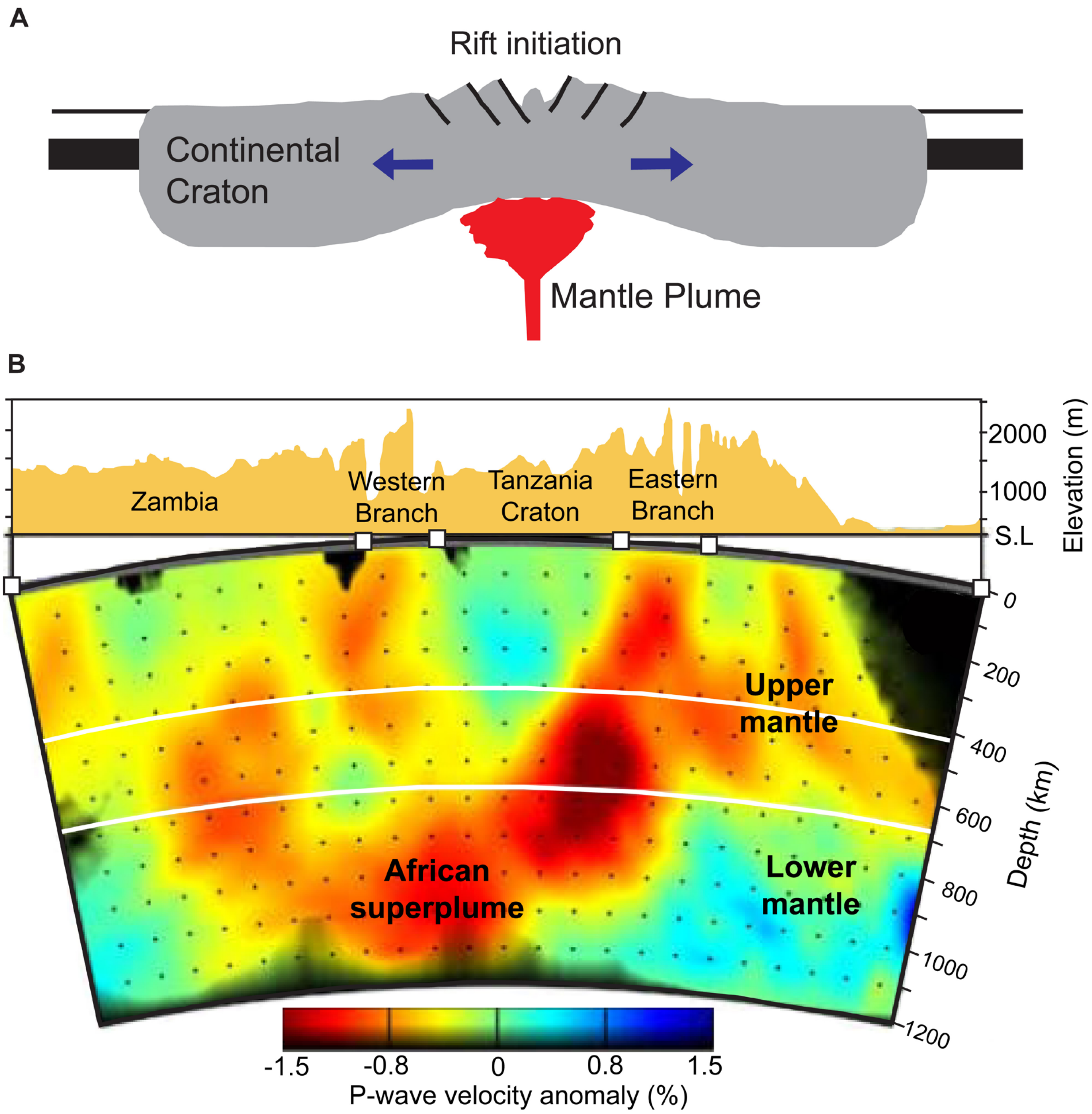

Fig. 2.4: (A) Stage b in Wilson cycle (Fig. 2.2) for rift initiation with the effect of Mantle plume. (B) Vertical cross-section of the whole mantle P-wave tomography from the surface down to the core-mantle boundary (CMB) beneath the EARS. Sowing the African superplume and hotspot anomalies beneath the Eastern and Western branches of the EARS. The perturbation coloured scale refers to velocities (red is slow). The white lines refer to the 410- and 660-km discontinuities of the mantle transition zone. Areas with hit counts of <5 are darkened. Small black squares represent station locations. (Mulibo and Nyblade 2013).

western branches of the EARS (Bastow et al., 2005; Benoit et al., 2006; Jakovlev et al., 2013). The EARS associated hotspots are located 100-200 km below the Eastern and Western rifts. While, at depths >350 to 900 km the low seismic anomalies become dominant beneath southern and central the East African Plateau (Mulibo and Nyblade, 2013).

2.4 VOLCANIC ISLANDS IN PASSIVE MARGINS

Generally, the hotspot related volcanic island chains are associated with an extensive lithospheric swell. These islands represent about 10% of the earth's topography making these islands significant factor in the Earth's landscaping (Crough, 1979; Kearey et al., 2009). The volcanic island chains are formed on an older oceanic crust from successive basaltic edifices where the lower are tholeiitic and the upper are alkaline (Karl et al., 1988). Their geochemical composition indicates a combination of juvenile mantle and depleted asthenosphere components (Schilling et al., 1976).

The Canary hotspot is underlain by two mantle plumes. One extends from the upper mantle to ~ 1500 km depth, the other from the core-mantle boundary to ~ 2200 km depth. The two plumes are connected by a weak seismic anomaly of low-velocity zone in the mid mantle (Fig. 2.55) (Zhao, 2015). Furthermore, the seismic receiver function data supports the presence of magma and partial melting beneath the Canary Islands (Lodge et al., 2012).

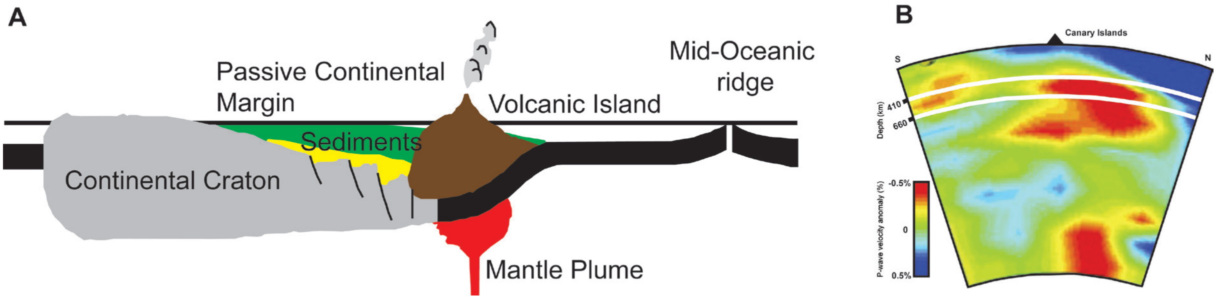

Fig. 2.5: (A) Stage c in Wilson cycle (Fig. 2.2) for volcanic island initiation on passive margin through interaction with Mantle plume. (B) Vertical cross section of whole mantle P-wave tomography from the surface down to the core-mantle boundary (CMB) beneath the Canary hotspot volcanoes in the Atlantic Ocean. The perturbation coloured scale refers to velocities (red is slow). The white lines refer to the 410- and 660-km discontinuities of the mantle transition zone (Zhao, 2007).

3

GEOLOGICAL BACKGROUND

CONTENTS

3.1 LANDSLIDES

Landslides and intense mass wasting are common features during volcanic growth. Most of the Andean volcanic cones with altitudes exceeding 2500 m have experienced collapse (Francis, 1994). The Japanese Quaternary volcanoes show more than 100 debris avalanche deposits (Inokuchi, 1988). Destruction and destabilization of all or parts of a volcanic edifice could be achieved on a short time-scale (weeks to months), or may develop on a longer time-scale (over thousands or tens of thousands of years).

Many factors would, altogether or some of them, integrate to trigger the landslide/mass wasting event occurrence in a volcanic island growing edifice, among them; a) overstepping of stratified materials on outward steep slopes (Murray and Voight, 1996), b) changes in edifice pore pressure which would be caused by magma reservoir refill, dyke emplacement (Day, 1996; Elsworth and Voight, 1996), large change in sea level and/or high precipitation rates commonly associated with elevated relief (McGuire, 1996), c) changes in morphology with endogenic intrusions (by plutonism and dikes) which decrease edifice stability and exogenic (by extrusion) addition of material at the surface leading to over-steepening and overloading (McGuire, 1996), d) nature of the sub-volcanic strata which are generally clay-rich, water-saturated and pelagic marine sediments characterized by low shear tendency and fast compaction beneath the volcanic weight which lead to the development of lateral spreading (Iverson, 1995; Smith et al., 1999; Oehler et al., 2005), e) dike swarms injections and rifting associated with dike emplacement which are commonly associated with a structural collapse (Siebert, 1984; McGuire, 1996), f) local seismicity, g) some discrete events, such as the emplacement of the dacite crypto-dome at Mount St Helens between March and May 1980, could speed-up the onset of instability (McGuire, 1996). h) environmental factors and major climatic changes (McGuire, 1996). Such environmental factors are important in controlling the possibility of landslide occurrence on volcanic islands by controlling many factors such as precipitation, changing sea levels, flanks overstepping, relief elevation, affecting the pore pressures and the sub-volcanic strata.

3.2 AREAS OF STUDY

3.2.1 The High Elevated Rift Flank (The Rwenzori Mountains)

The Rwenzori Mountains are unusually up to 5 km a.s.l high, non-volcanic mountains striking in extensional environment of the EARS (Fig. 3.11), representing a challenging problem for the geodynamics (Kaufmann and Romanov, 2012). The Rwenzori Mountains have been studied kinematically, structurally, geodynamically, stratigraphicaly, and chronologicaly (e.g., Michot, 1938; McConnell, 1959; Livingstone, 1967; Tanner, 1971; Ollier and Pain, 2000; Ring, 2008; Koehn et al., 2008; 2010; Link et al., 2010; Sachau et al., 2011; Bauer et al., 2012). While, the exhumation history of the mountains' different blocks is less known (MacPhee, 2006; Bauer et al., 2013).

The Rwenzoris are horst blocks with 120 km length and 50 km width and glaciated beaks, consisting mainly from metamorphic basement rocks of Archean and Proterozoic ages. The Rwenzoris represent the eastern flank of the Neogene Albertine Rift that represents the northern extend of the western branch of the EARS. The western flanks of the Albertine Rift have an average altitudes of ~1.5 km and elevated peaks of ~2–3 km (Ring, 2008).

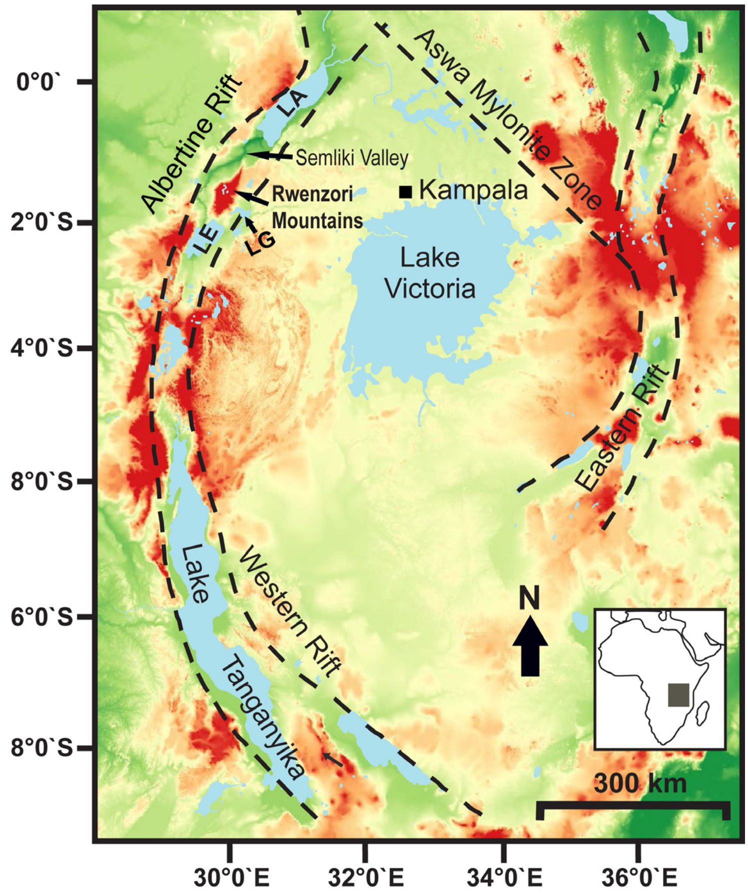

Fig. 3.1: The East African Rift System map representing important landmarks and main tectonic features. The Rwenzori Mountains is located within the Albertine rift (Sachau et al., 2015). The inset shows location of the EARS within the African continent.

3.2.2 The Low Elevated Rift Flank (The Samra Mountain Area)

The Samra mountain area is located at West-Central Sinai, occupying an area of about 120 km^2 representing the eastern flank of the Gulf of Suez (Fig. 3.22). The area is mountainous with a moderate relief whose highest peak is the Gebel Samra (693m). The basement rocks consist mainly of gneisses, schist, metagabbro-diorite complex, migmatites, old (syn-orogenic) granite and young (post-orogenic) granite intruded by sets of dikes of different compositions and trends. They represent the northern end of the East African Orogenic (EAO) basement complex where the basement rocks are unconformably overlain by Lower Paleozoic sediments.

3.2.3 Canary Islands (Fuerteventura and La Gomera)

The Canary archipelago comprises seven islands located 100–700 km western the African continental margin (Fig. 3.33). The spatial, chronological, morphological and evolutionary history for the Canaries volcanism shows a propagation trend from east to west due to the movement of the African plate above a mantle plume (Carracedo et al. 1998; Stillman, 1999; Allibon et al., 2011). Commonly, the Canary Islands can be separated into an internal group; Fuerteventura and Lanzarote, with sub-parallel alignment to the African continental margin and an external group; La Gomera, El Hierro, La Palma, Tenerife and Gran Canaria, with an E–W alignment (Allibon et al., 2011).

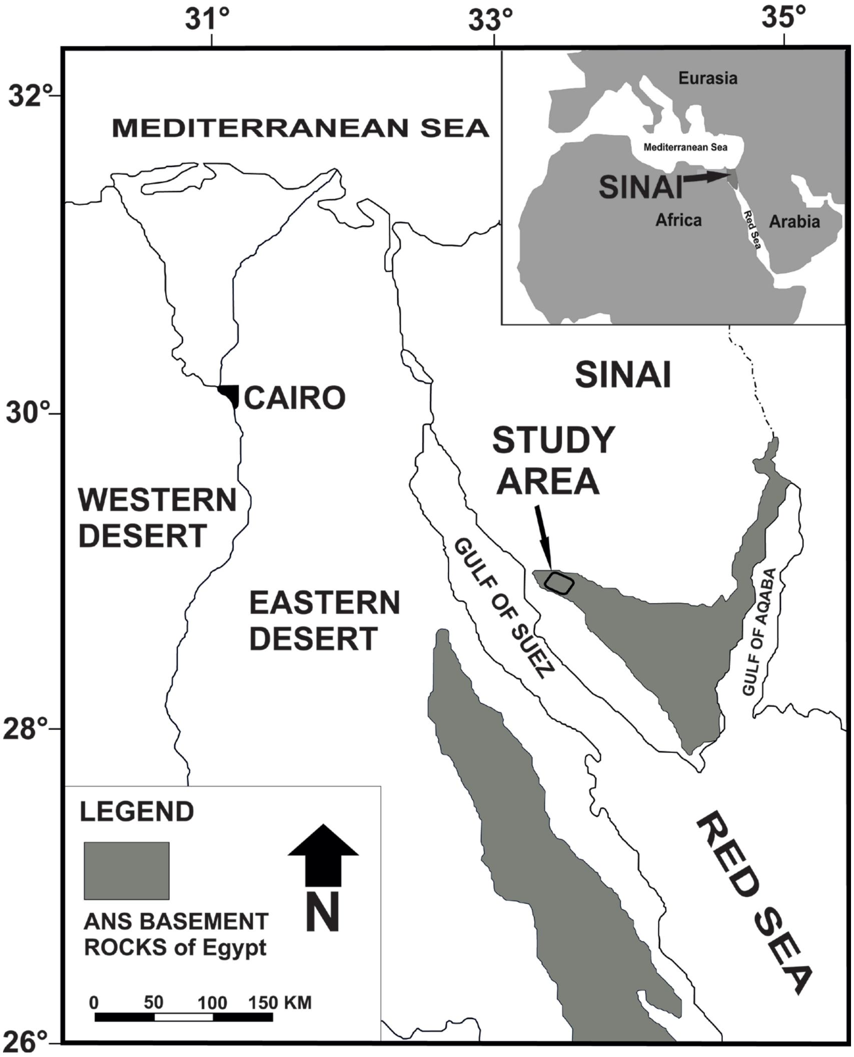

Fig. 3.2: Location map of the Samra mountain area, Gulf of Suez, Gulf of Aqaba, the Red Sea and the ANS in Sinai. The inset shows Sinai location with respect to African, Arabian and Eurasian plates.

Lithologically, each island consists of two major units: the Basal Complex (BC) which builds up of a set of sedimentary rocks, submarine volcanics, plutonic intrusions and major dike swarms inserted mostly during the submarine (pre-shield) phase (Bravo 1964; Fúster et al., 1968a; Stillman et al., 1975; Fúster et al., 1980; Le Bas et al., 1986; Stillman, 1987; Casillas et al. 2008a), and a more recent Subaerial Volcanic Series (SVS) consist of Miocene and Pliocene–Quaternary sequence (Fúster et al., 1968a; Coello et al., 1992; Ancochea et al., 1996; 2006). The BC always reveal an interesting record of shifting from ocean-floor deposition to building up a distinct oceanic island (Stillman et al., 1975). The BC was exposed to the surface due to several landslides and intense mass wasting, comprising the island entire geologic record. Therefore, this study concentrates on the BC of Fuerteventura and La Gomera islands.

Fuerteventura Island (Fig. 3.33); is the oldest, eastern-most and nearest to the African continent, with wide exposures of submarine seamount stage, unclear erosional history and belongs to the internal islands group. Fuerteventura has being shaped by three distinct nearby large volcanoes composing;

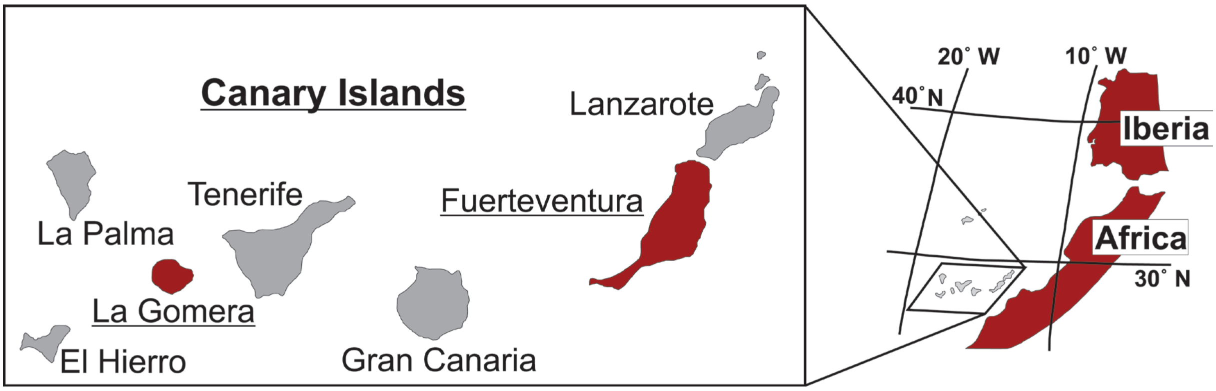

Fig. 3.3: Location map of the Canary Islands with respect to Africa and Iberia, where underlining Fuerteventura and La Gomera Islands.

the Southern (SVC), the Central (CVC), and the Northern (NVC) (Ancochea et al., 1996). On this island, the BC is only exposed in the western part along with the Miocene volcanics because of a Miocene giant landslide (Stillman, 1999).

La Gomera Island (Fig. 3.33); is the smallest, lesser known among all the Canary Islands, exclusively without Quaternary volcanicity, prolonged volcanic edifice, and represents the external islands group. La Gomera has been shaped by a huge single complex where the BC is only exposed in the northwestern sector together with the Miocene volcanics because of Late Miocene landslide(s) (Ancochea et al. 2006; Herrera et al., 2008; Casillas et al., 2010).

3.3 Geological Settings

3.3.1 The High Elevated Rift Flank (The Rwenzori Mountains)

The East African region has experienced a long history with several orogenic cycles since Meso-Archean till Recent times (Petters, 1991; Aanyu and Koehn, 2011). The major Precambrian tectono-metamorphic cycles are Archean (>2.9 Ga), Ubendian (~2.0–1.8 Ga), Kibaran (~1,200–900 Ma), and the Pan-African (~900–500 Ma) (Leggo, 1974; Theunissen et al., 1996; Appel et al., 2005; Fritz et al., 2005). While, the Phanerozoic started by deformations led to intense erosion events affected the Pan-African basement complexes to form peneplain surfaces in East Africa (Fabre, 1988; Said, 1990) and regional unconformity in Congo basin (western the area of study) and Western Africa (Daly et al., 1992; Griesse, 2005; Guiraud et al., 2005). Afterwards, the tectonic regime was dominated by rifting, extensional forces and basin fillings processes (Baker and Wohlenberg, 1971;Shackleton, 1978; Delvaux, 1991). Which started in the western rift region by the Permo-Triassic Karoo rifting event that developed grabens and the corresponding Karoo sediments deposition which ended by a widely recognised major erosional event (e.g., Wopfner, 1990; 1993; Delvaux, 1991). That was followed by the Cenozoic rifting phases which formed the East African Rift System (EARS).

The Rwenzoris blocks are captured between two segments of the Albertine Rift (the northern extend of the western rift) developing against one another (Koehn et al., 2008; 2010). The horst blocks are extraordinarily high surrounded by the rift grabens of Lake Albert to the north, Semliki Valley to the west, Lake Edward to the south and Lake George to the southeast (Fig. 3.11) (Bahat and

Mohr, 1987;Schlueter, 1997; Karner et al., 2000). The Rwenzoris lithologies comprises; Archean and Paleoproterozoic schists, gneisses and amphibolites, lesser plutonic rocks of diverse metamorphic overprint and quartzite (e.g., Michot, 1938; McConnell, 1959;Tanner, 1971; Link et al., 2010), and Pleistocene to Holocene glacial sediments in the depressions (Livingstone, 1967; Bauer et al., 2010b).

From north to south the Rwenzoris can be differentiated into three different blocks, the northern block of a long and narrow nature, the central block with the high-peaks and extensive widths, and the southern block with declining altitudes and widths (Fig. 3.4). The initial landscaping of the Rwenzoris were shaped by fluvial erosion and readapted by glaciations (Ollier and Pain, 2000), as signified by wide U-shaped valleys and differentiated blocks movement along faults (Bauer et al., 2010b; 2012; 2013). The slope is more abrupt on the western flank of central Rwenzoris than on the eastern one. The slope of the western flank of central Rwenzoris is much steeper (slope: 0.22) compared to that

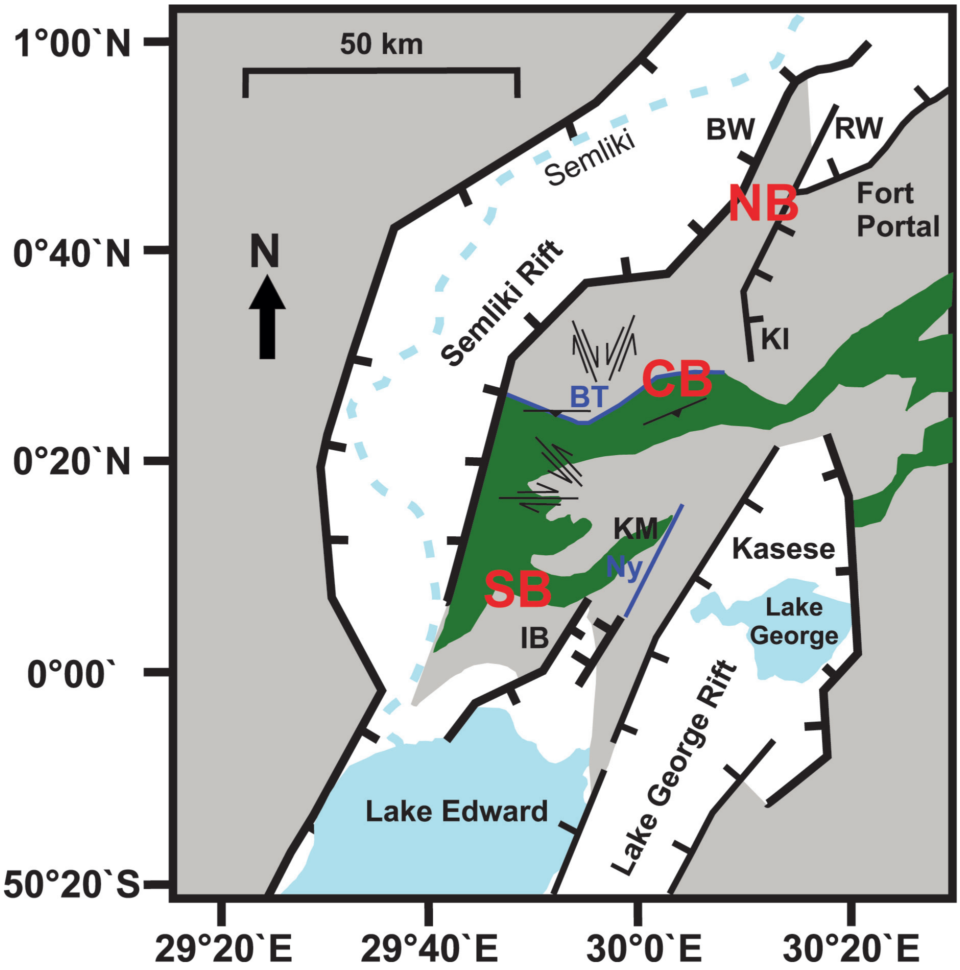

Fig. 3.4: Simplified geographical and geological overview map of the Rwenzori area (Link et al., 2010; Sachau et al., 2015). Gray units represent gneisses of the Gneissic-Granulite Complex and sandstones, conglomerates, and argillaceous sediments of the Kibaran Belt. Green units represent the Buganda-Toro Belt, consisting mainly of schists, amphibolites, and quartzites. Thick black lines mark major boundary faults of the rifts and within the Rwenzori horst, blue lines mark important ductile shear zones. Thin black lines indicate populations of small brittle faults. NB; northern block, CB; central block, SB; southern block of Rwenzori Mountains, BT; Buganda-Toro shear, Bw; Bwamba fault, Ny; Nyamwamba ductile shear zone, IB; Ibimbo fault, RW; Ruimi-Wasa fault, KI; Kisomoro fault.

of the eastern flank (slope: 0.11) (Bauer et al., 2013). That asymmetry can be illustrated by a sharply distinct fault escarpment in the western flank cut by the Bwamba bound-fault against the adjacent Semliki rift valley (Koehn et al., 2008). While, the eastern flank shows a complex array of faults causing a gradual decrease in topography (Fig. 3.4). The northern block of the Rwenzoris is bounded on its eastern side by the Ruimi-Wasa fault, while, the northern part of the central block still connected to the Victoria plate. Within the Rwenzoris itself, the central block of the horst apparently has been distressed by various stress fields as well as thrust trending northward. Comprising not less than three strike slip movements with compression at N–S, NW–SE and E–W trends and normal faults with mixed normal and strike slip movements (Koehn et al., 2008, 2010; Ring, 2008; Link et al., 2010; Sachau et al., 2011). The northern and the southern blocks of the Rwenzoris represent one major fault striking parallel to the mountain range and some minor faults striking perpendicular to it.

The EARS is ~3000 km long, controls much of East Africa, and extends from Afar triple junction in the north to Mozambique in the south (Ebinger, 1989a, b;Ring, 1993; Koehn et al., 2008). The EARS is fractured into Eastern and Western Branches (Fig. 3.11) around the mechanically resistant Tanzanian Archean Craton following the mechanically weaker mobile Proterozoic belts (McConnell, 1972; Ebinger, 1989a; Ring, 1993; Morley, 1999; Nyblade et al., 2000). The rifting processes have started in Palaeogene times through the earliest volcanic activity in Turkana region on the Kenyan-Ethiopian border (45-37 Ma; Furman et al., 2006). These processes still active creating horst and graben structures with vast escarpments (Petters, 1991; Bauer et al., 2010b). Where, the rift flanks have reasonable elevations (1-2.5 km) in match with the flexural isostatic rebound based kinematic models (Weissel and Karner, 1989; Ebinger et al., 1991; Upcott et al., 1996; Karner et al., 2000).

The western branch of the EARS (the Albertine Rift represents the northern part of it) extends over ~2100 km (Fig. 3.11) from Lake Albert in the north to Lake Malawi in the south. It was initiated in Oligocene-Miocene times by linking originally isolated basins with rifting to the north and the south (Ebinger, 1989; Morley, 1999; Bauer et al., 2010b; Roberts et al., 2012) (Fig. 3.11). The main volcanisms here occurs in four episods; at ~25 Ma in Rukwa basin (Roberts et al., 2012), ~12 Ma in Virunga, 9–8 Ma in the Rungwe and Kivu regions, ~70 ka in the Toro-Ankole region (Boven et al., 1998; Kampunzu et al., 1998), and ≤8 ka the carbonatites of Fort Portal (Barker and Nixon, 1989). The Western Rift, compared to the Eastern Rift, is probably younger with minor volcanicity, higher seismic activity (Morley et al., 1999; Woelbern et al., 2010), is identified by rift related deep lakes, and steep fault escarpments with kilometres-scale uplift next to the graben floor (Bauer et al., 2012).

Generally, Bauer et al., 2010b summarized the following stages for the Western Rift evolution; 1) at ~20–18 Ma started faulting and subsidence in region of the Albertine Rift (Abeinomugisha and Mugisha, 2004; Delvaux and Barth, 2010), 2) the ~12 Ma volcanicity, faulting and subsidence in the Virunga Province (Ebinger, 1989), 3) at ~10–8 Ma started the tectonic activities in Lake Albert rift basin and Lake Kivu, 4) at ~8.5–8 Ma initiated the main period of rifting and flanks uplift in the Albertine rift region (Ring et al., 1992; Ebinger et al., 1993; Ring and Betzler, 1995), 5) at ~3–2 Ma a fault movement caused uplifting in the Albertine Rift region (Pickford et al., 1993; Ring, 2008). The last tectonic movement was proposed to be responsible for the Rwenzoris exhumation and the related tilting in the rifted basins

(Ebinger, 1989; Pickford et al., 1993; Taylor and Howard, 1998). Furthermore, caused splitting of the palaeo-Lake Obweruka which was presented from ~7.5 to 2.5 Ma and covered the whole Albertine Rift region into the present Lakes Albert and Edward (Pickford et al., 1993; Taylor and Howard, 1998; Van Damme and Pickford, 2003).

Thermochronology of the EARS; Many thermochronological studies were applied on the different parts of the rift systems in the EARS using different LTT methods giving a protracted cooling history. Although, the given cooling ages shows a wide scatter, they could be collectively categorized into main cooling age groups; 1) ≤497 Ma (ZHe ages from Albertine rift flank, Bauer et al., 2015), 2) ~350-300 Ma (AFT ages from Malawi and Rukwa rifts, Van der Beek et al., 1998; ZFT and AFT ages Albertine rift flank, Bauer et al., 2015), 3) ~200-150 Ma (AFT ages from Central Kenya, Foster and Gleadow, 1992, 1996; AHe ages Albertine rift flank, Bauer et al., 2015), 4) ~85-30 Ma (AFT ages from Central Kenya, Foster and Gleadow, 1992, 1996; Malawi and Rukwa rifts, Van der Beek et al., 1998), 5) ~30 Ma (AHe ages from Kenya rift, Spiegel et al., 2007; Ethiopia, Pik et al., 2003; 2008).

These cooling ages were interpreted as episodes of rapid exhumation and denudation which could be collectively categorized into; 1) ~450-400 Ma (southern block of Rwenzoris, Bauer et al., 2013; Albertine rift western flank, Bauer et al., 2015), 2) ~250-200 Ma (Central Kenya, Foster and Gleadow, 1992, 1996; Malawi and Rukwa rifts, Van der Beek et al., 1998; northern block of Rwenzoris, Bauer et al., 2010b), 3) ~175-115 Ma (Central Kenya, Foster and Gleadow, 1992, 1996; Eastern Tanzania, Nobel et al., 1997; Malawi and Rukwa rifts, Van der Beek et al., 1998; central block and western flank of the northern block of Rwenzoris, Bauer et al., 2010b), 4) ~70-60 Ma (Central Kenya, Foster and Gleadow, 1992, 1996; Eastern and Southern Tanzania, Nobel et al., 1997; Kenya rift, Spiegel et al., 2007; central block of Rwenzoris, Bauer et al., 2010b), 5) ~50-40 Ma (Malawi and Rukwa rifts, Van der Beek et al., 1998; Kenya rift, Spiegel et al., 2007; central block of Rwenzoris, Bauer et al., 2010b), 6) ~33-11 Ma (Ethiopian, Pik et al., 2003, 2008; Kenya rift, Spiegel et al., 2007; central block of Rwenzoris, Bauer et al., 2010b).

Only few thermochronological studies were reported from the Rwenzori Mountains (MacPhee, 2006; Bauer et al., 2010b; Bauer et al., 2013). The Rwenzoris' northern block gives ZHe ages between 451.7±7 and 348.1±8.4 Ma (MacPhee, 2006; Bauer et al., 2010b), AFT ages between 195±8.4 Ma and 85.3±5.3 Ma (Bauer et al., 2010b), and AHe ages between 209.9±6 and 66.8±1.5 Ma (MacPhee, 2006; Bauer et al., 2010b). Bauer et al., 2012 recognized that the samples on the western flank of the northern block have younger AFT ages than those on the eastern flank. While, the central block gives ZHe ages between 477.3±10.7 and 309.1±6.2 Ma (MacPhee, 2006; Bauer et al., 2010b), AFT ages in the northern part of the central block mainly scatter around 130 Ma and in the southern part scattering around 300 Ma (Bauer et al., 2010b), and AHe ages are between 113.4±2.4 and 24.9±0.5 Ma (MacPhee, 2006; Bauer et al., 2010b). Whereas, the southern block shows ZHe ages between 540.2±13.0 and 376.4±7.5 Ma (Bauer et al., 2013) and AFT ages between 330.3±58.3 Ma and 225.5±20.6 (Bauer et al., 2013).

3.3.2 The Low Elevated Rift Flank (The Samra Mountain area)

Sinai Peninsula forms a small part of the Arabian-Nubian Shield (ANS) along the eastern edge of the Gulf of Suez (Fig. 3.22). The ANS basement rocks outcrop over ~14,000 km^2 in southern Sinai, where the Samra mountain area occupy the northwestern corner of it. The growth of the ANS was through the East African Orogeny (EAO) formed via accretion of continental fragments, island arcs, and oceanic plateaus during the 900-650 Ma interval (Gass 1982, Kröner 1979, Engel et al. 1980, Fleck et al. 1980, Shackleton et al. 1980, Shimron 1980, Greenberg 1981, Reymer 1983, Ries et al. 1983; Stern, 1994; Meert and Van der Voo, 1997; Meert, 2003).

In general, the ANS basement rocks are mainly; (1) syn-orogenic metasediments and metavolcanics formed in the earliest stage of the EAO with formation ages extended from 820 to 750 Ma (e.g., Kröner et al., 1990; 1994), generally limited to the lower greenschist facies and rarely achieve the amphibolite facies conditions (Bentor, 1985), (2) late-orogenic older granites (mainly diorite and trondhjemite) created through a compressional regime with formation ages between 750 and 610 Ma (e.g., Stern and Hedge 1985; Moghazi, 1999), (3) post-orogenic younger granites with 12 to 1 relative abundance against the older granite in Sinai (Bentor, 1985), formed between 610 to 550 Ma (Greenberg 1981; Stern and Hedge 1985; Beyth et al. 1994) synchronous with an extensional collapse stage by the end of the EAO (e.g., Dewey, 1988; Platt and England, 1993), and (4) succeeding sets of dikes (590-550 Ma; Stern and Hedge 1985; Stern and Manton 1987) of bimodal chemistry (rhyolitic and basaltic), indicating the continuity of the extensional conditions (Fig. 3.5).

The basement complex was eroded by Cambrian time and cycles of fluvial to near shore marine sediments with Lower Cambrian age fossils were deposited (Said, 1990; Seilacher, 1990; Bosworth et al., 2005). That deep erosion is related to crustal thickening along subduction zones during the EAO (Karig, 1974; Hussong et al., 1976; Gloss and Shreve, 1988; Von Huene, and Lallemand, 1990; Von Huene, Scholl, 1991). Afterwards, a period of tectonic stability characterized by platform sedimentation has conceded (Alsharhan and Nairn, 1997). This was interrupted by number of vertical movements and unconformities (e.g., Vermeesch et al., 2009). Hereafter, the Hercynian (Variscan) tectonic event occurred during the Devonian-Carboniferous by collision between Gondwana and Laurasia (Zeigler, 1989; Stampfli et al., 2002; Craig et al., 2008; Dixon et al., 2010). This collision caused the dominant northward dipping of Sinai to be reversed into southward (Klitzsch, 1986) as well as strong uplifting and erosion by Late Carboniferous (Gvirtzman and Weissbrod, 1985; Klitzsch, 1986; Bojar et al., 2002). Therefore, the lower Paleozoic sediments were completely eroded from Sinai except only for minor localities (e.g., end of Wadi Baba, 130 m Cambrian (Moustafa and Yousif, 1993) plus 225 m of mainly dolomitic Carboniferous sediments (Klitzsch, 1990) at the eastern border of the studied area) (Fig. 3.5). While, a complete lower Paleozoic succession of 2 to 2.5 km thickness was preserved in south Jordan and Saudi Arabia (Kohn et al., 1992). Afterwards, the Eastern Mediterranean basin was opening during the Triassic-Early Jurassic (Garfunkel and Derin, 1985). Then, Gondwana started to broke apart in Jurassic-Cretaceous times leaving its evidence in the Egyptian ANS by localized volcanic flows of the late Jurassic-Early Cretaceous age (Hashad, 1980; Meneisy, 1986). Consequently the old northward dipping and drainage became dominant again (Klitzsch, 1986). Simultaneously, in mid-Jurassic, the mid-Atlantic opening was initiated causing Africa to move eastward with respect to Eurasia. This movement generated a sinistral shear on various fractures of the North African continent (Dewey et al. 1973) and an extensive alkaline magmatic activity and

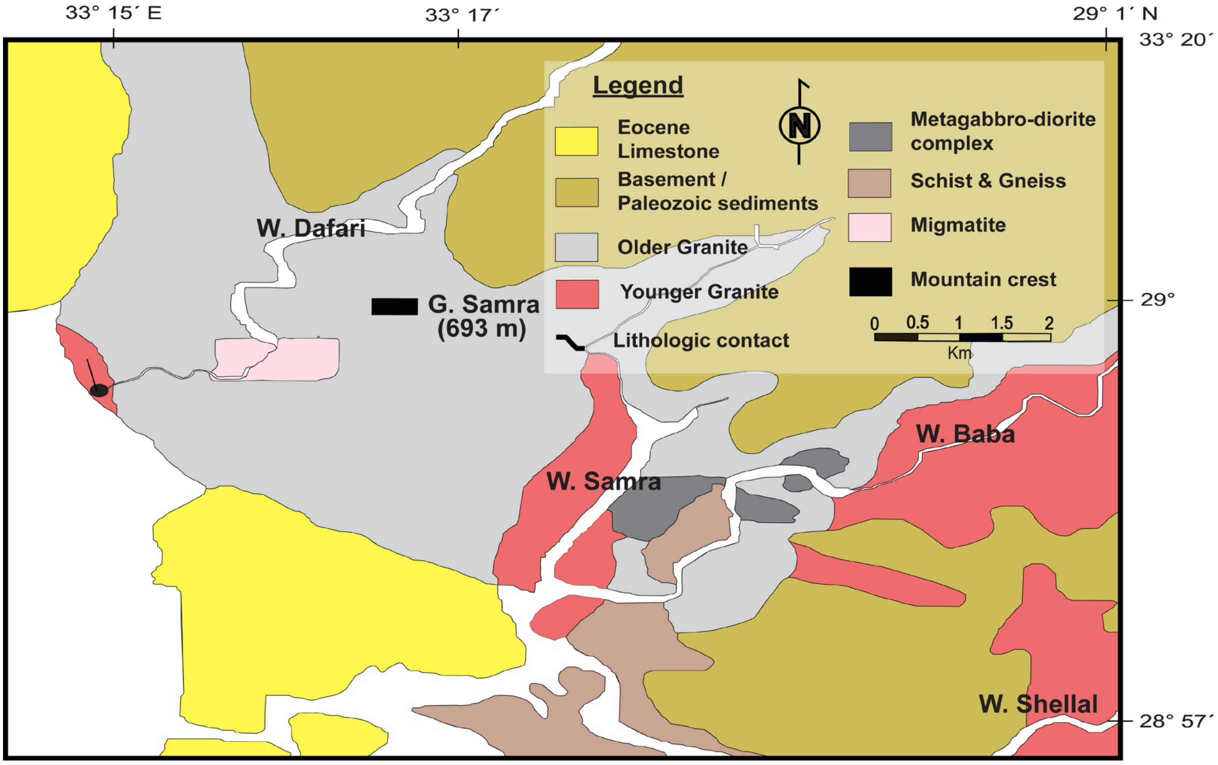

Fig. 3.5: Geologic map of the samra mountain area (modified after El Bialy, 2004).

normal NW-SE and N-S striking faults at the northern Egyptian margin (e.g., Girdler, 1985; Greiling et al., 1988). Furthermore, it caused the formation of the broad northeast trending folds of the Syrian Arc domal system (e.g., Awad, 1984; Said, 1962; Sestini, 1984). Finally, the Oligocene-Miocene continental rifting that formed the Red Sea-Gulf of Suez was developed causing uplift and erosion in the ANS along their flanks and producing basaltic dikes and normal faults.

The Gulf of Suez is a large, elongated and semi-enclosed shallow sea continental rift with ~300 km in length and ~50 km in width across its widest point (Fig. 3.22). It was developed in Oligocene-Miocene time occupying an area of ~10000 km^2 that opened by a normal extensional motion with a minor left-lateral strike-slip component. The pole of this motion is at 31˚N 29˚E, offshore of Alamein city about 320 km west of the Nile Delta (Feinstein et al., 1996). The Gulf of Aqaba was developed since the Middle Miocene to become the main northern plate boundary for the African-Arabian separation with activity of 4-8 times more than in the Gulf of Suez (Steckler et al., 1988). Since then, the spreading rate in the Gulf of Suez reduced to about 0.1 cm/yr and the angle of rotation is 0.9˚ (Badawy and Horvath, 1999) resulted in an opening of 15 km. While, the rest of the motion (45 km) occurred mainly through the first phase of the development before the Middle Miocene. There is debate about uplifting processes of the flanks accompanied by the rift initiation. One hypothesis considering only isostatic rebound due to the early development of these flanks (Omer et al., 1989; Omer and Steckler, 1995). This idea needs anomalously large amount of uplifting (~5 km) to explain thermochronological ages. The other hypothesis suggests additional thermal component based on increasing the present day heat flow southward with increasing the tectonic uplift (Steckler, 1985; Buck, 1986; Feinstein et al., 1996).

Thermochronology in northern the ANS; The thermochronological studies applied on the different parts of northern the ANS using different LTT methods gave a protracted cooling history. All studies reveal dominance of non-uniform uplift between fault-bound blocks. The Gulf of Suez flanks reveal AFT ages between 379±23 and 11.1±1.7 Ma (Kohn and Eyal, 1981; Omer et al., 1989; Kohn et al., 1997). While, the Gulf of Aqaba flanks give AFT ages between 265±13 and 10.18±0.26 Ma (Kohn and Eyal, 1981; Feinstein et al., 2013). The Eilat area shows 40Ar/39Ar ages clustering around 535 Ma (Vermeesch et al., 2009), ZFT ages between 373±26 and 293±21 Ma (Kohn et al., 1992; Vermeesch et al., 2009) and AFT and AHe ages for detrital samples around 270 Ma and 70 Ma, respectively (Vermeesch et al., 2009). The Red Sea western flank reveals sphene FT ages between 410 and 339 Ma (Bojar et al., 2002), ZFT ages between 366 and 315 Ma (Bojar et al., 2002), and AFT ages between 191±7 and 28.5±1.5 Ma (Omer et al., 1987).

3.3.3 The Canary Islands

The origin of the Canary archipelago was earlier described by the hotspot hypothesis (e.g., Burke and Wilson, 1972; Schmincke, 1973; Hoernle and Tilton, 1991; Hoernle and Schmincke, 1993). But the difference in orientation between external and internal islands (Fig. 3.33) was an argument against this hypothesis (Stillman, 1999). Alternatively, decompression melting of the asthenosphere through two linear volcanic trails, associated with propagation the Cretaceous tectonics of the nearby Moroccan Atlas Mountains was proposed (Anguita and Hernán, 1975; Araña and Ortis, 1991; Ancochea et al., 1996). But reported isotopic studies on Fuerteventura volcanic materials (Hoernle and Tilton, 1991; Demény et al., 1998; Hoernle et al., 2002; Demény et al., 2004; Abu El-Rus et al., 2006) have pointed to a strong HIMU (mantle with high 238U/204Pb ratio) component characteristic of a plume-type origin including recycled oceanic crust with sediments integration and metasomatised lithosphere from oceanic mantle (Hoernle and Tilton, 1991; Hoernle et al., 1991; 1995; Hoernle and Schmincke, 1993; Geldmacher et al., 2001; 2005). These features have brought hotspot origin again into reconsideration. Slow movement of the lithospheric plate above the mantle plume (0.16 to 0.18 cm/yr; Cogné and Humler, 2004) could has caused its distribution to several, semi-isolated and/or isolated blobs below the Canary Islands (Hoernle and Schmincke, 1993; Carracedo et al., 1998; Hoernle et al., 2002; Duggen et al., 2009).

Detailed study by Ancochea et al. (2006) has given a chronological evolution of the volcanicity on the archipelago. The earliest recorded activity on the Canary Islands is indicated by the Oligocene age submarine activity the BC of Fuerteventura (Stillman et al., 1975; Robertson and Bernouilli, 1982) and Lanzarote (Sánchez Guzmán and Abad 1986). In the Oligocene–Lower Miocene, Fuerteventura started to emerge (Muñoz and Sagredo, 2004). In the Lower Miocene, Fuerteventura was completely emerged and La Gomera has initiated its seamount stage. In the Middle Miocene, Fuerteventura's old edifices, Lanzarote's Ajaches Edifice and Gran Canaria's the basaltic shield reached their peak (Coello et al., 1992; McDougall and Schmincke, 1976; Bogaard et al., 1988). In the Upper Miocene, started the large basaltic edifices of La Gomera and Tenerife, the Famara Edifice on Lanzarote and the felsic emissions On Gran Canaria (Coello et al., 1992; Ancochea et al., 1996; McDougall and Schmincke, 1976; Bogaard et al., 1988). In the Lower Pliocene, Minor and dispersed activities have shown on Fuerteventura after a calm period of ~7 Ma. The Young Edifice was constructed on La Gomera. The Famara Edifice activity on Lanzarote was continued. The huge volcano Roque Nublo expands on Gran Canaria. The old edifices activity on Tenerife became restricted to the eastern side while Anaga Edifice and the Cañadas Edifice have already started to raise. (Ancochea et al., 2006). La Palma has started its seamount construction edifice (Staudigel et al., 1986). The Upper Pliocene is identified by the lack of basaltic volcanic activity. On Fuerteventura, only the eastern ridge of the central depression was active. On Gran Canaria, emissions were started and continued to recent times in its north-eastern region. On Tenerife, felsic flow, fall deposits and other materials were accumulated in the Cañadas Edifice (Huertas et al., 2002). The seamount edifice of La Palma possibly continued active. In the Lower Pleistocene, the activity on Fuerteventura, Gran Canaria and Tenerife residues. On Lanzarote, abundant basaltic emissions produced the central ridge and it remains active (Ancochea et al., 2006). Started the exceptional event of emergence of the most recent islands La Palma and then El Hierro (Fúster et al., 1993; Ancochea et al., 1994; Guillou et al., 1996; Guillou et al., 2001; Carracedo et al., 2001). The Upper Pleistocene up to present, is characterized by activity maintenance. Tenerife, Lanzarote, La Palma and El Hierro still active. Fuerteventura and Gran Canaria show less activity. While, La Gomera only is entirely calm.

3.3.3.1 Fuerteventura

Fuerteventura comprises three separate volcanoes; SVC, CVC, and NVC. Where each of them consists of two main stages: the Basal Complex (BC) and the Subaerial volcanic series (SVS) (Fig. 3.6) (Ancochea et al., 1996).

The topography of the NVC and the CVC can be divided into three regions from west to east; the BC domes, the Central Depression, and the Miocene lava cuchillo and valleys (Stillman, 1999).

The earliest pillow lavas (from BC) are dated to be Paleocene to early Eocene and the earliest dated sub-aerial volcanic has age of 20.4 (0.4) Ma (Coello et al., 1992). Indicating continuation of the submarine stage from Palaeocene to late Oligocene times when the island started to emerge (Stillman, 1999; Wipf et al., 2010). The main bulk of the NVC and the CVC was constructed by ~20 Ma. Afterwards, a recess in the volcanic activity has occurred concurrent with major mass wasting/landslide event which stripped away the shield stage basalts of the subaerial volcanic series (SVS), exposing and weathering the BC (Stillman, 1999). At that time the plain surface of the Central Depression may have expanded westward to the ocean prior to the uplift of the western dome which supports localised and relatively recent uplift (Coello et al., 1992; Stillman, 1999).

The Basal Complex (BC) consists of thick Late Cretaceous sedimentary succession covered by interbedded Cretaceous-Oligocene sediments, submarine volcanics, and intruded by a bulk NNE-SSW trending dyke swarms and alkaline plutons (Bravo, 1964; Fúster and Aguilar, 1965; Fúster et al., 1968a; Stillman et al., 1975; Robertson and Bernouilli, 1982; Le Bas et al., 1986; Colette et al., 1992; Ancochea et al., 2006).

The Subaerial Volcanic Series (SVS) forms the shield stage. The Miocene volcanic activities formed the SVS with several eruptive cycles, started ~20 Ma. The post-Miocene volcanicity on Fuerteventura occurred only in the NVC and CVC with eruptive cycles ages of 5, 2.9-2.4, 1.8-1.7, 0.8-0.4 and <0.1 Ma (Colette et al., 1992), and have reached its maximum elevation of 3000 m in the CVC in the early Miocene (Stillman, 1999). The

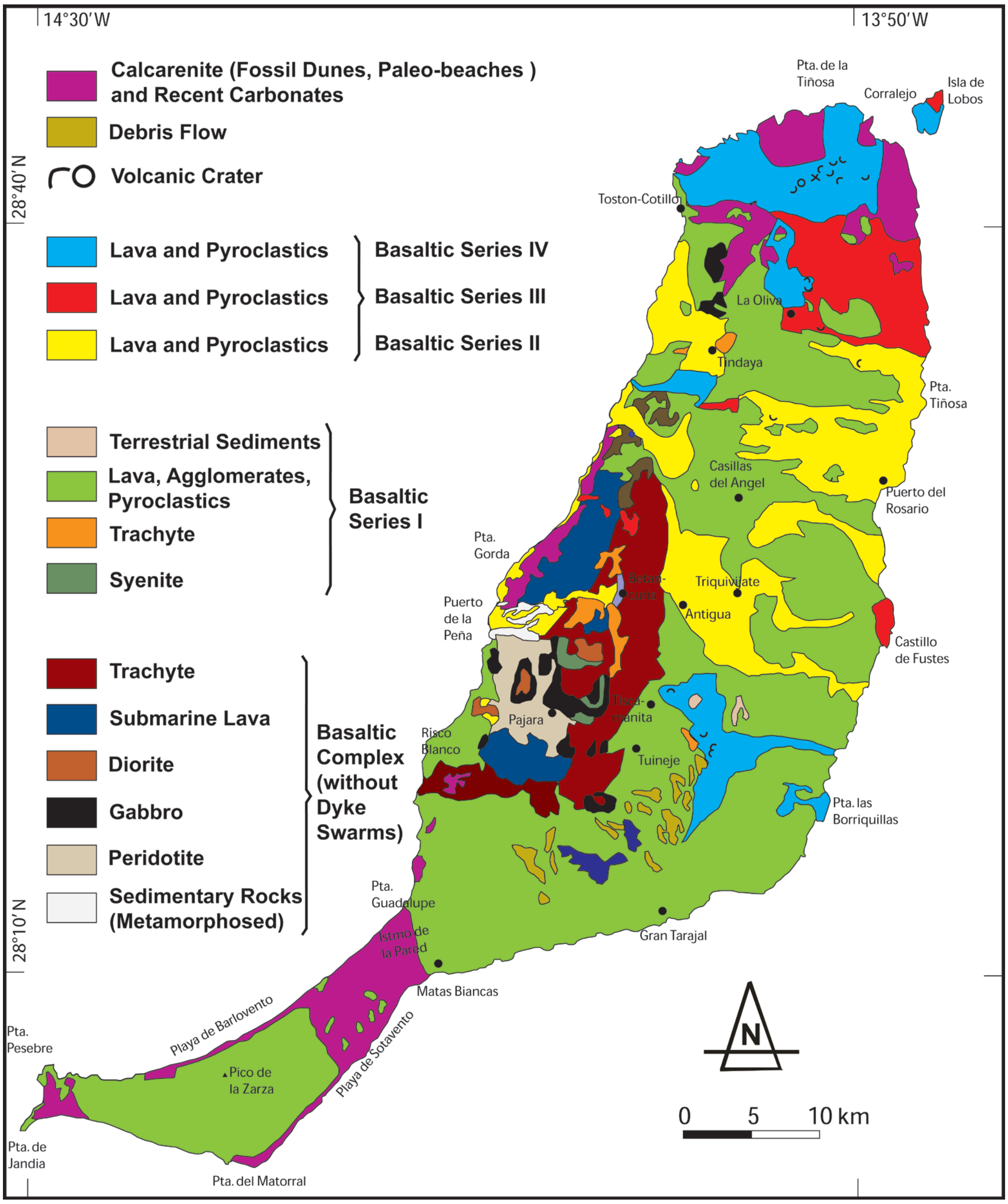

Fig. 3.6: Geologic map of Fuerteventura Island with the main rock units and lithologies (modified by Wipf, 2007 after Muñoz et al., 2003).

SVS consists of sequence of series. Series I of Miocene age, crosscut by numerous dykes (Ruiz, 1969), unconformably overly the eroded surface of the BC. It consists of a succession of basaltic lavas, pyroclastics, ankaramitic accumulates, trachybasaltic differentiates and few trachytes (Fúster et al., 1968a; Ibarrola, 1969; Hernández-Pacheco and Ibarrola, 1973). Series I is, in turn, unconformably overlain by the following series (Coello et al., 1992). Series II was constructed through three periods of volcanic activity; the Lower Pliocene, the Upper Pliocene, and the Pliocene-Pleistocene boundary (Fúster et al., 1968a; Ibarrola et al., 1989b). Series III outcrops in few localities with Pleistocene age while Series IV is of Upper Pleistocene to Holocene age (Coello et al., 1992).

Fernandez et al. (2006) have observed three phases of Miocene extensional deformation (M-D1, M-D2, and M-D3) on Fuerteventura Island. The M-D1 (25-20 Ma) is identified by a NW-SE trending extension which produced an asymmetric fault system with a mainly top-to-NW displacement concurrent with intrusion of intense dike swarm, rupture of several fissural volcanic materials, and folding of the older and syn-strata. Phase M-D2 (20–17.2 Ma) started by change in extension to NNE-SSW direction along with beginning of the central volcanic edifices on the island. Phase M-D3 (17.2–12 Ma) was identified by a ENE-WSW extension.

Fuerteventura Landslide; a giant landslide occurred at the western part of the island during the Miocene and exposed a large mass of the BC. This landslide has removed ~3500 km^3 of lavas and volcano-clastics from the shield stage and has transported it as debris flows to the Ocean (Stillman, 1999). While remnants of the shield stage volcanics are preserved on the eastern side of Fuerteventura. Stillman (1999) suggested, alteration of submarine strata from pillow lavas to weak coherent clay minerals, the emplacement of dyke swarms and high-level plutons during the shield stage, the influence of gravity, and over-steepening and overloading due to growing the edifice as the main reasons triggered the landslide.

3.3.3.2 La Gomera island

La Gomera is a prolonged volcanic edifice formed by a single huge complex. It has been constructed through three main phases: the Submarine Edifice (SE or BC), the Old Edifice (OE) and the Young Edifice (YE) (Fig. 3.7). The BC mainly represents the submarine development stage and its hypabyssal roots which formed predominantly from marine sedimentary rocks, submarine volcanics and intruded plutonic rocks and dikes (Bravo 1964; Cendrero 1971). While, the OE is separated from the previously formed BC by thick sedimentary deposits which state deep erosion events of the BC (Ancochea et al., 2006). The OE basaltic flow can be divided into: a Lower Old Edifice (LOE) with ~10.5–10 Ma age with initial and brief submarine features (Cubas et al., 1994) and an upper Old Edifice (UOE) with volcanic breccia. The NW and NE borders of the shield have experienced flank failure which led to the disappearance of the LOE materials around 9.4-8.6 Ma in this region (Ancochea et al., 2006). After a short hiatus of less than 1 million years the YE erupted to unconformably overly an erosional surface of the OE (Ancochea et al., 2006). The YE can be divided into: a Young Edifice-1 (YE-1) of volcanic floods from the central region of La Gomera descending towards the south and southwest and a Young Edifice-2 (YE-2) of widespread sub-horizontal and broad detached volcanic floods wrapping a wide area extends to the N, W and NE margins. La Gomera has experienced no vocanic activity in the last 2 Ma representing an exceptional case in the Canary Islands (Ancochea et al., 2006).

The Submarine Edifice (SE or BC) of La Gomera represents the oldest outcropping rocks (Fig. 3.7), analogous to the BC of Fuerteventura (Stillman et al., 1975; Le Bas et al., 1986). The BC outcrops in the northwestern region of the island and consists of markedly deformed basaltic pillow lavas, mafic plutonic rocks and trachytic breccias cross cut by an intense network of dikes with mainly basic composition (Cendrero 1971; Casillas et al. 2008a; Casillas et al., 2010). The BC sequence is intensely faulted and has been influenced by hydrothermal metamorphism of greenschist phase (Cendrero 1971; Casillas et al., 2010).

The BC has experienced multiple stages of metamorphic and/or metasomatic reworking along with each intrusive episode. This made dating of the BC rocks complicated especially when all the chronologic studies on

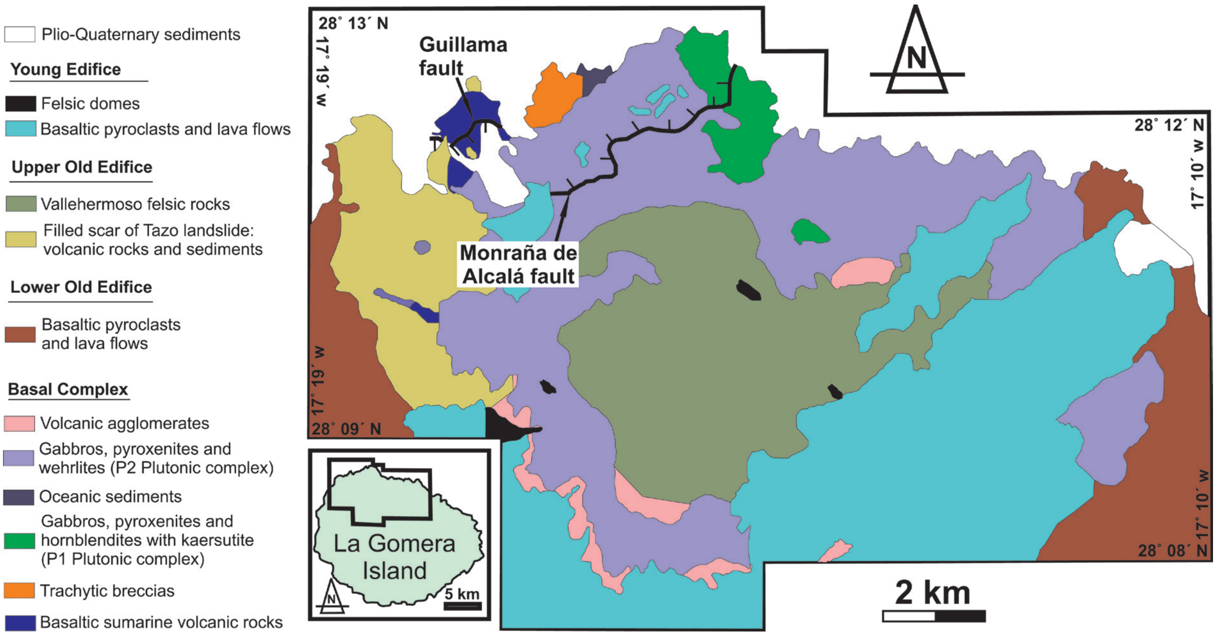

Fig. 3.7: Geologic map of the northern sector La Gomera Island with the main rock units and lithologies. The inset shows the area covered by the map from the La Gomera Island (after Casillas et al., 2010).

it were using K/Ar or Ar/Ar techniques (Abdel Monen et al., 1971; Féraud, 1981; Cantagrel et al., 1984; Féraud et al., 1985; Ancochea et al., 2006). Despite that, hornblendes from alkaline plutons and alkaline intrusions from different areas gave ages of 19.8, 19.3, 15.5, 15, and 14.6Ma (Abdel Momen et al., 1971; Cantagrel et al., 1984), assigning the rocks into three plutonic events; (P1) hornblende pyroxenite, hornblendite, and amphibole gabbro, (P2) clinopyroxenite, wehrlite, gabbro, olivine gabbro and (P3) alkaline gabbro, monzodiorite and syenite (Cendrero 1971; Casillas et al., 2010; Démeny et al. 2010).

The OE (10.5-6.4 Ma) presents the main structure on La Gomera Island and reaches up to 1100 m near the Island's centre. The OE rests unconformably on the BC or on the BC eroded surface (Ancochea et al., 2006). In general the present-day OE can be expressed as a swell of smoothly outward-dipping basaltic volcanic floods, thick breccia and scattered felsic rock fragments (Cubas et al., 2002). The OE rock units are characteristically cross cut intensely by dikes (1 every 10 m or even less) of basaltic composition (10.5 (0.2)-8.1 (0.5) Ma) and less frequent felsic (trachytic to phonolitic) ones (8.0 (0.4) Ma) (Féraud et al., 1985; Ancochea et al., 2006).

The activity then has migrated to the south during the UOE eruptions which rest unconformably on the OE rocks or exceptionally on the BC with a 500 m thick sequence of pyroclastics, basalt and trachybasalt volcanic floods (Cendrero, 1971; Cubas, 1978a; Cantagrel et al., 1984; Rodríguez-Losada, 1988). Radiometric ages indicate that, the UOE can be divided into two episodes of eruption (Ancochea et al., 2006). The first episode includes the UOE-1 with ages ranging between 8.6 (0.4) and 8.0 (0.2) Ma, basaltic dikes with ages between 8.6 (0.3) and 8.1 (0.5) Ma, and felsic rocks in range of 8.6 (0.4) and 7.8 (0.4) Ma (Féraud, 1981; Cantagrel et al., 1984; Ancochea et al., 2006). The second episode contains the UOE-2 basaltic lava flows dated 7.5 (0.15) to 5.9 (0.15) Ma, felsic rocks with ages ranging from 7.5 (0.6) to 6.4 (0.5) Ma, basaltic dikes with ages of 7.5

(0.5) Ma, and trachybasaltic dikes dated 7.0 (0.1) and 6.5 (0.3) Ma (Féraud, 1981; Cantagrel et al., 1984; Ancochea et al., 2006).

The Young Edifice (YE) is built of over 1000 m thick basaltic pyroclasts, felsic lava domes, and basaltic, trachyandesitic and trachybasaltic volcanic floods. Ancochea et al. (2006) investigated local unconformities within the YE strata and suggested differentiation into two units, YE-1 show ages between 5.7 and 4.7 Ma and YE-2 between 4.6and 3.9 Ma.

La Gomera Landslide(s); several flank failure processes occurred (e.g., Tazo and San Marcos) in the NW sector of the island removing the NW flank of the LOE unit which was formed at 9.4-8.7 Ma (Fig. 3.7) (Ancochea et al. 2006). Casillas et al. (2010) suggested, continuous magma injection, the emplacement of dikes, low mechanical resistance of the the BC rocks and the gravitational collapse of the topping magmatic edifices as the main triggers for these landslide as well as the displacement associated with the normal faulting of Guillama and Montaña de Alcalá (Fig. 3.7) (Casillas et al. 2008b).

4

METHODS AND TECHNIQUES

CONTENTS

4.1 BASIC PRINCIPLES

The different thermochronologic methods (e.g., Fission track and (U-Th)/He techniques) are based on accumulation and retention of radiation damages or isotopes which were produced by nuclear decay in the crystal lattice. The decay daughters are sensitive to a certain temperature zone which is function of the applied technique and used mineral (Gleadow and Duddy, 1981;Yamada et al., 1995; Farley, 2000; Reiners et al., 2002, 2004; Reiners and Brandon, 2006). Consequently this thermal sensitivity provides information about the rock cooling through a certain isotherm rather than the formation age. On the other hand, the thermo-kinematic models are tools to test the possible time-temperature (t-T) evolutionary scenarios against the thermochronological data using a computer code (e.g., HeFTy v1.8.3, Ketcham, 2005; Ketcham et al., 2007a,b, 2009).

A given mineral can be dated thermochronologically if enough time has passed since its cooling through the probable isotherm to accumulate a significant number of radioactive daughters. The number or amount of the daughter products is a function of the mineral's cooling age and its parent isotopes concentrations.

$$D=Do+N(e^{\lambda t}-1) \quad (1)$$

where

D: Quantity of daughter product

Do: Quantity of daughter isotope in the original composition

N: Number of the parent isotopes

λ: Decay constant

t: Age of the decay

Assuming decay of the radiogenic parent isotopes to the daughter products in a closed system, the age equation can be modified to

$$t=1/\lambda \ \ln(1+D/N) \quad (2)$$

With the substitution of D by the spontaneous track density ρs and N by the induced track density ρi

Where

$$\rho_s=\lambda_f/\lambda_d \ N(e^{\lambda dt}-1) \quad (3)$$

and

$$\rho_i={}^{238}N/\sigma\phi \quad (4)$$

these modifications will convert the general decay equation to a fission track age equation (Hurford and Green, 1982; Wagner and Van den Haute, 1992; Galbraith and Laslett, 1993).

$$t=1/\lambda_\alpha \ \ln\{(1+\lambda_\alpha \rho_s QGI\sigma\phi)/(\lambda_f \rho_i)\} \quad (5)$$

where

t: Age of decay

λ_α: Decay constant for α-emission of 238U, = 1.55125 X 10^{-10} a^{-1} (Wagner and Van den Haute, 1992)

ρ_s: Density of spontaneous tracks

Q: Factor for etching conditions and individual counting of the operator

G: Geometry factor (0.5 for external detector method)

I: The 235U/238U isotopic ratio (7.2527 X 10^{-3} (Cowan and Adler, 1976)

σ: Thermal neutron fission cross section for 235U, = 580.0 X 10^{-24} cm^2 (Hanna et al., 1969)

ϕ: Thermal neutron fluency

λ_f: Decay constant for spontaneous fission of 238U, = ~8.5 X 10^{-17} a^{-1} (Wagner and Van den Haute, 1992)

ρ_i: Density of induced tracks

While, the decay equation by α-emission of 238U, 235U, 232Th, and 147Sm to 4He can be expressed by Farley, (2002) decay equation

$$^{4}He=8\,^{238}U(e^{\lambda_{238}t}-1)+7(^{235}U/137.88)(e^{\lambda_{235}t}-1)+6\,^{232}Th(e^{\lambda_{232}t}-1)+^{147}Sm(e^{\lambda_{147}t}-1) \qquad (6)$$

where
t: Age of 4He accumulations
λ: Decay constant (λ_{238}= 1.55125 X 10^{-10} a^{-1}, λ_{235}= 9.849 X 10^{-10} a^{-1}, λ_{232}= 4.948 X 10^{-11} a^{-1}, λ_{147}= 6.54 X 10^{-12} a^{-1}) (Lugmair and Marti, 1978; Farley, 2002).

Whenever possible all thermochronometers (ZFT, ZHe, AFT and AHe) and t-T history modelling were applied on the same sample to allow for quantifying the spatial and chronological cooling trends progresses through the upper crust. For this study, a total 33 samples were collected from the Rwenzoris, through one transect from the foot (1407 m a.s.l.) of the western flank of the Rwenzori Mountains to a height of 4442 m a.s.l. (Table 4-1). From the Samra area, 26 samples were collected along the main valleys and facing the Gulf of Suez to represent the main rock units of the ANS basement in Sinai with elevations ranging between ~73 m a.s.l. and ~525 m a.s.l. (Table 4-2). From the Canary islands, 23 Samples were collected; 12 from Fuerteventura and 11 from La Gomera, at elevation from 3 to 400 m a.s.l. (Table 4-3).

The ZFT and AFT analyses were performed at the laboratory of Heidelberg except of the AFT analysis for the Samra area samples, which was performed at the laboratory of Kanazawa as part of my master research (Mansour, 2010). The ZHe and AHe analyses were conducted at the Arizona Radiogenic Helium Lab.

4.2 FISSION-TRACK THERMOCHRONOLOGY

A fission track is a damage zone formed in the crystal lattice by spontaneous fission of heavy nuclei (Fig. 4.1). Three naturally occurring isotopes spontaneously fission: Thorium232, uranium235, and uranium238. From these only 238U produces a significant number of fission events due to its relative abundance and half life for spontaneous fission.

A nucleus of 238U eventually splits into two heavy fragments of approximately equal mass, releasing ~200 MeV of energy. The two nuclei travel in opposite directions disrupting the electronic balance of the atoms in the mineral lattice along their path producing a trail of positive charged ions (Wagner and Van den Haute, 1992). These positive charged ions repulse each other, forming a damage zone or a track in the crystal structure (Fig. 4.1). The newly formed track is only angstroms wide and about 10-20 µm long. Therefore, they are only visible using an electron microscope. Price and Walker (1962) discovered that by using appropriate chemical etchant (nitric acid for apatite; Gleadow et al., 1984, and concentrates basic solutions and fluxes for zircon; Fleischer et al., 1975) the fission track width enlarge sufficient enough to be observable under an optical microscope.

Fission tracks can reverse their formation process by track fading (annealing) with increasing temperature (Fleischer et al., 1965b). This annealing process occurs when some of the displaced ions during the track formation start to move back into the track and heal some of the broken bonds. This diffusion caused by increasing ions' kinetic energy through a temperature increase which in turn is time-dependent (Naeser and Faul, 1969). Wagner (1979) divided the track behaviour during annealing process into

Table 4-1: Information of the collected samples from the Rwenzori Mountains.

S.-No.	**Lithology**	**Coordinates UTM**		**Elevation (m a.s.l.)**
		N	**E**	
DRC 10-01	Mica Schist	812660	38177	2007
DRC 10-02	Green Schist	813492	37721	2048
DRC 10-03	Amphibolite	813492	37721	2048
DRC 10-04	Amphibolite	813470	37763	2048
DRC 10-05	Green Schist	813385	37722	2059
DRC 10-06	Amphibolite	816607	38858	3230
DRC 10-07	Mica Shist	815969	38741	3221
DRC 10-08	Mica Schist	816148	38897	3311
DRC 10-09	Amphibolite	817418	40168	3962
DRC 10-10	Amphibolite	817535	40237	4006
DRC 10-11	Amphibolite	817492	40769	4105
DRC 10-12	M.A. Green Schirt	817688	41049	4174
DRC 10-13	Mylot. Amphibolite	817859	41151	4239
DRC 10-14	Amphibolite	818086	41436	4278
DRC 10-15	Amphibolite	818115	41565	4294
DRC 10-16	Amphibolite	818365	41141	4228
DRC 10-17	Amphibolite	818149	41264	4175
DRC 10-18	Amphibolite	818050	41199	4308
DRC 10-19	Carbonatite	818079	41244	4290
DRC 10-20	Amphibolite	817823	41449	4228
DRC 10-21	Amphibolite	818386	41354	4442
DRC 10-22	Amphibolite	818251	41317	4375
DRC 10-23	Amphibolite	817177	42031	4178
DRC 10-24	Amphibolite	816710	42109	4397
DRC 10-25	Amphibolite	816647	42165	4438
DRC 10-26	Mica Shist	815402	38247	2976
DRC 10-27	Mica Schist	815360	38180	2911
DRC 10-28	Mica Schist	814288	37538	2439
DRC 10-29	Green Shist	813385	37722	2059
DRC 10-30	Schist-Greiss	812130	37896	2018
DRC 10-31	Green Schist	811880	38035	2076
DRC 10-32	Mica Schist	810007	38209	1846
DRC 10-33	Phyllite-Mica Schist	807825	37911	1407

S.-No.: corresponding sample numbers. lithology M.A.: metamorphic amphibolite, Mylot.: mylonite. Elevations (m a.s.l): elevation with meters above sea level.

three depth/temperature sectors; the uppermost total track stability zone (TSZ) where all formed tracks are survived, beneath it the partial annealing zone (PAZ) in which the formed tracks partially fade, and the deeper total annealing zone (TAZ) in which all formed tracks are annealed (Fig. 4-2).

The PAZ for zircon is affected by the degree of metamictization through changing the annealing kinetic. Metamictization is re-

Table 4-2: Information of the collected samples from the Samra Mountain area.

S.-No.	Lithology	Coordinates UTM		Elevation (m a.s.l.)
		N	E	
D4	Syenite	3205959	526060	298
D5	Syenite	3208866	523166	189
D7	Syenite	3208780	524027	525
D8	Diorite	3209042	524144	520
S1	Diorite	3210195	527377	204
S2	Rhyolitic Dyke	3210195	527377	204
S4	Gneiss	3210218	527170	316
S6	Rhyolitic Dyke	3209895	526909	188
S10	Synite	3210600	526740	202
B1	Diorite	3207453	527495	195
B2	Gneissos Syenite	3207453	527495	202
B4	Gneissos Granite	3207453	527495	195
B5	Granitic Dyke	3207453	527495	195
B6	Basaltic Dyke	3207728	528879	245
B7	Syenite	3208112	529298	229
B9	Diorite	3206397	527214	195
B11	Synite	3209812	522817	100
Z1	Granitic Dyke	3204911	526742	152
Z2	Gneiss	3204911	526742	152
Z3	Gneiss	3203314	527965	192
N1	Basaltic Sill	3203337	529921	338
N3	Synite	3203911	530750	299
N4	Basalt	3202790	528434	237
F1	Gneiss	3207586	524102	188
F3	Syenitic Dyke	3207790	523907	73
F4	Gneiss	3207790	523907	182

S.-No.: corresponding sample numbers. Elevations (m a.s.l): elevation with meters above sea level.

sulted from interaction between alpha particles and alpha-recoil nucleus within the crystal structure (Nasdala 2009; Zhang et al. 2008a). Therefore, it is sufficient in zircon as it commonly contains higher (e.g., than apatite) concentrations of radioactive nuclei. According to the degree of metamictization, the PAZ of ZFT is between 330 and 190 °C/10 Ma (Rahn, 2001; Garver, 2002; Garver and Kamp, 2002; Garver, 2003; Rahn et al., 2004; Reiners and Brandon, 2006a, 2006b). Consequently, a closure temperature of ~240 °C/10 Ma is typical for an average degree of metamictization (Hurford, 1986; Yamada et al., 1995). While, the PAZ in apatite is controlled by the tracks crystallographic and the single grain chemical composition, tracks parallel to the c-axis in chlorine dominant apatite anneal slower (e.g., Green et al., 1986; Carlson et al., 1999; Donelick et al., 2005). Therefore, c-axis projection was performed for the measured track lengths and the kinetic parameter Dpar (etch pit diameter) was used as an indicator on the chemical domi-

Table 4-3: Information of the collected samples from the Canary Islands (Fuerteventura and la Gomera)

S.-No.	**Lithology**	Formation Age	**Coordinates UTM**		**Elevation (m a.s.l.)**
			N	**W**	
Fuerteventura					
FU-38-09	Carbonatite	Lower Miocene	3168170	599292	177
FU-39-09	Pyroxenite	Lower Miocene	3168009	599168	134
FU-40-09	Carbonatite	Lower Miocene	3171307	599699	149
FU-41-09	Lolith	Lower Miocene	3171307	599699	149
FU-42-09	Pyroxenite	Lower Miocene	3166635	599036	108
FU-43-09	Syenite	Lower Miocene	3166793	598866	102
FU-44-09	Lolith	Lower Miocene	3167805	595072	3
FU-45-09	Syenite	Lower Miocene	3167805	595072	3
FU-01-10	C.G. Syenite	Oligo-Miocene	3142246	592080	333
FU-02-10	Trachyte	Oligo-Miocene	3142363	592042	328
FU-03-10	C.G. Syenite	Oligo-Miocene	3142371	592376	353
FU-04-10	C.G. Syenite	Oligo-Miocene	3142338	592423	357
La Gomera					
Lag 1	Basaltic Pillow-Lava	Lower Miocene	3121536	273943	200
Lag 2	Trachytic Breccias	Lower Miocene	3122075	275033	70
Lag 3	Tamargada Monzonite	Lower-Middle Miocene	3119425	279777	350
Lag 4	Tamargada Syenite	Lower-Middle Miocene	3119316	279794	400
Lag 5	Syenite P2	Lower-Middle Miocene	3121333	277348	280
Lag 6	Amphibolic Gabbro P1	Lower Miocene	3121607	277370	310
Lag 7	Amphibolic Gabbro P2	Lower-Middle Miocene	3121878	277969	3
Lag 8	Pegmatitic Gabbro P2	Lower-Middle Miocene	3121876	277972	350
Lag 9	Trachyte P1	Lower Miocene	3121869	277985	325
Lag 10	Amphibolic Pyroxinite P1	Lower Miocene	3121301	278413	75
Lag 11	Trachyte P1	Lower Miocene	3121289	278279	65

S.-No.: corresponding sample numbers. lithology C.G.: coarse grained. Elevations (m a.s.l): elevation with meters above sea level.

nance of individual apatite crystals (Donelick et al., 2005). The PAZ for the dominant fluorapatite is typically in the range of ~100–60 °C/10 Ma (e.g., Gleadow and Duddy, 1981) with a general closure temperature (Tc) of ~110 °C for 1 °C/Ma cooling rate and ~10 Ma holding time (e.g., Green and Durrani, 1977; Donelick et al., 1999) (Fig. 4.2).

The newly formed fission tracks have the same length in a given mineral but eventually shorten by the thermal annealing. Each of these tracks was formed at a different moment and has experienced a different segment of the entire cooling history of the sample. Therefore, the track length distribution has a sufficient importance in investigating the thermal history of the studied samples. Although lengths cannot be measured for tracks which penetrate the mineral's polished surface since fraction of the whole length must be lost. Instead the horizontal confined tracks (CTs), where both ends are confined within the mineral and are reached by the chemical etchant via other etched

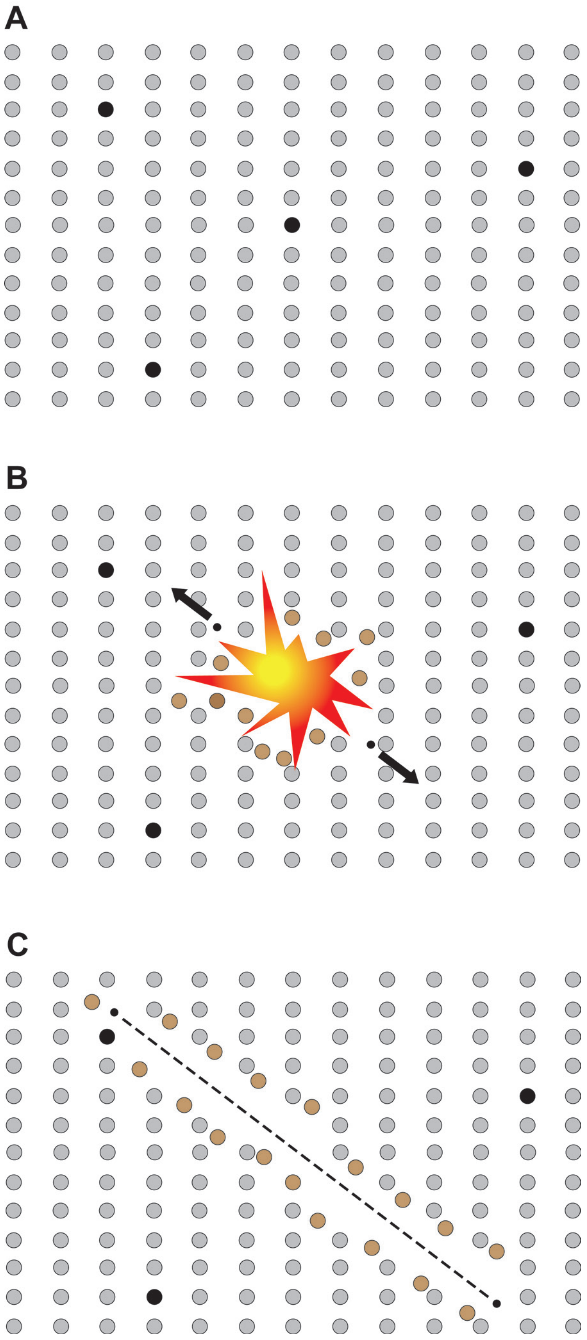

Fig. 4.1: Track formation in a crystal lattice according to the ion explosion spike theory of Fleischer, Price, and Walker. (A) The crustal lattice with trace amounts of radioactive ^{238}U (dark circles). (b) Spontaneous fission of ^{238}U giving two heavy and charged particles. These particles recoil each other and cause other atoms in the lattice initially by electron stripping or ionization. This leads to further deformation of the lattice as the ionized lattice atoms repel each other.(c) The fission particles slow down after capture electrons and lose energy until they come to rest, leaving a damage trail or a fission track. These can be observed optically after being chemically etched (Modified after Fleischer et al., 1975).

features (track or crack) are measured (Fig. 4.3). Moreover, the analysis of CT distributions can be used to differentiate between samples that have experienced long or short periods in the PAZ before exhumation. A longer stay in the PAZ produces CTs which are positively skewed, have relatively short mean track lengths with a quite wide lengths distribution of either a small peak or a tail of shorter tracks with a distinct peak of long tracks. On the other hand, samples cooled from the TAZ show a negative sleekness and tight long tracks distribution (Gleadow et al., 1986 a,b).

The fission track dating conventional external detector method was used (Hurford and Green, 1983; Wagner et al., 1992). For the analysis, zircon and apatite grains were separated from the collected samples using the conventional techniques (e.g., Grist and Ravenhurst, 1992a, b; Donelick et al., 2005). The ZFT grain mounts were etched in a NaOH–KOH eutectic melt at 220 (5) °C for 3.5-36 hours. While, the AFT grain mounts were etched in 5.5 N HNO3 for 20 (1) s at 21 (1) °C. Then all grain mounts were covered by U-free detection muscovite. The samples were irradiated in the research reactor FRM II in Munich, Germany along with standard glass neutron dosimeters with a known uranium content (CN1 with zircons and CN5 with apatites) and age standard minerals (Fish Canyon tuff with zircons and Durango with apatites). The detection micas, after irradiation, were etched in 48% HF for 20 (0.1) min at 20 (1) °C (Fig. 4.4). After that, track densities (tracks/cm^2) from both spontaneous and induced fission, CTs lengths and c-axis related angles and the c-axis oriented Dpars were measured with the Heidelberg FT-1 system (Fig. 4.5). This system includes an optical microscope (Leitz) with a 3-axis microscope Autoscan®-stage, a high resolution Peltier-cooled CCD color Olympus® CCD camera, and a high per-

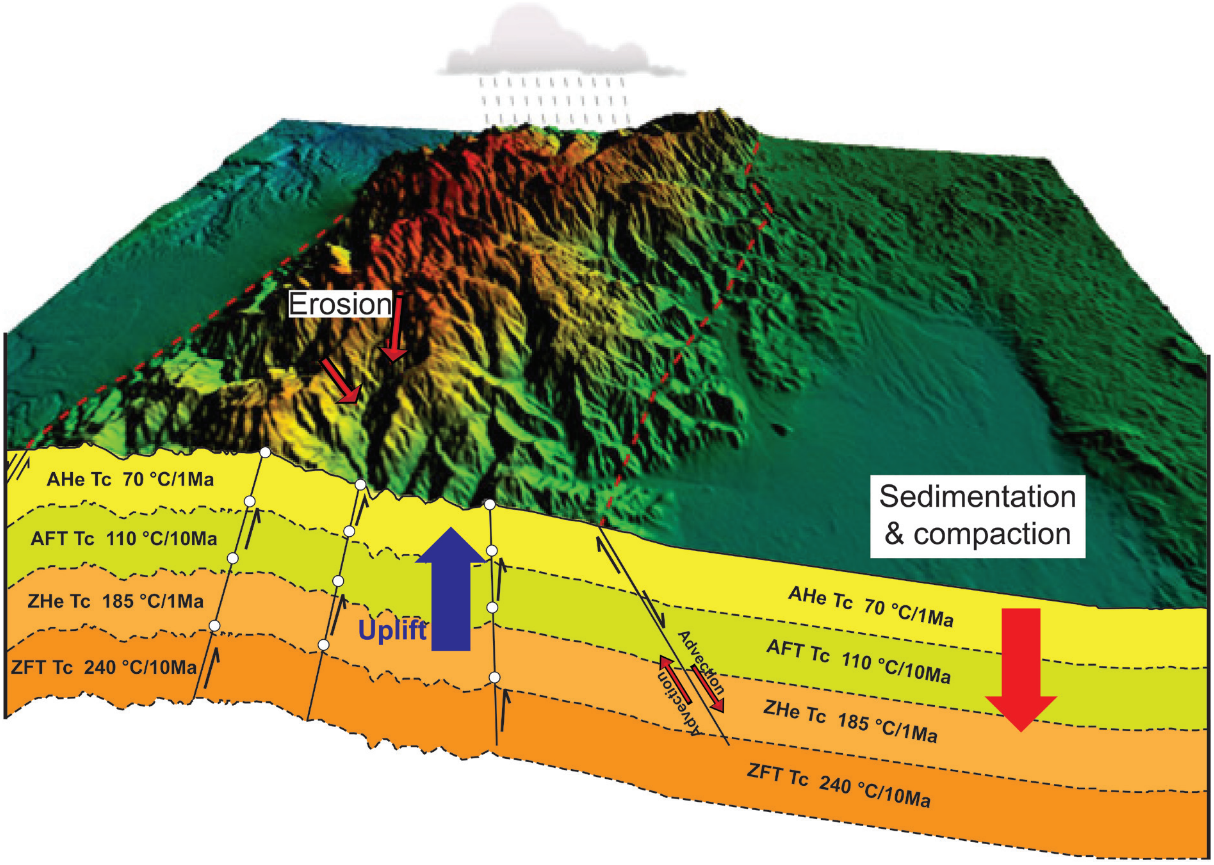

Fig. 4.2: Depth-Temperature relation for different thermochronometers (based on the DEM-90 m by Bauer et al., 2010) at a high-elevated Rwenzori Mountains and the adjacent low-elevated basin of lake George. Tc; the closure temperature for each thermochronometer.

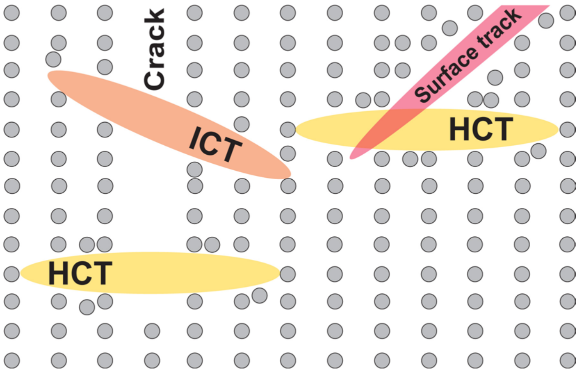

Fig. 4.3: Sketch for different types of tracks. The horizontal confined track (HCT) and inclined confined track (ICT) in which etchant arrive via either surface track or cracks.

forming Windows® based computer system with two flat screens. For more precision of the stage each axis is equipped with an external laser controlled Sony® sensor (BL 55 RE). These sensors guarantee a deviation of less than 500 nm along a movement of 4-5 cm. The whole setup is controlled by the Autoscan® Software trackscan® which also calculate the track densities. By applying the largest possible resolution, each pixel covers an area of less than 250 nm. Tracks were counted using 128x objectives (Fig. 4.5).

Central ages for the treated samples were calculated by applying the ζ- calibration method (Hurford and Green, 1982; 1983). All ages with (1σ-errors) were calculated using the computer code TRACKKEY (Dunkl, 2002). All the AFT data and CTs are presented according to the recommendations of Hurford (1990).

The LA-ICP-MS fission track method was used during the AFT study from the Samra area. The AFT parameters (track density,

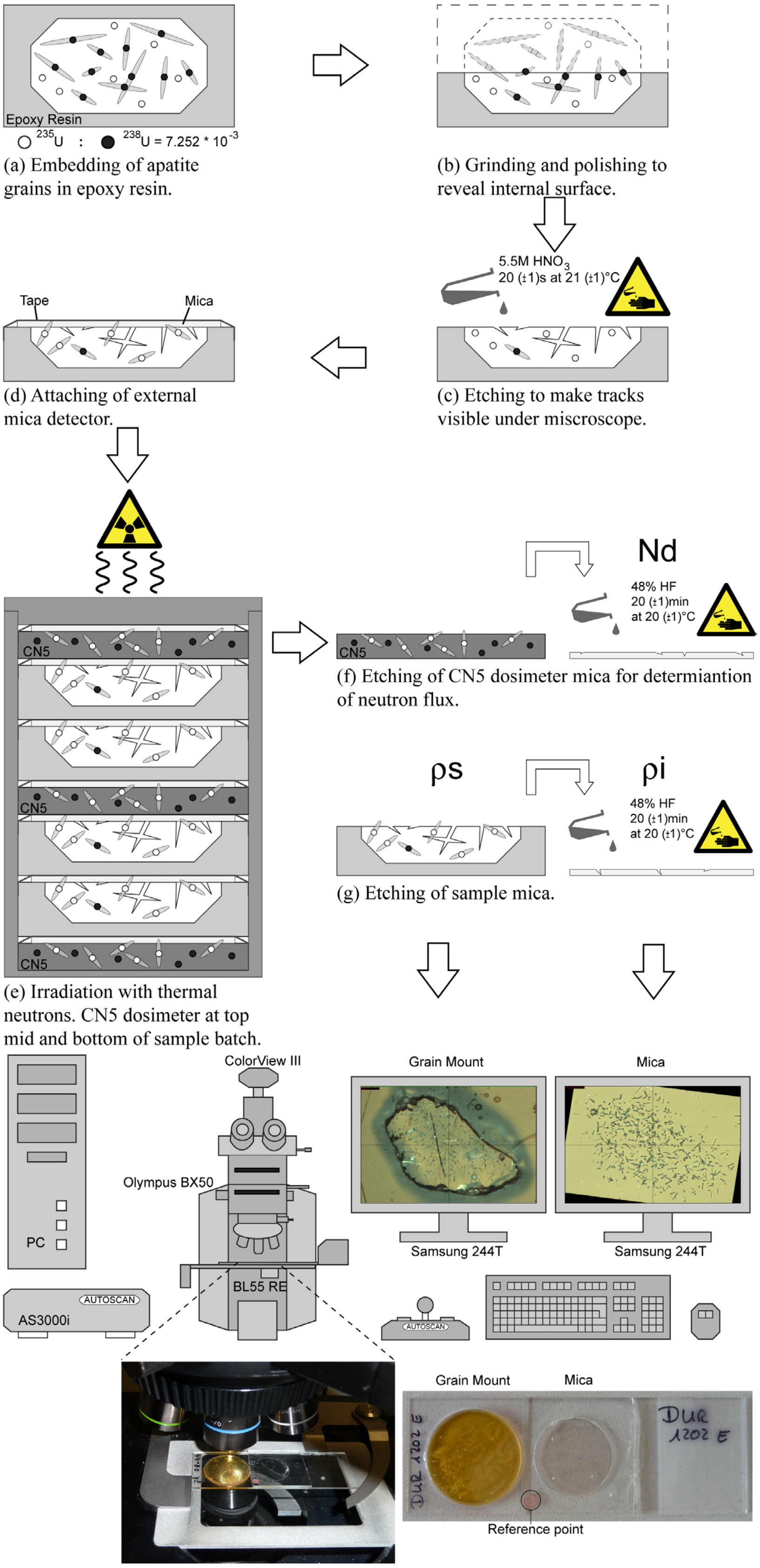

(a) Embedding of apatite grains in epoxy resin.

(b) Grinding and polishing to reveal internal surface.

(c) Etching to make tracks visible under miscroscope.

(d) Attaching of external mica detector.

(e) Irradiation with thermal neutrons. CN5 dosimeter at top mid and bottom of sample batch.

(f) Etching of CN5 dosimeter mica for determiantion of neutron flux.

(g) Etching of sample mica.

(h) Data acquisiton on the Heidelberg FT-1 system.

Fig. 4.4: Workflow for the fission track analysis (apatite and zircon) at the laboratory of Heidelberg. Different chemical etchant were used for zircon (see text) (modified by Grobe, 2011 after Juez-Larre, 2003).

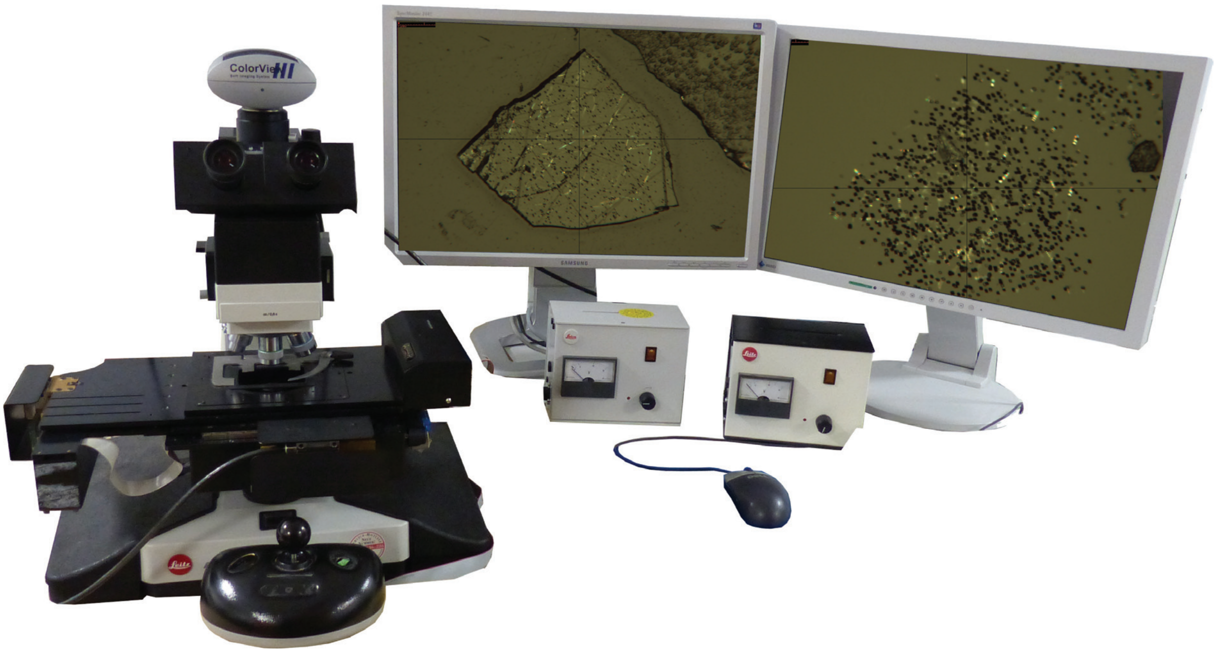

Fig. 4.5: Leitz FT-1 system for data acquisition (picture by Kollenz, 2015).

CTs, Dpars) and U concentrations were measured in thermochronology laboratory at Kanazawa University, Japan (during my master research; Mansour, 2010). The detailed operating conditions of the LA-ICP-MS were reported by Morishita et al. (2005) and are summarized in Table 4-4. The U signal intensity was calibrated against the reference material SRM 610 with a known U concentration (Longerich et al,. 1996; Carpenter and Reimer, 1974; Pearce et al., 1997). 43Ca was used as an internal standard for apatite, using chemical data obtained previously (e.g., Barbarand et al., 2003). The NIST 610 glasses were sandwiched between every five analysed samples and simultaneously measured and treated as unknown samples. An optical microscope (Nikon Eclipse 80i) with a total magnification of 100x was used to count the spontaneous tracks and to measure the CTs and Dpars. Whenever possible, 3 Dpars were measured for each grain with CTs.

The weighted mean ages and 1σ error range were calculated using the standard LA-ICP-MS apatite FT age equation (Hasebe et al., 2004). While, the measured U concentrations were used in the age equation with 10% error.

During the Canary islands study; the spontaneous track densities were generally low with values ranging from ~0.1 to ~0.7, therefore, no sufficient number of CTs was etched. Other sets of apatite mounts (other than those used for track counting) from both Fuerteventura and La Gomera were made. These apatites were irradiated by 197Au ion in the UNILAC (Universal Linear Accelerator) facility, GSI Helmholtz zentrum für Schwerionenforschung GmbH in Darmstadt, Germany with an energy of 11.1 MeV/nucleon, a fluence of $1X10^6$ ions/cm^2, and an angle of 15˚ with the vertical ions beam. This radiation has produced large numbers of latent tracks on the surface of the apatite grains (Albrecht et al., 1985; Afra et al., 2011). Afterwards, apatite mounts were etched and sufficient numbers of CTs were produced in some sample mounts.

Table 4-4: Operating conditions for the LA-ICP-MS.

ICP-MS	
Model	Agilent 7500s
Forward power	1200 W
Reflected power	1 W
Carrier gas flow	1. 31/min-1 (Ar)
	0.31/min-1 (He)
Auxiliary gas flow	1.01/min-1
Plasma gas flow	151/min-1
Interface	Ni sample cone
	Ni skimmer cone
Laser	
Model	MicroLas GeoLas Q plus
Wavelength	193 nm (Excimer ArF)
Repetition rate	5 Hz
Pulse energy	8 J/cm2
Pit diameter	20 µm

4.3 (U-TH-SM)/HE THERMOCHRONOLOGY

(U–Th–Sm)/He thermochronology (He dating) is based on the accumulation of the radiogenic 4He during α-decay of 238U, 235U, 232Th and 147Sm. The 4He diffusion rate is mainly sensitive to the temperature and the radiation damage (intensity and nature) in the crystal lattice (Farley, 2000, 2002; Reiners and Brandon, 2006). Therefore, helium will not be retained in the mineral system till it cools below a certain isotherm (closure temperature Tc) which differs from mineral to mineral. The zircon He dating (ZHe) system has a Tc of ~185 °C (Reiners et al., 2002, 2004), while the apatite He dating (AHe) system has a Tc of ~70 °C for a cooling rate of 10 °C/Ma and sub-grain domain sizes >60 µm (Farley, 2000) (Fig. 4.2), and a larger crystal has a higher closure temperature (Farley, 2000; Reiners and Farley, 2001). Furthermore, the partial retention zone (PRZ; the temperature range at which the decay products are only partially retained) varies depending on the cooling rates, the alpha doses, the crystal geometry, the diffusional pathway length and the thermal diffusivity (Dodson, 1973; Wolf et al., 1998; Reiners and Brandon, 2006; Flowers et al., 2009). In general, the helium system has PRZ ranging between ~30 and 90 °C in apatites (Flowers et al., 2009) and from ~140 to 220 °C in zircons (Guenthner et al., 2013) (Fig. 4.2).

There are some complications in the He dating which could have sufficient influence on the produced cooling ages. The radiation damage is one of the main demonstrators controlling the helium diffusivity and consequently affecting its cooling ages. Therefore, corrections for its effect were recently introduced (Shuster et al., 2006; Flowers et al., 2006; Shuster and Farley, 2009; Flowers et al., 2009). Shuster et al., 2006 suggested the eU (effective Uranium concentration) factor to examine the dependency of 4He diffusivity on the radiation damage. In apatites the radiation damage influence on the AHe ages is expressed by a positive eU-AHe relationship. This positive relationship results from 4He trapping in the radiation damage of the apatite crystal lattice (e.g., Shuster et al., 2006; Flowers et al., 2009; Shuster and Farley, 2009). In zircon the eU-ZHe relationship could be negative or positive depending on the radiation damage being connected or not (Reiners et al., 2004; Farley, 2007; Guenthner and Reiners, 2010; Guenthner et al., 2013). In case of such an eU-He age trend, mineral grains with the lower eU values present the most reliable cooling ages. Other complication is caused by the emission of α-particles during the radioactive decay of U and Th with high kinetic energy (70-161 keV; Guenthner et al., 2013), which makes it travel a long distance before it stops (e.g., 25µm in apatite, 20µm in zircon). Within this distance the α-particles could be ejected out of the crystal or injected into it from any nearby crystal (Farley et al., 1996; Wolf et al., 1996; Farley, 2000). Therefore, an α-stopping distance correction was applied to compensate the lost or gained helium fraction (Farley, 2000; Ketcham et al., 2011). This factor is strongly correlated to the grain size and its geometry. Moreover, the U/Th-rich inclusion (especially in apatites), zonation, and variation in grain sizes can affect the produced ages. Therefore, inclusions and cracks free grains with satisfactory size were selected. Despite that, the grain zonation and U/Th-rich inclusions cannot be entirely excluded as a cause for inappropriate He cooling age and/or intra-sample age scatter (Fitzgerald et al., 2006; Bauer et al., 2013; 2015).

For the analysis, the zircon and apatite single grain selection for (U-Th-Sm)/He dating was performed at Heidelberg thermochronology laboratory by using an Olympus SZX 16 stereo microscope, equipped with two different lenses (Olympus SDF PLAPO 1XPF and the Olympus SDF PLAPO 2XPF) and an Olympus XC 50 with an Olympus TV1X-2 video adaptor. Olympus Stream Enterprise software v1.5.1 was used to photograph grains and measure their geometry for standard morphometric α-ejection age corrections. The aliquots were filled in Nb foil tubes and sent to the Radiogenic Helium Laboratory, at the University of Arizona. There, the grains were loaded in the automated (U-Th-Sm)/He laser extraction line to extract the radiogenic 4He in an ultrahigh vacuum chamber by heating the grains to temperatures of ~900-1250 °C for several minutes. The released gas was measured and quantified in terms of 4He/^{3}He ratios with a quadrupole helium mass spectrometry system. After complete degassing the aliquots were dissolved for U, Th, and Sm determination. Zircons were dissolved using standard U-Pb double pressure-vessel digestion procedures (HF-HNO3 and HCl) for 4 days. The apatite samples were spiked with 233U, 229Th, and 147Sm solutions and dissolved in 20% HNO3 at 90 °C for 2 hours. After the dissolution, the single aliquots were analysed for U, Th, and Sm using a high-resolution (single-collector) inductively-coupled plasma mass spectrometer (Element2 HR-ICP-MS). Reported errors are 10% for zircons and 6% for apatites based on the respective reproducibility of the Fish Canyon and Durango age standards, respectively. If the reproducibility of aliquots within one sample is poorer than 10% (zircon) or 6% (apatite) the corresponding error is reported. All quantities were measured on a single crystal to eliminate uncertainties that arise from grain to grain heterogeneities. Afterwards, the resulted He ages were corrected for α-ejection. Further information on the analytical method is documented in the Radiogenic Helium Laboratory report (Reiners and Nicolescu, 2006).

4.4 THERMO-KINEMATIC MODELLING AND EXHUMATION RATES CALCULATIONS

Thermal history modelling using the well established computer code HeFTy v1.8.3 (Ketcham, 2005; Ketcham et al., 2007a,b, 2009) provides a tool to test the probable time–temperature (t–T) paths against the revealed thermochronological data sets and distinct geological information (t-T constrains-boxes). Consequently the thermotectonic history could be reconstructed and the cooling rates, exhumation rates and the corresponding episodical rock uplift could be calculated for the studied areas. The rock uplift is identified according to Likster et al. (2009 and reference therein), as it is the change in the vertical position of rocks with respect to a fixed reference, such as the geoid or in this case an isotherm, while the surface uplift represents changes in the surface elevations.

Representative t-T histories were reconstructed (during this study whenever possible) from ZFT (revealed central ages), ZHe (U, Th, Sm concentrations, grain radius, diffusion kinetics of Reiners et al. (2004), and uncorrected grain age), AFT data (c-axes projected CTs, Dpar, the multi-kinetic annealing model of Ketcham et al. (2007), and single grain ages), AHe (U, Th concentrations, grain radius, diffusion kinetics of Guenthner et al. (2013), and uncorrected grain age) and the well documented geologic events (e.g., initiation of the Gulf of Suez). The different cooling ages (ZFT, ZHe, AFT and AHe ages) were used as t–T constraints that extended to cover the 2σ error range. To approach the most likely cooling history the initial inverse modelling was based on the best forward model with excellent fit to the used thermochronological data. Afterwards, the inverse models were run with 200,000 or 50,000 t–T paths tried (iteration). In HeFTy each modelled t-T path has a goodness of fit (GOF) value which refers to the degree of its fitting to the inputted data. Paths with GOF values <0.05 (<5%) are not an acceptable result (do not appear as a possible t-T paths), ≥0.05 (≥5%) are an acceptable paths (displayed as green paths), GOF values ≥0.5 (≥50%) are a good paths (displayed as purple paths). The program also displays the best GOF path (displayed as black path) and the weighted mean path (displayed as blue path) of the GOF value (Ketcham 2009; Ketcham et al. 2009).

Preliminary wider t-T constrain boxes were used to test the behaviour of the t-T paths with high degree of freedom. These showed not much difference but much less appropriate paths. Models with reheating and cooling evolutionary history were tested for all studied areas although the scarcity of any geologic information refers to occurrence of subsidence or increased heat flow and being such thermal history is not supported by the thermochronological data and no concordant scenario could be achieved. Consequently, cooling-only models will be presented and discussed.

5

RIFT WITH HIGH ELEVATED FLANKS (THE RWENZORI MOUNTAINS)

CONTENTS

In order to achieve the aims of this part of the study 33 metamorphic samples were collected from the main rock units of the western flank (D. R. Congo side) of the Rwenzori Mountains. Sampling was made along a vertical transect starting with a phyllite-mica schist sample (DRC 10-33) located 1407 m a.s.l to the amphibolite sample (DRC 10-21) located 4442 m a.s.l (Fig. 5.1). Due to a scarcity in suitable apatites and zircons among these rocks, only 3 samples provided suitable zircons for ZHe dating, 28 samples supplied suitable apatites for AFT dating and only 3 samples provided suitable apatites for AHe dating. The t-T modelling was performed using HeFTy v.1.8.3 code (Ketchem, 2009) based on the obtained cooling ages, He data, CTs lengths distribution and Dpar values.

5.1 Zircon (U-Th-Sm)/He data

The ZHe thermochronology technique was performed on 15 single grains from three samples (Table 5-1). The corrected single grain ages and (1σ) errors array between 588.4 (9.0) and 157.7 (2.3) Ma with the majority of the grains clustering around ~400 (13) or ~235 (20) Ma. This clustering of ZHe ages around Devonian and Triassic times dates for the onset of rapid cooling/exhumation of the area across the ZHe PRZ.

There is no clear relationship between ZHe ages and their grain dimensions (Fig. 5.2) which refers to the absence of any diffusional domain size effect on ZHe ages. That concentrates most of intra-sample age differentiation (Table 5-1) on the radiation damage effect (eU). The eU values ranging from 1113.2 to 134.2 µg/g (Table 5-1). In general, the analyzed grains show a negative ZHe age-eU relationship which is obvious between sample DRC10-29 single zircon grains (Fig. 5.3). For the ZHe data, a critical threshold of ~600 µg/g for the eU concentration in the Rwenzori area was reported (Bauer et al., 2013; 2015). Therefore, grains with eU<600 µg/g expressed more stress and grains with the lowest eU value were considered as providing the most reliable ZHe ages (Table 5-1). Consequently, the age of DRC10-23-zr2 grain was considered as the most reliable age for this sample because grain zr1 has exceeded the eU threshold value and grain zr3 has a higher eU value and consequent an older ZHe age. In sample DRC10-29-zr1 and zr4 grains were excluded because they have passed the Rwenzoris eU threshold value. On the other hand, grain zr6 has the lowest eU content, therefore its age was considered as the most reliable age for this sample (Table 5-1).

5.2 Apatite fission track data

The treated samples provided AFT central ages and (1σ) errors ranging from 56.2 (15.8) to 10.9 (1.1) Ma (Fig. 5.1) with a positive age-elevation relationship (Fig. 5.4). The AFT ages can be divided spatially into three age/elevation groups; the first with ages between 56.2 (15.8) and 42.0 (12.7) Ma with an average of ~49 (4) Ma, the second ranging from 29.9 (2.5) to 21.7 (4.3) Ma with an average of ~26 (3) Ma, and the third has ages of 12.6 (2.1) and 10.9 (1.1) Ma with an average of ~12 (2) Ma (Figs. 5.1; 5.4). This age grouping with a spatial separation pattern indicates non-uniform uplift of the studied area as it consists of smaller blocks, moving independently from each other across bounding faults. Such an exhumation pattern is dominant in the Rwenzoris (Ring, 2008, Bauer et al., 2010b, 2013; Sachau et al., 2015). Although, 4 samples; DRC10-06 (39.3 (11.4) Ma), DRC10-20 (24.6 (7.9) Ma), DRC10-24 (29.4 (9.1) Ma), and DRC10-25 (21.7 (4.3) Ma) break that spatial distribution pattern. However, the last three samples are geographically separated from the sur-

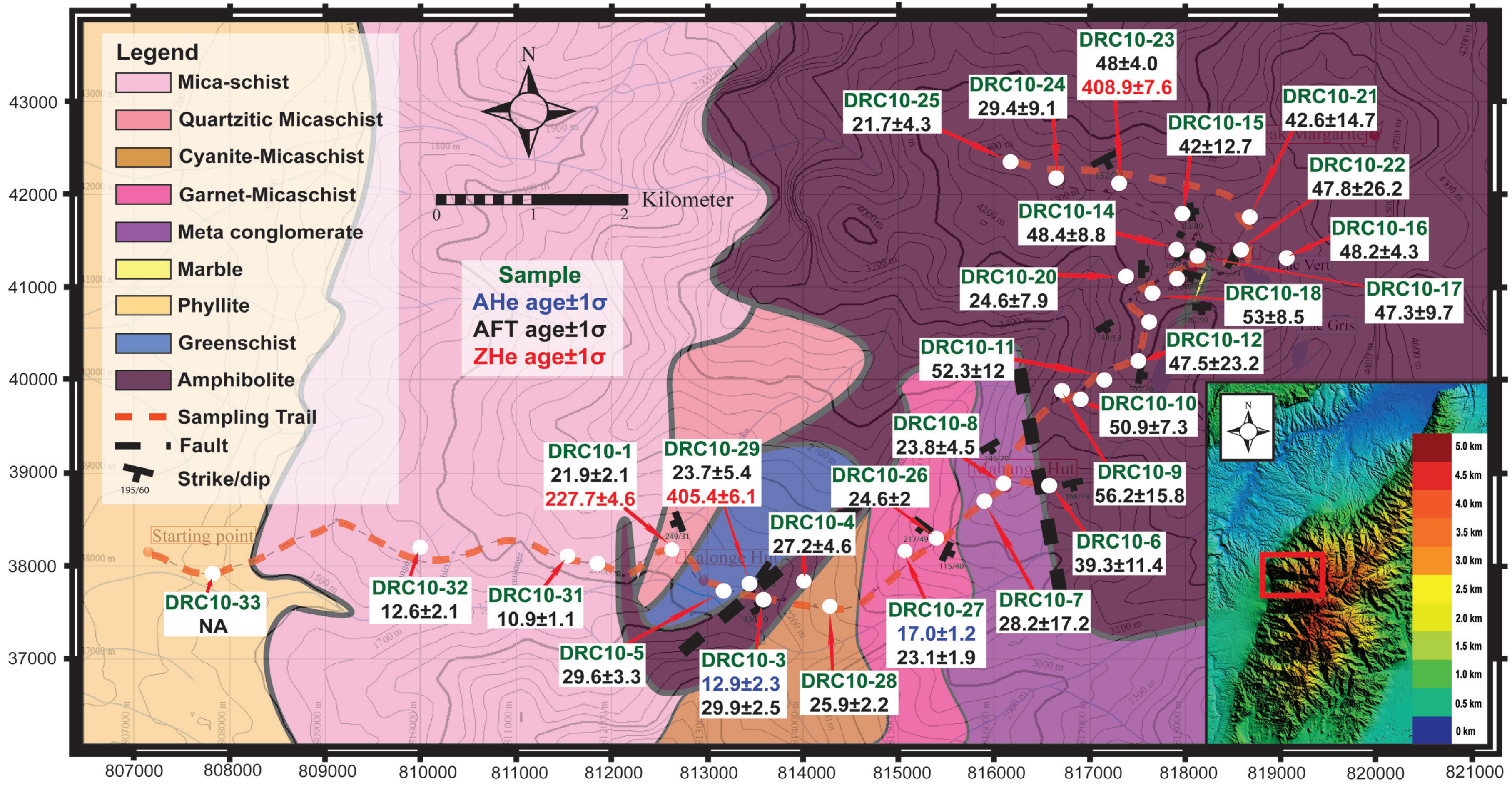

Fig. 5.1: Geologic map of the studied area of the Rwenzoris with the main rock units lithologies, locations and ages of the dated samples along with the sampling trail. The inset shows the area covered by the map from the Rwenzori Mountains (modified by Starz, 2012 after Bon et al., 1981).

Table 5-1: Summary of Rwenzoris zircon (U-Th)/He data.

Sample No.	M [µg]	Av. r [µm]	U [µg/g]	Th [µg/g]	4He [nmol/g]	eU [µg/g]	Ft	Raw age (1σ) [Ma]	Corr. age (1σ) [Ma]
DRC10-01-zr1	3.75	50.4	817.3	352.4	831.6	900.1	0.76	168.9 (2.5)	**222.2 (3.3)**
DRC10-01-zr2	2.45	47.7	523.2	225.3	536.4	576.2	0.75	170.2 (3.4)	**227.7 (4.6)**
DRC10-01-zr3	3.42	49.3	996.3	497.5	1018.4	1113.2	0.76	167.3 (2.5)	**221.7 (3.3)**
DRC10-01-zr4	1.79	39.5	668.6	295.0	748.8	738.2	0.70	185.2 (2.9)	**264.5 (4.2)**
DRC10-01-zr5	1.89	41.1	568.7	306.6	511.6	640.7	0.71	146.3 (2.3)	**206.2 (3.2)**
DRC10-01-zr6	3.40	44.1	690.4	312.9	836.5	763.9	0.73	199.6 (3.8)	**273.6 (5.3)**
DRC10-23-zr1	2.46	46.2	475.4	796.9	636.5	662.6	0.74	175.5 (2.1)	**239.4 (2.9)**
DRC10-23-zr2	3.79	50.6	171.6	129.7	348.7	202.1	0.76	311.5 (5.7)	**408.9 (7.6)**
DRC10-23-zr3	1.61	39.8	296.9	105.8	751.7	321.8	0.70	417.4 (6.2)	**588.4 (9.0)**
DRC10-29-zr1	2.01	43.6	922.3	356.1	626.3	1006.0	0.73	114.4 (1.7)	**157.7 (2.3)**
DRC10-29-zr2	1.84	39.4	516.7	165.8	454.7	555.7	0.70	149.8 (2.2)	**214.1 (3.2)**
DRC10-29-zr3	9.05	35.6	214.0	124.6	341.5	243.3	0.67	254.7 (3.8)	**378.9 (5.7)**
DRC10-29-zr4	1.56	45.9	661.6	66.7	645.0	677.2	0.74	174.0 (2.7)	**234.8 (3.6)**
DRC10-29-zr5	1.00	35.6	573.0	60.1	542.5	587.1	0.67	168.9 (2.5)	**250.7 (3.8)**
DRC10-29-zr6	1.33	38.8	101.9	137.8	207.7	134.2	0.70	280.4 (4.2)	**405.4 (6.1)**

Sample No.; sample number, M; mass, U, Th, and He; isotopic concentrations, eU; effective Uranium concentration (eU= [U]+0.235[Th] concentration in weight %; Shuster et a., 2006), Ft; α-ejection factor for zircons calculated after Farley et al. (2000), Raw age; (raw) ages and 1σ error, Corr. age; corrected age for α-ejection with accordant 1σ error.

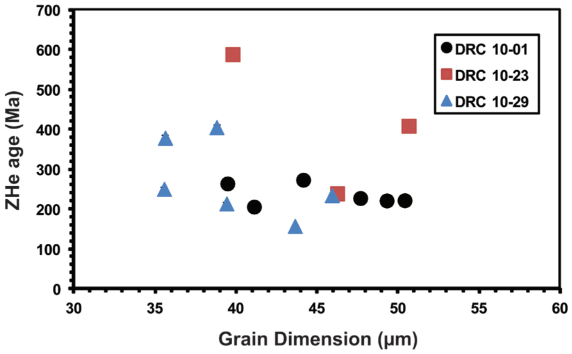

Fig. 5.2: ZHe ages-Grain dimensions plot representing detachment ZHe ages from the He diffusion domain for each sample grains.

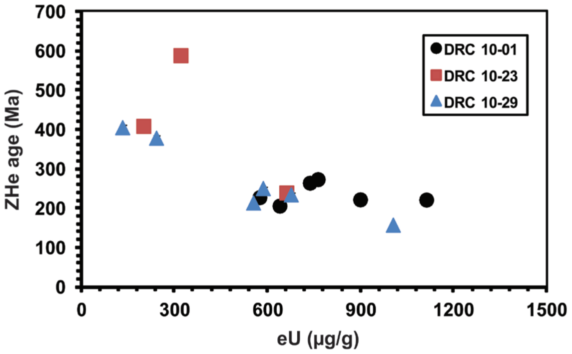

Fig. 5.3: ZHe ages-eU plot showing a negative relationship and dependency of ZHe ages on the eU values for each sample grains.

rounding samples recommending the presence of unnoticed faults, activated within the second age group time range. While, sample DRC10-06 is located spatially and in the age range of both the first and second age/elevation groups, it fits to either of them (Table 5-2; Figs. 5.1; 5.4).

All the treated samples have passed the Chi-square (χ2) statistics test with percentages ranging from 70 to 100% (Table 5-2). In general, the samples with lower χ2 values are mainly those with fewer countable apatites and consequent with higher AFT age error values. Despite that, their AFT ages are within the age range of the other sample

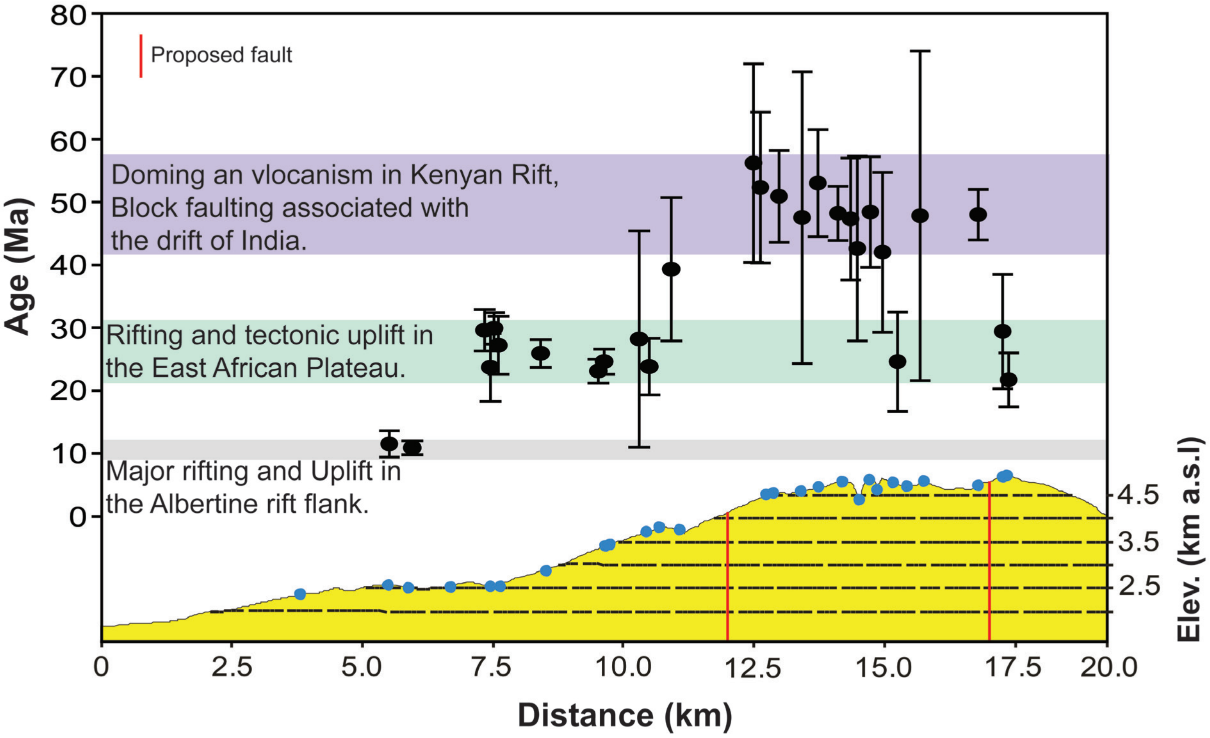

Fig. 5.4: Plotted are the Rwenzoris samples AFT ages against their elevations along the sampling transect. Samples show a positive age-elevation relationship, with cooling ages matching roughly three age groups. In addition major geological events associated with the evolution of the Albertine Rift are given: Doming and volcanism in Kenyan Rift (Ebinger, 1989), block faulting in the Rwenzoris associated with the drift of India (Bauer et al., 2013), Rifting and tectonic uplift in the East African Plateau after Roberts et al.(2012) and major rifting and Uplift in the Albertine rift flank (Ring et al., 1992). AFT ages with large errors are from samples with low certainty due to few countable apatites. Schematic transect with sample locations to the bottom.

from their age group. In general, the Uranium concentration in most of the apatites was low, ranging between 3.6±7.5 and 0.9±0.4 µg/g, with the exception of 7 samples where the concentrations range between 29.3±16.7 and 10.7±3.1 µg/g (Table 5-2).

There was scarcity in good enough grains for FT counting and lengths measurements in many samples (Tables 6.2; 6.3). These samples yielded insufficient CTs, where a maximum of 21 CTs (in one sample) could be measured. The CTs lengths range between 10.0 (0.5) and 13.1 (1.7) µm. These CTs were corrected against their crystallographic orientation using the software HeFTy v.1.8.3 (Donelick et al., 1999; Ketcham et al., 2009) resulting in c-axis-corrected CTs range between 10.7 (1.2) and 14.3 (0.9) µm with a negative skewness for most of the samples (all but 4 samples) ranging between -0.037 and -1.006 referring to a rapid cooling through the PAZ of AFT. Those samples with positive skewness vaying between 0.004 and 1.179 indicating a relative slow cooling through the PAZ of AFT. Along with CTs a total 1248 Dpar were measured (Table 5-3) providing values ranging between 1.4 (0.1) and 1.7 (0.1) µm indicating the dominance of near-end-member calcian-fluorapatites (Burtner et al., 1994; Donelick, 2004; Donelick et al., 2005).

The sampling strategy through a vertical transect has enabled testing the age-elevation relationship and detecting the t-T history changes along vertical cross-section. The positive age-elevation relationship (Fig. 5.4) is represented by being the sample with the youngest AFT age (DRC 10-31) was collected near the mountains foot, close to the rift and its AFT age overlap within the error

Table 5-2: The Rwenzoris' sample information and apatite fission track data.

S.-No.	Elev.	Lithology	U	n	Sp. Tracks		Ind. Tracks		χ^2	Central age (1σ)	Dpar (µm)
	[m a.s.l.]		[µg/g]		ρ_s	N_s	ρ_i	N_i	[%]	[Ma]	Av. (std)
DRC 10-01	2007	Mica Schist	15.9	11	1.847	166	22.946	2062	99	**21.9 (2.1)**	1.7 (0.1)
DRC 10-03	2048	Amphibolite	10.9	18	1.749	258	15.597	2301	70	**29.9 (2.5)**	1.7 (0.1)
DRC 10-04	2048	Amphibolite	3.7	8	0.559	43	5.448	419	91	**27.2 (4.6)**	1.4 (0.2)
DRC 10-05	2059	Green Schist	3.1	24	0.482	110	4.408	1006	100	**29.6 (3.3)**	1.4 (0.1)
DRC 10-06	3230	Amphibolite	3.2	7	0.574	14	3.852	94	71	**39.3 (11.4)**	1.4 (0.1)
DRC 10-07	3221	Mica Schist	1.2	4	0.152	3	1.423	28	77	**28.2 (17.2)**	1.3 (0.2)
DRC 10-08	3311	Mica Schist	4.9	12	0.513	35	5.792	395	92	**23.8 (4.5)**	1.3 (0.2)
DRC 10-09	3962	Amphibolite	3.1	6	0.437	16	2.019	74	99	**56.2 (15.8)**	1.6 (0.2)
DRC 10-10	4006	Amphibolite	2.9	22	0.734	66	3.734	336	100	**50.9 (7.3)**	1.3 (0.1)
DRC 10-11	4105	Amphibolite	2.8	10	0.664	24	3.263	118	100	**52.3 (12.0)**	1.5 (0.1)
DRC 10-12	4174	M.A. Green Schist	5.0	4	0.98	5	5.294	27	88	**47.5 (23.2)**	1.3 (0.2)
DRC 10-14	4278	Amphibolite	2.8	13	0.543	39	2.87	206	99	**48.4 (8.8)**	1.5 (0.2)
DRC 10-15	4294	Amphibolite	0.9	12	0.166	13	1.01	79	100	**42.0 (12.7)**	1.3 (0.2)
DRC 10-16	4228	Amphibolite	6.3	26	1.404	228	7.408	1203	89	**48.2 (4.3)**	1.6 (0.1)
DRC 10-17	4175	Amphibolite	1.7	14	0.39	30	2.093	161	100	**47.3 (9.7)**	1.4 (0.2)
DRC 10-18	4308	Amphibolite	2.2	14	0.606	52	2.891	248	100	**53.0 (8.5)**	1.5 (0.2)
DRC 10-20	4228	Amphibolite	3.0	6	0.394	11	4.044	113	98	**24.6 (7.9)**	1.3(0.1)
DRC 10-21	4442	Amphibolite	2.6	8	0.484	10	2.857	59	100	**42.6 (14.7)**	1.5 (0.2)
DRC 10-22	4375	Amphibolite	2.6	3	0.613	4	3.22	21	77	**47.8 (26.2)**	1.4 (0.1)
DRC 10-23	4178	Amphibolite	29.3	9	6.391	266	33.252	1384	84	**48.0 (4.0)**	1.4 (0.1)
DRC 10-24	4397	Amphibolite	6.2	9	0.889	12	7.558	102	100	**29.4 (9.1)**	1.2 (0.1)
DRC 10-25	4438	Amphibolite	5.6	14	0.509	30	5.833	344	100	**21.7 (4.3)**	1.5 (0.2)
DRC 10-26	2976	Mica Schist	10.7	27	1.395	260	15.248	2842	100	**24.6 (2.0)**	1.3 (0.1)
DRC 10-27	2911	Mica Schist	12.9	24	1.565	258	16.758	2763	100	**23.1 (1.9)**	1.4 (0.1)
DRC 10-28	2439	Mica Schist	26.3	25	3.5	250	33.335	2381	99	**25.9 (2.2)**	1.5 (0.1)

DRC 10-29	2059	Green Schist	5.3	10	0.324	22	3.606	245	100	**23.7 (5.4)**	1.4 (0.2)
DRC 10-31	2076	Green Schist	17.9	17	1.089	144	26.118	3455	99	**10.9 (1.1)**	1.4 (0.1)
DRC 10-32	1846	Mica Schist	4.5	18	0.31	43	6.333	878	100	**12.6 (2.1)**	1.4 (0.1)

Sample information and apatite fission track data given as central ages with uncertainty of 1-sigma. S.-No.; samples number, Elev. [m a.s.l.]; elevation in meters above sea-level, Lithology M.A.; metamorphic amphibolite, U; Uranium concentration in µg/g, n; number of counted apatite grains, ps; density of spontaneous tracks (105 tr/cm2), Ns; number of spontaneous tracks, pi; density of induced tracks (105 tr/cm2), Ni; number of induced tracks, χ2; chi square test: probability of single grain ages belonging to one population. Test is passed if P(χ2) > 5% (Galbraith, 1981), Dpar (std); average etch pit in µm and standard deviation. Central ages were calculated with Trackkey v.4.2 (Dunkl, 2002) using a ζ-value of 330.60 ± 16.47. Nd (tracks counted on CN5 dosimeter glass) = 15167 tracks.

range with the sample with the lowest elevation (DRC 10-32). While, the sample with the oldest AFT age (DRC 10-09) was taken from the high peak region and its AFT age overlap within the error range with the sample with the highest elevation (DRC 10-21) (Fig. 5.1; 5.4).

5.3 APATITE (U-TH)/HE DATA

The AHe thermochronology technique was carried out on 9 single apatite grains from three samples (Table 5-4). The corrected single-grain ages and (1σ) errors ranging from 38.3 (2.4) to 12.9 (2.3) Ma (Table 5-4) with the exception of two grains which are anomalously older (DRC10-26-ap3; with 117.5(4.6) Ma) to younger (DRC10-03-ap1; with 3.0 (5.7) Ma).

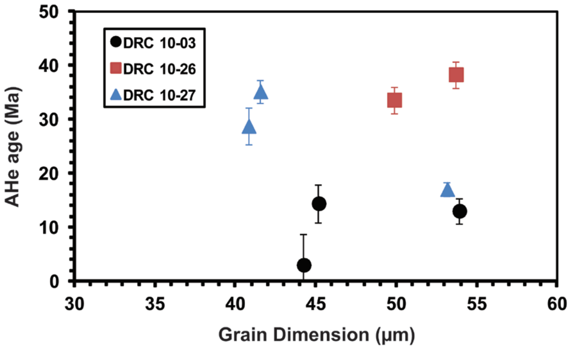

Fig. 5.5: AHe ages-Grain dimensions plot representing detachment AHe ages from the He diffusion domain for each sample grains.

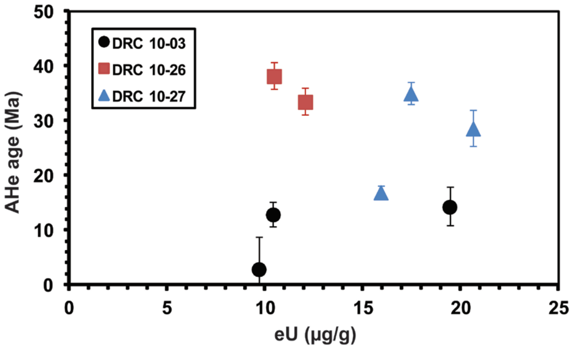

Fig. 5.6: AHe ages-eU plot showing no relationship and detachment of AHe ages from the eU values for each sample grains.

Table 5-3: Rwenzoris detailed apatite confined fission track length and Dpar data.

Sample	CT n	CT mean (µm)	CT std. (µm)	CT skew.	Lc mean (µm)	Lc std. (µm)	Lc skew.	Dpar n	Dpar mean (µm)	Dpar std. (µm)	Dpar skew.
DRC 10-01	19	**12.2**	1.5	0.616	**13.5**	1.0	1.025	42	**1.7**	0.1	1.179
DRC 10-03	13	**13.1**	1.7	-1.279	**14.3**	0.9	-0.370	44	**1.7**	0.1	-0.285
DRC 10-23	21	**11.5**	1.8	-0.178	**13.4**	1.3	-0.297	42	**1.4**	0.1	0.261
DRC 10-27	11	**12.5**	1.3	0.576	**13.5**	1.3	-0.843	33	**1.4**	0.1	0.473
DRC 10-04	6	**10.7**	1.1	0.948	**12.6**	0.8	1.237	121	**1.4**	0.2	-1.006
DRC 10-06	3	**11.2**	2.3	-0.214	**12.1**	1.3	1.571	16	**1.4**	0.1	-0.855
DRC 10-08	1	**7.5**	NA	NA	**9.7**	NA	NA	31	**1.3**	0.2	-0.072
DRC 10-14	4	**9.5**	1.2	-0.835	**11.5**	0.8	0.168	52	**1.5**	0.2	-0.363
DRC 10-16	11	**11.9**	1.4	0.474	**13.5**	1.3	-0.772	46	**1.6**	0.1	0.004
DRC 10-18	4	**12.5**	2.2	-0.580	**13.8**	1.4	-0.702	79	**1.5**	0.2	-0.130
DRC 10-25	1	**11.0**	NA	NA	**12.7**	NA	NA	35	**1.5**	0.2	-0.202
DRC 10-26	2	**10.0**	0.5	NA	**10.8**	1.3	NA	177	**1.3**	0.1	-0.037
DRC 10-28	11	**11.2**	2.4	0.237	**13.1**	1.5	0.403	44	**1.5**	0.1	-0.478
DRC 10-31	2	**10.0**	0.5	NA	**10.7**	1.2	NA	9	**1.4**	0.01	NA

Samples DRC 10-01, 03, 23 and DRC 10-27 were used in modelling as (U-Th)/He data were available. n CT; number of measured confined tracks, CT mean; mean confined track length, std; standard deviation, skew; skewness of distribution relative to the mean value (measure of asymmetry of the distribution), Lc mean; mean track length after c-axis correction, n Dpar; number of measured etch pit diameters, Dpar mean; mean etch pit diameter.

Table 5-4: Summary of Rwenzoris apatite (U-Th)/He data.

Sample No.	M [µg]	Av. r [µm]	U [µg/g]	Th [µg/g]	Sm [µg/g	4He [nmol/g]	eU [µg/g]	Ft	Raw age (1σ) [Ma]	Corr. age (1σ) [Ma]
DRC10-03-ap1	1.07	44.2	8.9	2.9	2.8	0.1	9.7	0.68	2.0 (3.3)	**3.0 (5.7)**
DRC10-03-ap2	2.37	53.9	10.3	0.4	3.4	0.5	10.4	0.74	9.5 (1.7)	**12.9 (2.3)**
DRC10-03-ap3	8.86	45.2	18.9	2.2	13.1	1.0	19.4	0.69	9.9 (2.4)	**14.4 (3.5)**
DRC10-26-ap1	3.46	53.7	10.3	0.5	49.8	1.6	10.5	0.73	28.1 (1.8)	**38.3 (2.4)**
DRC10-26-ap2	1.61	49.8	11.8	0.9	51.3	1.6	12.1	0.72	24.0 (1.7)	**33.6 (2.4)**
DRC10-26-ap3	1.16	37.7	11.9	10.2	54.4	5.8	14.4	0.64	73.9 (2.9)	**117.5 (4.6)**
DRC10-27-ap1	1.28	40.8	20.2	1.8	50.5	2.1	20.6	0.66	18.9 (2.2)	**28.7 (3.3)**
DRC10-27-ap2	2.66	53.1	15.7	0.9	48.7	1.1	15.9	0.73	12.5 (0.9)	**17.0 (1.2)**
DRC10-27-ap3	1.48	41.5	17.1	1.4	50.6	2.2	17.4	0.67	23.3 (1.4)	**35.1 (2.0)**

Sample No.; sample number, M; mass, U, Th, Sm, and He; isotopic concentrations, eU; effective Uranium concentration (eU = [U] + 0.235[Th] + 0.0053[Sm], concentrations in wt.%; after Spiegel et al., 2009); Ft: α-ejection correction factor, Raw age; (raw) ages and 1σ error, Corr. age; corrected age for α-ejection with accordant 1σ error.

There is no clear relationship between AHe ages and their grain dimensions (Fig. 5.5) which refers to an absence of any diffusional domain size effect on AHe ages. The eU values ranging between 20.6 and 9.7 µg/g reflecting a low U and Th concentrations (Table 5-4) with no AHe ages-eU values relationship (Fig. 5.6) indicating the absence of a clear systematic effect of the radiation damage on the AHe ages. However, the AHe ages-Th concentrations plot shows negative relationship (Fig. 5.7) indicating a probability of Th-rich micro-inclusions existence within the Rwenzoris apatites. Therefore, the grains with the lower Th concentrations seem to have the most reliable AHe cool-

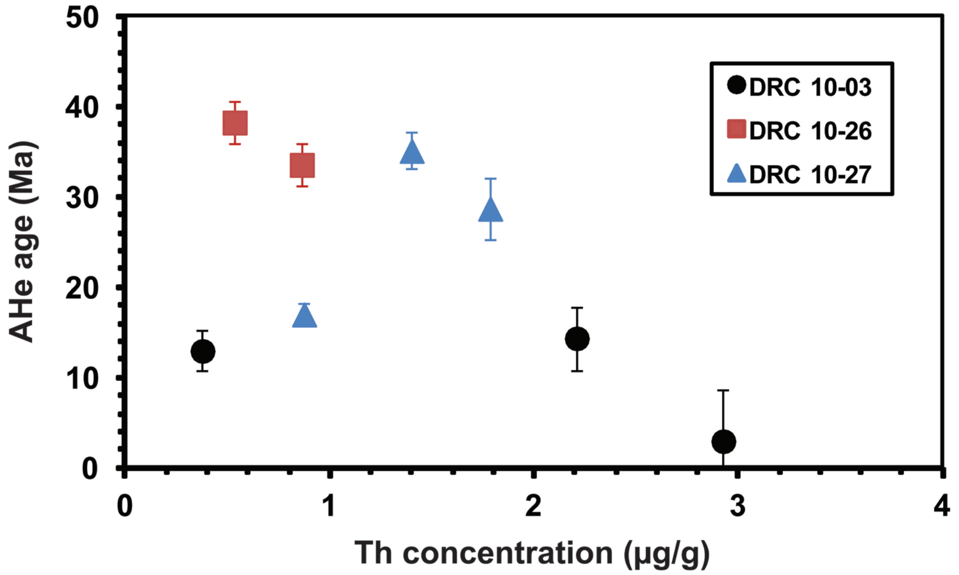

Fig. 5.7: AHe ages-Th concentration plot showing a negative relationship and dependency of AHe ages on the Th concentrations.

ing ages. That is supported by being the anomalously older grain DRC10-26-ap3 with an anomalously high Th concentration (10.2 µg/g) compared to all other grains (Table 5-4). Moreover, the anomalously younger grain DRC10-03-ap1 shows a relatively high Th concentration (2.9 µg/g) compared to other grains, in addition to a near blank He value (0.1 µg/g) indicating a possibility of helium diffusion (Table 5-4). Therefore, these two grains were excluded.

5.4 THERMO-KINEMATIC MODELLING AND EXHUMATION RATES

There was a scarcity in the existence of CTs with a sufficient number, therefore, the samples were only modelled if the AFT data was supported by ZHe and/or AHe data.

Here the cooling-only model is concordant with the general geology of high elevated mountains exhumation and the thermochronological data. Modelling solutions for all samples show a goodness-of-fit (GOF) greater than 95% for all modelled parameters (AFT cooling ages, CT length distribution, ZHe diffusion, and AHe diffusion) with except for only 2 models revealing a GOF greater than 69% (Fig. 5.8; Fig. 5.9).

The produced t-T models show a similar cooling pattern for all samples. While, the only difference was the onset timing of the rapid cooling events through the block bounding faults (Fig. 5.8; Fig. 5.9). In general, all modelled samples have experienced two rapid cooling/exhumation events. The first event started either in Silurian or Triassic times to uplift the samples from ZHe PRZ (≥7 km depth) to depths slightly greater than the AFT PAZ (≥3 km depth). The second event was more continuous has started in Eocene or Oligocene-Miocene till Recent times. Between these two rapid cooling/exhumation events there was a long period of almost thermal stability (Fig. 5.8; Fig. 5.9).

The cooling and exhumation rates as well as the rock uplift (vertical rock uplift corresponding to a single event) were calculated from the t-T modelling, considering an average geothermal gradient (25 (5) °C/km; Bauer et al., 2013) (Table 5-5). As in northern the Albertine rift ~30 °C/km geothermal gradient

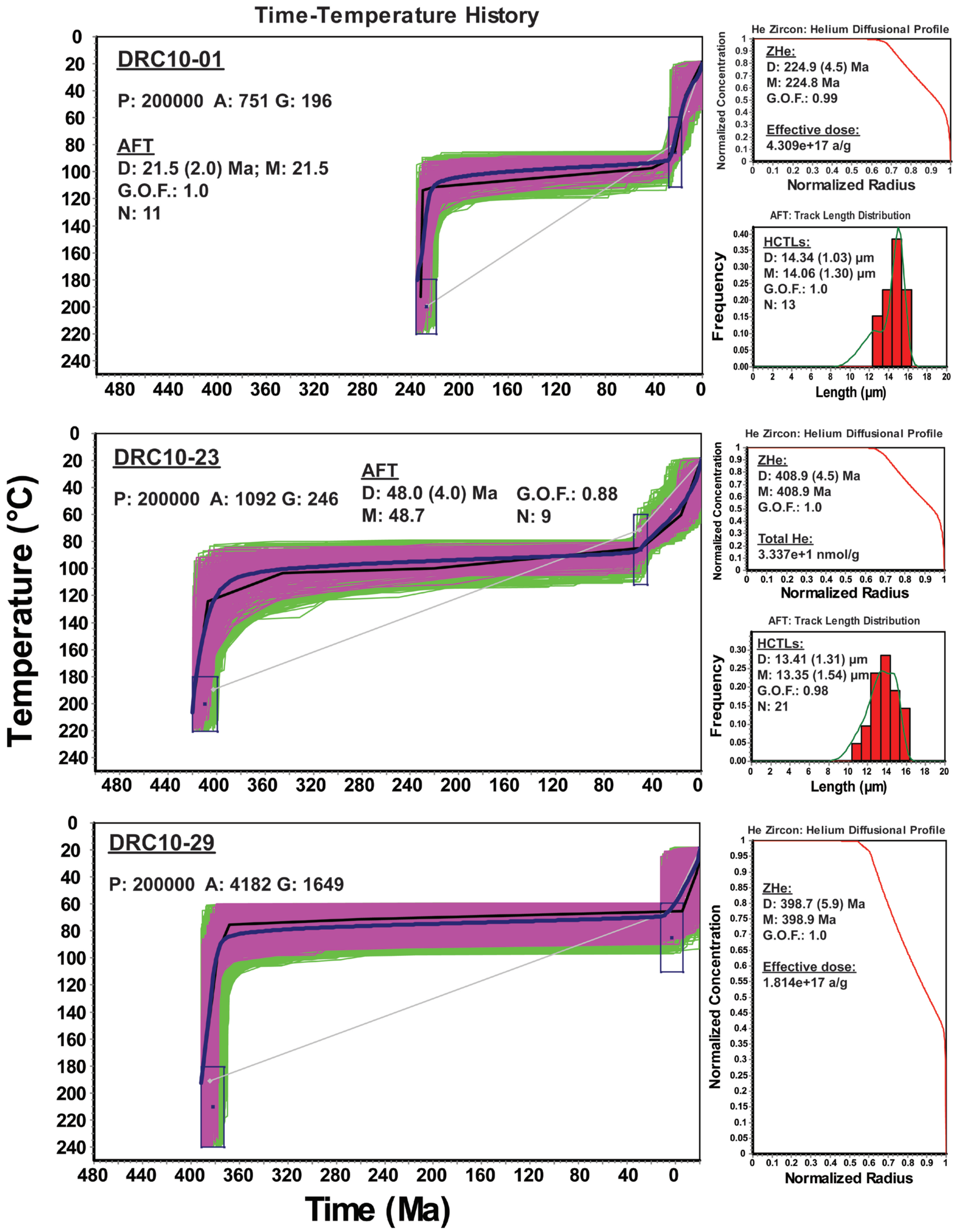

Fig. 5.8: Thermal history modelling using HeFTy v.1.8.3 (Ketcham et al., 2009); representative t–T paths illustrate the cooling history of samples of Rwenzori Mountains with ZHe and AFT data. Displayed are; on the left: the t–T paths, on the right: zircon helium diffusion profile and the c-axes corrected horizontal confined track lengths (HCTLs) distribution overlain by a calculated probability density function (best fit). Resulting t–T curves show four different reliability levels; green paths: acceptable fit (all t–T paths with a merit function value of at least 0.05), purple paths: good fit (all t–T paths with a merit function value of at least 0.5), black line: best fit and dashed blue line: the weighted mean path (Ketcham et al., 1999, 2009). The used constrains (t-T boxes) are ZHe and AFT aes. A: acceptable fit models, G: good fit models, D: determined FT age and HCTLs (1-σ error), M: modelled FT age and HCTLs, G.O.F.: goodness of fit, N: number of single grains and HCTLs.

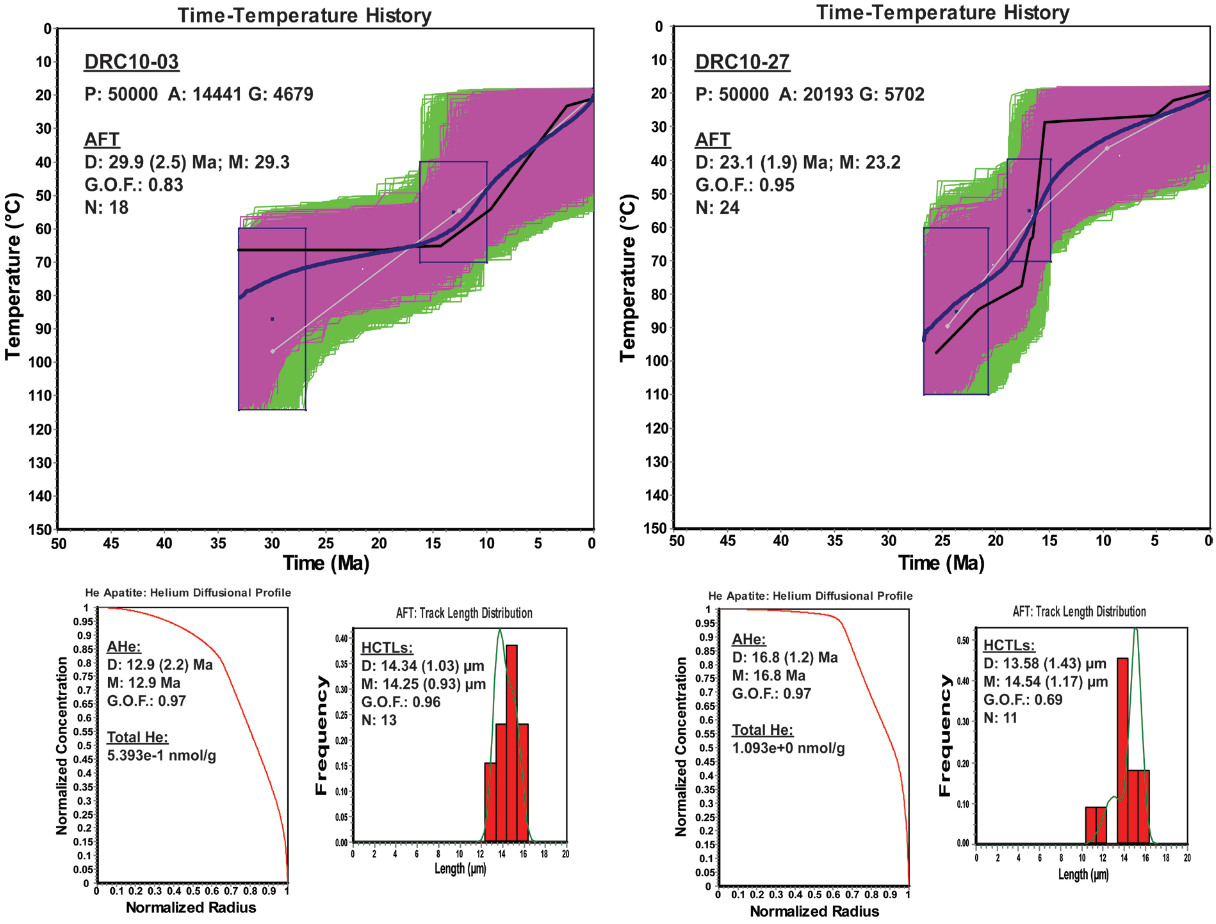

Fig. 5.9: Thermal history modelling of Rwenzori Mountains samples with AFT and AHe ages using HeFTy v.1.8.3 (Ketcham et al., 2009). The used constrains (t-T boxes) are AFT and AHe ages. For further explanation see Fig. 5.8

was calculated based on heat flow values ≥70 mW/m^2 and thermal conductivity values of 2.5 W/m K (Albaric et al., 2009). While, the heat flow values in the Rwenzori area are between 54 and 66 mW/m^2 and the thermal conductivity are ~3 W/m K (Tugume and Nyblade, 2009). Thus, an average geothermal gradient of 25 (5) °C/km seems reasonable (Bauer et al., 2015). The geothermal gradient is expressed as a range of 25 (5) °C/km (Table 5-5) for exhumation rate calculations but in the text, for simplicity sake, an average geothermal gradient of 25 °C/km was used. The recent average surface temperature (20 °C) was reduced by 6.5 °C for each km a.s.l. elevation of the modelled sample (Fig. 5.8; Fig. 5.9).

The modelled samples show a change in their cooling pattern/rate three or four times. **Sample DRC10-01** t-T model represents 4 phases of cooling patterns (Table 5-5; Fig. 5.8; Fig. 5.9). Starting by a rapid cooling event during the Triassic (from ~235 to 217 Ma) with a ~4.3 °C/Ma cooling rate, ~0.173 km/Ma exhumation rate (Fig. 5.10) and ~3.1 km of corresponding rock uplift over ~15 Ma. Afterwards, there was a period of almost a thermal stability extended from Triassic to Oligocene times (from ~217 to 30 Ma) with slow cooling and exhumation rates of ~0.1 °C/Ma and ~0.004 km/Ma respectively, resulting in ~0.7 km of corresponding rock uplift (Table 5-5; Fig. 5.10). Hereafter, the cooling pattern changed to more rapid cooling and exhumation rates of ~2.33 °C/Ma

Table 5-5: The Rwenzori Mountains Cooling rates, Exhumation rates and Rock uplift extracted from the HeFTy t-T modelling.

S.- No.	Elev. (m a.s.l)	Phase	t-t Segment (Ma)	Δt	T-T Segment (°C)	ΔT	Cooling Rate (°C/Ma)	Exhumation Rate			Rock uplift		
								(km/Ma) 20 °C/km	(km/Ma) 25 °C/km	(km/Ma) 30 °C/km	(km/Δt) 20 °C/km	(km/Δt) 25 °C/km	(km/Δt) 30 °C/km
DRC10-01	2007	1	235-217	18	185-107	78	**4.33**	0.217	**0.173**	0.144	3.9	**3.1**	2.6
		2	217-30	187	108-90	18	**0.1**	0.005	**0.004**	0.003	0.9	**0.7**	0.6
		3	30-15	15	90-55	35	**2.33**	0.117	**0.093**	0.078	1.8	**1.4**	1.2
		4	15-0	15	55-10	45	**3.0**	0.15	**0.12**	0.1	2.3	**1.8**	1.5
DRC10-03	2048	1	33-14	19	90-63	27	**1.42**	0.071	**0.057**	0.047	1.4	**1.1**	0.9
		2	14-9	5	63-44	19	**3.80**	0.190	**0.152**	0.127	1.0	**0.8**	0.6
		3	9-0	9	44-20	24	**2.67**	0.133	**0.107**	0.089	1.2	**1.0**	0.8
DRC10-23	4178	1	420-395	25	180-117	63	**2.52**	0.126	**0.101**	0.084	3.2	**2.5**	2.1
		2	395-55	340	117-87	30	**0.09**	0.004	**0.004**	0.003	1.5	**1.2**	1.0
		3	55-15	40	87-52	35	**0.88**	0.044	**0.035**	0.029	1.8	**1.4**	1.2
		4	15-0	15	52-22	30	**2.0**	0.1	**0.08**	0.067	1.5	**1.2**	1.0
DRC10-27	2911	1	25-19	6	90-72	18	**3.0**	0.150	**0.12**	0.100	0.9	**0.7**	0.6
		2	19-13	6	72-40	32	**5.33**	0.267	**0.213**	0.178	1.6	**1.3**	1.1
		3	13-0	13	40-20	20	**1.54**	0.077	**0.062**	0.051	1	**0.8**	0.7
DRC10-29	2059	1	410-392	18	180-85	95	**5.28**	0.264	**0.211**	0.176	4.8	**3.8**	3.2
		2	392-32	360	85-70	15	**0.04**	0.002	**0.002**	0.001	0.8	**0.6**	0.5
		3	32-22	10	70-55	15	**1.50**	0.075	**0.060**	0.050	0.8	**0.6**	0.5
		4	22-0	22	55-10	45	**2.05**	0.102	**0.082**	0.068	2.3	**1.8**	1.5

The cooling phases and cooling rates were extracted from HeFTy t-T models. The exhumation rates were calculated from the cooling rates, a geothermal gradients of 20, 25 and 30 °C/km and an average surface temperature which was calculated from the recent average 20 °C minus 6.5 °C for each km a.s.l. elevation. The recent geothermal gradient is calculated to be 25 °C/km (Bauer et al., 2013). The rock uplift was calculated as episodical vertical rock uplift from multiplying the exhumation rate by the duration in each single cooling event. Elev. (m a.s.l.) is elevation with meters above sea level. t–t: time segment; ~t: average time; Δt: phase (event) duration; T–T: Temperature segment; ΔT: temperature reduction during a single event.

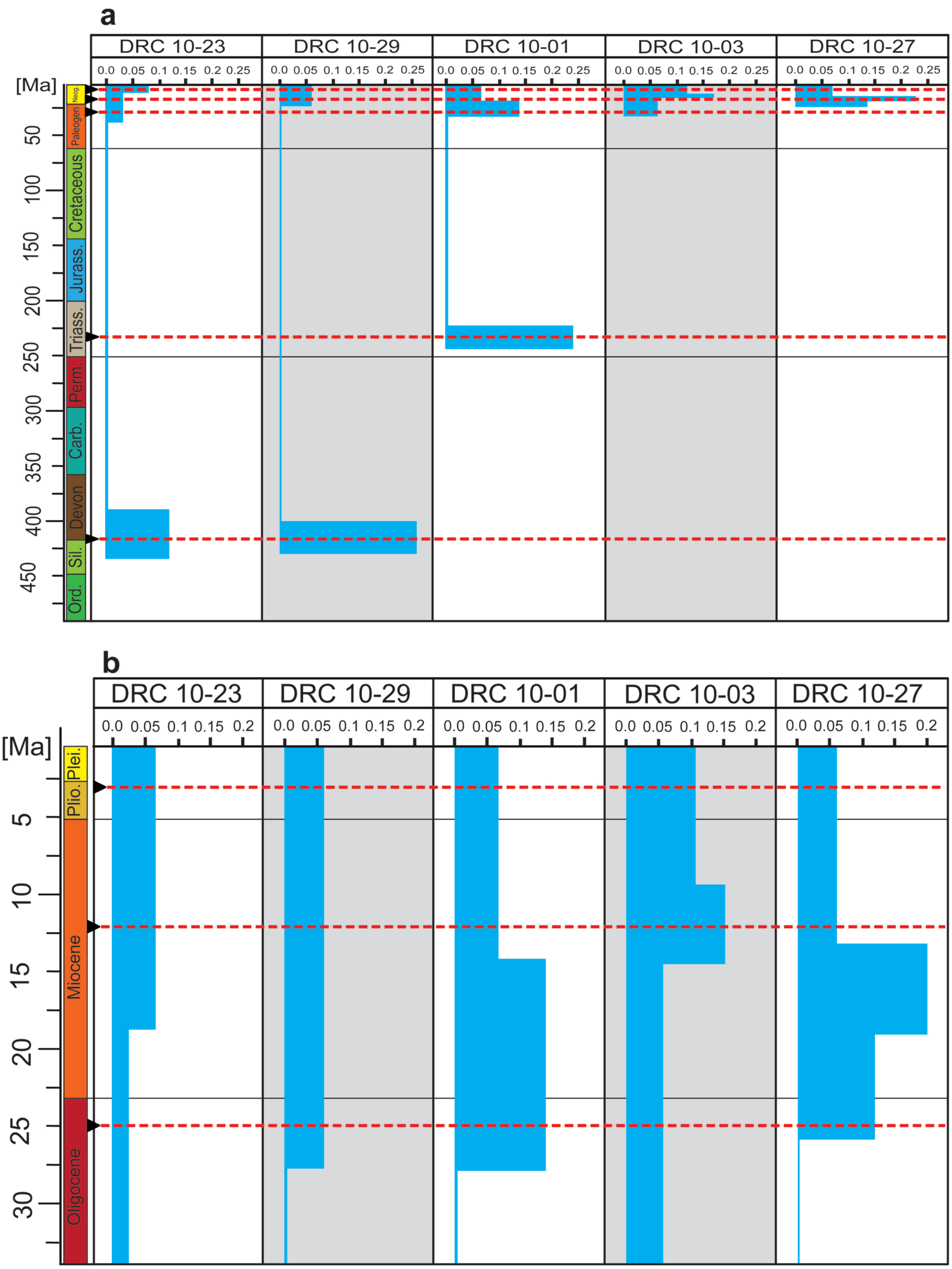

Fig. 5.10: Exhumation rates in (km/Ma) diagram of The Rwenzori Mountains. Based on the data from the thermal history from Fig. 5.8, Fig. 5.9 and from Table 5-5. Five major exhumation events presented (red dashed lines) synchronous with major cooling/exhumation events. (a) is the total recorded history by LTT. (b) represents a focus on the Cenozoic events.

and ~0.093 km/Ma respectively (Figs. 5.8; 5.10), introducing ~1.4 km of corresponding rock uplift. Then, a slight change in the cooling pattern started since ~15 Ma causing increased cooling and exhumation rates to ~3.0 °C/Ma and ~0.12 km/Ma respectively and a corresponding ~1.8 km of rock uplift. **Sample DRC10-23** t-T model represents 4 different phases of cooling patterns (Table 5-5; Fig. 5.10). Starting with a rapid cooling event during Silurian-Devonian times (from ~420 to 395 Ma) with a ~2.52 °C/Ma cooling rate, ~0.101 km/Ma exhumation rate (Fig. 5.10) and ~3.5 km of corresponding rock uplift over ~35 Ma. Afterwards, there was a period of almost a thermal stability extending into Eocene time (from ~395 to 55 Ma) with a ~0.09 °C/Ma cooling rate, ~0.004 km/Ma exhumation rate and ~1.2 km of corresponding rock uplift (Table 5-5; Fig. 5.10). Hereafter, the cooling pattern changed to a more rapid, from the Eocene till the Miocene (from ~55 to 15 Ma) with a ~0.88 °C/Ma cooling rate, ~0.035 km/Ma exhumation rate and ~1.4 km of corresponding rock uplift. Followed by another rapid phase from the Miocene (from ~15 Ma to recent), resulting in a ~2.0 °C/Ma cooling rate, ~0.08 km/Ma exhumation rate (Fig. 5.10) and ~1.2 km of corresponding rock uplift. **Sample DRC10-29** t-T model shows 4 different phases of cooling patterns (Table 5-5; Fig. 5.10). Started by a rapid cooling event during Devonian time (from ~410 to 392 Ma) with a ~5.3 °C/Ma cooling rate, ~0.211 km/Ma exhumation rate (Fig. 5.10) and ~3.8 km of corresponding rock uplift over ~17 Ma. Afterwards, there was a period of almost a thermal stability extended till Oligocene time (from ~392 to 32 Ma) with a ~0.04 °C/Ma cooling rate, ~0.002 km/Ma exhumation rate and ~0.6 km of corresponding rock uplift over ~360 Ma (Table 5-5; Fig. 5.10). Then, a change in the cooling pattern to a more rapid one occurred since Oligocene (from ~32 to 22 Ma) resulting in a ~1.5 °C/Ma cooling rate, ~0.06 km/Ma exhumation rate (Fig. 5.10) and ~0.6 km of corresponding rock uplift. Followed by a slight change in the cooling pattern to a more rapid, from the Miocene (from 22 Ma to recent), with a ~2.1 °C/Ma cooling rate, ~0.082 km/Ma exhumation rate and a corresponding ~1.8 km of rock uplift. **Sample DRC10-03** t-T model shows 3 changes in cooling patterns (Table 5-5; Fig. 5.10). Initiated by a relatively slow cooling event between Oligocene and Miocene times (from ~33 to 14 Ma) with a ~1.42 °C/Ma cooling rate, ~0.057 km/Ma exhumation rate (Fig. 5.10) and 1.1 km of corresponding rock uplift. Then, an increase in the cooling and exhumation rates occurred during the Miocene (from ~14 to 9 Ma) to values of ~3.8 °C/Ma and ~0.152 km/Ma respectively, producing ~0.8 km of corresponding rock uplift (Table 5-5; Fig. 5.10). Afterwards, the pattern changes to a less steeper one (from ~9 Ma to recent) showing a ~2.67 °C/Ma cooling rate, ~0.107 km/Ma exhumation rate (Fig. 5.10) and a corresponding ~1.0 km of rock uplift. **Sample DRC10-27** t-T model shows 3 changes in cooling patterns (Table 5-5; Fig. 5.10). Initiated by a rapid cooling event between Oligocene and Miocene times (from ~25 to 19 Ma) with a ~3.0 °C/Ma cooling rate, ~0.12 km/Ma exhumation rate (Fig. 5.10) and ~0.7 km of corresponding rock uplift. Then, an increase in the cooling and exhumation rates occurred during the Miocene (from ~19 to 13 Ma), with values of ~5.33 °C/Ma and ~0.213 km/Ma respectively (Fig. 5.10), resulting in ~1.3 km of corresponding rock uplift. Afterwards, the pattern changes to a less steeper one from the Miocene (~13 Ma) to recent time, showing a ~1.54 °C/Ma cooling rate, ~0.062 km/Ma exhumation rate and ~0.8 km of corresponding rock uplift (Table 5-5; Fig. 5.10).

6

Rift with low elevated flanks (The Samra Mountain area)

Contents

In order to achieve the aims of this part of the study 26 samples were collected from the main rock units of the Arabian-Nubian Shield (ANS) basement complex representing the eastern flank to the Gulf of Suez. There was a scarcity in suitable zircons and apatites in some of these samples. Among them 8 samples provided suitable zircons for ZFT dating (Table 6-1), and 14 samples yielded suitable apatites for AFT dating (Table 6-2) of these 8 samples provided CTs for t-T modelling (Table 6-3).

6.1 ZIRCON FISSION TRACK DATA

The treated samples gave ZFT central ages and (1σ) errors ranging from 673.9 (76.9) to 381.4 (26.1) Ma (Fig. 6.1) that could be divided into two spatially separated ZFT age groups. The first consists from the northward located samples (Fig. 6.1, Group A) with older ZFT ages ranging from 673.9 (76.9) to 619.1 (59.7) Ma. These ages extend over 54.8 Ma but they are overlapping within the error range (Table 6-1) indicating a cooling throw ZFT PAZ ~651.9 (24.9) Myr ago. The second, represented by all other samples, (Fig. 6.1, Groups B and C) includes ZFT ages between 461.7 (32.0) and 381.4 (26.1) Ma. The ZFT ages of these samples are spread over a relatively wider range (~80.3 Ma) but they are overlapping within the error range indicating a cooling throw ZFT PAZ ~426.2 (31.3) Myr ago.

All the treated samples have passed the Chi-square ($\chi 2$) statistics test indicating one age population (Table 6-1). These samples have uranium concentrations varying between 205.5 and 79.3 µg/g (Table 6-1) with no relationship to zircon single grain ages (Fig. 6.2). This, in addition to the lower uranium concentrations, indicates the absence of any metamictization effect on the ZFT ages (Table 6-1).

6.2 APATITE FISSION TRACK DATA

The AFT data from the Samra area were analysed as part of my master research (Mansour, 2010) that was reinterpreted and remodelled with integration of the new ZFT data which was revealed during the recent study.

The analysed samples provided AFT ages ranging from 484.5 (8.2) to 83.7 (10.9) Ma. These ages are separated into three distinctive age groups (Table 6-2); group A with Ordovician ages (3 samples), group B with Carboniferous-Triassic ages (6 samples), and group C with Cretaceous ages (5 samples). These three age groups are differentiated spatially indicating a differentiated thermo-tectonic history for each group (Fig. 6.1). Interestingly, the oldest age group A, is located in the north similar to the samples of the western flank of the Gulf of Suez (Omer et al., 1989). The AFT age-elevation relationship shows no preferable trend (Fig. 6.3).

Most of the analysed samples have a positive skewed CTs distribution with more or less wide patterns and short mean CTs which range from 9.4 (2.1) to 10.7 (2.6) µm with one exception of 12.5 (2.8) from sample **D5** (Table 6-3). The c-axis-corrected CTs lengths (Lc) range from 11.5 (2) to 13.3 (3) µm. Most of them show a positive skewness with a tail of longer tracks indicating spending a relatively long period in the AFT PAZ for most of the samples (Gleadow et. al., 1986). Along with the CTs a total 1383 Dpars were measured. The Dpar values are ranging between 1.7 (0.2) and 1.3 (0.2) µm indicating the dominance of a fluoroapatite composition. Only 2 samples **D8** and **S4** have higher Dpar values of 1.8 (0.2) and 2.0 (0.2) respectively, indicating a Cl-rich apatite composition (Burtner et al., 1994; Donelick, 2004; Donelick et al., 2005) (Table 6-3). There is no relationship between the Dpar values and apatite FT ages (5) which indicates, the age

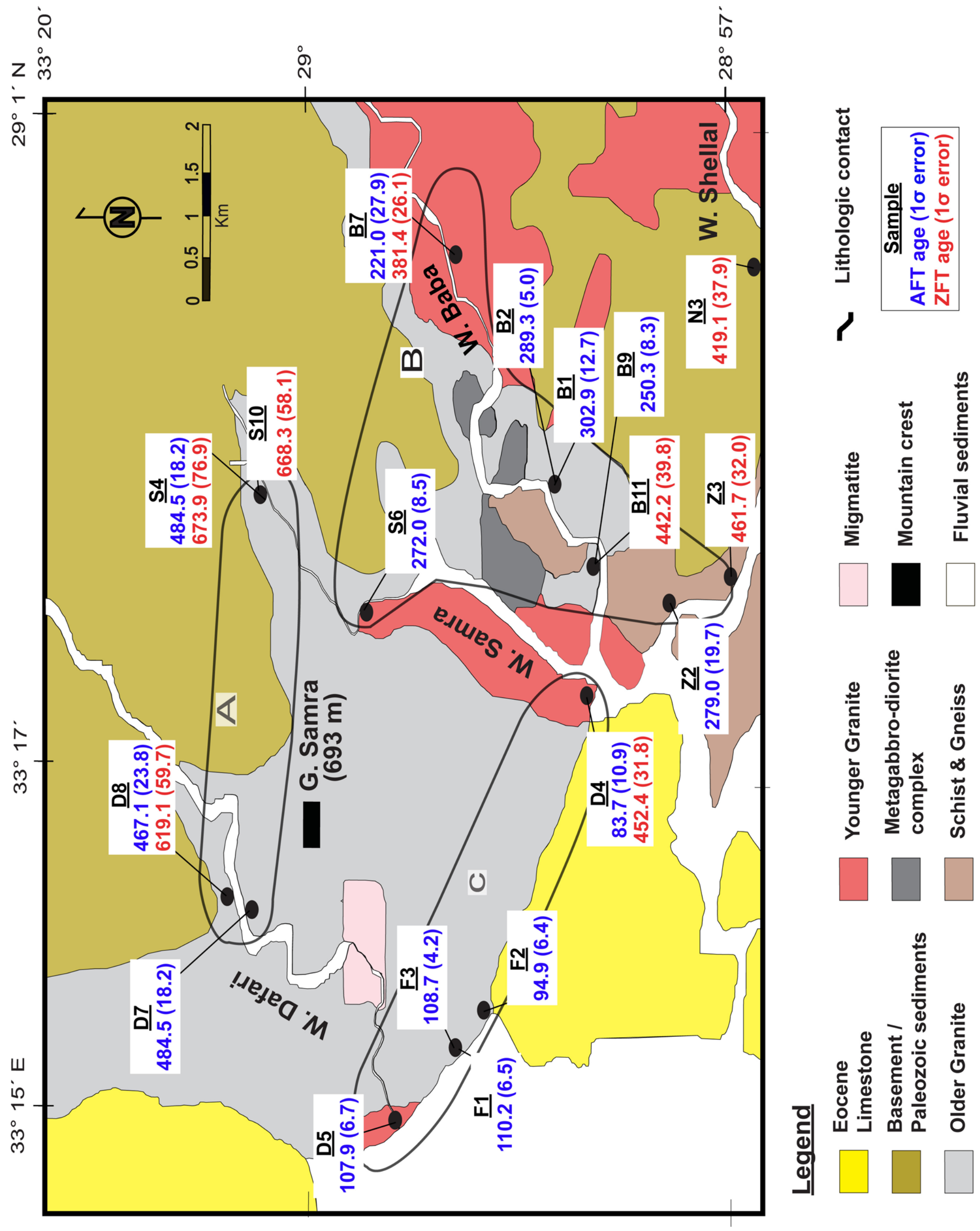

Fig. 6.1: Geologic map of the Samra mountain area with the main rock units lithologies and locations of the dated samples. The analysed AFT samples can be spatially divided into three regions A, B and C. W.; Wadi (valley), G.; Gebel (mountain) (modified by Mansour, 2010 after El Bialy, 2004).

differences are not related to the annealing kinetics variety of tracks caused by different chemistry of apatite grains.

The NIST SRM 612 reference glass was frequently measured during the analysis to monitor the precision and accuracy of the analytical techniques in U concentrations measurement. A total of 151 measurements were taken and concentrations of 238U were calculated using the 43Ca as an internal standard and compared with the reference values (Carpenter and Reimer, 1974; Walder et al., 1993; Pearce et al., 1997). The average 238U concentration is 37.8 µg/g with a standard deviations of less than 1.5% which is consistent with the reference values of 37.1 µg/g (Pearce et al., 1997), demonstrating the accuracy and precision of the measurement system.

Table 6-1: The Samra mountain area sample information and zircon fission track data.

S.-No.	Elev. [m a.s.l.]	Lithology	U [µg/g]	n	Sp. Tracks		Ind. Tracks		χ^2 [%]	Central age (1σ) [Ma]
					ρ_s	N_s	ρ_i	N_i		
Group A										
D8	520	Diorite	135.96	17	375.606	2229	24.097	143	100	**619.1 (59.7)**
S4	316	Gneiss	177.02	13	629.447	1581	37.823	95	100	**673.9 (76.9)**
S10	202	Synite	95.42	21	318.172	2981	19.852	186	100	**668.3 (58.1)**
Group B										
B7	229	Synite	205.51	23	357.661	3546	39.538	392	99	**381.4 (26.1)**
B11	100	Synite	179.67	12	389.588	1823	37.612	176	100	**442.2 (39.8)**
N3	299	Synite	179.99	21	316.264	1808	30.262	173	100	**419.1 (37.9)**
Z3	192	Gneiss	168.92	24	383.761	4112	34.624	371	100	**461.7 (32.0)**
Group C										
D4	298	Synite	163.8	22	393.192	3875	36.021	355	100	**452.4 (31.8)**

Sample information and zircon fission track data given as central ages with uncertainty of 1-sigma. Group A, B and C are from Fig. 6.1. S.-No.; samples number, Elev. [m a.s.l.]; elevation in meters above sea-level, U; Uranium concentration in µg/g, n; number of counted apatite grains, ρs; density of spontaneous tracks (10^5 tr/cm^2), Ns; number of spontaneous tracks, ρi; density of induced tracks (10^5 tr/cm^2), Ni; number of induced tracks, χ2; chi square test: probability of single grain ages belonging to one population. Test is passed if P(χ2) > 5% (Galbraith, 1981), Central ages calculated with Trackkey v.4.2 (Dunkl, 2002) using a ζ-value of 120.36 ± 5.09. Nd (tracks counted on CN1 dosimeter glass) = 15525 tracks.

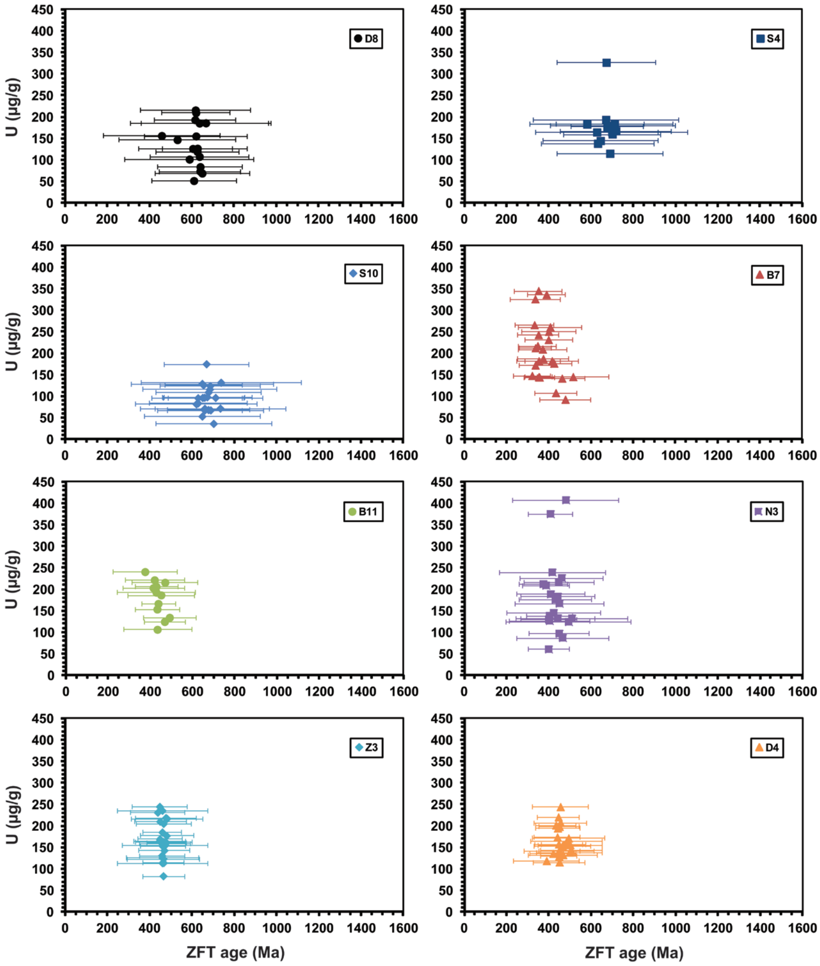

Fig. 6.2: ZFT single grain ages versus uranium concentrations for Samra mountain area samples. No relationship between them is represented.

Table 6-2: The Samra area sample information and apatite fission track data.

S.-No.	Elev.	Lithology	U	n	Sp. Tracks		χ²	Central age (1σ)[Ma]	Dpar (µm)
	[m a.s.l.]		[µg/g]		ρ_s	N_s	[%]		Av. (std)
Group A									
D7	525	Syenite	7.52	18	2.5	1198	46	**484.5 (18.2)**	1.6 (0.2)
D8	520	Diorite	7.56	38	2.4	2207	43	**467.7 (15.3)**	1.8 (0.2)
S4	316	Gneiss	7.58	31	1.9	444	41	**467.1 (23.8)**	2.0 (0.2)
Group B									
B1	195	Diorite	14.11	30	2.3	921	44	**302.9 (12.7)**	1.4 (0.2)
B2	202	Gneissos Syenite	39.3	85	5.8	4923	68	**289.3 (5.0)**	1.5 (0.2)
B7	229	Syenite	12.46	6	1.5	38	31	**221.0 (27.9)**	1.7 (0.2)
B9	195	Diorite	17.42	50	2.5	1267	66	**250.3 (8.3)**	1.6 (0.2)
S6	188	Rhyolitic Dyke	31.32	27	4.5	1503	41	**272.0 (8.5)**	1.4 (0.2)
Z2	152	Gneiss	22.14	8	4.2	420	44	**279.0 (19.7)**	1.4 (0.3)
Group C									
D4	298	Syenite	7.60	25	0.3	61	41	**83.7 (10.9)**	1.4 (0.2)
D5	189	Syenite	4.28	83	0.2	254	66	**107.9 (6.7)**	1.3 (0.2)
F1	188	Gneiss	21.8	26	1.4	339	41	**94.9 (6.3)**	1.5 (0.1)
F3	73	Syenitic Dyke	41.33	17	3.5	626	39	**110.2 (6.5)**	1.7 (0.2)
F4	182	Gneiss	29.81	49	1.7	806	57	**108.7 (4.2)**	1.6 (0.2)

Sample information and apatite fission track data given as weighted mean ages with uncertainty of 1-sigma. S.-No.; samples number, Elev. [m a.s.l.]; elevation in meters above sea-level, U; Uranium concentration in µg/g calculated based on Donelick et al. (2005) equation, n; number of counted apatite grains, ρs; density of spontaneous tracks (10^5 tr/cm^2), Ns; number of spontaneous tracks, χ2; chi square test: probability of single grain ages belonging to one population. Test is passed if P(χ2) > 5% (Galbraith, 1981), W.M. age; weighted mean age in million years calculated based on Hasebe et al. (2004) equation with $\lambda_f = 8.46 \text{ X}10^{-17}$ yr^{-1}, Dpar (std); average etch pit in µm and standard deviation.

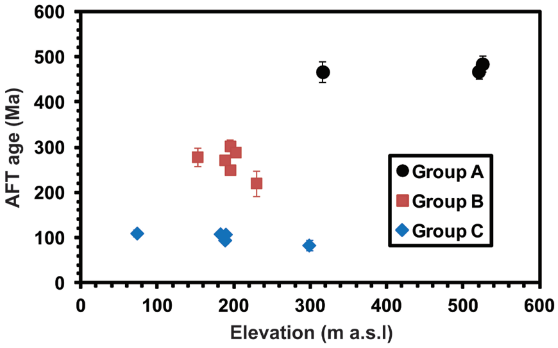

Fig. 6.3: AFT age-elevation plot of Samra mountain area samples showing no AFT age-elevation relationship.

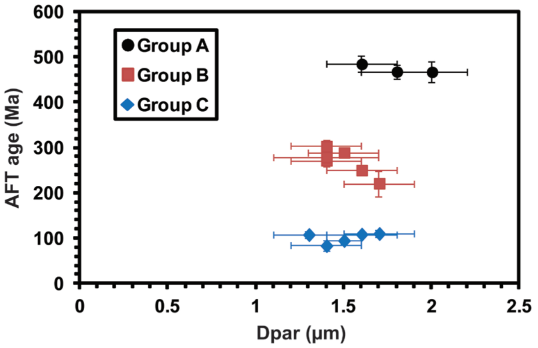

Fig. 6.4: AFT age-Dpar plot of Samra mountain area samples showing no relationship.

Table 6-3: The Samra mountain area detailed apatite confined fission track length and Dpar data.

Sample	CT n	CT mean (µm)	CT std. (µm)	CT skew.	Lc mean (µm)	Lc std. (µm)	Lc skew.	Dpar n	Dpar mean (µm)	Dpar std. (µm)	Dpar skew.
Group A											
D7	53	**10.4**	1.8	0.829	**12.4**	1.0	1.376	75	**1.6**	0.2	-0.223
D8	83	**10.4**	1.7	0.403	**12.5**	1.0	0.048	117	**1.8**	0.2	-0.249
S4	56	**10.3**	2.1	0.428	**12.4**	1.1	1.143	113	**2.0**	0.2	-0.925
Group B											
B1	73	**10.1**	2.4	-0.029	**12.3**	1.5	0.141	228	**1.4**	0.2	0.092
B2	185	**10.2**	1.7	0.437	**12.5**	1.0	0.785	190	**1.5**	0.2	0.046
B7	15	**10.3**	3.1	0.502	**12.7**	1.6	1.162	28	**1.7**	0.2	-0.475
B9	162	**9.8**	1.8	0.327	**12.5**	1.0	0.707	192	**1.6**	0.2	-0.486
S6	37	**9.4**	1.9	0.060	**12.2**	1.0	0.338	131	**1.4**	0.2	-0.521
Z2	17	**10.0**	2.2	0.582	**12.2**	1.5	-0.167	26	**1.4**	0.3	-0.812
Group C											
D4	11	**9.4**	3.1	0.094	**12.7**	1.2	0.605	14	**1.4**	0.2	0.426
D5	7	**12.5**	2.8	-0.799	**13.3**	3.0	-1.231	7	**1.3**	0.2	0.712
F1	10	**9.7**	2.8	-0.675	**12.7**	1.0	1.699	16	**1.5**	0.1	-0.123
F3	47	**10.7**	2.6	0.282	**12.7**	1.7	0.549	61	**1.7**	0.2	0.188
F4	106	**10.2**	2.5	0.400	**11.5**	2.0	0.345	185	**1.6**	0.2	0.048

n CT; number of measured confined tracks, CT mean; mean confined track length, std; standard deviation, skew; skewness of distribution relative to the mean value (measure of asymmetry of the distribution), Lc mean; mean track length after c-axis correction, n Dpar; number of measured etch pit diameters, Dpar mean; mean etch pit diameter.

6.3 THERMO-KINEMATIC MODELLING AND EXHUMATION RATES

The addressed thermal histories were produced with the HeFTy v.1.8.3 (Ketcham, 2009) using the revealed ZFT ages, AFT data and opening of the Gulf of Suez event as t-T constrains (Fig. 6.5; Fig. 6.6; Fig. 6.7). The strength of these t-T modelling codes on producing t-T paths are correlated to the number of used CTs. Therefore, in this study, the t-T modelling was performed on samples with sufficient CTs and those samples with an insufficient number were used for comparison (Table 6-3).

Modelling solutions for all samples show a goodness-of-fit (GOF) higher than 85% for all modelled parameters (AFT cooling ages and CT length distribution) except only for two samples with a GOF of 76% and 36% (Figs. 6.5; 6.6; 6.7). Here the cooling-only model is the simplest solution concordant with the general geology and the thermochronological data of the samples. Nevertheless, modelling with a reheating possibility was also tested and shows a possibility of slow reheating with a small wavelength, similar to the slow reheating processes proposed in the cooling only solution (Table 6-4; Figs. 6.5; 6.6; 6.7).

The produced t-T models show a similar cooling pattern where the difference is the onset timing of the first cooling event between samples from the three different age groups. The samples of the group A region show the first rapid cooling event during the Precambrian (Fig. 6.5). Then, it has experienced a period of slow reheating till Late Oligocene time when the cooling rates started to accelerate again (Table 6-4; Fig. 6.6). The samples from the group B region represent an onset of the first rapid cooling event between late Proterozoic and Early Permian times. While, the main cooling event for all t-T paths were either during the Cambrian-Ordovician or the Carboniferous-Permian (Fig. 6.6). Afterwards, this region has experienced a period of slow reheating till Late Oli-

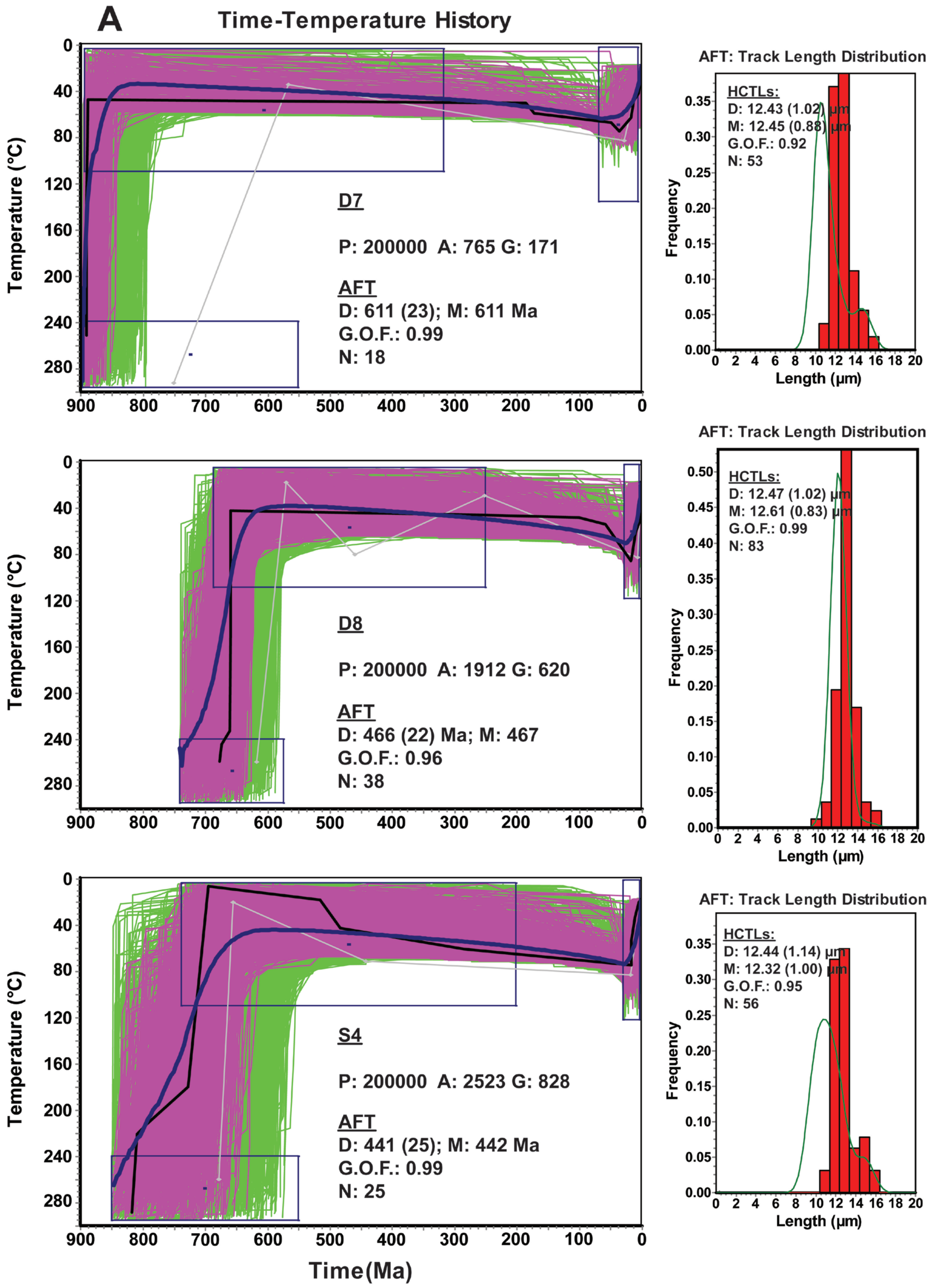

Fig. 6.5: Thermal history modelling using HeFTy v.1.8.3 (Ketcham et al., 2009); representative t–T paths illustrate the cooling history of Group A samples of Samra mountain area (Fig. 6.1). Displayed are; on the left: the t–T paths, on the right: the c-axes-corrected horizontal confined track lengths (HCTLs) distribution overlain by a calculated probability density function (best fit). Resulting t–T curves show four different reliability levels; green paths: acceptable fit (all t–T paths with a merit function value of at least 0.05), purple paths: good fit (all t–T paths with a merit function value of at least 0.5), black line: best fit and dashed blue line: the weighted mean path (Ketcham et al., 1999, 2009). The used constrains (t-T boxes) are ZFT age, AFT age and the Gulf of Suez opening. A: acceptable fit models, G: good fit models, D: determined FT age and HCTLs (1-σ error), M: modeled FT age and HCTLs, G.O.F.: goodness of fit, N: number of single grains and HCTLs.

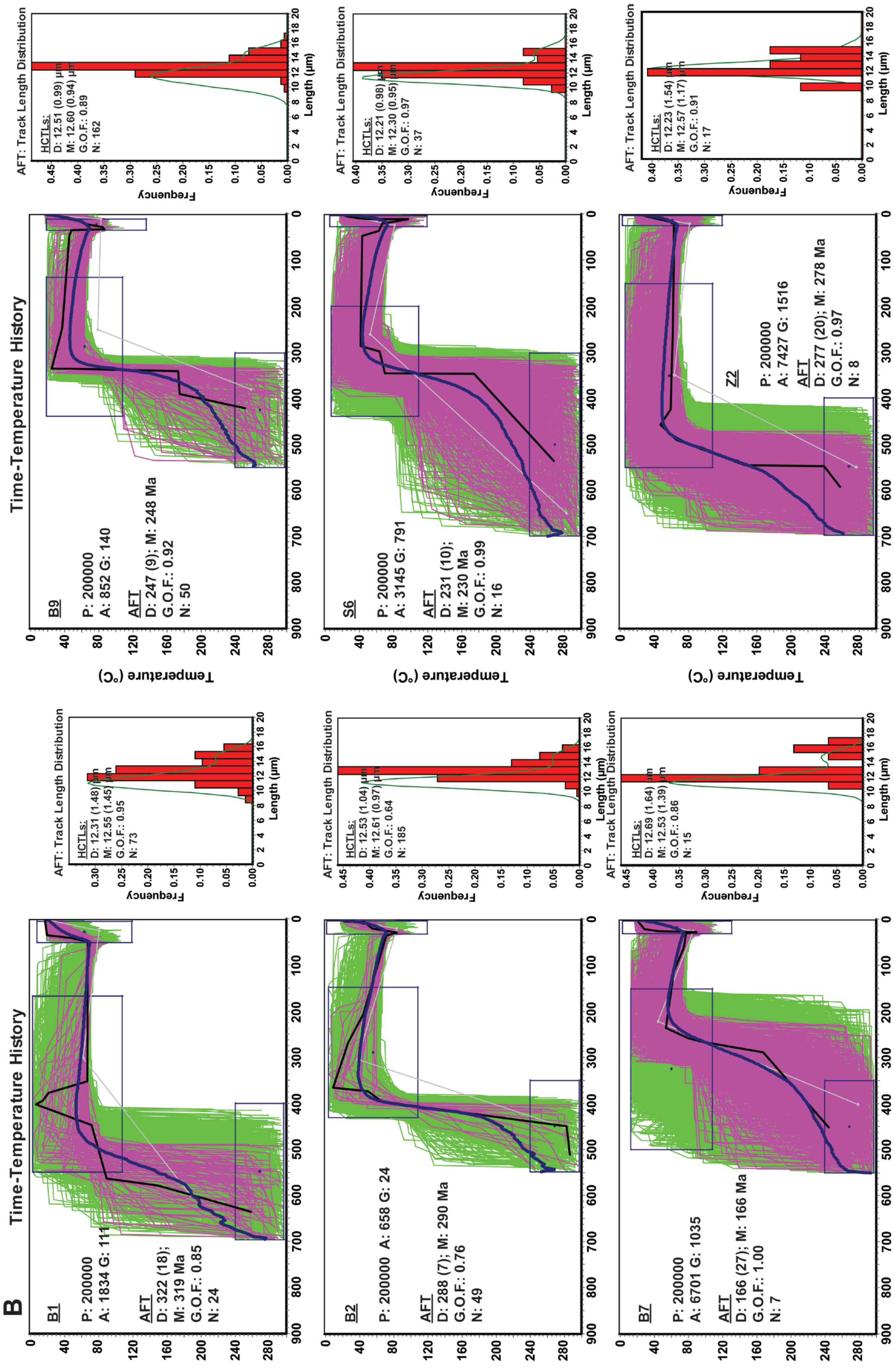

Fig. 6.6: Thermal history modelling using HeFTy v.1.8.3 (Ketcham et al., 2009); representative t–T paths illustrate the cooling history of Group B samples of Samra mountain area (Fig. 6.1). For further explanation see Fig. 6.5

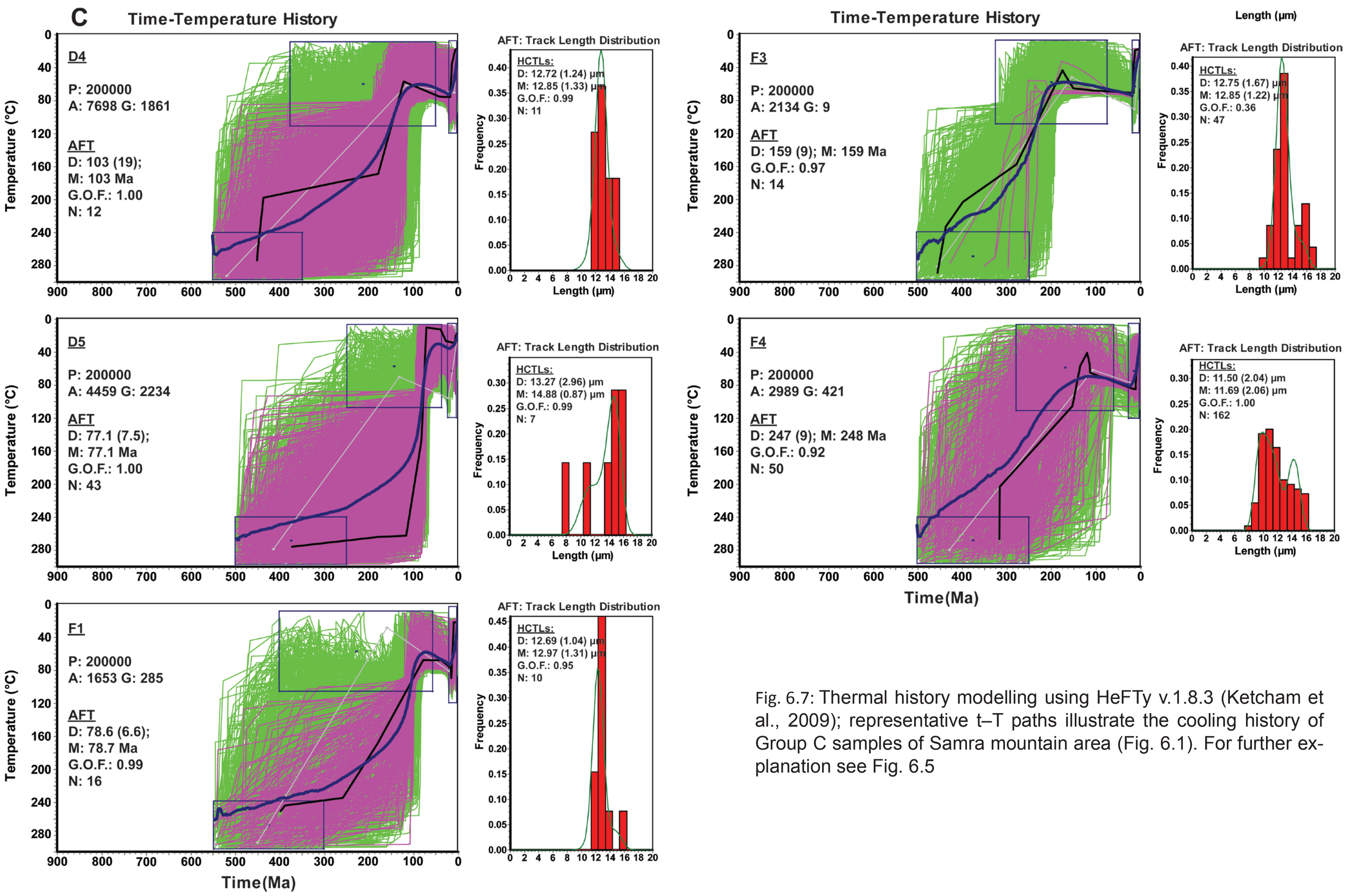

Fig. 6.7: Thermal history modelling using HeFTy v.1.8.3 (Ketcham et al., 2009); representative t–T paths illustrate the cooling history of Group C samples of Samra mountain area (Fig. 6.1). For further explanation see Fig. 6.5

gocene times where the cooling rates started to accelerate again (Table 6-4; Fig. 6.8). The samples of group C region represents onset of the first rapid cooling event between the Proterozoic and Cretaceous times. While, the main cooling event for all t-T paths was during the Jurassic-Cretaceous (Fig. 6.7). Afterwards, this region has experiences a period of slow reheating till Late Oligocene time when the cooling rates started to accelerate again (Table 6-4; Fig. 6.8).

In general, all the samples have experienced two rapid cooling/exhumation events. The first event shows a different onset timing and caused sample uplifting from ZFT PAZ (≥8 km depth) to depths slightly greater than the AFT PAZ (≥3 km depth) or to the surface (Group A samples). Although this cooling event is complicated in younger samples, showing an extension of possibility over a long time span. While the second cooling event was less complicated, starting in the Oligocene till Recent times. Between these two rapid cooling/exhumation events there was a period characterized by a slow reheating process (Figs. 6.5; 6.6; 6.7).

The cooling and exhumation rates as well as the rock uplift (vertical rock uplift corresponding to a single event) were calculated from the t-T modelling, assuming an average geothermal gradient (30 (10) °C/km) (Table 6-4). Considering the recent geothermal gradient is ~20 ºC/km (Morgan et al., 1985). It is expected to be doubled in active tectonic conditions in the Gulf of Suez (Moore et al., 1986; Omar et al., 1987; Vermeesch et al., 2009). Therefore, a geothermal gradient of 40 °C/km was used in the text and a range of 30 (10) °C/km for exhumation rates calculations was expressed in Table 6-4.

The modelled samples show 3 or 4 changes in cooling pattern/rates. **Sample D7** t-T model shows 3 changes in cooling patterns (Table 6-4; Fig. 6.8). Starting with a rapid cooling event during the Neoproterozoic (from ~880 to ~837 Ma) with a ~5.47 °C/Ma cooling rate, ~0.137 km/Ma exhumation rate (Table 6-4) and ~5.9 km of corresponding rock uplift over ~43 Ma. Afterwards, there was a period of reheating extending from Neoproterozoic to Oligocene times (from ~837 to ~27 Ma) with cooling and exhumation rates of -0.04 °C/Ma and -0.001 km/Ma respectively, causing ~0.8 km of corresponding rock subsidence (Table 6-4; Fig. 6.8). Hereafter, the cooling pattern started to change to rapid cooling and exhumation rates of ~1.67 °C/Ma and ~0.042 km/Ma respectively (Fig. 6.5), causing ~1.1 km of corresponding rock uplift. **Sample D8** t-T model represents 3 different phases of cooling (Table 6-4; Fig. 6.8). Starting with a rapid cooling event during the Neoproterozoic (from ~700 to ~615 Ma) with a ~2.71 °C/Ma cooling rate, ~0.068 km/Ma exhumation rate (Table 6-4) and ~5.8 km of corresponding rock uplift over ~85 Ma. Afterwards, there was a period of reheating extended till Oligocene times (from ~615 to 25 Ma) with a -0.05 °C/Ma cooling rate, -0.001 km/Ma exhumation rate and ~0.8 km of corresponding rock subsidence (Table 6-4; Fig. 6.8). Hereafter, the cooling pattern started to change to rapid cooling, beginning in the Oligocene (from ~25 Ma to recent) with a ~2.0 °C/Ma cooling rate, ~0.05 km/Ma exhumation rate and ~1.3 km of corresponding rock uplift. **Sample S4** t-T model shows 3 phases of cooling patterns (Table 6-4; Fig. 6.8). Starting with a fast cooling event during the Neoproterozoic (from ~750 to ~668 Ma) with a ~2.8 °C/Ma cooling rate, ~0.07 km/Ma exhumation rate (Fig. 6.8) and ~5.8 km of corresponding rock uplift over ~82 Ma. Afterwards, there was a period of slow reheating extending from the Neoproterozoic to the Oligocene (from ~668 to ~25 Ma) with cooling and exhumation rates of -0.05 °C/Ma and -0.001 km/Ma respectively, causing ~0.9 km of corresponding rock subsidence (Table 6-4; Fig. 6.8).

Table 6-4: The Samra Mountain area Cooling rates, Exhumation rates and Rock uplift extracted from the HeFTy t-T modelling.

S.- No.	Elev. (m a.s.l)	Phase	t-t Segment (Ma)	Δt	T-T Segment (°C)	ΔT	Cooling Rate (°C/Ma)	Exhumation Rate			Rock uplift		
								(km/Ma) 20 °C/km	(km/Ma) 30 °C/km	(km/Ma) 40 °C/km	(km/Δt) 20 °C/km	(km/Δt) 30 °C/km	(km/Δt) 40 °C/km
Group A													
D7	434	1	880-837	43	270-35	235	**5.47**	0.273	**0.182**	0.137	11.8	**7.8**	5.9
		2	837-27	810	35-65	-30	**-0.04**	-0.002	**-0.001**	-0.001	-1.5	**-1.0**	-0.8
		3	27-0	27	65-20	45	**1.67**	0.083	**0.056**	0.042	2.3	**1.5**	1.1
D8	520	1	700-615	85	270-40	230	**2.71**	0.135	**0.090**	0.068	11.5	**7.7**	5.8
		2	615-25	590	40-70	-30	**-0.05**	-0.003	**-0.002**	-0.001	-1.5	**-1.0**	-0.8
		3	25-0	25	70-20	50	**2.00**	0.100	**0.067**	0.050	2.5	**1.7**	1.3
S4	316	1	750-668	82	270-40	230	**2.80**	0.140	**0.093**	0.070	11.5	**7.7**	5.8
		2	668-25	643	40-75	-35	**-0.05**	-0.003	**-0.002**	-0.001	-1.8	**-1.2**	-0.9
		3	25-0	25	75-20	55	**2.20**	0.110	**0.073**	0.055	2.8	**1.8**	1.4
Group B													
B1	195	1	600-450	150	275-55	220	**1.47**	0.073	**0.049**	0.037	11.0	**7.3**	5.5
		2	450-25	425	55-70	-15	**-0.04**	-0.002	**-0.001**	-0.001	-0.8	**-0.5**	-0.4
		3	25-0	25	70-20	50	**1.00**	0.050	**0.033**	0.025	2.5	**1.7**	1.3
B2	202	1	450-370	80	270-40	230	**2.88**	0.144	**0.096**	0.072	11.5	**7.7**	5.8
		2	370-23	347	40-70	-30	**-0.09**	-0.004	**-0.003**	-0.002	-1.5	**-1.0**	-0.8
		3	23-0	23	70-20	50	**2.17**	0.109	**0.072**	0.054	2.5	**1.7**	1.3
B7	229	1	450-280	170	270-160	110	**0.65**	0.032	**0.022**	0.016	5.5	**3.7**	2.8
		2	280-225	55	160-60	100	**1.82**	0.091	**0.061**	0.045	5.0	**3.3**	2.5
		3	225-27	198	60-75	-15	**-0.08**	-0.004	**-0.003**	-0.002	-0.8	**-0.5**	-0.4
		4	27-0	27	75-20	55	**2.39**	0.120	**0.080**	0.060	2.8	**1.8**	1.4
B9	202	1	400-310	90	270-50	220	**2.44**	0.122	**0.081**	0.061	11.0	**7.3**	5.5
		2	310-27	283	50-70	-20	**-0.07**	-0.004	**-0.002**	-0.002	-1.0	**-0.7**	-0.5
		3	27-0	27	70-20	50	**1.85**	0.093	**0.062**	0.046	2.5	**1.7**	1.3

S6	297	1	550-390	160	275-165	110	**0.69**	0.034	**0.023**	0.017	5.5	**3.7**	2.8
		2	390-315	75	165-40	125	**1.67**	0.083	**0.056**	0.042	6.3	**4.2**	3.1
		3	315-23	292	40-75	-35	**-0.12**	-0.006	**-0.004**	-0.003	-1.8	**-1.2**	-0.9
		4	23-0	23	75-20	55	**2.39**	0.120	**0.080**	0.060	2.8	**1.8**	1.4
Z2	152	1	600-490	110	270-50	220	**2.00**	0.100	**0.067**	0.050	11.0	**7.3**	5.5
		2	490-24	466	50-70	-20	**-0.04**	-0.002	**-0.001**	-0.001	-1.0	**-0.7**	-0.5
		3	24-0	24	70-20	50	**2.08**	0.104	**0.069**	0.052	2.5	**1.7**	1.3
Group C													
D4	298	1	450-190	260	270-150	120	**0.46**	0.023	**0.015**	0.012	6.0	**4.0**	3.0
		2	190-118	72	150-55	95	**1.32**	0.066	**0.044**	0.033	4.8	**3.2**	2.4
		3	118-23	95	55-75	-20	**-0.21**	-0.011	**-0.007**	-0.005	-1.0	**-0.7**	-0.5
		4	23-0	23	75-20	55	**2.39**	0.120	**0.080**	0.060	2.8	**1.8**	1.4
D5	73	1	375-115	260	270-170	100	**0.38**	0.019	**0.013**	0.010	5.0	**3.3**	2.5
		2	115-63	52	170-25	145	**2.79**	0.139	**0.093**	0.070	7.3	**4.8**	3.6
		3	63-23	40	25-35	-10	**-0.25**	-0.013	**-0.008**	-0.006	-0.5	**-0.3**	-0.3
		4	23-0	23	35-20	15	**0.65**	0.033	**0.022**	0.016	0.8	**0.5**	0.4
F1	182	1	425-150	275	270-165	105	**0.38**	0.019	**0.013**	0.010	5.3	**3.5**	2.6
		2	150-90	60	165-55	110	**1.83**	0.092	**0.061**	0.046	5.5	**3.7**	2.8
		3	90-23	67	55-75	-20	**-0.30**	-0.015	**-0.010**	-0.007	-1.0	**-0.7**	-0.5
		4	23-0	23	75-20	55	**2.39**	0.120	**0.080**	0.060	2.8	**1.8**	1.4
F3	187	1	375-275	100	270-165	105	**1.05**	0.053	**0.035**	0.026	5.3	**3.5**	2.6
		2	275-200	75	165-60	105	**1.40**	0.070	**0.047**	0.035	5.3	**3.5**	2.6
		3	200-22	178	60-75	-15	**-0.08**	-0.004	**-0.003**	-0.002	-0.8	**-0.5**	-0.4
		4	22-0	22	75-20	55	**2.50**	0.125	**0.083**	0.063	2.8	**1.8**	1.4
F4	187	1	375-150	225	270-70	200	**0.89**	0.044	**0.030**	0.022	10.0	**6.7**	5.0
		2	150-27	123	70-80	-10	**-0.08**	-0.004	**-0.003**	-0.002	-0.5	**-0.3**	-0.3
		3	27-0	27	80-20	60	**2.22**	0.111	**0.074**	0.056	3.0	**2.0**	1.5

The cooling phases and cooling rates were extracted from HeFTy t-T models. The exhumation rates were calculated from the cooling rates, a geothermal gradients of 20, 30 and 40 °C/km and surface temperature which was calculated from the recent average 20 °C. The recent geothermal gradient in near area is 20 °C/km (Morgan et al., 1985). The rock uplift was calculated as episodical vertical rock uplift from multiplying the exhumation rate by the duration in each single cooling event. Elev. (m a.s.l.): elevation with meters above sea level. t–t: time segment; ~t: average time; Δt: phase (event) duration; T–T: Temperature segment; ΔT: temperature reduction during a single event.

Hereafter, the cooling pattern changed to rapid cooling and exhumation rates of ~2.2 °C/Ma and ~0.055 km/Ma respectively, (Fig. 6.8), causing ~1.4 km of rock uplift. **Sample B1** t-T model represents 3 different phases of cooling (Table 6-4; Fig. 6.8). Starting with a rapid cooling event between Neoproterozoic to Ordovician times (from ~600 to 450 Ma) with a ~1.47 °C/Ma cooling rate, ~0.037 km/Ma exhumation rate and ~5.5 km corresponding rock uplift over ~150 Ma (Table 6-4). Afterwards, there was a period of reheating extending till Oligocene time (from ~450 to 25 Ma) with a -0.04 °C/Ma cooling rate, -0.001 km/Ma exhumation rate and ~0.4 km of corresponding rock subsidence (Table 6-4; Fig. 6.8). Then, a change in the cooling pattern to a rapid one occurred since the Oligocene (from ~25 to recent) resulting in a ~1.0 °C/Ma cooling rate, ~0.025 km/Ma exhumation rate and ~1.3 km of corresponding rock uplift (Table 6-4). **Sample B2** t-T model represents 3 different phases of cooling (Table 6-4; Fig. 6.8). Starting with a rapid cooling event between Ordovician and Devonian times (from ~450 to 370 Ma) with a ~2.88 °C/Ma cooling rate, ~0.072 km/Ma exhumation rate (Table 6-4) and ~5.8 km of corresponding rock uplift over ~80 Ma. Afterwards, there was a period of reheating extending to Oligocene time (from ~270 to 23 Ma) with a -0.09 °C/Ma cooling rate, -0.002 km/Ma exhumation rate and ~0.8 km of corresponding rock subsidence (Table 6-4; Fig. 6.8). Then, a change in the cooling pattern to a more rapid one in the Oligocene (from ~23 to recent) resulting in a ~2.17 °C/Ma cooling rate, ~0.054 km/Ma exhumation rate and ~1.3 km of corresponding rock uplift (Table 6-4). **Sample B7** model shows 4 different phases of cooling (Table 6-4; Fig. 6.8). Starting with a rapid cooling event between the Ordovician and the Permian (from ~450 to 280 Ma) with a ~0.65 °C/Ma cooling rate, ~0.016 km/Ma exhumation rate (Table 6-4) and ~2.8 km of corresponding rock uplift over ~170 Ma. Hereafter, the cooling pattern accelerated between Permian and Triassic times (from ~280 Ma to 225 Ma) giving a ~1.82 °C/Ma cooling rate, ~0.045 km/Ma exhumation rate and ~2.5 km of corresponding rock uplift over ~55 Ma. Afterwards, there was a period of reheating extending till Oligocene time (from ~225 to 27 Ma) with a -0.08 °C/Ma cooling rate, -0.002 km/Ma exhumation rate and ~0.4 km of corresponding rock subsidence (Table 6-4; Fig. 6.8). Hereafter, the cooling pattern changed to rapid cooling in the Oligocene (from ~27 Ma to recent) with a ~2.39 °C/Ma cooling rate, ~0.06 km/Ma exhumation rate and ~1.4 km of corresponding rock uplift (Fig. 6.8). **Sample B9** t-T model represents 3 different phases of cooling (Table 6-4; Fig. 6.8). Starting with a rapid cooling event between Devonian and Carboniferous times (from ~400 to 310 Ma) with a ~2.44 °C/Ma cooling rate, ~0.061 km/Ma exhumation rate (Table 6-4) and ~5.5 km of corresponding rock uplift over ~90 Ma. Afterwards, there was a period of reheating extending till Oligocene times (from ~310 to 27 Ma) with a -0.07 °C/Ma cooling rate, -0.002 km/Ma exhumation rate and ~0.5 km of corresponding rock subsidence (Table 6-4; Fig. 6.8). Then, a change in the cooling pattern to a rapid one started in the Oligocene (from ~27 to recent), resulting in a ~1.85 °C/Ma cooling rate, ~0.046 km/Ma exhumation rate (Table 6-4) and ~1.3 km of corresponding rock uplift. **Sample S6** t-T model represents 4 different phases of cooling (Table 6-4; Fig. 6.8). Starting with a cooling event extending from Cambrian and Devonian times (from ~550 to 390 Ma) with an average cooling rate of ~0.69 °C/Ma, exhumation rate of ~0.017 km/Ma (Table 6-4) and a corresponding rock uplift of ~2.8 km over ~160 Ma. Afterwards, the cooling rate accelerated during Devonian-Carboniferous times (from ~390 to 315 Ma) giving a ~1.67 °C/Ma cooling rate,

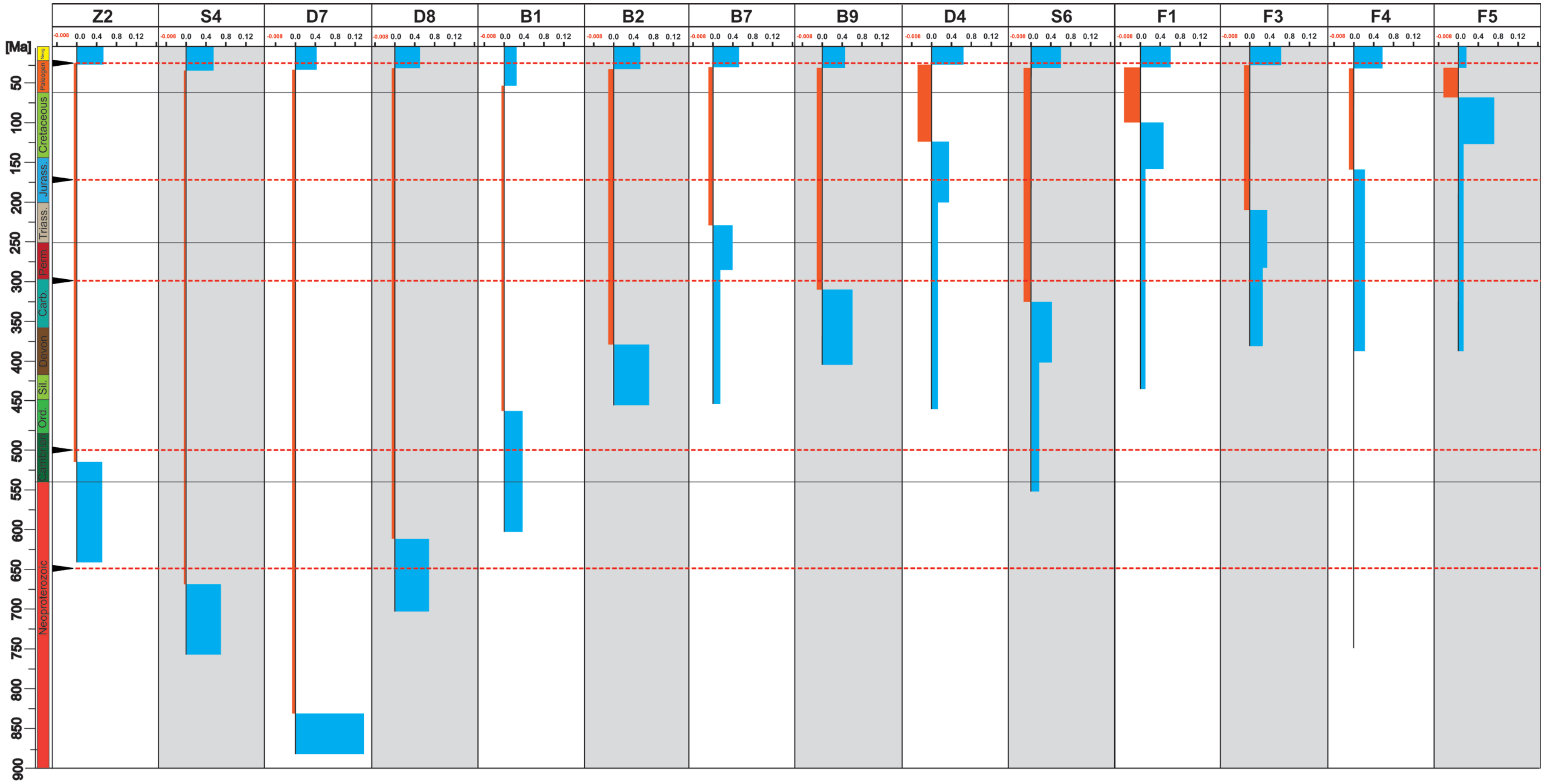

Fig. 6.8: Exhumation rates in (km/Ma) diagram of The Samra mountain area (exhumation rates expressed by km/Ma). Based on the data from the thermal history from Fig. 5.85, Fig. 5.96.6, Fig. 6.7 and Table 5-54. Five major exhumation events presented (red dashed lines) synchronous with major tectonic events.

~0.042 km/Ma exhumation rate and ~3.1 km of corresponding rock uplift over ~75 Ma (Table 6-4; Fig. 6.8). Then, the cooling pattern changed to reheating pattern till the Oligocene (from ~315 to 23 Ma) resulting in a -0.12 °C/Ma cooling rate, -0.003 km/Ma exhumation rate (Table 6-4) and ~0.9 km of corresponding rock subsidence (Fig. 6.8). Followed by a considerable change in the cooling pattern to a more rapid since then (from 23 Ma to recent) with a ~2.39 °C/Ma cooling rate, ~0.06 km/Ma exhumation rate and a corresponding ~1.4 km of rock uplift (Table 6-4; Fig. 6.8). **Sample Z2** t-T model shows 3 changes in cooling patterns (Table 6-4; Fig. 6.8). Starting with a rapid cooling event during the Neoproterozoic-Cambrian boundary (from ~600 to ~490 Ma) with a ~2.0 °C/Ma cooling rate, ~0.05 km/Ma exhumation rate (Fig. 6.8) and ~5.5 km of corresponding rock uplift over ~110 Ma. Afterwards, there was a period of reheating extending from late Cambrian to Oligocene times (from ~490 to 24 Ma) with cooling and exhumation rates of -0.04 °C/Ma and -0.001 km/Ma respectively, causing ~0.5 km of corresponding rock subsidence (Table 6-4; Fig. 6.8). Hereafter, the cooling pattern changed to rapid cooling and exhumation rates of ~2.08 °C/Ma and ~0.052 km/Ma respectively (Fig. 6.8), giving ~1.3 km of corresponding rock uplift. **Sample D4** t-T model represents 4 different phases of cooling patterns (Table 6-4; Fig. 6.8). Starting with a cooling event with wide range of possibility extending from Ordovician to Jurassic times (from ~450 to 190 Ma) with an average cooling rate of ~0.46 °C/Ma, exhumation rate of ~0.012 km/Ma (Table 6-4) and a corresponding rock uplift of ~3.0 km over ~260 Ma. Afterwards, there was a period of acceleration in cooling trend extending till Cretaceous time (from ~190 to 118 Ma) producing a ~1.32 °C/Ma cooling rate, ~0.033 km/Ma exhumation rate and ~2.4 km of corresponding rock uplift over ~72 Ma (Table 6-4; Fig. 6.8). Then, a change in the cooling pattern to reheating one occurred till Oligocene time (from ~118 to 23 Ma) resulting in a -0.21 °C/Ma cooling rate, -0.005 km/Ma exhumation rate (Table 6-4) and ~0.5 km of corresponding rock subsidence. Followed by a change in the cooling trend to more rapid since then (from 23 Ma to recent) with a ~2.39 °C/Ma cooling rate, ~0.06 km/Ma exhumation rate and a corresponding ~1.4 km of rock uplift (Table 6-4; Fig. 6.8). **Sample D5** t-T model represents 4 different phases of cooling patterns (Table 6-4; Fig. 6.8). Starting with a cooling event extended from Devonian to Cretaceous times (from ~375 to 115 Ma) with an average cooling rate of ~0.38 °C/Ma, exhumation rate of ~0.01 km/Ma (Table 6-4) and a corresponding rock uplift of ~2.5 km over ~260 Ma. Afterwards, the cooling rate was accelerated during Cretaceous time (from ~115 to 63 Ma) to ~2.79 °C/Ma, with an exhumation rate of ~0.07 km/Ma and ~3.6 km of corresponding rock uplift over ~52 Ma (Table 6-4; Fig. 6.8). Then, the cooling pattern was changed to reheating pattern till the Oligocene (from ~63 to 23 Ma) resulting in a -0.25 °C/Ma cooling rate, -0.006 km/Ma exhumation rate (Table 6-4) and ~0.3 km of corresponding rock subsidence. Followed by a significant change in the cooling pattern to more rapid since then (from 23 Ma to recent) with a ~0.65 °C/Ma cooling rate, ~0.016 km/Ma exhumation rate and a corresponding ~0.4 km of rock uplift (Table 6-4; Fig. 6.8). **Sample F1** t-T model represents 4 different phases of cooling (Table 6-4; Fig. 6.8). Starting with a cooling event extended from Silurian and Jurassic times (from ~425 to 150 Ma) with an average cooling rate of ~0.38 °C/Ma, exhumation rate of ~0.01 km/Ma (Fig. 6.8) and a corresponding rock uplift of ~2.6 km over ~275 Ma. Afterwards, the cooling rate was accelerated during the Carboniferous (from ~150 to 90 Ma) to ~1.83 °C/Ma, with ~0.046 km/Ma exhumation rate and ~2.8 km of corresponding rock uplift over ~60 Ma (Table 6-4; Fig. 6.8). Then, the cooling pattern was changed to reheating pattern till the Oligocene (from ~90 to 23 Ma) resulting in a -0.3 °C/Ma cooling rate, -0.007 km/Ma exhumation rate and ~0.5 km of corresponding rock subsidence (Table 6-4). Followed by a significant change in the cooling pattern to rapid since then (from 23 Ma to recent) with a ~2.39 °C/Ma cooling rate, ~0.06 km/Ma exhumation rate and a corresponding ~1.4 km of rock uplift (Table 6-4; Fig. 6.6). **Sample F3** t-T model represents 4 different phases of cooling (Table 6-4; Fig. 6.8). Starting with cooling event extending from Devonian to Permian times (from ~375 to 275 Ma) with an average cooling rate of ~1.05 °C/Ma, exhumation rate of ~0.026 km/Ma and a corresponding rock uplift of ~2.6 km over~100 Ma (Table 6-4). Afterwards, the cooling rate was accelerated during Permian-Triassic times (from ~275 to 200 Ma) to ~1.4 °C/Ma, with ~0.035 km/Ma exhumation rate and ~2.6 km of corresponding rock uplift over ~75 Ma (Table 6-4; Fig. 6.8). Then, the cooling pattern was changed to reheating pattern till the Early Miocene (from ~200 to 22 Ma) resulting in a -0.08 °C/Ma cooling rate, -0.002 km/Ma exhumation rate and ~0.4 km of corresponding rock subsidence (Table 6-4). Followed by a considerable change in the cooling pattern to rapid one since then (from 22 Ma to recent) with a ~2.5 °C/Ma cooling rate, ~0.063 km/Ma exhumation rate and a corresponding ~1.4 km of rock uplift (Table 6-4; Fig. 6.8). **Sample F4** t-T model represents 3 different phases of cooling (Table 6-4; Fig. 6.8). Starting with a rapid cooling event between Devonian and Jurassic times (from ~375 to 150 Ma) with a ~0.89 °C/Ma cooling rate, ~0.022 km/Ma exhumation rate and ~5.0 km of corresponding rock uplift over ~225 Ma (Table 6-4). Afterwards, there was a period of reheating extending till Oligocene time (from ~150 to 27 Ma) with a -0.08 °C/Ma cooling rate, -0.002 km/Ma exhumation rate and ~0.3 km of corresponding rock subsidence (Table 6-4; Fig. 6.8). Then, a change in the cooling pattern to rapid one occurred since the Oligocene (from ~27 to recent) resulted in a ~2.22 °C/Ma cooling rate, ~0.056 km/Ma exhumation rate (Table 6-4) and ~1.5 km of corresponding rock uplift (Fig. 6.8).

7

VOLCANIC ISLANDS IN A PASSIVE MARGIN ENVIRONMENT (CANARY ISLANDS)

CONTENTS

In order to achieve the aims of this part of the study, 12 samples were collected from Fuerteventura Island. The sampling strategy built on collecting samples from the different rock units of the Basal Complex (BC) in north volcanic complex (NVC) and central volcanic complex (CVC) along the western part of the island. Where the BC is exposed as response to the Miocene giant landslide. Similarly, 11 samples were collected from La Gomera, particularly from the northwestern sector of the island, where the BC is exposed and successive landslides took place (e.g., Tazo landslide).

All the zircon fission track (ZFT) and apatite fission track (AFT) ages of both Fuerteventura and La Gomera are overlapping within the error range (for each island data set) with two exceptional AFT ages from La Gomera (Lag 1 and Lag 8) which are older than all other La Gomera samples. The thermal histories (t-T record) were modelled for nine samples using the HeFTy code v.1.8.3 (Ketcham et al., 2009). The cooling and exhumation rates as well as the rock uplift over a single event (vertical uplift corresponding to a single event) were calculated from the t-T modelling assuming an average geothermal gradient (28 °C/km; Rimi, 1990).

7.1 FUERTEVENTURA ISLAND

From Fuerteventura 4 samples have provided sufficient zircon grains to carry out ZFT dating (Fig. 7.1; Table 7.1). While, 12 samples yielded suitable apatite grains to perform AFT dating (Fig. 7.1; Table 7.2), of these 6 samples produced sufficient confined tracks (CTs) for t-T modelling.

7.1.1 Zircon fission track data

From Fuerteventura, one sample from the Oligocene-Miocene submarine lava and three samples from the Lower Miocene Basaltic series II (one syenite and two carbonatite samples) could be dated. The treated samples have ZFT central ages ranging between 20.1 (1.3) and 19.6 (1.1) Ma (Fig. 7.1; Table 7-1). Although the sample with the oldest intrusion age has the oldest ZFT age, all samples overlap within the error range (Table 7-1). Obviously, all the samples are younger than their corresponding intrusion and magmatic ages. These samples have uranium concentrations between 243.5 and 86.8 µg/g (Table 7-1). Noticeably, there is no clear relationship between the zircon single grain age and the uranium concentration (Fig. 7.2) which refers to the absence of any metamictization effect on the ZFT ages in Fuerteventura. The χ2 values range between 99 and 100% indicating a single population (Table 7-1).

7.1.2 Apatite fission track data

From Fuerteventura, 4 samples from the Oligocene-Miocene submarine strata and 8 samples from the successive Lower Miocene Basaltic series have provided sufficient apatites to be dated. The treated samples have AFT central age ranges between 20.5 (2.4) and 12.5 (4.1) Ma (Fig. 7.1; Table 7-2). The age distribution does not allow samples to be separated spatially (Table 7-2), indicating a uniform tectonic history independent from the sample locations. Generally the AFT age values are close and in most samples overlap within the error range. Moreover, there is a scarcity in any remarkable elevation difference (the sample with the heights elevation ~350 m a.s.l.). Therefore, the age-elevation relationship is unclear (Fig. 7.3), this may represent fast cooling through the AFT PAZ caused by the progressive accretion of new magmatic materials and removal of top materials.

The χ2-test for all AFT cooling ages have been passed with values between 76 and 100 % indicating a single cooling population. Only two samples, FU-02-10 and FU-38-09,

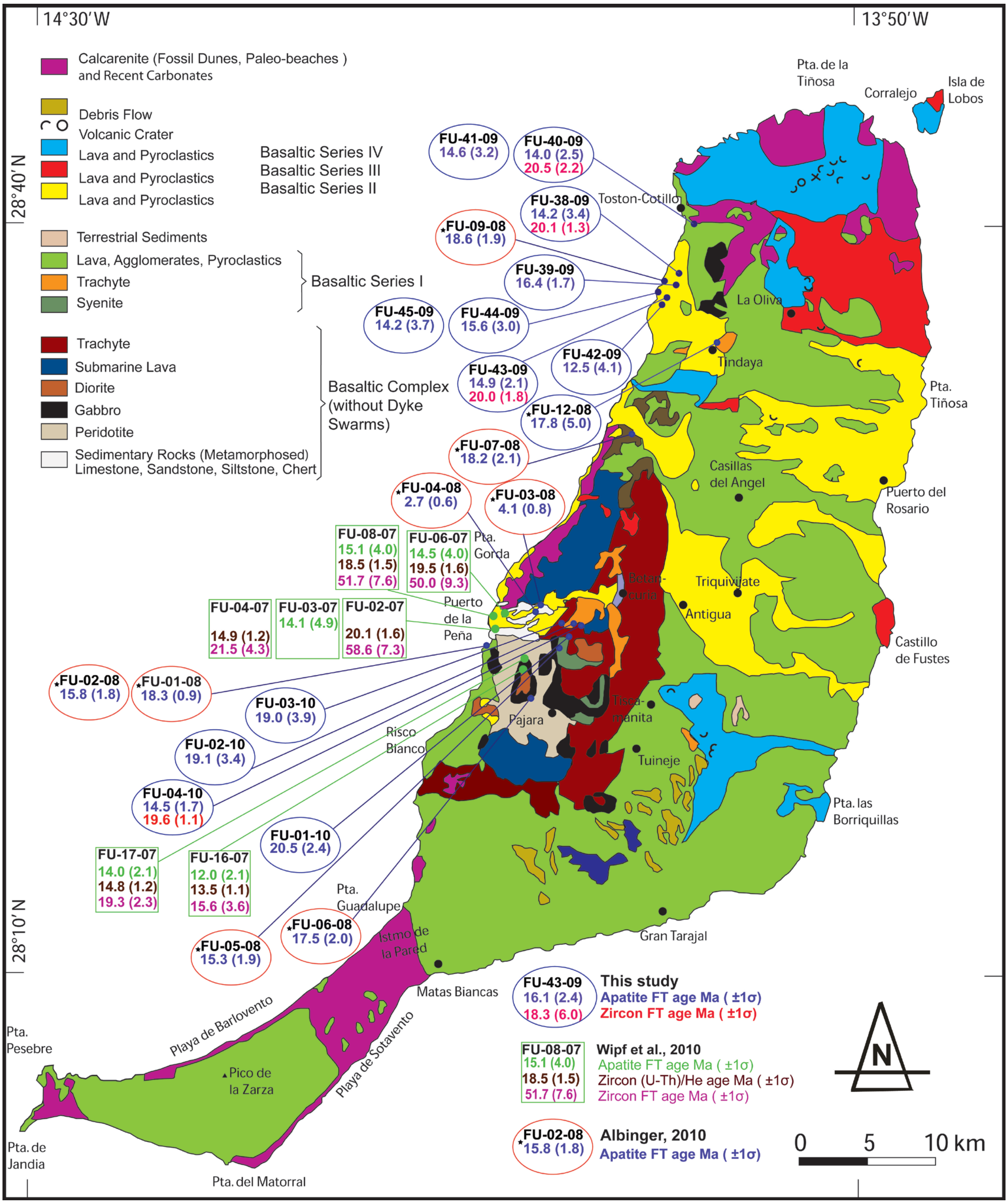

Fig. 7.1: Geologic map of Fuerteventura Island with the main rock units lithologies (modified by Wipf, 2007 after Muñoz et al., 2003) and locations of the dated samples from this study and (Albinger, 2010; Wipf et al., 2010).

have lower χ2 values of 55, 50 %, respectively (Table 7-2). These lower values are related to the high number of grains with zero tracks in these samples, while the uranium concentration is generally low, with values between 2.3 and 7.2 μg/g.

Only 6 samples from Fuerteventura yield a sufficient number of CTs to be modelled (sample FU-44-09 has only 25 CTs therefore it was used only for comparison). Mean CTs lengths distribution range between 11.8 (2.4) and 14.0 (1.4) μm with negative skewness of

Table 7-1: Fuerteventura Island’s sample information and zircon fission track data.

S.-No.	Elev. [m a.s.l.]	Lithology	Formation age	U [µg/g]	n	Sp. Tracks ρ_s	N_s	Ind. Tracks ρ_i	N_i	χ^2 [%]	Central age (1σ) [Ma]
FU-38-09	177	Carbonatite	Lower Miocene	154.9	20	831	14.967	1545	27.826	100	**20.1 (1.3)**
FU-40-09	149	Carbonatite	Lower Miocene	86.8	8	171	9.492	311	17.262	100	**20.5 (2.2)**
FU-43-09	102	Syenite	Lower Miocene	243.5	8	257	20.864	482	39.13	99	**20.0 (1.8)**
FU-04-10	357	Submarine Lava	Oligo-Miocene	212.3	23	1676	19.672	3143	36.979	100	**19.6 (1.1)**

Sample information and zircon fission track data given as central ages with uncertainty of 1-sigma. S.-No.; samples number, Elev. [m a.s.l.]; elevation in meters above sea level, U; Uranium concentration in µg/g, n; number of counted apatite grains, ρs; density of spontaneous tracks (10^5 tr/cm^2), Ns; number of spontaneous tracks, ρi; density of induced tracks (10^5 tr/cm^2), Ni; number of induced tracks, χ2; chi square test: probability of single grain ages belonging to one population. Test is passed if P(χ2) > 5% (Galbraith, 1981), Central ages calculated with Trackkey v.4.2 (Dunkl, 2002) using a ζ-value of 123.0 ± 6.09. Nd (tracks counted on CN1 dosimeter glass) = 16413 tracks.

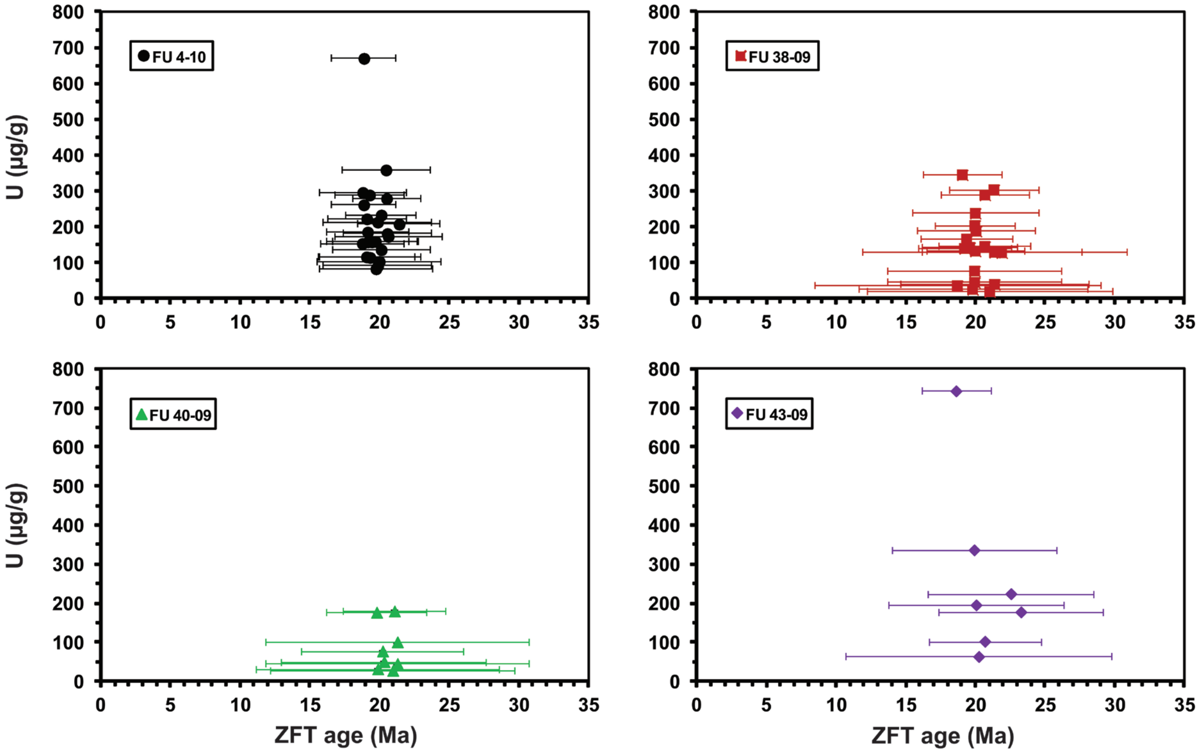

Fig. 7.2: ZFT single grain ages versus uranium concentrations of Fuerteventura samples. No relationship between them is represented.

the values between −0.099 and −1.301 (Table 7-3). The measured CTs were corrected against their crystallographic c-axis using HeFTy v.1.8.3 (Donelick et al., 1999; Ketcham et al., 2007a, b) resulting in c-axis projected CTs between 13.1 (1.8) and 14.7 (1.4) µm, with a negative skewness from −0.319 to −1.677 µm (Table 7-3). This CTs distribution, for all samples, indicate a typical undisturbed magmatic rock with a homogenous cooling history that exhumed rapidly through the PAZ (Gleadow et. al., 1986). Along with CTs, 2285 Dpar values (etch pit size) were measured (Table 7-3). The mean Dpar value for single grains range between 1.6 (0.2) and 2.9 (0.5) µm. These values indicate an uniform typical Cl rich apatite, except for samples FU-41-09 and FU-04-10 which occupy

Table 7-2: Fuerteventura Island's sample information and apatite fission track data.

S.-No.	Elev.	Lithology	Form. age	U	n	Sp. Tracks		Ind. Tracks		χ^2	Central age (1σ)	Dpar (µm)
	[m a.s.l.]			[µg/g]		ρ_s	N_s	ρ_i	N_i	[%]	[Ma]	Av. (std)
FU-38-09	177	Carbonatite	Lower Miocene	7.2	20	0.403	23	7.044	402	50	14.2 (3.4)	2.2 (0.3)
FU-39-09	134	Pyroxenite	Lower Miocene	5.5	34	0.444	140	6.380	2013	84	16.4 (1.7)	1.8 (0.2)
FU-40-09	149	Carbonatite	Lower Miocene	2.3	29	0.173	37	2.906	622	76	14.0 (2.5)	2.1 (0.4)
FU-41-09	149	Lolith	Lower Miocene	2.4	28	0.181	24	2.843	378	96	14.6 (3.2)	1.7 (0.3)
FU-42-09	108	Pyroxenite	Lower Miocene	2.4	20	0.151	10	2.771	184	97	12.5 (4.1)	1.8 (0.3)
FU-43-09	102	Syenite	Lower Miocene	4.1	29	0.303	77	4.624	1176	63	14.9 (2.1)	1.9 (0.3)
FU-44-09	3	Lolith	Lower Miocene	2.9	20	0.222	32	3.211	462	77	15.6 (3.0)	1.9 (0.4)
FU-45-09	3	Syenite	Lower Miocene	3.5	20	0.211	16	3.334	253	96	14.2 (3.7)	1.9 (0.4)
FU-01-10	333	C.G. Syenite	Oligo-Miocene	4.9	20	0.503	97	5.471	1055	92	20.5 (2.4)	2.9 (0.5)
FU-02-10	328	Trachyte	Oligo-Miocene	4.6	23	0.420	41	4.972	485	55	19.1 (3.4)	2.2 (0.6)
FU-03-10	353	C.G. Syenite	Oligo-Miocene	3.6	14	0.320	28	3.853	337	94	19.0 (3.9)	2.4 (0.4)
FU-04-10	357	C.G. Syenite	Oligo-Miocene	9.1	22	0.735	99	11.69	1575	98	14.5 (1.7)	1.6 (0.2)

Sample information and apatite fission track data given as central ages with uncertainty of 1-sigma. S.-No.; samples number, Elev. [m a.s.l.]; elevation in meters above sea-level, Lithology C.G.; coarse grained, U; Uranium concentration in µg/g, n; number of counted apatite grains, ρs; density of spontaneous tracks (10^5 tr/cm^2), Ns; number of spontaneous tracks, ρi; density of induced tracks (10^5 tr/cm^2), Ni; number of induced tracks, χ2; chi square test: probability of single grain ages belonging to one population. Test is passed if P(χ2) > 5% (Galbraith, 1981), Dpar (std); average etch pit in µm and standard deviation. Central ages were calculated with Trackkey v.4.2 (Dunkl, 2002) using a ζ-value of 330.60 ± 16.47. Nd (tracks counted on CN5 dosimeter glass) = 15236 tracks.

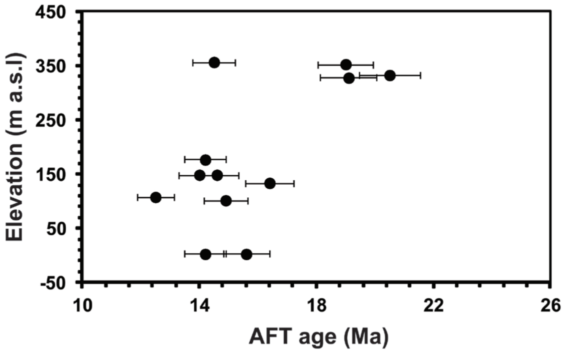

Fig. 7.3: AFT age-elevation plot of Fuerteventura Island samples showing unclear AFT age-elevation relationship.

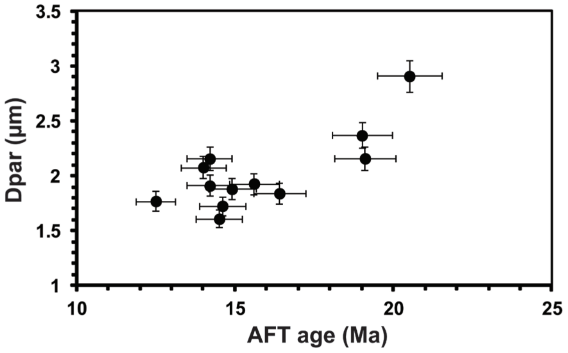

Fig. 7.4: AFT age-Dpar plot of Fuerteventura Island samples showing no relationship. Indicating absence of the grains chemistry effect on AFT ages.

a border value (1.7 µm) between the Cl rich and calcian-fluorapatites (Table 7-2) (Burtner et al., 1994; Carlson et al. 1999; Donelick, 2004; Donelick et al., 2005). Despite that, a clear relationship between the Dpar value and AFT ages was absent (Fig. 7.4) which indicates that age difference is not related to the different annealing kinetics of tracks which could result from chemistry differences between apatite grains. Sample FU-01-10 is the only exception, being the oldest AFT sample (20.5 (2.4) Ma) and having a greater Dpar value (2.9 (0.5) µm) which recommends being more resistant to track annealing. However, its age is overlapping with the younger samples within the error range. The annealing algorithm of Ketcham et al., 2007 and c-axis projected CTs were used during modelling to avoid the anisotropy of the annealing mechanism in apatite (Green and Durrani, 1977; Laslett et al., 1984; Barbarand et al., 2003).

Table 7-3: Fuerteventura Island detailed apatite confined fission track length and Dpar data.

Sample	CT n	CT mean (µm)	CT std. (µm)	CT skew.	Lc mean (µm)	Lc std. (µm)	Lc skew.	Dpar n	Dpar mean (µm)	Dpar std. (µm)	Dpar skew.
FU-39-09	101	14.0	1.5	-1.101	14.7	1.4	-1.677	505	2.2	0.3	0.851
FU-40-09	76	11.8	2.4	-0.099	13.1	1.9	-0.319	380	1.9	0.5	-0.372
FU-41-09	61	12.8	2.2	-0.602	13.8	1.6	-0.528	305	2.3	0.3	-0.602
FU-42-09	88	13.1	2.4	-0.873	14.1	1.8	-0.762	440	2.5	0.3	-0.228
FU-43-09	106	13.3	2.0	-1.301	14.1	1.6	-1.287	530	2.1	0.2	-0.238
FU-44-09	25	12.1	3.0	-0.416	13.3	2.2	-0.347	125	2.3	0.5	-1.315

n CT; number of measured confined tracks, CT mean; mean confined track length, std; standard deviation, skew; skewness of distribution relative to the mean value (measure of asymmetry of the distribution), Lc mean; mean track length after c-axis correction, n Dpar; number of measured etch pit diameters, Dpar mean; mean etch pit diameter.

7.1.3 Thermo-kinematic modelling and exhumation rates

For Fuerteventura, the cooling-only model is concordant with the general geology of continuous plutonism and huge mass wasting, and the thermochronological data. Modelling solutions for all samples show a goodness-of-fit (GOF) greater than 95% for all modelled parameters (AFT cooling ages, CT length distribution) with only 1 model revealing a GOF greater than 73% (Fig. 7.5; Fig. 7.6).

All modelled samples show 4 phases of change in the cooling pattern; at first (concordant to ZFT ages) samples cool rapidly, then before ~10 Myr they show a decrease in the cooling rate, followed by a re-increase in the cooling rate, and finally the samples reach surface temperature (Fig. 7.5; Fig. 7.6). The weighted mean t-T path was used for cooling rates, exhumation rates and the corresponding rock uplift calculations (Fig. 7.5; Fig. 7.6). Sample FU-39-09 (Fig. 7.1) t-T model shows a rapid cooling activity since ~21 Ma, indicating a raise of the sample block from depths equivalent to temperature of ~180 ˚C to depths equivalent to temperature of ~98 ˚C in ~2 Ma with a ~41 ˚C/Ma cooling rate, ~1.464 km/Ma exhumation rate and ~2.9 km of corresponding rock uplift (Table 7-4). Hereafter, the sample has experienced a short time of reduction in the cooling rate to achieve a temperature of ~85 ˚C in ~7 Ma with a ~1.86 ˚C/Ma cooling rate, ~0.066 km/Ma exhumation rate and ~0.5 km of corresponding rock uplift. Then, the cooling rate increase again at ~12 Ma, indicating a raise of the sample block to depths equivalent to a temperature of ~25 ˚C in ~4 Ma with a ~15 ˚C/Ma cooling rate, ~0.536 km/Ma exhumation rate and ~2.1 km of corresponding rock uplift. Afterwards, the cooling rate slowed down again to raise the sample to depths equivalent to a temperature of ~20 ˚C in ~8 Ma with a ~0.63 ˚C/Ma cooling rate, ~0.0225 km/Ma exhumation rate and ~0.2 km of corresponding rock uplift (Fig. 7.7; Table 7-4). Sample FU-40-09 (Fig. 7.1) t-T model shows a fast cooling phase since ~22 Ma. The sample block raised from depths equivalent to a temperature of ~185 ˚C to depths equivalent to a temperature of ~100 ˚C in ~2 Ma with a ~42.5 ˚C/Ma cooling rate, ~1.518 km/Ma exhumation rate and ~3.0 km of corresponding rock uplift. Afterwards, the sample has experienced a long period of a slower cooling rate to achieve a temperature of ~78 ˚C in ~14 Ma with a ~1.57 ˚C/Ma cooling rate, ~0.056 km/Ma exhumation rate and ~0.8 km of corresponding rock uplift. Then, the cooling rate increased again to raise the sample to depths equivalent to a temperature of ~20 ˚C in ~3 Ma with a ~23.2 ˚C/Ma cooling rate, ~0.829 km/Ma exhumation rate and ~2.5 km

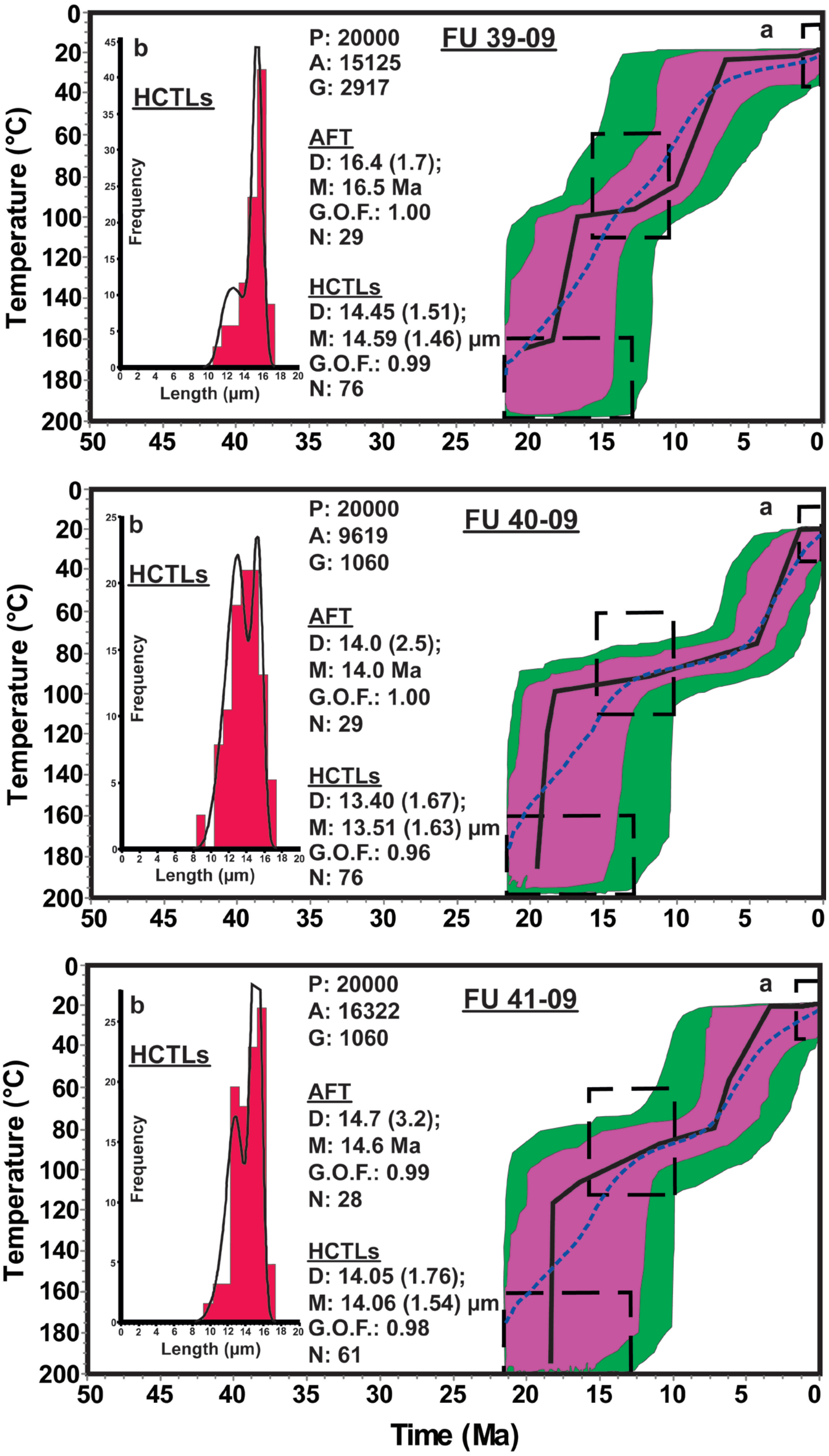

Fig. 7.5: Thermal history modelling using HeFTy v.1.8.3 (Ketcham et al., 2009); representative t–T paths illustrate the cooling history of samples of Fuerteventura Island. Displayed are; (a) the t–T paths, (b) the c-axes corrected horizontal confined track lengths (HCTLs) distribution overlain by a calculated probability density function (best fit). Resulting t–T curves show four different reliability levels; green paths: acceptable fit (all t–T paths with a merit function value of at least 0.05), purple paths: good fit (all t–T paths with a merit function value of at least 0.5), black line: best fit and dashed blue line: the weighted mean path (Ketcham et al., 1999, 2009). The used constrains (t-T boxes) are ZFT ages, AFT ages and the recent surface temperature. A: acceptable fit models, G: good fit models, D: determined FT age and HCTLs (1-σ error), M: modeled FT age and HCTLs, G.O.F.: goodness of fit, N: number of single grains and HCTLs.

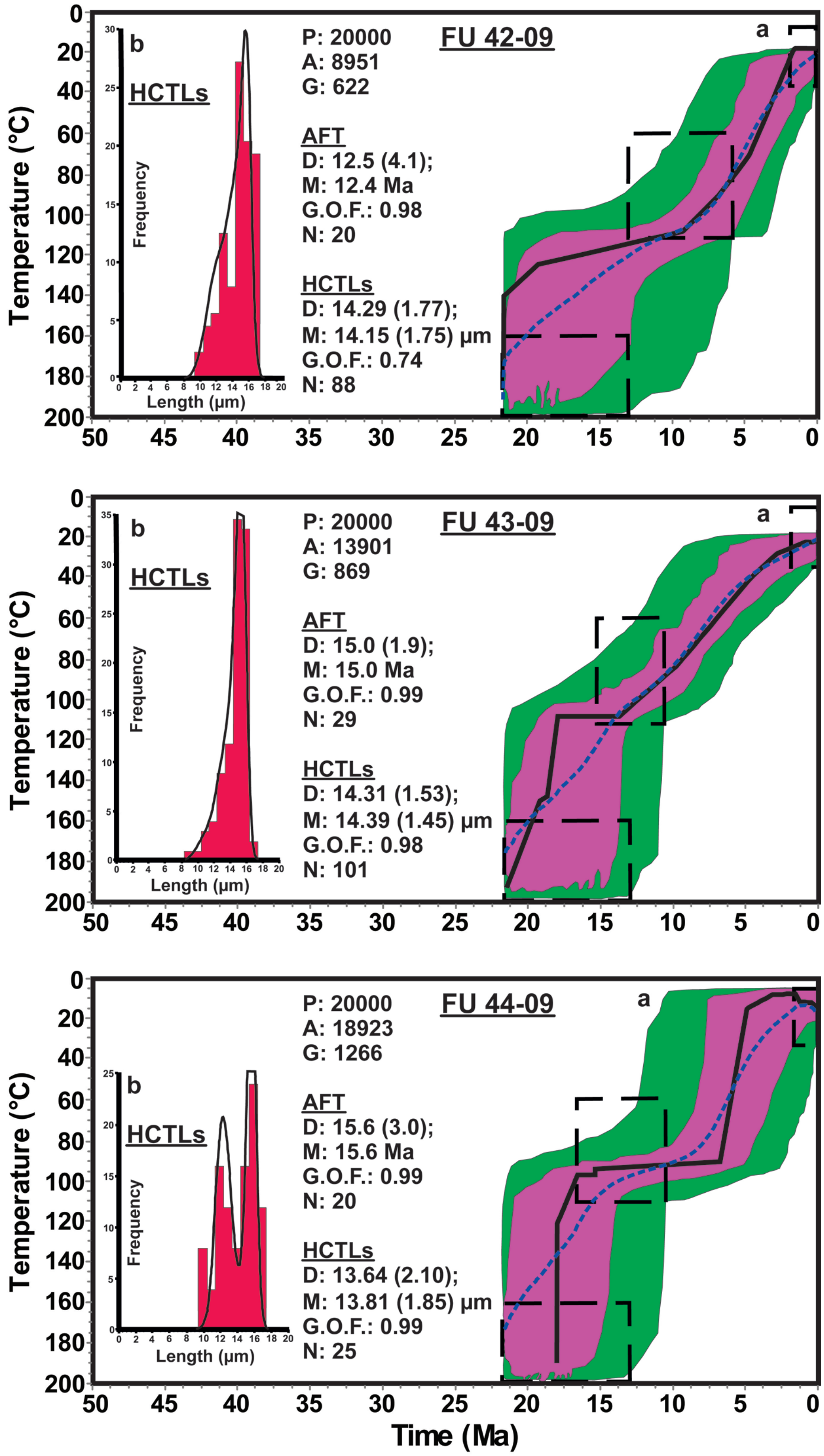

Fig. 7.6: Thermal history modelling of Fuerteventura Island samples using HeFTy v.1.8.3 (Ketcham et al., 2009). For further explanation see Fig. 7.5

of corresponding rock uplift. Subsequently, the cooling rate slowed down again to raise the sample to depths equivalent to a temperature of ~19.8 ˚C in ~3 Ma with a ~0.07 ˚C/Ma cooling rate, ~0.002 km/Ma exhumation rate and ~0.01 km of corresponding rock

Table 7-4: Fuerteventura Island Cooling rates, Exhumation rates and Rock uplift extracted from the HeFTy t-T modelling.

S.- No.	Elev. (m a.s.l)	Phase	t-t Segment (Ma)	~t	Δt	T-T Segment (°C)	ΔT	Cooling Rate (°C/Ma)	Exhumation Rate			Rock uplift		
									(km/Ma) 20 °C/km	(km/Ma) 28 °C/km	(km/Ma) 40 °C/km	(km/Δt) 20 °C/km	(km/Δt) 28 °C/km	(km/Δt) 40 °C/km
FU 39-09	134	1	21-19	20	2	180-98	82	**41.0**	2.050	**1.464**	1.025	4.1	**2.9**	2.1
		2	19-12	15.5	7	98-85	13	**1.86**	0.093	**0.066**	0.047	0.7	**0.5**	0.3
		3	12-8	10	4	85-25	60	**15.0**	0.750	**0.536**	0.375	3.0	**2.1**	1.5
		4	8-0	4	8	25-20	5	**0.63**	0.032	**0.022**	0.016	0.3	**0.2**	0.1
FU 40-09	149	1	22-20	21	2	185-100	85	**42.5**	2.125	**1.518**	1.063	4.3	**3.0**	2.1
		2	20-6	13	14	100-78	22	**1.57**	0.079	**0.056**	0.039	1.1	**0.8**	0.5
		3	6-3	4.5	3	78-20	58	**23.2**	1.160	**0.829**	0.580	3.5	**2.5**	1.7
		4	3-0	1.5	3	20-19.8	0.2	**0.07**	0.004	**0.002**	0.002	0.0	**0.01**	0.0
FU 41-09	149	1	21-19	20	2	190-108	82	**41.0**	2.050	**1.464**	1.025	4.1	**2.9**	2.1
		2	19-8	13.5	11	108-80	28	**2.55**	0.128	**0.091**	0.064	1.4	**1.0**	0.7
		3	8-4.5	6.25	3.5	80-20	60	**17.14**	0.857	**0.612**	0.429	3.0	**2.1**	1.5
		4	4.5-0	2.25	4.5	20-19.5	0.5	**0.11**	0.006	**0.004**	0.003	0.0	**0.02**	0.0
FU 42-09	108	1	20-18.5	19.25	1.5	180-130	50	**33.33**	1.667	**1.190**	0.833	2.5	**1.8**	1.2
		2	18.5-8	13.25	10.5	130-98	32	**3.05**	0.153	**0.109**	0.076	1.6	**1.1**	0.8
		3	8-3	5.5	5	98-25	73	**14.6**	0.730	**0.521**	0.365	3.7	**2.6**	1.8
		4	3-0	1.5	3	25-20	5	**1.67**	0.084	**0.06**	0.042	0.3	**0.2**	0.1
FU 43-09	102	1	21-19	20	2	180-107	73	**36.5**	1.825	**1.304**	0.913	3.7	**2.6**	1.8
		2	19-11	15	8	107-85	22	**2.75**	0.138	**0.098**	0.069	1.1	**0.8**	0.6
		3	11-3.5	7.25	8.5	85-25	60	**7.06**	0.353	**0.252**	0.177	3.0	**2.1**	1.5
		4	3.5-0	1.75	3.5	25-23	2	**0.57**	0.029	**0.02**	0.014	0.1	**0.1**	0.0
FU 44-09	3	1	21-19	20	2	180-100	80	**40.0**	2.000	**1.429**	1.000	4.0	**2.9**	2.0
		2	19-8	13.5	11	100-80	20	**1.82**	0.091	**0.065**	0.046	1.0	**0.7**	0.5
		3	8-5	6.5	3	80-23	57	**19.0**	0.950	**0.679**	0.475	2.9	**2.0**	1.4
		4	5-0	2.5	5	23-20	3	**0.6**	0.030	**0.021**	0.015	0.2	**0.1**	0.1

The exhumation rates were calculated from the cooling rates, a geothermal gradients of 20, 28 and 40 °C/km and an average surface temperature of 20 °C. The rock uplift was calculated as episodical vertical rock uplift from multiplying the exhumation rate by the duration of each single cooling event. The recent geothermal gradient is 28 °C/km (Rimi, 1990) and corresponding data were used in text. Elev. (m a.s.l) is elevation with meters above sea level. t–t: time segment; ~t: average time; Δt: phase (event) duration; T–T: Temperature segment; ΔT: temperature reduction during a single event.

uplift (Fig. 7.7; Table 7-4). Sample FU-41-09 (Fig. 7.1) t-T model shows a rapid cooling phase since ~21 Ma. The sample block raised from depths equivalent to a temperature of ~190 ˚C to depths equivalent to temperature of ~108 ˚C in ~2 Ma with a ~41 ˚C/Ma cooling rate, ~1.464 km/Ma exhumation rate and ~2.9 km of corresponding rock uplift. Afterwards, the sample has experienced a long period of dropping in the cooling rate to achieve a temperature of ~80 ˚C in ~11 Ma with a ~2.55 ˚C/Ma cooling rate, ~0.091 km/Ma exhumation rate and ~1.0 km of corresponding rock uplift. Then the cooling rate increased again to raise the sample to depths equivalent to a temperature of ~20 ˚C in ~3.5 Ma with a ~17.14 ˚C/Ma cooling rate, ~0.612 km/Ma exhumation rate and ~2.1 km of rock uplift. Hereafter, the cooling rate slowed down again to raise the sample to depths equivalent to a temperature of ~19.5 ˚C in ~4.5 Ma with a ~0.11 ˚C/Ma cooling rate, ~0.004 km/Ma exhumation rate and ~0.02 km of corresponding rock uplift (Fig. 7.7; Table 7-4). Sample FU-42-09 t-T model shows a moderate cooling activity since ~20 Ma. The sample block raised from depths equivalent to a temperature of ~180 ˚C to depths equivalent to a temperature of ~130 ˚C in ~1.5 Ma with a ~33.33 ˚C/Ma cooling rate, ~1.19 km/Ma exhumation rate and ~1.8 km of corresponding rock uplift. Hereafter, the sample has experienced a long time span of slower cooling to achieve a temperature of ~98 ˚C in ~10.5 Ma with a ~3.05 ˚C/Ma cooling rate, ~0.109 km/Ma exhumation rate and ~1.1 km of corresponding rock uplift. Then the cooling rate slightly increased again to raise the sample to depths equivalent to a temperature of ~25 ˚C in ~5 Ma with a ~14.6 ˚C/Ma cooling rate, ~0.521 km/Ma exhumation rate and ~2.6 km of corresponding rock uplift. Afterwards, the cooling rate reduced again to raise the sample block to depths equivalent to a temperature of ~20 ˚C in ~3 Ma with a ~1.67 ˚C/Ma

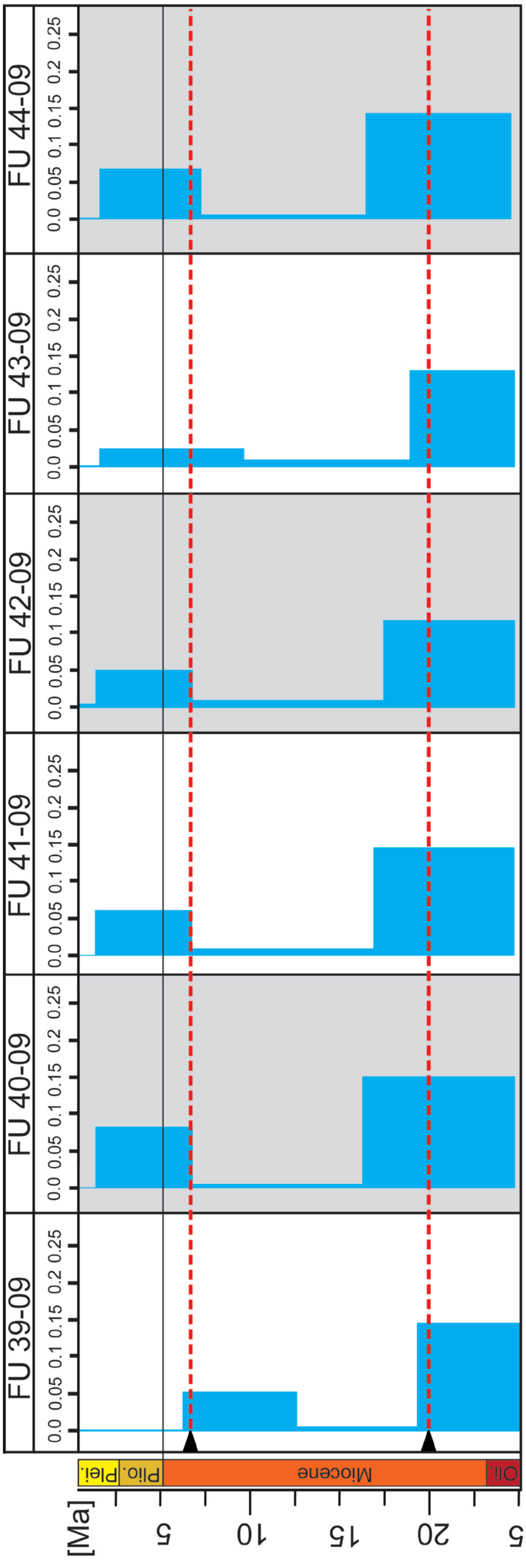

Fig. 7.7: Exhumation rates in (km/Ma) diagram for Fuerteventura Island. Based on the data from the thermal history from Fig. 7.5, Fig. 7.6 and Table 7-4. Two major cooling/exhumation events presented (red dashed lines) synchronous with major tectonic events.

cooling rate, ~0.06 km/Ma exhumation rate and ~0.2 of corresponding rock uplift (Fig. 7.7; Table 7-4). Sample FU-43-09 t-T model shows a rapid cooling activity since ~21 Ma. The sample block raised from depths equivalent to a temperature of ~180 ˚C to depths equivalent to a temperature of ~107 ˚C in ~2 Ma with a ~36.5 ˚C/Ma cooling rate, ~1.304 km/Ma exhumation rate and ~2.6 km of corresponding rock uplift. Hereafter, the sample has experienced a long period of a slower cooling rate to achieve a temperature of ~85 ˚C in ~8 Ma with a ~2.75 ˚C/Ma cooling rate, ~0.098 km/Ma exhumation rate and ~0.8 km of corresponding rock uplift. Then the cooling rate increased again to raise the sample to depths equivalent to a temperature of ~25 ˚C in ~8.5 Ma with a ~7.06 ˚C/Ma cooling rate, ~0.252 km/Ma exhumation rate and ~2.1 km of corresponding rock uplift. Afterwards, the cooling rate reduced again to raise the sample to depths equivalent to a temperature of ~23 ˚C in ~3.5 Ma with a ~0.57 ˚C/Ma cooling rate, ~0.02 km/Ma exhumation rate and ~ 0.1 km of corresponding rock uplift (Fig. 7.7; Table 7-4). Sample FU-44-09 t-T model shows a fast cooling phase since ~21 Ma. The sample block raised from depths equivalent to a temperature of ~180 ˚C to depths equivalent to a temperature of ~100 ˚C in ~2 Ma with a ~40 ˚C/Ma cooling rate, ~1.429 km/Ma exhumation rate and ~2.9 km of corresponding rock uplift. Afterwards, the sample has experienced a long period of slower cooling rate to achieve a temperature of ~80 ˚C in ~11 Ma with a ~1.82 ˚C/Ma cooling rate, ~0.065 km/Ma exhumation rate and ~0.7 km of corresponding rock uplift. Then the cooling rate fasten again to raise the sample to depths equivalent to a temperature of ~23 ˚C in ~3 Ma with a ~19 ˚C/Ma cooling rate, ~0.679 km/Ma exhumation rate and ~2.0 km of corresponding rock uplift. Hereafter, the cooling rate dropped again to raise the sample block to depths equivalent to a temperature of ~20 ˚C in ~5 Ma with a ~0.6 ˚C/Ma cooling rate, ~0.021 km/Ma exhumation rate and ~0.1 km of corresponding rock uplift (Fig. 7.7; Table 7-4).

7.2 La Gomera Island

From La Gomera 6 samples have provided sufficient zircon grains to perform ZFT (Fig. 7.8; Table 7-5). While, 8 samples have provided enough apatite grains to carry out AFT dating (Fig. 7.8; Table 7-6), of these 3 samples yielded sufficient CTs for t-T modelling.

7.2.1 Zircon fission track data

From La Gomera, the dated 6 samples are from the BC; two samples from Tamargada magmatic unit, two samples from the P1 plutonic complex, and two samples from the P2 plutonic complex (see section 3.3.1.2; Fig. 7.8; Table 7-5). Although, there is a scarcity in precise intrusion ages of the different rock units in the BC, they are believed to have ages between 15 (>20?) and 10.5 Ma (Ancochea et al., 2006). The treated samples have ZFT central ages ranging between 10.3 (0.5) and 8.3 (0.7) Ma (Fig. 7.8; Table 7-5), indicating a slight difference between ZFT ages and corresponding formation ages. In other words samples were exhumed short after their emplacement. The ZFT age distribution does not allow a spatial separation as they are overlapping within the error range (Table 7-5). The uranium concentrations vary between 230.8 and 524.2 µg/g (Table 7-5) with no clear relationship to the zircon single grain age (Fig. 7.9). That documents the absence of any metamictization affect on the ZFT ages on La Gomera. The $\chi 2$ values ranges between 86 and 100% indicating a single age population (Table 7-5).

7.2.2 Apatite fission track data

From La Gomera, 8 samples from the BC were dated; one sample form the sub-marine

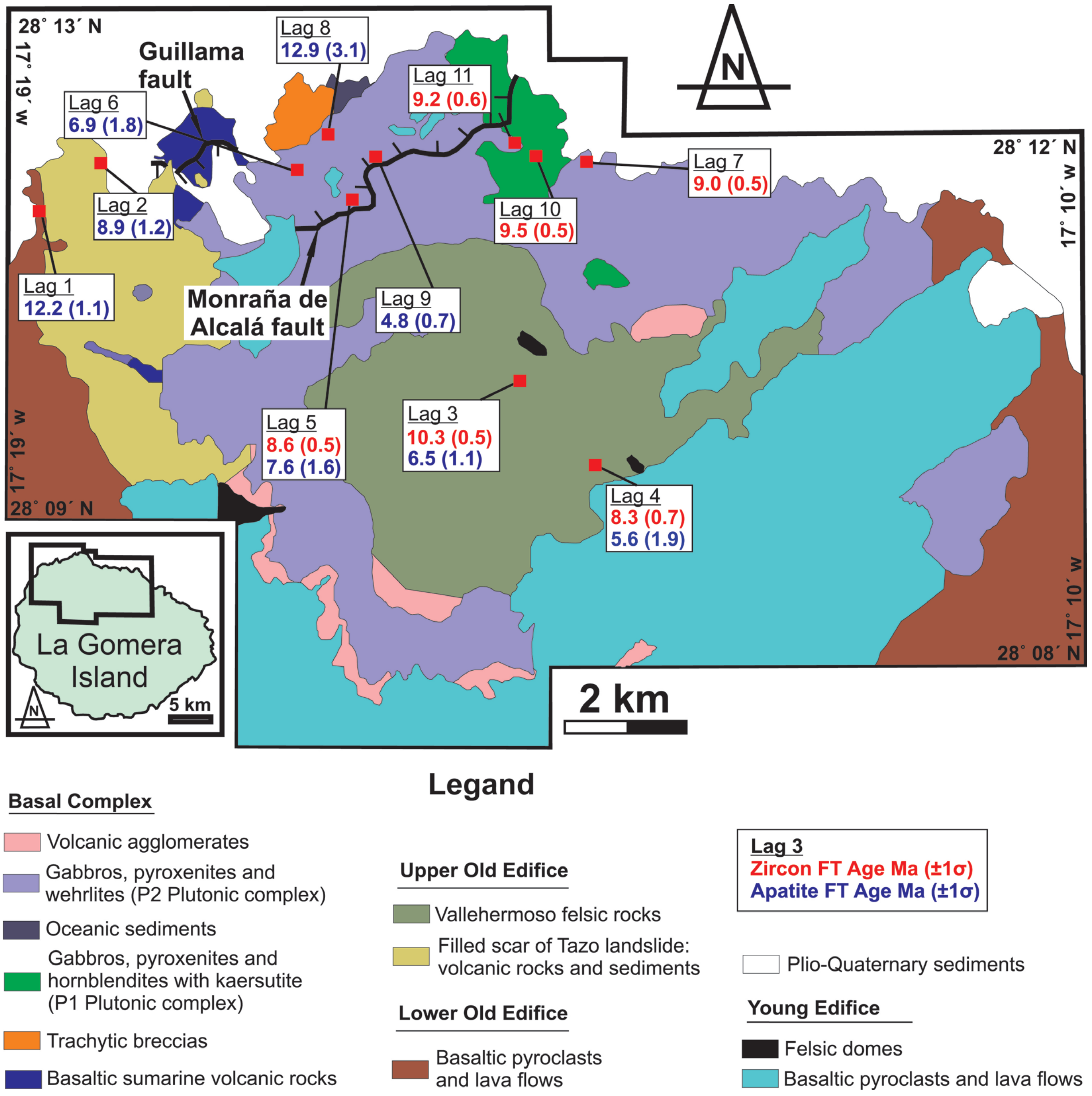

Fig. 7.8: Geologic map of the northern sector of La Gomera Island with the main rock units lithologies and locations, numbers and ages of the dated samples. The inset shows the area covered by the map from La Gomera Island (after Casillas et al., 2010).

basaltic series, two samples from the Tamargada magmatic unit, two samples from the P1 plutonic complex, two samples from the P2 plutonic complex, and one sample from the trachytic breccias (see section 3.3.1.2; Fig. 7.8; Table 7-6). The treated samples show AFT central ages ranging between 12.9 (3.1) and 4.8 (0.7) Ma (Fig. 7.8, Table 7-6). The age distribution does not allow samples to be spatially separated (Fig. 7.8). The uranium concentration in these samples is generally low and varies between 3.6 and 26.0 µg/g. The χ2 values ranging from 93 to 100 % with except of one sample (Lag 6) which has a lower χ2 value of 52 % (Table 7-6) due to the lack of countable apatites in this sample. Despite that the χ2 values indicating a single age population.

The age-elevation relationship (Fig. 7.10) is more complex and can be separated into

Table 7-5: La Gomera Island’s sample information and zircon fission track data.

S.-No.	Elev. [m a.s.l.]	Lithology	Formation age	U [µg/g]	n	Sp. Tracks		Ind. Tracks		χ^2 [%]	Central age (1σ) [Ma]
						ρ_s	N_s	ρ_i	N_i		
Lag 3	350	Tamargada Monzonite	Lower-Middle Miocene	417.2	21	21.822	1244	82.306	4692	92	**10.3 (0.5)**
Lag 4	400	Tamargada Syenite	Lower-Middle Miocene	230.8	23	8.13	218	37.814	1014	100	**8.3 (0.7)**
Lag 5	280	Syenite P2	Lower-Middle Miocene	258.2	25	11.716	624	52.385	2790	86	**8.6 (0.5)**
Lag 7	310	Amphibolic Gabbro P1	Lower Miocene	524.2	22	21.8	996	92.127	4209	100	**9.0 (0.5)**
Lag 10	75	Amphibolic Pyroxinite P1	Lower Miocene	418.6	23	20.914	1415	82.43	5577	100	**9.5 (0.5)**
Lag 11	65	Trachyte P1	Lower Miocene	277.2	21	13.596	544	54.957	2199	100	**9.2 (0.6)**

Sample information and apatite fission track data given as central ages with uncertainty of 1-sigma. S.-No.; samples number, Elev. [m a.s.l.]; elevation in meters above sea level, U; Uranium concentration in µg/g, n; number of counted apatite grains, ρs; density of spontaneous tracks (10^5 tr/cm^2), Ns; number of spontaneous tracks, ρi; density of induced tracks (10^5 tr/cm^2), Ni; number of induced tracks, χ2; chi square test: probability of single grain ages belonging to one population. Test is passed if P(χ2) > 5% (Galbraith, 1981), Central ages calculated with Trackkey V.4.2 (Dunkl, 2002) using a ζ-value of 123.0 ± 6.09. Nd (tracks counted on CN1 dosimeter glass) = 16413 tracks.

Table 7-6: La Gomera Island’s sample information and apatite fission track data.

S.-No.	Elev. [m a.s.l.]	Lithology	Formation age	U [µg/g]	n	Sp. Tracks		Ind. Tracks		χ^2 [%]	Central age (1σ) [Ma]	Dpar (µm)
						ρ_s	N_s	ρ_i	N_i			Av. (std)
Lag 1	200	Basaltic Pillow-Lava	Lower Miocene	9.9	27	0.651	202	14.373	4461	99	**12.2 (1.1)**	2.8 (0.5)
Lag 2	70	Trachytic Breccias	Lower Miocene	15.5	14	0.742	65	22.360	1959	93	**8.9 (1.2)**	3.0 (0.4)
Lag 3	350	Tamargada Monzonite	Lower-Middle Miocene	3.6	34	0.120	36	4.963	1484	100	**6.5 (1.1)**	1.9 (0.3)
Lag 4	400	Tamargada Syenite	Lower-Middle Miocene	4.9	20	0.140	9	6.598	424	95	**5.6 (1.9)**	1.6 (0.2)
Lag 5	280	Syenite P2	Lower-Middle Miocene	26.0	5	0.930	24	32.314	834	98	**7.6 (1.6)**	2.1 (0.5)
Lag 6	310	Amphibolic Gabbro P1	Lower Miocene	14.9	4	0.568	15	21.559	569	52	**6.9 (1.8)**	2.3 (0.5)
Lag 8	350	Pegmatitic Gabbro P2	Lower-Middle Miocene	6.9	9	0.460	19	9.225	381	100	**12.9 (3.1)**	2.3 (0.4)
Lag 9	325	Trachyte P1	Lower Miocene	12.2	24	0.286	60	15.270	3205	100	**4.8 (0.7)**	1.8 (0.2)

Sample information and apatite fission track data given as central ages with uncertainty of 1-sigma. Central ages were calculated with Trackkey V.4.2 (Dunkl, 2002) using a ζ-value of 330.60 ± 16.47. Nd (tracks counted on CN5 dosimeter glass) = 15236 tracks. Dpar (std); average etch pit in µm and standard deviation. For further description see Table 7-5

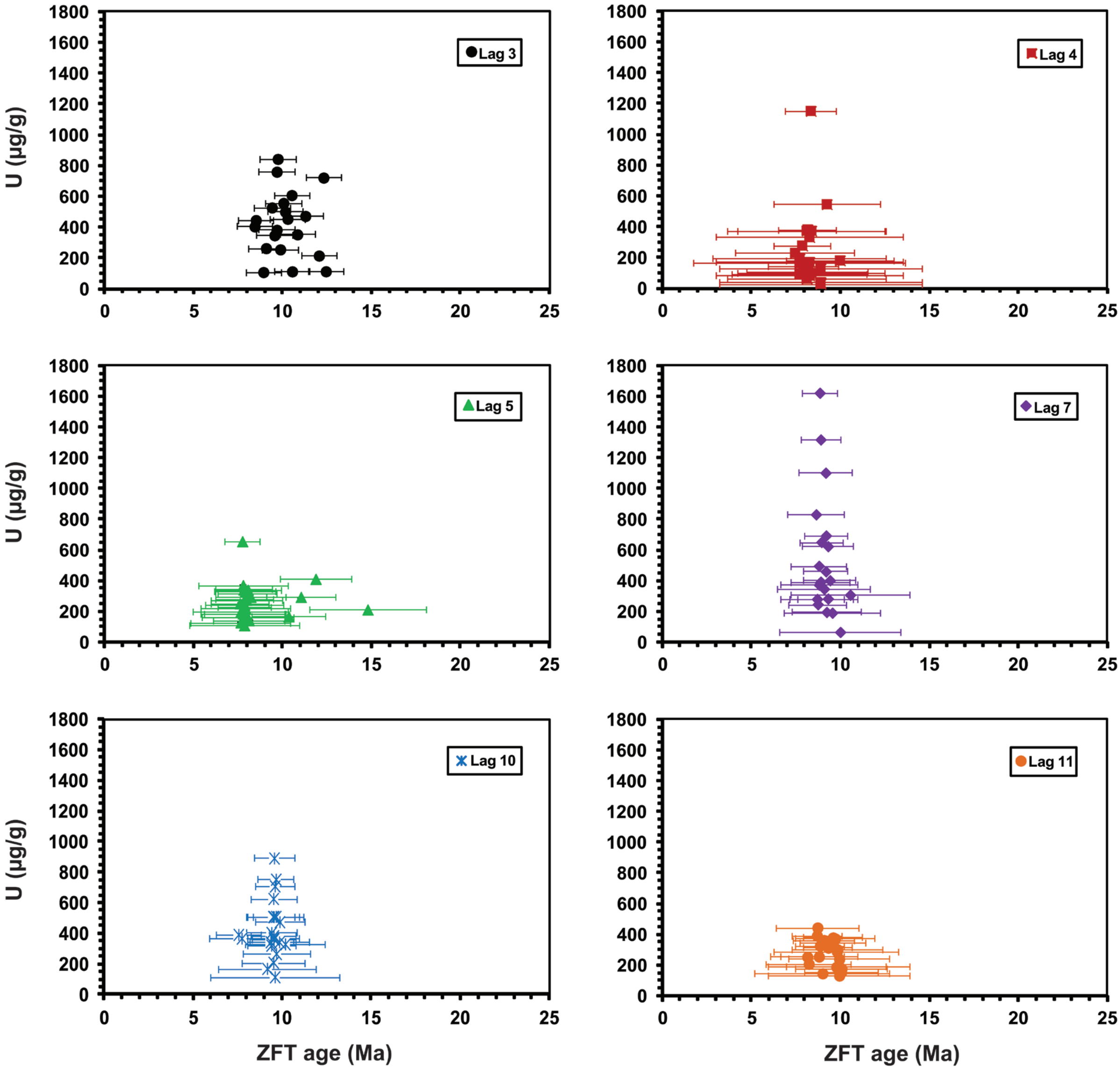

Fig. 7.9: ZFT single grain ages versus uranium concentrations for La Gomera samples. No relationship between them is represented.

two groups; one with a positive age-elevation relationship (A group in Fig. 7.10) consisting of the most northern samples Lag-1, Lag-2, and Lag-8 which represent static uplift, caused by the progressive removal of top material. The second group shows a negative age-elevation relationship (B group in Fig. 7.10), consisting of the samples Lag 3, Lag 4, Lag 5, Lag6, and Lag 9, which may be explained by differential uplift by movement along a fault boundary, an anticline-syncline relationship or a selective denudation pattern (Fig. 7.10).

Three samples from La Gomera yield sufficient CTs for t-T modelling (sample Lag 4 has only 8 CTs therefore it was used only for comparison). The CTs mean lengths distribution varies between 12.8 (2.4) and 14.4 (1.4) µm with negative skewness varying between −0.511 and −1.507. The measured CTs were corrected against their crystallographic c-axis using HeFTy V.1.8.3 (Donelick et al., 1999; Ketcham et al., 2007a; b) result-

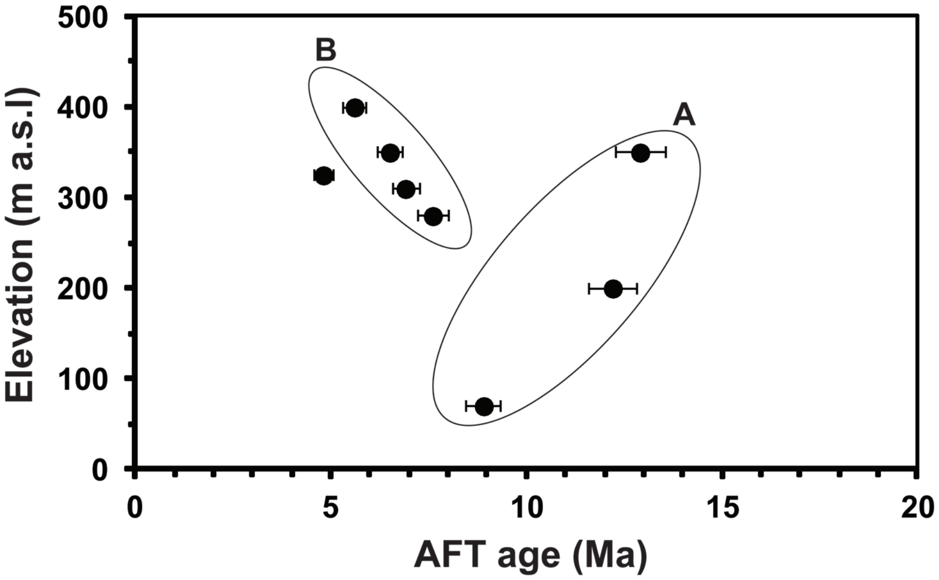

Fig. 7.10: AFT age-elevation plot of La Gomera Island samples. The samples are divided in two groups; one with a positive age-elevation relationship (group A), the other with a negative age-elevation relationship (group B).

Table 7-7: La Gomera Island detailed apatite confined fission track length and Dpar data.

Sample	CT n	CT mean (µm)	CT std. (µm)	CT skew.	Lc mean (µm)	Lc std. (µm)	Lc skew.	Dpar n	Dpar mean (µm)	Dpar std. (µm)	Dpar skew.
Lag 1	141	**14.4**	1.4	-1.507	**15.0**	1.2	-1.665	705	**2.9**	0.4	-0.437
Lag 3	51	**13.6**	1.7	-1.009	**14.2**	1.5	-0.783	255	**2.1**	0.2	0.100
Lag 4	8	**12.8**	2.4	-0.511	**13.6**	2.3	-0.831	40	**1.9**	0.2	0.644

n CT; number of measured confined tracks, CT mean; mean confined track length, std; standard deviation, skew; skewness of distribution relative to the mean value (measure of asymmetry of the distribution), Lc mean; mean track length after c-axis correction, n Dpar; number of measured etch pit diameters, Dpar mean; mean etch pit diameter.

ing in c-axis projected CTs lengths between 13.6 (2.2) and 15.0 (1.2) µm with a negative skewness from −0.783 to −1.665 (Table 7-7). This CTs distribution, for all samples, indicate a typical undisturbed magmatic rock with a homogenous cooling history, where samples exhumed rapidly through the PAZ (Gleadow et. al., 1986). Along with CTs a total of 1000 Dpars were measured from the analysed apatite single grains (Table 7-7). The mean Dpar values varying between 1.6 (0.2) and 3.0 (0.4) µm (Table 7-7) indicating uniform typical Cl rich apatites, except for sample Lag 4 which occupies a border value (1.7 µm) between the Cl rich and calcian-fluorapatites (Burtner et al., 1994; Donelick, 2004; Donelick et al., 2005). There is a positive relationship between AFT ages and Dpar values (Fig. 7.11). Referring to a slight effect of the apatites chemistry differences on the AFT ages. Therefore, the annealing algorithm of Ketcham et al., 2007 and c-axis projected CTs were used to avoid the anisotropy of the annealing mechanism in apatites (Green and Durrani, 1977; Laslett et al., 1984; Barbarand et al., 2003).

7.2.3 Thermo-kinematic modelling and exhumation rates

For La Gomera, the cooling-only model is concordant with a general geology of continuous plutonism and huge mass wasting, and

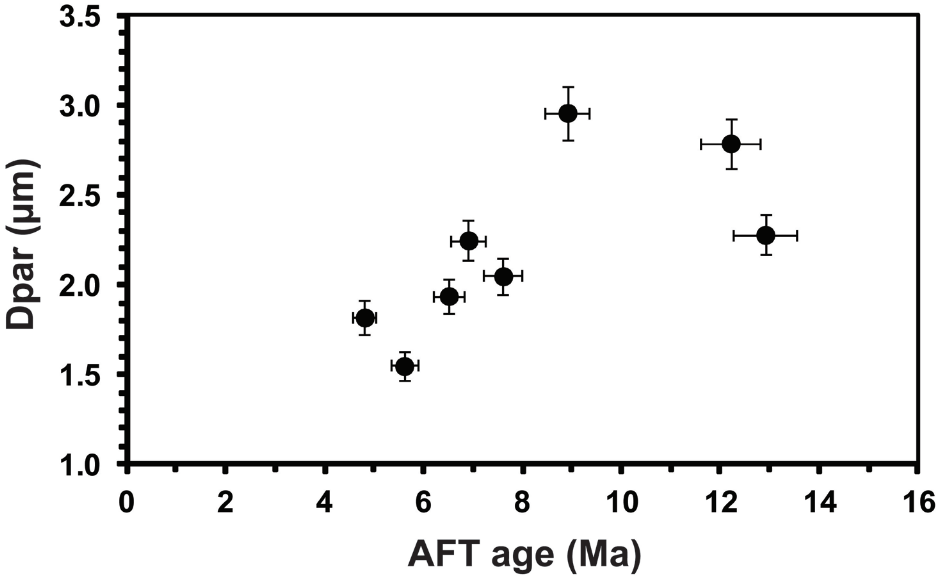

Fig. 7.11: AFT age-Dpar plot of La Gomera Island samples showing a positive relationship. Indicating a slight effect of the grains chemistry on AFT ages.

the thermochronological data. Modelling solutions for all samples show a goodness-of-fit (GOF) greater than 83% for all modelled parameters (AFT cooling ages, CTs length distribution) (Fig. 7.12).

The modelled samples show one long-lived rapid cooling trend which could be divided into four phases based on a slight changes in the cooling pattern. At first samples cool rapidly (synchronous with ZFT ages), then before ~7 Myr they show a decrease in the cooling rate, followed by a re-increasing cooling rate, and finally the samples reach the surface temperature (Fig. 7.12; Table 7-8). The weighted mean t-T path was used for cooling rates, exhumation rates and the corresponding rock uplift calculations (Fig. 7.12). sample Lag 1 (Fig. 7.8) the t-T model shows one rapid cooling event for the basaltic pillow lava sample between ~15 and ~7 Ma, cooling the sample from ~180 to ~30 ˚C in less than 8 Ma with a cooling rate of ~18.75 ˚C/Ma. Afterwards, the sample cooled to ~20 ˚C in ~7 Ma with a ~1.43 ˚C/Ma cooling rate, ~0.957 km/Ma exhumation rate and ~0.4 km of corresponding rock uplift (Fig. 7.13; Table 7-8). Sample Lag 3 (Fig. 7.8) t-T model shows a rapid cooling phase since ~10 Ma. The sample block raised from depths equivalent to a temperature of ~180 ˚C to depths equivalent to a temperature of ~103 ˚C in ~3 Ma with a ~25.67 ˚C/Ma cooling rate, ~0.917 km/Ma exhumation rate and ~2.8 km of corresponding rock uplift. Afterwards, the sample has experienced a period of slower cooling, to achieve a temperature of ~92 ˚C in ~3 Ma with a ~3.67 ˚C/Ma cooling rate, ~0.131 km/Ma exhumation rate and ~0.4 km of corresponding rock uplift. Then, the cooling rate fasten again to raise the sample to depths equivalent to a temperature of ~27 ˚C in ~1 Ma with a ~65 ˚C/Ma cooling rate, ~2.321 km/Ma exhumation rate and ~2.3 km of corresponding rock uplift. Hereafter, the cooling rate slowed down to raise the sample to depths equivalent to a temperature of ~20 ˚C in ~3 Ma with a ~2.33 ˚C/Ma cooling rate, ~0.083 km/Ma exhumation rate and ~ 0.2 km of corresponding rock uplift (Fig. 7.13; Table 7-8). Sample Lag 4 (Fig. 7.8) t-T model shows a rapid cooling activity since ~7.5 Ma. The sample block raised from depths

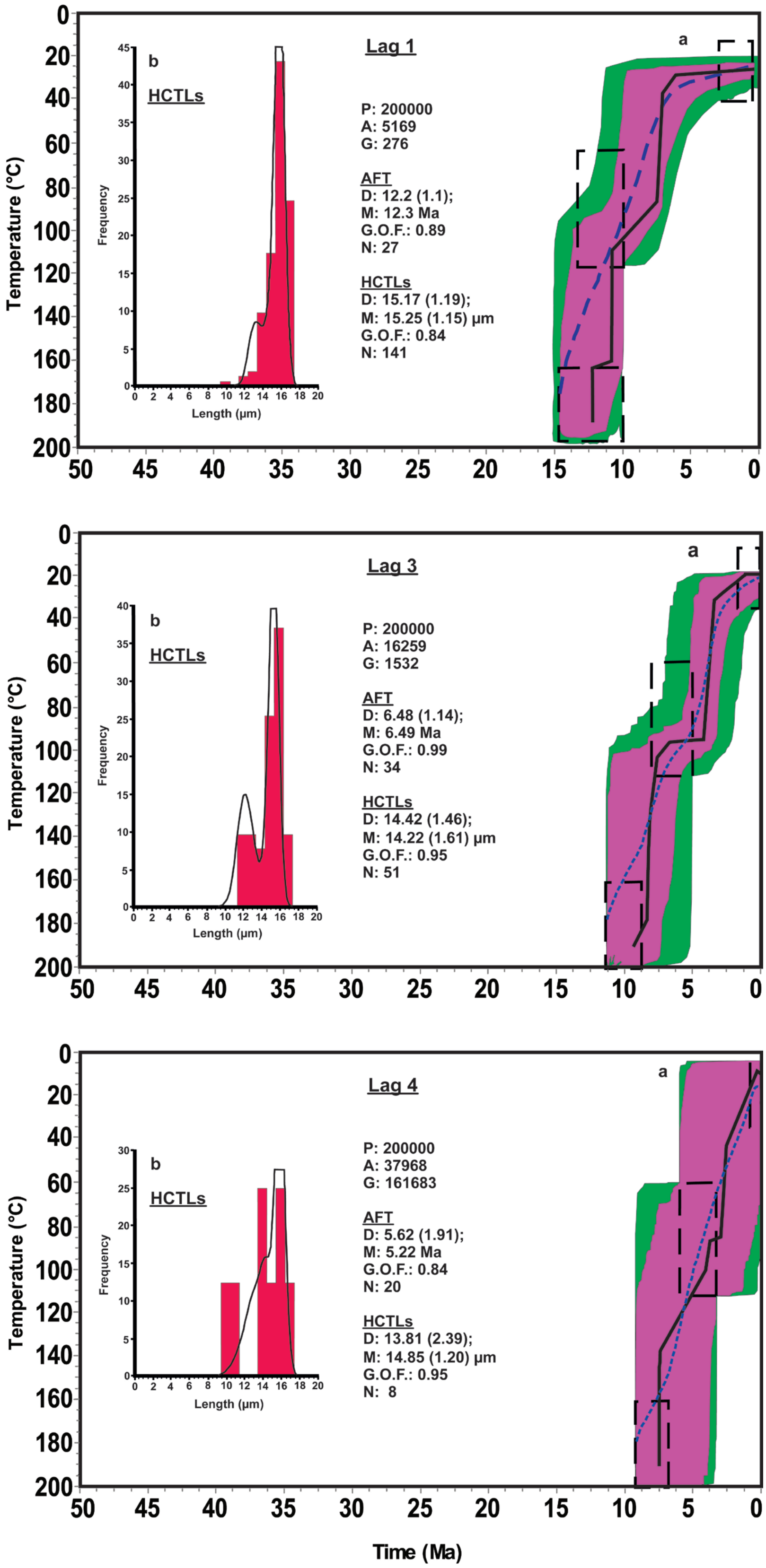

Fig. 7.12: Thermal history modelling of La Gomera Island samples using HeFTy v.1.8.3 (Ketcham et al., 2009). For further explanation see Fig. 7.5

Table 7-8: La Gomera Island Cooling rates, Exhumation rates and Rock uplift extracted from the HeFTy t-T modelling.

S.- No.	Elev. (m a.s.l)	Phase	t-t Segment (Ma)	~t	∆t	T-T Segment (°C)	∆T	Cooling Rate (°C/Ma)	Exhumation Rate			Rock uplift		
									(km/Ma) 20 °C/km	(km/Ma) 28 °C/km	(km/Ma) 40 °C/km	(km/∆t) 20 °C/km	(km/∆t) 28 °C/km	(km/∆t) 40 °C/km
Lag 1	200	1	15-7	11	8	180-30	150	**18.75**	0.938	**0.670**	0.469	7.5	**5.4**	3.8
		2	7-0	3.5	7	30-20	10	**1.43**	0.072	**0.957**	0.036	0.5	**0.4**	0.3
Lag 3	350	1	10-7	8.5	3	180-103	77	**25.67**	1.284	**0.917**	0.642	3.9	**2.8**	1.9
		2	7-4	5.5	3	103-92	11	**3.67**	0.184	**0.131**	0.092	0.6	**0.4**	0.3
		3	4-3	3.5	1	92-27	65	**65**	3.250	**2.321**	1.625	3.3	**2.3**	1.6
		4	3-0	1.5	3	27-20	7	**2.33**	0.117	**0.083**	0.058	0.3	**0.2**	0.2
Lag 4	400	1	7.5-5.5	6.5	2	180-100	80	**40**	2.000	**1.429**	1.000	4.0	**2.9**	2.0
		2	5.5-3.5	4.5	2	100-75	25	**12.5**	0.625	**0.446**	0.313	1.3	**0.9**	0.6
		3	3.5-2.5	3	1	75-25	50	**50**	2.500	**1.786**	1.250	2.5	**1.8**	1.3
		4	2.5-0	1.25	2.5	25-20	5	**2**	0.100	**0.029**	0.050	0.3	**0.2**	0.1

The exhumation rates were calculated from the cooling rates, a geothermal gradients of 20, 28 and 40 °C/km and an average surface temperature of 20 °C. The rock uplift was calculated as episodical vertical rock uplift from multiplying the exhumation rate by the duration of each single cooling event. The recent geothermal gradient is 28 °C/km (Rimi, 1990) and corresponding data were used in text. Elev. (m a.s.l) is elevation with meters above sea level. t–t: time segment; ~t: average time; ∆t: phase (event) duration; T–T: Temperature segment; ∆T: temperature reduction during a single event.

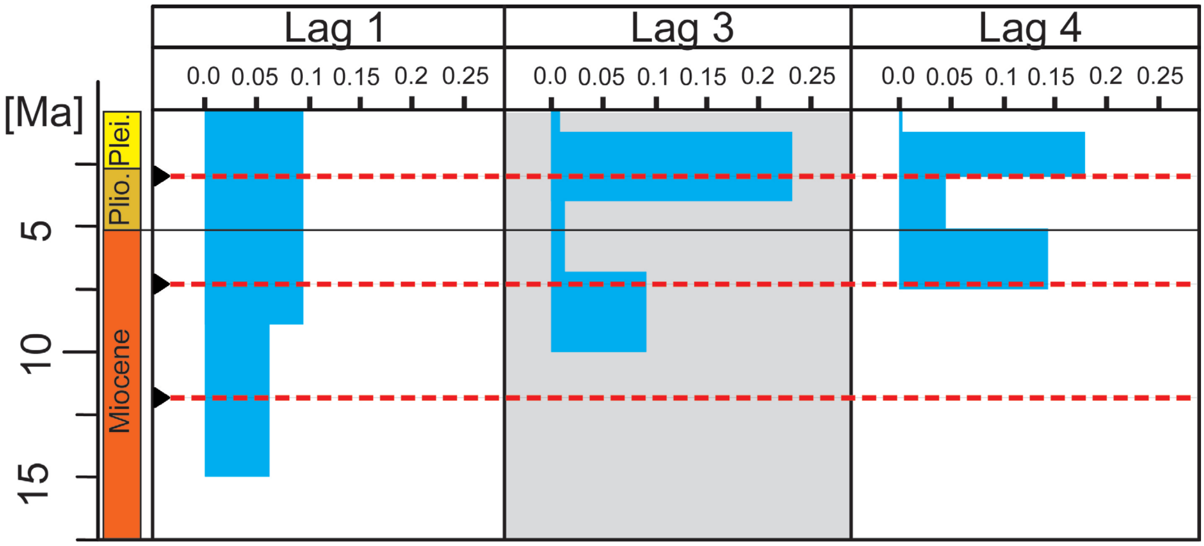

Fig. 7.13: Exhumation rates in (km/Ma) diagram of La Gomera Island. Based on the data extracted from the thermal history from Fig. 7.12 and Table 7-8. Three major cooling/exhumation events presented (red dashed lines) synchronous with major tectonic events.

equivalent to a temperature of ~180 ˚C to depths equivalent to a temperature of ~100 ˚C in ~2 Ma with a ~40 ˚C/Ma cooling rate, ~1.429 km/Ma exhumation rate and ~2.9 km of corresponding rock uplift. Afterwards, the sample has experienced a time span of a relatively reduced cooling to achieve a temperature of ~75 ˚C in ~2 Ma with a ~12.5 ˚C/Ma cooling rate, ~0.446 km/Ma exhumation rate and ~0.9 km of corresponding rock uplift. Then, the cooling rate increased again to raise the sample to depths equivalent to a temperature of ~25 ˚C in ~1 Ma with a ~50 ˚C/Ma cooling rate, ~1.786 km/Ma exhumation rate and ~1.8 km of corresponding rock uplift. Hereafter, the cooling rate slowed down again to raise the sample to depths equivalent to a temperature of ~20 ˚C in ~2.5 Ma with a ~2 ˚C/Ma cooling rate, ~0.029 km/Ma exhumation rate and ~0.2 km of corresponding rock uplift (Fig. 7.13; Table 7-8).

8

INTERPRETATION WITHIN THE FRAMEWORK OF PLATE TECTONICS

CONTENTS

8.1 INTERPRETATION

8.1.1 THE RWENZORI MOUNTAINS

The majority of the ZHe analysed grains have ages of ~397.8 (13.3) or ~235.5 (20.7) Ma recording the concurrent cooling/exhumation events. The AFT ages were spatially separated with a positive age-elevation relationship over three age/zone groups; ~48.7 (3.9) Ma, ~25.7 (2.8) Ma, ~12 (2) Ma, indicating non-uniform cooling/exhumation during these episodes. While, the AHe treated grains have ages varying between 38.3 (2.4) and 12.9 (2.3) recording the cooling events through the AHe closure temperature.

These cooling ages derived from different thermochronometers and the t-T modelling provide a record for the cooling/exhumation history of the western flank of Rwenzoris since L. Silurian to Recent times. Consequently 3 rapid cooling/exhumation events were revealed (Fig. 5.8; Fig. 5.9).

The first cooling/exhumation event, was addressed by ZHe ages and the t-T modelling, occurred in Silurian-Devonian times (420-390 Ma) with an average cooling rate of ~3.9 (1.95) ˚C/Ma, exhumation rate of ~0.156 (0.078) km/Ma and a corresponding rock uplift of ~3.2 (0.9) km (Table 5-5; Fig. 5.10). This exhumation event was occurred as response to the deep erosion which affected East Africa after the Pan-African orogeny (Fabre, 1988; Said, 1990). This event was reported in other parts of the Rwenzoris and the Albertine region (MacPhee, 2006; Bauer et al., 2010b; 2013; 2015; for more details see chapter 3 section 3.3.2).

The second cooling/exhumation event, is represented by ZHe ages and the t-T modelling, took place during the Triassic (240-220 Ma) with a cooling rate of ~4.33 ˚C/Ma, exhumation rate of ~0.173 km/Ma and a corresponding rock uplift of ~3.1 km (Table 5-5; Fig. 5.10). This event is associated with the Karoo rifting activation in East Africa during the Permo-Triassic (Ring, 1995; Delvaux, 2001; Delvaux et al., 2012) which caused strike-slip and thrust faulting in the Rwenzoris (Aanyu, 2011). Followed by major erosional events occurred in the Triassic, ending of the Karoo sedimentary regime in the whole region (Schlueter, 1994; Van der Beek et al., 1998; Bradley et al., 2010). This event was recorded in other parts of the Rwenzoris and the EARS (Foster and Gleadow, 1992, 1996; Van der Beek et al., 1998; Bauer et al., 2010b).

The third cooling/exhumation event is more continuous, it is reported by the AFT, AHe ages and the t-T modelling. It took place between the Eocene and the Miocene (52-10 Ma) with an average cooling rate of ~3.45 (3.81) ˚C/Ma, exhumation rate of ~0.138 (0.152) km/Ma and a corresponding rock uplift of ~2.8 (0.5) km (Table 5-5; Fig. 5.10). This event is concurrent with a list of events starting with the Late Cretaceous-Early Eocene drifting of India which might have caused block faulting and subsequent erosion in the area (Bauer et al., 2013). Afterwards, during the Eocene, the magmatism in South Ethiopia started, followed by significant doming in the Eastern Rift in Kenya in the Oligocene (Ebinger, 1989; Ebinger and Sleep, 1998). By ~20 Ma much of the eastern rift was established (Ebinger et al., 1989; Morley et al., 1992; Wolfeden et al., 2004; Chorowicz, 2005; McDougall and Brown, 2009) synchronous with the initiation of volcanism in the western rift (~25 Ma; Roberts et al., 2012). This event has been reported in other parts of the Rwenzoris and the EARS (Foster and Gleadow, 1992, 1996; Van der Beek et al., 1998; Pik et al., 2003, 2008; Spiegel et al., 2007; Bauer et al., 2010b).

From modelling, the third cooling/exhumation event can be divided into two events with a slight change in the nature of the cooling patterns; one is ≥20-13 Ma and responsible for ~1.4 km rock uplift, and the other is ≤20-

13 Ma and responsible for ~1.6 km rock uplift (Table 5-5; Fig. 5.10).

The high topography (≥4 km) in the Rwenzori Mountains is restricted to a relatively small area in the central block (Fig. 8.1). Altitudes in the northern and southern blocks reduced to elevations of ~1.5 km with local peaks of ~2–3 km (Ring, 2008) which are concordant with elevations in the rift flanks allover the EARS. Furthermore, the Rwenzoris are tilted eastward along a NNE-SSW trending axis (e.g., Sachau et al., 2015), and exhumed as an independent small blocks (e.g., Bauer et al., 2013). The Rwenzoris west flank shows steep stream channels, Neogene AHe cooling age (Macphee, 2006), Neogene AFT and AHe cooling ages (Fig. 5.1; this study). While, the eastern flank shows older cooling ages (Jurassic-Cretaceous) with no age-elevation relationship (Bauer et al., 2010b; 2013). This information refers to undetected cooling/exhumation event affecting the western flank of the central block of the Rwenzoris providing additional uplift. This event accompanied uplift has to be less than the AHe thermochronometer sensitivity zone (≤2 km). Fortunately, the cooling age could provide more details. Generally, the Neogene cooling ages recognized by the AFT or AHe systems record the onset of the Albertine rift flanks uplift, causing exhumation of these samples through the AFT PAZ or AHe PRZ. Considering an average surface temperature of 20°C and an average geothermal gradient of 25°C/km, these samples were uplifted from depths between ~2 and ~4 km. Today they are elevated ~2 km a.s.l., resulting in a total surface uplift of ~4 to ~6 km (plus what was eroded). Consequently, this surface uplift was produced by Albertine rift flanks uplift (~12-8 Ma) causing ~2.8 (0.5) km of rock uplift plus a later event responsible for ≤2 km of rock uplift. That later exhumation event is necessary to bring the Neogene aged samples to the surface and to compensate the difference between rock and surface uplift. This uplifting phase is most probably associated with the splitting of the palaeo-Lake Obweruka (~3-2.5 Ma; Pickford et al., 1993).

Collectively, this information and findings indicate two different phases of Cenozoic uplifting events in the Rwenzoris during Neogene time; the first is regional and rifting related which started in Miocene times affecting the whole mountain range with 2-4 km rock uplift, and the second is local and caused by uplifting of the Bwamba border fault footwall which started in Pliocene times. Providing

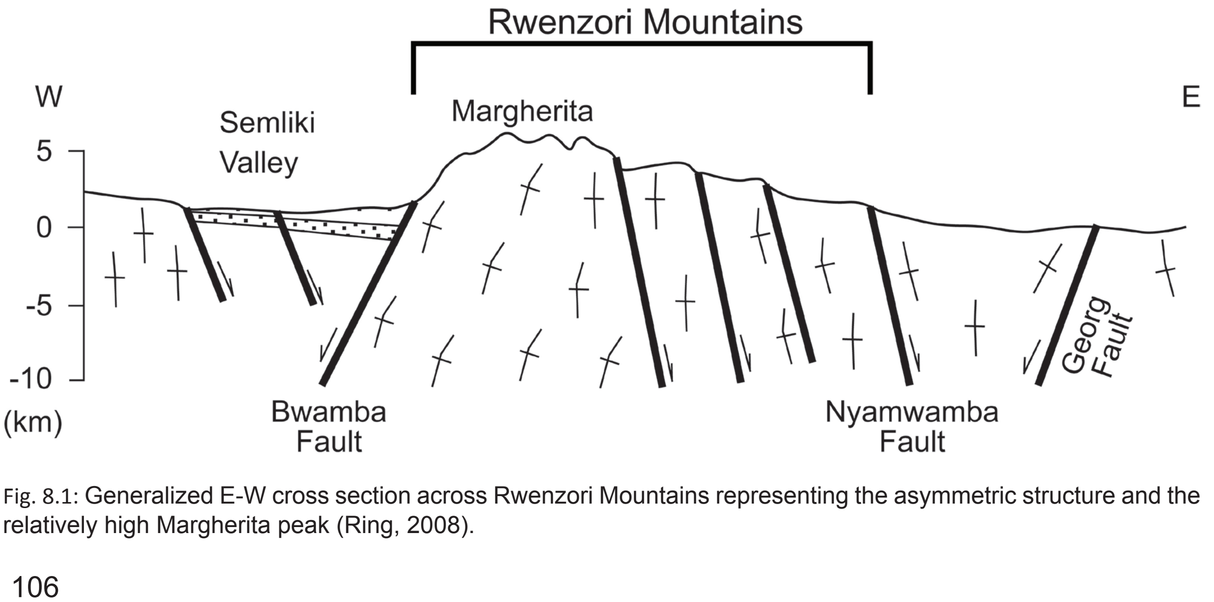

Fig. 8.1: Generalized E-W cross section across Rwenzori Mountains representing the asymmetric structure and the relatively high Margherita peak (Ring, 2008).

additional ≤2 km of corresponding rock uplift to the western flank of the Rwenzoris central block to produce the pronounced elevations. The Pliocene exhumation event caused splitting of the palaeo-Lake Obweruka, changes the drainage patterns, and in the Rwenzoris it caused tilting, asymmetric geometry and high glaciated peaks in the central block. The sum of the rock uplift produced by these two successive uplifting events is sufficient to produce the Rwenzori elevations.

The Albertine rift is an active type with a mantle plume effect which produced a mechanism for thermal doming creating the accompanied highly elevated rift flanks (Fig. 8.2). Whereas, the Rwenzoris block was captured between two propagated rift segments. Numerical models refers to either branches the rift around the mechanically strong Archean block following the less resistant Proterozoic belts (Koehn et al., 2010; Fig. 8.3) and/or propagating with an offset of ≥5 times than the thickness of the crust's brittle layer (Allken et al., 2012; Fig. 8.4).

8.1.2 THE SAMRA MOUNTAIN AREA

The ZFT ages represent two spatially separated age groups of 651.9 (24.9) Ma and 426.2 (31.2) Ma, while the AFT ages represent three spatially separated age groups of 473.1 (9.9) Ma, 269.1 (29.4) Ma, and 101.1 (11.5) Ma. These ages refer to concurrent cooling/exhumation events with a non-uniform pattern of exhumation.

The obtained cooling ages and thermal history modelling provide a record for the cooling/exhumation history in the eastern flank of the Gulf of Suez from the Neoproterozoic till the Oligocene-Miocene. Consequently 5 rapid cooling/exhumation events were presented.

The first cooling/exhumation event, is addressed by the ZFT ages and the t-T modelling, occurred in Neoproterozoic time (775-640 Ma) with an average cooling rate of ~3.66 (1.57) ˚C/Ma, exhumation rate of ~0.092 (0.04) km/Ma and a corresponding rock uplift of ~ 5.8 (0.1) km (Table 6-4; Figs. 6.5). This exhumation event is related to the accretion and plutonism during the

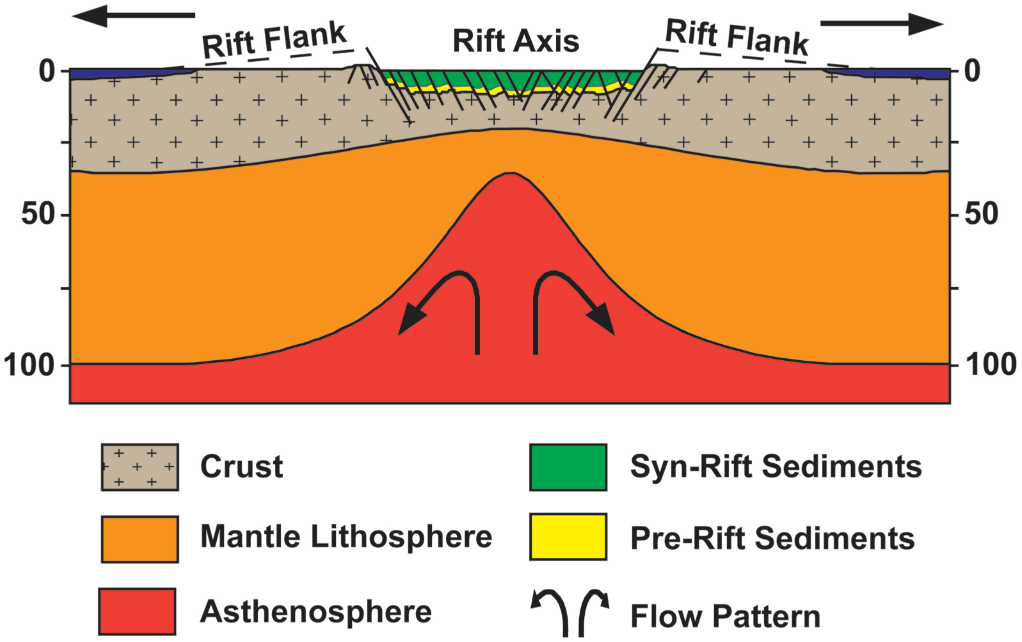

Fig. 8.2: Model for rift initiation associated with mantle plume (Ziegler and Cloetingh, 2004). This model represents the possibility of thermal doming and rift flanks uplift as response to the plume intrusion

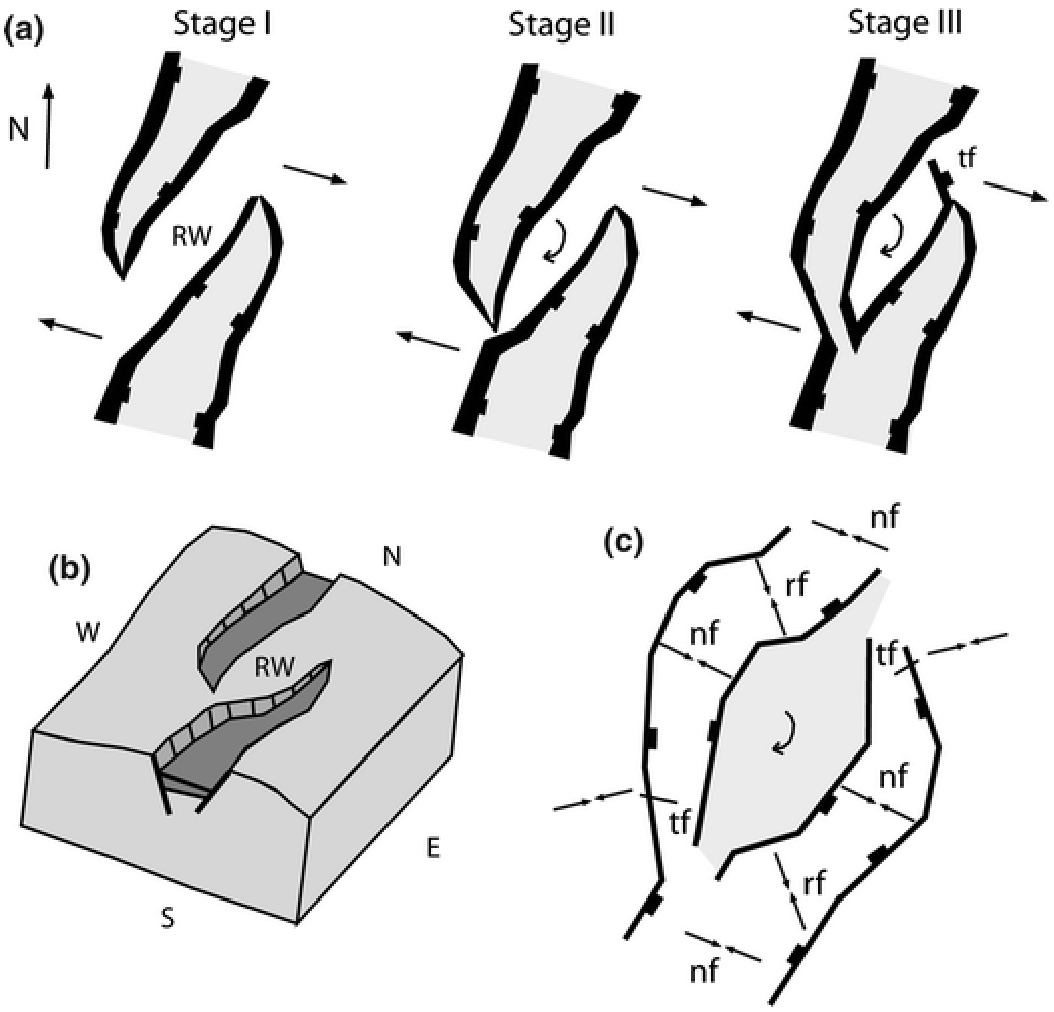

Fig. 8.3: (a) Evolution model for the Rwenzori Mountain region capturing between two propagated rift segments (Koehn et al., 2010). Stage I initial development, stage II block rotation, stage III capturing and detachment. tf = currently active transsection fault (Kisomoro fault). (b) Block diagram of stage II of the rift evolution. (c) Orientation of major faults nf = normal rift faults perpendicular to far-field stress, tf = transsection faults that form during block rotation and rf = repelling transsection faults that form during initial rift interaction

late phases of the EAO (Gass 1982, Kröner 1979; Meert, 2003).

The second cooling/exhumation event, is addressed by the ZFT ages and the t-T modelling, occurred in Cambrian-Devonian time (507-457 Ma) with an average cooling rate of ~2.12 (0.71) ˚C/Ma, exhumation rate of ~0.053 (0.02) km/Ma and a corresponding rock uplift of ~5.6 (0.2) km (Table 6-4; Fig. 6.8). This exhumation event formed as a response to the deep erosional event affecting the entire area after the EAO (Fabre, 1988; Said, 1990). It is synchronous with reported cooling ages in other parts of the northern ANS (Bojar et al., 2002; Vermeesch et al., 2009).

The third cooling/exhumation event, is represented by the ZFT, AFT ages, and the t-T modelling, took place during the Carboniferous-Permian (390-230 Ma) with an average cooling rate of ~1.62 (1.02) ˚C/Ma, exhumation rate of ~0.04 (0.03) km/Ma and a corresponding rock uplift of ~4.2 (1.6) km (Table 6-4; Fig. 6.8). This exhumation event was caused by the Hercynian tectonic event (Devonian-Carboniferous) which caused uplifts in Sinai during the Late Carboniferous (Gvirtzman and Weissbrod, 1985; Klitzsch,

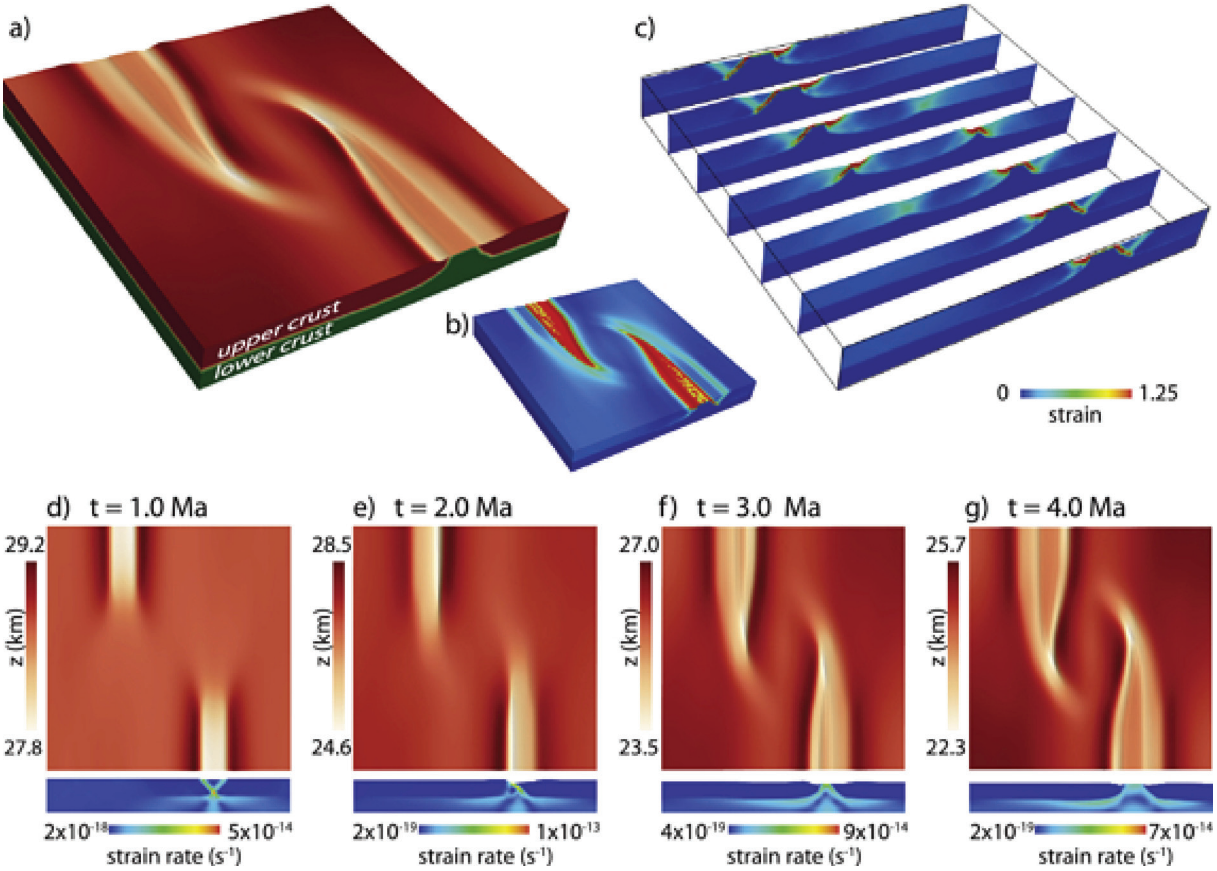

Fig. 8.4: Evolution of model with offset by D = 5 h and the brittle-ductile coupling is weak (Allken et al., 2012). 3D view of deformed domain after 4 Ma of extension, showing (a) free surface elevation superimposed on the frictional-plastic upper crust (red) and viscous lower crust (green), (b) strain and (c) cross-sections of the strain. (d–g) Top view of elevation, juxtaposed with side view of cross-section of strain rate after 1 Ma, 2 Ma, 3 Ma and 4 Ma.

1986; Bojar et al., 2002). This event is synchronous with other reported cooling ages in northern the ANS (Kohn and Eyal, 1981; Omer et al., 1989; Kohn et al., 1992; Kohn et al., 1997; Vermeesch et al., 2009; Feinstein et al., 2013).

The fourth cooling/exhumation event, is represented by the AFT ages and the t-T modelling, took place during the Jurassic-Cretaceous (170-70 Ma) with an average cooling rate of ~1.84 (0.67) ˚C/Ma, exhumation rate of ~0.046 (0.02) km/Ma and a corresponding rock uplift of ~2.9 (0.5) km (Table 6-4; Fig. 6.8). This event is concurrent with the Gondwana breakup and/or the Mid-Atlantic opening (Jurassic-Cretaceous) causing uplift of the Syrian Arc domal system in the whole region (Said, 1962; Dewey et al. 1973; Awad, 1984; Sestini, 1984; Girdler, 1985; Greiling et al., 1988). This event is synchronous with reported cooling ages in northern the ANS (Kohn and Eyal, 1981; Omer et al., 1987; Omer et al., 1989; Kohn et al., 1997; Vermeesch et al., 2009; Feinstein et al., 2013).

The fifth cooling/exhumation event, is represented by t-T modelling, took place during the Oligocene-Miocene (27-22 Ma) with an average cooling rate of ~2.07 (0.47) ˚C/Ma, exhumation rate of ~0.052 (0.012) km/Ma and a corresponding rock uplift of ~1.3 (0.3) km (Table 6-4; Fig. 6.8). This exhumation event represents the rift flanks uplift associated with the Red Sea/Gulf of Suez opening during Oligocene-Miocene time. This event is synchronous with reported cooling ages in northern the ANS (Kohn and Eyal, 1981; Omer et al., 1987; Omer et al., 1989; Kohn et al., 1997; Feinstein et al., 2013).

The Samra Mountain area is characterized by non-uniform uplift between fault bounded blocks during its whole history except for the last event that accompanied the rift flanks uplift of the Gulf of Suez. The t-T models of the different age groups (Fig. 6.1; Fig. 6.5; Fig. 6.6; Fig. 6.7) show differential responses to the different tectonic events. Group A samples (Fig. 6.1) were affected only by the EAO and the Gulf of Suez events. Groups B samples were affected by the post EAO erosion, the Hercynian, and the Gulf of Suez events. Group C samples were affected by Gondwana breakup and the Gulf of Suez events. These differential exhumations must have been controlled by differential movement between fault-bounded blocks or development of fold systems. Each age group region has experienced a reheating event between the first cooling/exhumation event and the Gulf of Suez event. This reheating event was most probably caused by burden under a column of a sedimentary succession. The group A as well as samples B1 and Z2 from group B show reversing in the cooling trend to reheating, starting between the Neoproterozoic and the Ordovician with an average cooling rate of -0.04 (0.003) ˚C/Ma, exhumation rate of -0.001 km/Ma and a corresponding rock subsidence of ~0.6 (0.1) km (Table 6-4; Figs. 6.6) under the sediment of the post-EAO erosional event. The rest of group B samples show reversing in the cooling trend to reheating, starting between Ordovician and Triassic times with an average cooling rate of -0.09 (0.02) ˚C/Ma, exhumation rate of -0.002 km/Ma and a corresponding rock subsidence of ~0.7 (0.2) km (Table 6-4; Figs. 6.8) under the lower Paleozoic succession which was eventually eroded (2-2.5 km thickness was preserved in south Jordan and Saudi Arabia; Kohn et al., 1992). While, the group C samples show reversing in the cooling trend to reheating, starting between Jurassic and Cretaceous times with an average cooling rate of -0.18 (0.1) ˚C/Ma, exhumation rate of -0.004 km/Ma and a corresponding rock subsidence of ~0.4 (0.1) km (Table 6-4; Figs. 6.8) under the a Mesozoic succession which was eventually eroded from the area of study except a 551 m thick unit in the end of Wadi Baba (Said, 1962; Kerdany and Cherif, 1990).

The studied area was affected by more or less equal thermal overprinting during the development of the Gulf of Suez. This was accompanied by synchronous uplifting from depths equivalent to temperature zones between 80 and 90 ºC to their present elevations. That is correspondent to 60 and 70 ºC above present surface temperature and equivalent to ~1.5 to ~1.75 km depth. Moreover, increasing the heat flow southward is not only associated with increasing the tectonic uplift but also with increasing extension and getting closer to the combination of the thermo-tectonic effect of the Red Sea and the Gulf of Aqaba along with the Gulf of Suez.

The Gulf of Suez is a pure-shear dominated rifting (Fig. 8.5) for many reasons namely; 1) the accompanied low to moderate thermal regime which did not exceed 90 ºC. 2) The absence of any considerable concurrent magmatic activity. 3) presence of the characteristic "steer's head" configuration of the syn- and post-rift sediments (Ziegler, 1990). 4) Accompanied by low elevated rift flanks. 5) Higher elevations and stripping of the basement southward with increasing the thermo-tectonic effect of the Red Sea and Gulf of Aqaba (Fig. 3.2). 6) More than 2000 Km away from the corresponding mantle plume (Afar plume).

Interestingly, all the Neoproterozoic uplifted samples (region A) are from large plutons overlain by lower Paleozoic sediments. While, the Carboniferous-Permian exhumed

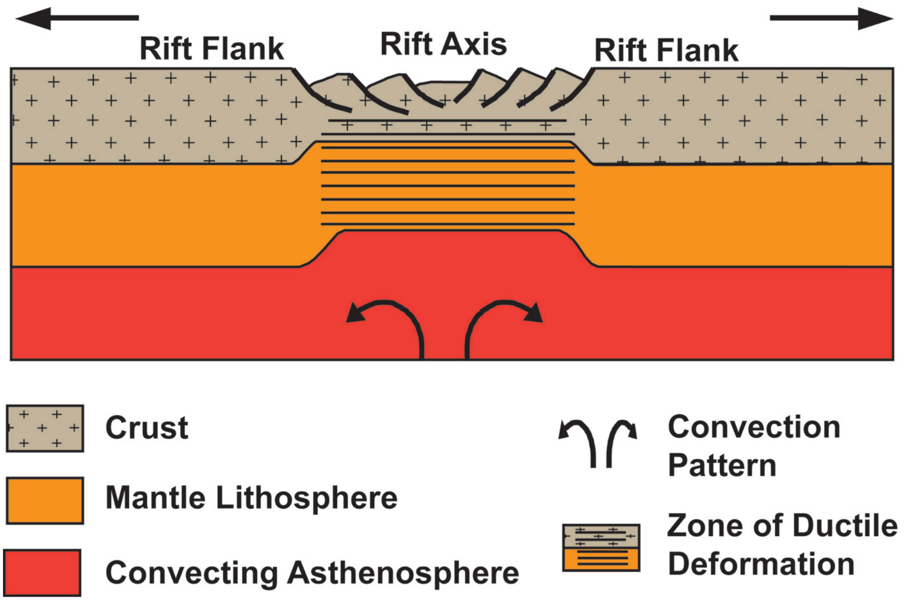

Fig. 8.5: Model for Pure-Shear rift initiation of McKenzie (1978) (Ziegler and Cloetingh, 2004). The rifting initiate by combination of convecting asthenosphere on the base of the lithosphere, deviatoric tensional stresses developing over mantle upwellings and far-field stresses related to plate boundary processes.

samples (region B) are farther from the lower Paleozoic sediments and were collected from smaller plutons which intrude into older plutons and are intruded by dikes. The samples exhumed during the Jurassic-Cretaceous (group C) are far from the lower Paleozoic sediments and were collected from the smallest plutons in the study area (Fig. 6.1). It is questionable, if the difference in pluton dimensions and distance from the lower Paleozoic sediment found in the study area as separated three age regions A, B, and C is a general case in the ANS and Sinai or not.

8.1.3 FUERTEVENTURA ISLAND

The ZFT cooling ages ranging between 20.1 (1.3) and 19.6 (1.1) Ma. While, the AFT cooling age ranging between 20.5 (2.4) and 12.5 (4.1) Ma. These ages specify concurrent cooling/exhumation events. The Lower Cretaceous sedimentary rocks have passed through the ZFT closure temperature (~240 ˚C) at around ~50 Ma with a cooling rate of ~1.5–3 ˚C/Ma which continued until ~20-18 Ma (Wipf et al., 2010). This age would document for the seamount stage in Fuerteventura.

By ~20 Ma all the modelled samples, show a sudden cooling/exhumation event which continued until ~15 Ma (Fig. 7.5; Fig. 7.6). This cooling/exhumation event has uplifted the area of study to depths equivalent to an average temperature of ~100 ˚C with an average cooling rate of ~39.06 (3.45) ˚C/Ma and exhumation rate of ~1.395 (0.123) km/Ma, adding a ~2.7 (0.5) km of rocks to the column of strata (Table 7-4; Fig. 7.7). Adding such huge magmatic materials to the volcanic edifice along with the major climatic changes during the MMCO would be the main reason for volcanic flank destabilization triggering the giant landslide at ≤20 Ma along the western side of the island. After this huge mass wasting, the lowland surface of the central depression of the island has extended westward to the sea.

Afterwards, a slow cooling/exhumation event dominated from ~15 Ma to ~10-~5 Ma (average ~14 Ma; Table 5-4; Fig. 5.5; Fig. 5.6) with an average cooling rate of ~2.27 (0.60) ˚C/Ma and exhumation rate of ~0.081 (0.021) km/Ma and ~0.8 (0.2) km of corresponding rock uplift.

At that time (average ~6.7 Ma; Table 7-4) a second rapid cooling/exhumation event occurred with an average cooling rate of ~16.0 (5.39) ˚C/Ma and exhumation rate of ~0.571 (0.192) km/Ma (Fig. 7.7) causing ~2.3 (0.2) km of corresponding rock uplift. Such uplifting documents the onset of the doming stage along the western side of Fuerteventura at ~6.7 Ma.

Finally, a slower cooling/exhumation phase occurred (average ~2.3 Ma; Table 7-4) with an average cooling rate of ~0.61 (0.58) ˚C/Ma and exhumation rate of ~0.022 (0.21) km/Ma causing ~0.1 (0.1) km of corresponding rock uplift. Synchronously, the western domes have been exposed to an intense erosion that executed their peaks and reduced the elevations to nowadays surfaces.

8.1.4 LA GOMERA ISLAND

The ZFT cooling ages range between 10.3 (0.5) and 8.3 (0.7) Ma. While, the AFT cooling ages range between 12.9 (3.1) and 4.8 (0.7) Ma. These ages refer to concurrent cooling/exhumation events.

The t-T models shows an early start for sample Lag-1 (pillow lava) from the pre-shield stage with older formation ages (Fig. 7.12). The pre-AFT age part of the thermal history suggest that the rock has cooled/exhumed rapidly since ~15 Ma or later with a cooling rate of ~18.75 ˚C/Ma (Fig. 7.13).

From ~10 Ma all the samples indicate a rapid cooling/exhumation event with an average cooling rate of ~30.82 (7.97) ˚C/Ma and exhumation rate of ~1.101 (0.285) km/Ma, adding a ~2.7 (0.2) km of rocks to the column of strata (Table 7-8; Fig. 7.13). Adding these magmatic material to the volcanic edifice in combination with the major climatic changes during the MMCO would be the main reasons for volcanic flank failure, and have triggered the giant landslide at ~10 Ma along the northwestern sector of the island.

Hereafter, a slower cooling/exhumation event was dominated, starting ~7.5 Ma to ~4 Ma with an average cooling rate of ~2.5 (1.65) ˚C/Ma and exhumation rate of ~0.09 (0.059) km/Ma causing ~0.4 km of corresponding rock uplift (Table 7-8; Fig. 7.13).

Afterwards, a short cooling/exhumation event affected only the southern samples (Lag-3 and Lag-4; Fig. 7.8) since ~4 Ma to ~2.5 Ma, with an average cooling rate of ~57.5 (10.61) ˚C/Ma and exhumation rate of ~2.054 (0.378) km/Ma (Fig. 7.13) causing ~2 (0.4) km of corresponding rock uplift. That event documents the shifting of the magmatic activity on the island southward at ~4 Ma.

Then, a cooling/exhumation phase in almost a steady state was dominant since ~3 (0.5) Ma till now with an average cooling rate of ~2.17 (0.23) ˚C/Ma and exhumation rate of ~0.056 (0.038) km/Ma producing ~0.2 km of corresponding rock uplift (Table 7-8; Fig. 7.13). Concurrently with an intense erosion that removed the peaks and reduced the elevations to nowadays surfaces.

In general, comparing and reconstructing the tectonic history of volcanic islands (Fuerteventura and La Gomera) which resulted from mantle plume interaction with passive margin revealed a relatively short cycle of life. That cycle started by emerging, followed by formation of the shield stage with adding a huge amount of magmatic materials forming a highly topographic island (Fuerteventura; ~20 Ma, La Gomera; ~10 Ma). Afterwards, the topography destruction starts with landsliding (Fuerteventura; ≤20 Ma, La Gomera; ~7 Ma) when suitable topographic and climatic conditions, among others, were dominated. Then the volcanic island experience other cycle, starting with constructing high topography by feeding with new magmatic materials till the hot spot related magmatic activities transfer to other regions forming another volcanic island. Duggen et al. (2009) referred to a lateral movement of the Canary plume materials through the continental lithospheric mantle beneath northwest Africa to west the Mediterranean Sea. That plume material travel has produced a track of intraplate volcanism through its course (Fig. 8.6).

8.2 COMPARISON WITHIN THE FRAMEWORK OF THERMOCHRONOLOGY

Comparing the landscaping behaviour as a response to different endogenic and exogenic processes of topographic changes in different geologic environments using LTT techniques was constructive. It has led to dating and quantifying major tectonic events such as orogenic belt, construction of a volcanic island, rifting, and rift flanks uplift as well as surface processes such as landslide, erosion, climatic effect and even sedimentation as addressed earlier. Moreover, the pre-

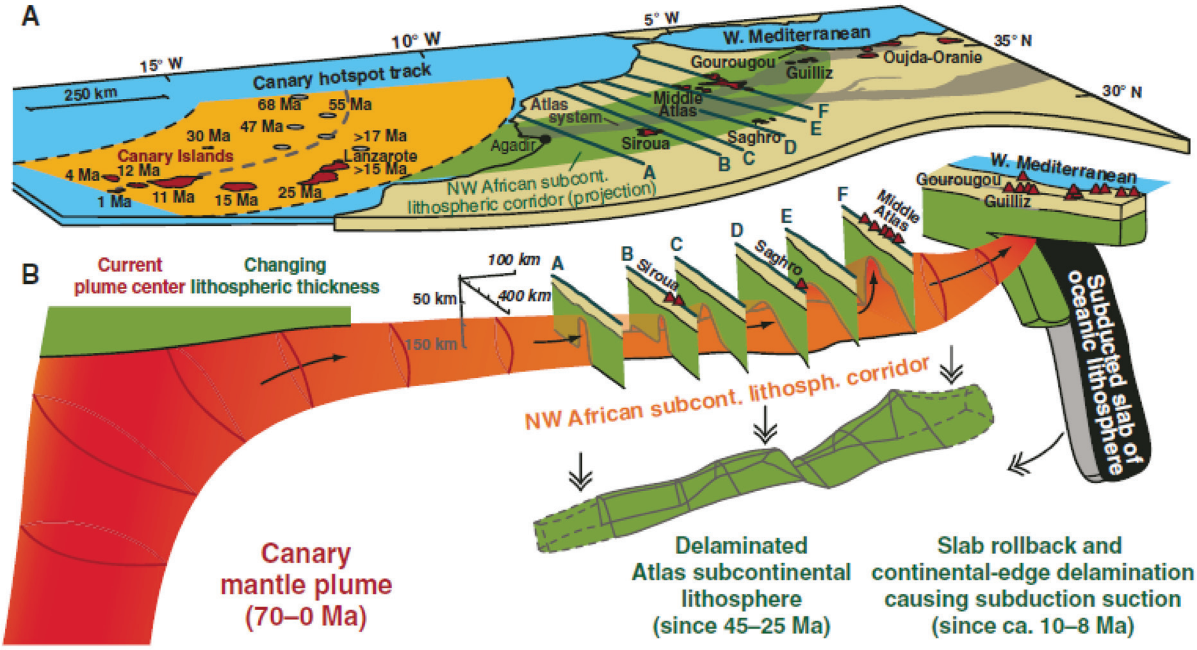

Fig. 8.6: (A) Map of the northwest African plate (B) and flow of Canary mantle plume material under northwest Africa through a subcontinental lithospheric corridor in a three-dimensional model (Duggen et al., 2009). A: The orange area displays the Canary hotspot track on the oceanic side of the northwest African plate with ages of the oldest lavas from each island (red areas) or seamount (gray circles), indicating a southwest-directed age progression and the location of the current plume center beneath the western Canary Islands (Geldmacher et al., 2005). Also shown are the Atlas Mountains (gray field), location of the northwest African subcontinental lithospheric corridor in green, inferred from profiles (A–F) based on geophysical data (Urchulutegui et al., 2006; Missenard et al., 2006; Teixell et al., 2005), and northwest African Neogene continental intraplate volcanic fields. B: The three-dimensional model illustrates how Canary mantle plume material flows along the base of the oceanic lithosphere that thins to the east (Neumann et al., 1995) and into the subcontinental lithospheric corridor beneath the Atlas system, reaching the western Mediterranean. Plume push, eastward-thinning lithosphere, delamination of northwest African subcontinental lithosphere, and subduction suction related to rollback of the subducting slab in the Mediterranean are proposed to be the main mechanisms for causing Canary plume material to flow 1500 km to the northeast.

ceding and the following thermo-tectonic history to these major landscaping processes could also be reconstructed.

8.2.1 RIFTS AND RIFT FLANKS

The rifted areas in old cratons usually have a long cycle of life which could be traced thermochronologically in both the Rwenzori Mountains and the Samra Mountain areas. During this long life, non-uniform uplift through fault-bounded blocks was the dominant mechanism of response to all the induced far-field continental scale tectonics and/or surface processes. Only a uniform uplift was demonstrative as a response to the rift flanks uplifting event.

The thermochronological record of the Samra area has started with the EAO plutonism and accretion. Afterwards, both areas (the Rwenzoris and the Samra) were affected by the post orogenic erosional event. Hereafter, each area of was affected differently by a series of far-field tectonic events that occurred nearby or at the closest plate boundary as well as by exogenic (deep erosion) events. Then, the rift started activation affecting the whole areas with corresponding flanks uplift. Afterwards, the Gulf of Suez was nearly deactivated by the movement along the Dead Sea transform fault in the Middle-Miocene. While, the movement along the footwall of Bwamba fault caused additional uplift to the Rwenzoris in the Pliocene.

8.2.2 VOLCANIC ISLAND

Volcanic islands on a passive margin have a relatively short cycle of life which could be traced thermochronologically on both Fuerteventura and La Gomera. The only difference between the two islands is the onset timing of the hot spot related magmatic activity. That was represented by the ZFT ages of ~20 Ma for Fuerteventura outcrops and of ~10 Ma for La Gomera outcrops. Afterwards, a huge amount of magmatic materials were supplied during the shield stage either due to plutonic emplacements or volcanic ruptures to construct a highly topographic volcanic island. At some point when suitable conditions of high elevations and climatic conditions (among other factors) were achieved, destruction of such high topography begins with landsliding. That landsliding occurred in Fuerteventura ≤20 myr ago and in La Gomera ~7 Myr ago and reduced their topography significantly. Then, the volcanic island may experiences other cycles starting with the construction of a high topography from new magmatic materials unless the hot spot related magmatic activities transfer to another region to form another volcanic island.

9

CONCLUSIONS

CONTENTS

9.1 CONCLUSIONS

In this study the landscape evolution of key areas in the African continent was investigated using LTT techniques. Specifically, examining the temporal topographic changes, investigating the ability of LTT in dating different temporal landscape events, and reconstructing and comparing the thermo-tectonic histories of the studied areas.

9.1.1 The first objective

The first objective related to the topographic changes and the ability of the LTT to detect, differentiate, and quantify the producing processes;

- From a thermochronological point of view, the landscaping does not perform differently as a response to nature of the producing event either endogenic or exogenic. For example, a vertical cooling trend in a t-T model could be formed as a response to an endogenic (tectonic) event as in adding new plutonic materials in Fuerteventura and La Gomera or the EAO and the Hercynian in the Samra area or it could be as response to an exogenic (surface) event as in the landsliding event in Fuerteventura and La Gomera or deep erosional event as in the post orogenic erosional events in the Rwenzoris and the Samra areas.
- The LTT techniques can detect rapid exogenic events namely; landslide events in Fuerteventura and La Gomera as well as the post orogenic erosional events in the Rwenzoris and the Samra areas.
- The landscape changes differently in a continental rift than in a volcanic island; the rifted regions have fast pulses of topographic changes separated by long intervals of relative thermo-tectonic stability On the other hand, the volcanic islands show a continuous cycle of topographic change till the hotspot related activity shift away.

9.1.2 The second objective

The second objective related to reconstructing and comparing of the thermo-tectonic histories of the studied areas;

- There is neither difference in the tectonic nor the erosional history between Fuerteventura and La Gomera; Fuerteventura has experienced two rapid cooling/exhumation events; one has started ~20 Ma with ~2.7 (0.5) km of corresponding rock uplift that caused the onset of the Fuerteventura landslide. The other has been initiated ~7 Ma with ~2.3 (0.2) km of corresponding rock uplift forming the doming stage on the western part of Fuerteventura island ~5 Ma. Finally, these domes were eroded to nowadays surfaces. La Gomera also has experienced two rapid cooling/exhumation events; the first event has started between ~10 and 7 Ma with corresponding ~2.7 (0.2) km of rock uplift causing the onset of the La Gomera landslide. The second rapid cooling event occurred by ~4 Ma resulting in ~2 km of rock uplift. Finally, this topography was eroded to reduce elevation to nowadays surfaces.
- The exceptional high Rwenzori Mountains were constructed in the EARS extensional regime as a rift flank within two stages; the first was during the Eocene-Miocene exhumation events, causing 3 (1) km of rock uplift, the second was during the Pliocene by exhumation of the footwall of the Bwamba fault causing ≤ 2 km of rock uplift.
- The Rwenzoris nature of uplifted as a non-uniform exhumation through fault-bounded blocks. While, the additional uplift through the footwall of the Bwamba fault caused tilt uplifting in the western flank of the mountains.
- The AFT and AHe cooling ages of the low elevated samples dated for the Albertine rift initiation. While, no cooling ages were revealed to date the Gulf of Suez opening due to the associated low elevated flanks but it was dated through the t-T models.

- The rift initiation did not overprint the previous events of topographic change from the thermochronological history. They were reconstructed namely; From Rwenzori Mountains 3 rapid cooling/exhumation events were quantified before the rifting event. 1) the Silurian-Devonian (420-390 Ma) event associated with ~3.5 (1.5) km of rock uplift as response to the post Pan-African orogeny deep erosional event. 2) The Triassic (240-220 Ma) event that caused ~3.0 km of rock uplift associated with rapid cooling and a major erosional event at the end of the Karoo sedimentary regime. 3) The Eocene-Miocene (52-10 Ma) event resulted in an average rock uplift of ~3.0 (0.2) km, the Early Eocene tectonic events were associated with India drifting afterwards the Eastern Rift activity was started.

While, from the Samra Mountain area 4 rapid cooling/exhumation events were quantified before the rifting event. 1) The Neoproterozoic (775-640 Ma) event caused ~5.8 (0.1) km of rock uplift as a response to the accretion and plutonism during the EAO. 2) The Cambrian-Devonian (507-457 Ma) event causing ~5.6 (0.2) km of rock uplift as response to the post-EAO erosional event. 3) The Carboniferous-Permian (390-230 Ma) event resulted in ~4.2 (1.6) km of rock uplift as response to the Hercynian tectonic event. 4) The Jurassic-Cretaceous (170-70 Ma) event resulted in ~2.9 (0.5) km of rock uplift as a response to the Gondwana breakup. Additional reheating event was reported in the time span extending between the uplift associated with the Gulf of Suez and the prior cooling event. This reheating event is associated with an average subsidence of ~0.6 (0.3) km under the weight of synchronous sedimentary succession.

- The Gulf of Suez flanks did not reach elevations higher than 1.3 (0.3) km in the studied area, although they have reached high elevations (>5 km) during the successive events prior to the Gulf of Suez formation.

- The Albertine rift flanks uplift is double the Gulf of Suez related flanks uplift which suggests an additional heat component during the Albertine rift formation.

9.2 FURTHER RESEARCH

- Detailed thermochronological studies, accompanied with careful geological survey are necessary on the ANS to test the relationship between pluton dimensions, distance from the lower Paleozoic sediment, and their exhumation history.
- Statistical studies on the connection between the rift flanks uplift and their distance from the corresponding mantle plume.
- Further research is required on landslides with known ages to verify the ability of LTT techniques to date landslides which was established during this study.

10

REFERENCES

Aanyu, K., 2011. Implications of Regional Fault Distribution and Kinematics for the Uplift of Rift Flanks Around the Rwenzori Mountains, South western Uganda. Thesis Johannes Gutenberg University, Mainz.

Aanyu, K., Koehn, D., 2011. Influence of pre-existing fabrics on fault kinematics and rift geometry of interacting segments: analogue models based on the Albertine Rift (Uganda), Western Branch-East African Rift System. Journal of African Earth Sciences 59 (2–3), 168–184. http://dx.doi.org/10.1016/j.jafrearsci.2010.10.003.

Abdel Monen, A., Watkins, N.D., Gast, P.W., 1971. Potassium-argon ages, volcanic stratigraphy, and geomagnetic polarity history of the Canary Islands: Lanzarote, Fuerteventura, Gran Canaria and La Gomera. American Journal of Science 271, 490–521.

Abeinomugisha, D., Mugisha, F., 2004. Structural Analysis of the Albertine graben, Western Uganda, Abstract, East African Rift System Evolution, Resources, and Environment Conference, Addis Ababa (June 2004).

Abu El-Rus, M.A., Neumann, E.R., Peters, V., 2006. Serpentinization and dehydration in the upper mantle beneath Fuerteventura (eastern Canary Islands): evidence from mantle xenoliths. Lithos 89, 24–46.

Afra, B., Lang, M., Rodriguez, M.D., Zhang, J., Giulian, R., Kirby, N., Ewing, R.C., Trautmann, C., 2011. Annealing kinetics of latent particle tracks in Durango apatite. Physical Review B 83, 064116. DOI: 10.1103/PhysRevB.83.064116

Ahnert, F., 2003. Einführung in die Geomorphologie. Ulmer, Stuttgart

Albaric, J., Déverchère, J., Petit, C., Perrot, J., Le Gall, B., 2009. Crustal rheology and depth distribution of earthquakes: insights from the central and southern East African Rift System. Tectonophysics 468, 28–41.

Albrecht, D., Armbruster, P., Spohr, R., 1985. Investigation of Heavy Ion Produced Defect Structures in Insulators by Small Angle Scattering. Applied Physics A 37, 37-46.

Albinger, M., 2010. Lithostratigraphische und strukturelle Entwicklung sowie Exhumierungsgeschite von Fuerteventura, Kanarische Inseln, Spanien. Master Thesis Institute of Earth Sciences, University of Heidelberg, p., 111.

Ali, B.H., Wilde, S.A., Gabr, M.M.A., 2008. Granitoid evolution in Sinai, Egypt, based on precise SHRIMP U-Pb zircon geochronology. Gondwana Research 284, 11 pp.

Allen, P.A., Allen, J.R., 2005. Basin Analysis: Principles and Applications. Blackwell Publishing, Incorporated, Oxford OX4 1JF, United Kingdom, 2nd edition edition. ISBN 0-632-05207-4.

Allibon J., Bussy F., Lewin É., Darbellay B., 2011. The tectonically controlled emplacement of a vertically sheeted gabbro-pyroxenite intrusion: Feeder-zone of an ocean-island volcano (Fuerteventura, Canary Islands). Tectonophysics 500 (1–4), 78-97.

Allken, V., Huismans, R.S., Thieulot, C., 2012. Factors controlling the mode of rift interaction in brittle-ductile coupled systems: A 3D numerical study. Geochemistry, Geophysics, Geosystems 13, 1525-2027.

Ancochea, E., Brändle, J.L., Cubas, C.R.,Hernán, F.,Huertas, M.J., 1996. Volcanic complexes in the eastern ridge of the Canary Islands: the Miocene activity of the Island of Fuerteventura. Journal of Volcanology and Geothermal Research 70, 183–204.

Ancochea, E., Fuster, J.M., Ibarrola, E., Cendrero, A., Coella, J., Hernan, F., Cantagrel, J.M., Jamond, C., 1990. Volcanic evolution of the island of Tenerife (Canary Islands) in the light of new K–Ar data. Journal of Volcanology and Geothermal Research 44, 231–249.

Ancochea, E., Hernan, F., Cendrero, A., Cantagrel, J.M., Fuster, J.M., Ibarrola, E., Coella, J., 1994. Constructive and destructive episodes in the building of a young Oceanic Island, La Palma, Canary Islands, and the genesis of the Caldera de Taburiente. Journal of Volcanology and Geothermal Research 60, 243–262.

Ancochea, E., Hernán, F., Huertas, M.J., Brändle, J.L., Herrera, R., 2006. A new chronostratigraphical and evolutionary model for La Gomera: implications for the overall evolution of the Canarian Archipelago. Journal of Volcanology and Geothermal Research 157, 271–293.

Anguita, F., Hernán, F., 1975. A propagating fracture model versus a hotspot origin for the Canary Islands. Earth and Planetary Science Letters 27, 11–19.

Appel, P., Schenk, V., Schumann, A., 2005. P-T path and metamorphic ages of peliticschists at Murchison Falls, NW Uganda: evidence for a Pan-African tectonometamorphic event in the Congo Craton. European Journal of Mineralogy 17, 655–664.

Araña, V., Ortis, R., 1991. The Canary Islands: tectonics, magmatism and geodynamic framework. In: Kampunzu, A.B., Lubala, R.T. (Eds.), Magmatism in Extensional Structural Settings (The Phanerozoic African Plate). Springer, Barcelona, pp. 209–249.

Awad, G. M., 1984. Habitat of oil in Abu Gharadiq and Faiyum basins, Western Desert, Egypt: AAPG Bull., v. 68, p. 564-573.

Badawy, A., Horváth, F., 1999. The Sinai subplate and tectonic evolution of the northern
Bahat, D., Mohr, P., 1987. Horst faulting in continental rifts. Tectonophysics 141, 61–73.

Baker, B., Wohlenberg, G., 1971. Structure and evolution of the Kenya rift valley. Nature 229, 538–542.

Balogh, K., Ahijado, A., Casillas, R., Fernández, C., 1999. Contributions to the chronology of the Basal Complex of Fuerteventura, Canary Islands. Journal of Volcanology and Geothermal Research 90, 81-101.

Bar, M., Kolodny, Y., Bentor, Y.K., 1974. Dating faults by fission track dating of epidotes- an attempt. Earth and Planetary Science Letters 22, 157-162.

Barbarand, J., Carter, A., Wood, I.G., Hurford, A.J., 2003. Compositional and structural control of fission-track annealing in apatite. Chemical Geology 198, 107-137.

Barker, D.S., Nixon, P.H., 1989.High-Ca, low-alkali carbonatite volcanism at Fort Portal, Uganda. Contributions to Mineralogy and Petrology 103, 166–177.

Bastow, I., Stuart, G., Kendall, J., Ebinger, C., 2005. Upper-mantle seismic structure in a region of incipient continental breakup: northern Ethiopian rift. Geophysical Journal International 162, 479–493.

Batt, G.E., Brandon, M.T., 2002. Lateral thinking: 2-D interpretation of thermochronology in convergent orogenic settings. Tectonophysics 349 (1–4), 185–201.

Bauer, F.U., Glasmacher, U.A., Ring, U., Grobe, R. W., Mambo, V. S., Starz, M., 2015. Long-term cooling history of the Albertine Rift: new evidence from the western rift shoulder, D.R. Congo. International Journal of Earth Science (GeolRundsch), DOI:10.1007/s00531-015-1146-6

Bauer, F.U., Glasmacher, U.A., Ring, U., Karl, M., Schumann, A., Nagudi, B., 2013. Tracing the exhumation history of the Rwenzori Mountains, Albertine Rift, Uganda, using low-temperature thermochronology. Tectonophysics 599, 8–28.

Bauer, F.U., Glasmacher, U.A., Ring, U., Schumann, A., Nagudi, B., 2010b. Thermal and exhumation history of the central Rwenzori Mountains, Western Rift of the East African Rift System, Uganda. International Journal of Earth Sciences 99, 1575–1597. http://dx.doi.org/10.1007/s00531-010-0549-7

Bauer, F.U., Karl, M., Glasmacher, U.A., Nagudi, B., Schumann, A., Mroszewski, L., 2012. The Rwenzori Mountains of western Uganda-an approach to unravel the evolution of a remarkable morphological feature within the Albertine Rift. Journal of African Earth Sciences 73–74, 44–56.

Beaumont, C., Fullsack, P., Hamilton, J., 1992. Erosional control of active compressional orogens, in Thrust Tectonics, edited by K.R. McClay, pp. 1-18, Chapman and Hall, New York.

Benoit, M., Nyblade, A., VanDecar, J., 2006. Upper mantle P-wave speed variations beneath Ethiopia and the origin of the Afar hotspot. Geology 34, 329–332.

Bentor, Y.K., 1985. The crustal evolution of the Arabian–Nubian massif with special reference to the Sinai Peninsula. Precambrian Research 28, 1–74.

Beyth, M., Stern, R.J., Altherr R., Kröner, A., 1994. The late Precambrian Timna igneous complex, Southern Israel: Evidence for comagmatic-type sanukitoid monzodiorite and alkali granite magma, Lithos 31, 103–124.

Bogaard, P.V.D., Schmincke, H.U., Freundt, A., Hall, C.M., York, D., 1988. Eruption ages and magma supply rates during the Miocene evolution of Gran Canaria. Naturwissenschaften 75, 616–617.

Bojar, A. V., Fritz, H., Kargl, S., Unzog, W., 2002. Phanerozoic tectonothermal history of the Arabian–Nubian shield in the Eastern Desert of Egypt: evidence from fission track and paleostress data. Journal of African Earth Sciences 34, 191–202.

Bon, A., Degay, J.C., Heinry, C., Joubert, M., Lonchampt, D., Moyroud, B., Pigeyre, H., Vyain, R., Pindi, M., Mutombo, M., Pholo, N., Mbenza, T., Chidubo, T., Lufuluabo, Y., 1981. Geologic map of Eastern D. R. Congo with scale 1:500000.

Bosworth, W., Huchon, P., and Mcclay K., 2005. The Red Sea and Gulf of Aden basins. Journal of African Earth Sciences 43, 334-378.

Boven, A., Pasteels, P., Punzalan, L.E., Yamba, T.K., Musisi, J.H., 1998. Quaternary perpotassic magmatism in Uganda (Tore-Ankole Volcanic Province): age assessment and significance for magmatic evolution along the East African Rift. Journal of African Earth Sciences 26 (3), 463–476.

Bradley, G., Carter, A., Taylor, R.G., 2010. Denudation History of Permo-Carboniferous Glacial Strata and Precambrian Basement on the East African Plateau adjacent to the Eastern Flank of the Western Rift.Thermo 2010, 12th International Conference on Thermochronology, Glasgow, 16–20 August, 2010.

Brandt, M., 2013. Middle mantle seismic structure of the African superplume. Pure Applied Geophysics 170, 845–861.

Braun, J., 2002b. Quantifying the effect of recent relief changes on age-elevation relationships. Earth and Planetary Science Letters 200, 331–343.

Braun, J., Robert, X., 2005. Constraints on the rate of post-orogenic erosional decay from thermochronological data: example from the Dabie Shan, China. Earth Surface Processes and Landforms 30, 1203–1225.

Braun, J., van der Beek, P., Valla, P., Robert, X., Herman, F., Glotzbach, C., Pedersen, V., Perry, C., Simon-Labric, T., Prigent, C., 2012. Quantifying rates of landscape evolution and tectonic processes by thermochronology and numerical modeling of crustal heat transport using PECUBE. Tectonophysics 524-525, 1-28.

Bravo, T., 1964. Estudio geológico y petrográfico de la isla de isla de la Gomera I. Estudio geológico. Estudio geológico20, 1–21.

Brown, R., Summerfield, M., Gleadow, A., 1994. Apatite fission track analysis: its potential for the estimation of denudation rates and implications for models of longterm landscape development. In: Kirby, M. (Ed.), Process Models and Theoretical Geomorphology. John Wiley and Sons Ltd, New York, pp. 23–53

Buck, W.R., 1986. Small-scale convection induced by passive rifting: the cause for uplift of rift shoulders. Earth Planet. Sci. Lett., 77: 362-372.

Burke, K., Wilson, J.T., 1972. Is the African plate stationary? Nature 239, 387–390.

Burtner, R.L., Nigrini, A. and Donelick, R.A., 1994. Thermochronology of lower Cretaceous source rocks in the Idaho-Wyoming thrust belt. American Association of Petroleum Geologists Bulletin, 78, 1613–1636.

Camp, V.E., Roobol, M.J., 1992. Upwelling asthenosphere beneath western Arabia and its regional implications. Journal of Geophysical Research 97, 15255–15271.

Cantagrel, J.M., Cendrero, A., Fúster, J.M., Ibarrola, E., Jamond, C., 1984. K–Ar chronology of the volcanic eruption in the Canarian Archipelago: Island of La Gomera. Bulletin of Volcanology 47, 597–609.

Carlson, W.D., Donelick, R.A. and Ketcham, R.A., 1999. Variability of apatite fission-track annealing kinetics: I. Experimental results. American Mineralogist 84, 1213-1223.

Carpenter, B.S., Reimer, G.M., 1974. Standard reference materials calibrated glass standards for fission track use. National Bureau of Standards Special Publication 260-49, 16 pp.

Carracedo, J.C., 1994. The Canary Islands: an example of structural control on the growth of large oceanic-island volcanoes. Journal of Volcanology and Geothermal Research 60, 225–241.

Carracedo, J.C., 1996. A simple model for the genesis of large gravitational landslide hazards in the Canary Islands. In: McGuire, W.J., Jones, A.P., Neuberg, J. (Eds.), Volcano Instability on the Earth and Terrestrial Planets. Geological Society London, Special Publication 110, 125–135.

Carracedo, J.C., Badiola, E.R., Guillou, H., de la Nuez, J., Pérez, Torrado, F.J., 2001. Geology and volcanology of La Palma and El Hierro, Western Canaries. Estudios Geológicos 57 (5-6), 175–273.

Carracedo, J.C., Day, S., Gillou, H., Rodríguez, E., Canas, J.A., Pérez, F.J., 1998. Hotspot volcanism close to a passive continental margin. Geological Magazine 135, 591–604.

Casillas, R., Fernández, C., Colmenero J.R., de la Nuez, J., García-Navarro, E., Martín, M.C., 2010. Deformation structures associated with the Tazo landslide (La Gomera, Canary Islands). Bulletin of Volcanology. DOI 10.1007/s00445-010-0373-8

Casillas, R., Fernández, C., De la Nuez, J., García Navarro, E., Colmenero, JR., Martín, MC., 2008b. Deformaciones asociadas al deslizamiento gravitacional de flanco del Edificio Antiguo Inferior en Tazo (La Gomera). Geotemas 10, 1269–1272.

Casillas, R., Nagy, G., Demény, A., Ahijado, A., Fernández, C., 2008a. Cuspidine-niocalite-baghdadite solid solutions in the metacarbonatites of the Basal Complex of Fuerteventura (Canary Islands). Lithos 105, 25–41.

Cendrero, A., 1971. Estudio geológico y petrológico del Complejo Basal de la Isla de La Gomera (Islas Canarias). Estudios Geológicos 27, 3–73.

Chang, S., Van der Lee, S., 2011. Mantle plumes and associated flow beneath Arabia and East Africa. Earth and Planetary Science Letters 302, 448–454.

Chorowicz, J., 2005. The East African rift system. Journal of African Earth Sciences 43, 379–410.

Cliff, R.A., Yardley, B.W.D., Bussy, F., 1996. U-Pb and Rb-Sr geochronology of magmatism and metamorphism in the Dalradian of Connemara, West reland. Journal of Geological Society 153, 109-120.

Coello, J., Cantagrel, J.M., Hernán, F., Fúster, J.M., Ibarrola, E., Ancochea, E., Casquet, C., Jamond, J.R., Cendrero, A., 1992. Evolution of the eastern volcanic ridge of the Canary Islands based on new K–Ar data. Journal of Volcanology and Geothermal Research 53, 251–274.

Cogné, J.P., Humler, E., 2004. Temporal variation of oceanic spreading and crustal production rates during the last 180 My. Earth and Planetary Science Letters 222, 427–439.

Condie, K., 2001. Mantle Plumes And Their Record In Earth History. Cambridge University Press, Cambridge, p. 306.

Cowan, G.A., Adler, H.H., 1976. The variability of natural abundance of 235U. Geochemica et Cosmochimica Acta, 40, 1487-1490.

Crough, S.T., 1979. Hotspot epeirogeny. Tectonophysics 61, 321–333.

Cubas, C.R., 1978a. Estudio de los domos sálicos de la isla de La Gomera (Islas Canarias): I. Vulcanología. Estudios Geológicos 34, 53–70.

Cubas, C.R., Ancochea, E., Hernán, F., Huertas, M.J., Brändle, J.L., 2002. Edad de los domos sálicos de la isla de La Gomera. Geogaceta 32, 71–74.

Cubas, C.R., Hernán, F., Ancochea, E., Brändle, J.L., Huertas, M.J., 1994. Serie Basáltica Antigua Inferior en el sector de Hermigua, Isla de la Gomera. Geogaceta 16, 15–18.

Daly, M.C., Lawrence, S.R., Diemu-Tshiband, K., Matouana, B., 1992. Tectonic evolution of Cuvette Centrale, Zaire. Journal of the Geological Society, London 149, 539–546. http://dx.doi.org/10.1144/gsjgs.149.4.0539

Davies, D., Goes, S., Davies, J., Schuberth, B., Bunge, H., Ritsema, J., 2012. Reconciling dynamic and seismic models of Earth’s lower mantle: the dominant role of thermal heterogeneity. Earth and Planetary Science Letters 353, 253–269.

Davis, W., 1899.The geographical cycle. Geography Journals 14, 481–504.

DAY, S. J., 1996. Hydrothermal pore-fluid pressure & the stability of porous, permeable volcanoes. Geological Society London, Special Publication 110, 77-93.

Delvaux, D., 1991. The Karoo to Recent Rifting in the Western Branch of the East-African Rift System: a Bibliographical Synthesis. Mus royAfrcentr, Tervuren (Belg). Dept Geol Min, Rapp ann 1989–1990, 63–83.

Delvaux, D., 2001. Tectonic and palaeostress evolution of the Tanganyika–Rukwa–Malawi rift segment, East African Rift System. In: Ziegler, P.A., Cavazza, W., Robertson, A.H.F., Crasquin-Soleau, S. (Eds.), Peri-TethysMemoir 6: PeriTethyan Rift/Wrench Basins and Passive Margins: MémoireMusée National Histoire naturelle, vol. 186, p. 545e567 (Paris).

Delvaux, D., Barth, A., 2010. African stress pattern from formal inversion of focal mechanism data. Tectonophysics 484, 105–128.

Delvaux, D., Kervyn, F., Macheyeki, A.S., Temu, E.B., 2012. Geodynamic significance of the TRM segment in the East African Rift (W-Tanzania): Active tectonics and palaeostress in the Ufipa plateau and Rukwa basin. Journal of Structural Geology 37, 161–180. http://dx.doi.org/10.1016/j.jsg.2012.01.008

Demény, A., Ahijado, A., Casillas, R., Vennemann, T.W., 1998. Crustal contamination and fluid/rock interaction in the carbonatites of Fuerteventura (Canary Islands, Spain); a C, O, H isotope study. Lithos 44, 101–115.

Démeny, A., Casillas, R., Hegner, E., Vennemann, T.W., Nagy, G., Sipos, P., 2010. Geochemical and H-O-Sr-Nd isotope evidence for magmatic processes and meteoric-water interactions in the Basal Complex of La Gomera, Canary Islands. Mineral Petrology 98, 181–195. doi:10.1007/s00710-009-0071-4

Demény, A., Venneman, T.W., Hegner, E., Ahijado, A., Casillas, R., Nagy, G., Homonnay, Z., Gutierrez, M., Szabò, Cs., 2004. H, O, Sr, Nd, and Pb isotopic evidence for recycled oceanic crust in the Transitional Volcanic Group of Fuerteventura, Canary Islands, Spain. Chemical Geology 205, 37–54.

Dewey, J.F., 1988. Extensional collapse of orogens, Tectonics 7, 1123–1139.

Dewey, J.F., Pitman III, W.C., Ryan, W.B.F., and Bonnin, J., 1973. Plate tectonics and the evolution of the Alpine system, Geol. Soc. Am. Bull. 84, pp. 3137–3180.

Dodson, M.H., 1973. Closure temperature in cooling geochronological and petrological systems. Contribution to Mineralogy and Petrology 40, 259–274.

Donelick, R.A. 1993. A method of fission track analysis utilizing bulk chemical etching of apatite. U.S. Patent #5,267-274.

Donelick, R.A., 1995. A method of fission track analysis utilizing bulk chemical etching of apatite. Australian Patent Number 658,800.

Donelick, R.A., 2004, Report on Pyrenean Fission Track Data.

Donelick, R.A., Ketcham, R.A., Carlson, W.D., 1999. Variability of apatite fission-track annealing kinetics II: crystallographic orientation effects. American Mineralogist 84, 1224–1234.

Donelick, R.A., O’sullivan P.B., Ketcham, R.A., 2005. Apatite fission-track analysis. Reviews in Mineralogy and Geochemistry 58, 49-94.

Duggen, S., Hoernle, K.A., Hauff, F., Klügel, A., Bouabdellah, M., Thirlwall, M.F., 2009. Flow of Canary mantle plume material through a subcontinental lithospheric corridor beneath Africa to the Mediterranean. Geology, 37, no. 3, 283-286.

Dunkl, I., 2002. Trackkey: a Windows program for calculation and graphical presentation of fission track data. Computers and Geosciences 28, 3–12.

Ebinger, C., Deino, A., Tesha, A., Becker, T., Ring, U., 1993b. Tectonic controls on rift basin morphology: evolution of the Northern Malawi (Nyasa) Rift. Journal of Geophysical Research 98(B10), 17, 821–17, 836.

Ebinger, C., Yemane, T., Wolde-Gabriel, G., Aronson, J., Walter, R., 1993a. Late Eocene–Recent volcanism and faulting in the southern main Ethiopian rift. Journal of the Geological Society 150, 99–108.

Ebinger, C.J., 1989a. Geometric and kinematic development of border faults and accommodation zones, Kivi–Rusizi Rift, Africa. Tectonics 8, 117–133.

Ebinger, C.J., 1989b. Tectonic development of the western branch of the East African Rift System. Geol. Soc. Am. Bull. 101, 885–903.

Ebinger, C.J., Deino, A., Drake, R., Tesha, A., 1989. Chronology of volcanism and rift basin propagation: Rungwe Volcanic Province, East African Journal of Geophysical Research 94, 15785-15803.

Ebinger, C.J., Karner, G.D., Weissel, J.K., 1991. Mechanical strength of extended continental lithosphere: constraints from the Western rift system, East Africa. Tectonics 10, 1239–1256.

Ebinger, C.J., Sleep, N.H., 1998. Cenozoic magmatism throughout east Africa resulting from impact of a single plume. Nature 395, 788–791.

Ehlers, T., Farley, K., 2003. Apatite (U–Th)/He thermochronometry: methods and applications to problems in tectonic and surface processes. Earth and Planetary Science Letters 206, 1–14.

El-Bialy, M.Z., 2004. Petrologic, geochemical and pertogenetic characterization of the old granites of Sinai, Egypt. Unpublished Ph.D. Thesis, Suez Canal University, Ismailia, Egypt, 230p.

Elsworth, D., Day, S.J., 1999. Flank collapse triggered by intrusion: the Canarian and Cape Verde Archipelagoes. Journal of Volcanology and Geothermal Research 94, 323–340.

Elsworth, D., Voight, B., 1992. Theory of dike intrusion in a saturated porous solid. Journal of Geophysical Research 97, 9105–9117.

Elsworth, D., Voight, B., 1996. Evaluation of volcano flank instability triggered by dyke intrusion. Geological Society London, Special Publication 110, 45-53.

Engel, A.E.J., Dixon, T.H., Sterner, J., 1980. Late Precambrian evolution of Afro-Arabian crust from ocean arc to craton. Bulletin of the Geological Society of America 91, 699-706.

Ernst, W., 2007. Speculations on evolution of the terrestrial lithosphere-asthenosphere system-plumes and plates. Gondwana Research 11, 38-49.

Fabre, J., 1988. Les se’riespale’ozoı¨quesd’Afrique: uneapproche. Journal of African Earth Sciences 7, 1–40.

Farley, K.A., 2000. Helium diffusion from apatite: general behaviour as illustrated by Durango fluorapatite. Journal of Geophysical Research 105 (B2), 2903–2914.

Farley, K.A., 2002. (U-Th)/He dating: Techniques, calibrations and applications. In: Porcelli, P.D., Ballentine, C.J., Wieler, R., (Eds.). Noble Gas Geochemistry. Rev. Min. Geoch., 47: 819-843.

Farley, K.A., 2007. He diffusion systematic in minerals: evidence from synthetic monazite and zircon structure phosphates. Geochimica et Cosmochimica Acta 71, 4015–4024.

Farley, K.A., Wolf, R.A., Silver, L.T., 1996. The effects of long-alpha-stopping distances on (U–Th)/He ages. Geochimica et Cosmochimica Acta 60, 4223–4229.

Feinstein, S., Kohn, B. P., Steckler, M. S., Eyal, M., 1996. Thermal history of the eastern margin of the Gulf of Suez, I. reconstruction from borehole temperature and organic maturity measurements. Tectonophysics 266, 203-220.

Féraud, G., 1981. Datation de Réseaux de Dykes et de Roches Volcaniques Sous-Marines par les M6thodes K- Ar et 40Ar-39Ar. Utilisation des Dykes comme Marqueurs de Paléocontraintes. Thesis, Univ. de Nice, 146 pp.

Féraud, G., Giannerini, G., Campredon, R., Stillman, C.J., 1985. Geochronology of some Canarian dyke swarms: contributions to the tectonic evolution of the archipelago. Journal of Volcanology and Geothermal Research 25, 29–52.

Fernandez, C., Casillas, R., Garcia, N.E., Gutierrez, M., Camacho, M.A., Ahijado, A., 2006. Miocene rifting of Fuerteventura (Canary Islands). Tectonics 25:TC6005. doi:10.1029/2005TC001941

Fitzgerald, P.G., Baldwin, S.L., Webb, L.E., O'Sullivan, P.B., 2006. Interpretation of (U–Th)/He single grain ages from slowly cooled crustal terranes: a case study from the Transantarctic Mountains of southern Victoria Land. Chemical Geology 225 (1–2), 91–120.

Flecker, J., Greenwood, W.R., Hadley, D.G., Anderson, R.E., Schmidtd, D.L., 1980. Rubidium-strontium geochronology and plate-tectonic evolution of the southern part of the Arabian Shield, United States Geological Survey Professional Paper, 1131.

Fleischer, R.L., Price, P.B., Walker, R.M., 1975. Nuclear tracks in solids. University of California Press, Berkeley, CA.

Fleischer, R.L., Price, P.B., Walker R.M., Leakey, L.S.B., 1965b. Fission track dating of Bed I, Olduvai Gorge, Science 148, pp. 72–74.

Flower, B.P., Kennett, J.P., 1994. The middle Miocene climatic transition: East Antarctic ice sheet development, deep ocean circulation and global carbon cycling. Palaeogeogr., Palaeoclimatol., Palaeoecol., 108, 537–555.

Flowers, R.M., Bowring, S.A., Reiners, P.W., 2006. Lowlong-termerosion rates and extreme continental stability documented by ancient (U–Th)/He dates. Geology 34, 925–928.

Flowers, R.M., Ketcham, R.A., Shuster, D.L., Farley, K.A., 2009. Apatite (U–Th)/He thermochronometry using a radiation damage accumulation and annealing model. Geochimica et Cosmochimica Acta 73 (8), 2347–2365. http://dx.doi.org/10.1016/ j.gca.2009.01.015

Foster, D.A., Gleadow, A.J.W., 1992. The morphotectonic evolution of rift-margin mountains in central Kenya: Constraints from apatite fission-track thermochronology. Earth and Planetary Science Letters 113, 157–171.

Foster, D.A., Gleadow, A.J.W., 1996. Structural framework and denudation history of the flanks of the Kenya and Anza Rifts, East Africa. Tectonics 15, 258–271.

Francis, P.W., 1994. Large volcanic debris avalanches in the central Andes. In: McGuire, W.J. (ed.) Proceedings of International Conference on Volcano Instability on the Earth and Other Planets. The Geological Society of London.

Fritz, H., Tenczer, V., Hauzenberger, C.A., Wallbrecher, E., Hoinkes, G., 2005. Central Tanzanian tectonic map: a step forward to decipher Proterozoic structural events in the East African Orogen. Tectonics 24, TC6013.

Furman, T., Kaleta, K.M., Bryce, J.G., Hanan, B.B., 2006. Tertiary mafic lavas of Turkana, Kenya: Constraints on East African plume structure and the occurrence of high-µ volcanism in Africa. Journal of Petrology 47, 1221-1244.

Fúster, J.M., Aguilar, M., 1965. Nota previa sobre la geologıa del Macizo de Betancuria, Fuerteventura Islas Canarias . Estudio geológico 21, 181–197.

Fúster, J.M., Cendrero, A., Gastesi, P., Ibarrola, E., Lopez Ruiz, J., 1968a. Geologia y Volcanologia de las Islas Canarias -Fuerteventura. Institut ‘Lucas Mallada’, Consejo Superior de Investigationes Cientificas, Madrid, 239 pp.

Fúster, J.M., Herna ´n, F., Cedrero, A., Coello, J., Cantagrel, J.M., Ancochea, E., Ibarrola, E., 1993. Geocronologı´a de la Isla de El Hierro (Islas Canarias). Bol. R. Soc. Esp. Hist. Nat., Secc. Geol. 88 (1-4), 85–97.

Fúster, J.M., Muñoz, M., Sagredo, J., Yebenes, A., Bravo, T., Hernández Pacheco, A., 1980. Excursión 121 A+C del 26˚ I.G.C. a las Islas Canarias. Boletín Geológico y Minero de España 91 (II), 351– 390.

Gallagher, K., 2012. Transdimensional inverse thermal history modeling for quantitative thermochronology. Journal of Geophysical Research, 117, p.B02408. doi:10.1029/2011JB008825

Galbraith, R.F., Laslett, G.M., 1993. Statistical models for mixed fission track ages. Nuclear Tracks and Radiation Measurements, 21, 459-470.

Gallagher, K., Charvin, K., Nielsen, S., Sambridge, M., and Stephenson, J., 2009. Markov chain Monte Carlo (MCMC) sampling methods to determine optimal models, model resolution and model choice for Earth Science problems, Marine and Petroleum Geolology 26, 525–535, doi:10.1016/j. marpetgeo.2009.01.003.

Gallagher, K., Hawkesworth, C.J., Mantovani, M.J.M., 1994. The denudation history of the onshore continental margin of SE Brazil inferred from apatite fission track data. Journal of Geophysical Research 99, 18117-18145.

Garfunkel, Z., 2002, Early Paleozoic sediments of NE Africa and Arabia: Products of continental-scale erosion, sediment transport, and deposition: Israel Journal of Earth Sciences, v. 51, p. 135–156, doi: 10.1560/WE3P-3EX8- X2L2-RMFG.

Garfunkel, Z., and Derin, B., 1985. Permian-Early Mesozoic tectonism and continental margin formation in Israel and its implications for the history of the Eastern Mediterranean, in Dixon, J.E., and Robertson, A.H.F., eds., The geological evolution of the eastern Mediterranean: Oxford, Blackwell, Special Publication of the Geological Society No. 17, p. 187–201.

Garver, J.I., 2002. Discussion: “Metamictization of natural zircon: accumulation versus thermal annealing of radioactivity-induced damage.” Contributions to Mineralogy and Petrology, 143, 756-757.

Garver, J.I., 2003. Etching age standards for fission track analysis. Radiation Measurements 37 (1), 47-54.

Garver, J.I., Kamp, P.J.J., 2002. Integration of zircon color and zircon fission track zonation patterns in Orogenic belts: application of the Southern Alps, New Zealand. Tectonophysics 349 (1–4), 203–219.

Gass, I. G., 1982. Upper Proterozoic (Pan-African) calcalkaline magmatism in northeastern Africa and Arabia. In: Thorpe, R.S. (Ed.), Andesites. Wiley, New York, 591–609.

Geldmacher, J., Hoernle,K., Bogaard, P. v. d., Duggen, S., Werner, R., 2005. New 40Ar/ 39Ar age and geochemical data from seamount in the Canary and Madeira volcanic provinces: Support for the mantle plume hypothesis. Earth and Planetary Science Letters 237, 85–101.

Geldmacher, J., Hoernle,K., Bogaard, P. v. d., Zankl, G., Garbe-Schönberg, D., 2001. Earlier history of the ≥70 Ma old Canary hotspot based on the temporal and geochemical evolution of the Selvagen archipelago and neighboring seamounts in the eastern North Atlantic. Journal of Volcanology and Geothermal Research 111, 55– 87.

Girdler, R.W., 1985. Problems concerning the evolution of oceanic lithosphere in the northern Red Sea. Tectonophysics 116, 109-122.

Giresse, P., 2005. Mesozoic–Cenozoic history of the Congo Basin. Journal of African Earth Sciences 43, 301–315.

Gleadow, A.J.W., 1981. Fission-Track Dating methods: What are the real alternatives? Nuclear Tracks 5, 3-14.

Gleadow, A.J.W., Brooks, C.K., 1979. Fission track dating, thermal histories and tectonics of igneous intrusions in East Greenland. Contributions to Mineralogy and Petrology 71, 45–60.

Gleadow, A.J.W., Duddy, I.R., 1981. A natural long-term track annealing experiment for apatite. Nuclear Tracks 5, 169–174.

Gleadow, A.J.W., Duddy, I.R., Green, P.E., Hegarty, K.A., 1986a. Fission track lengths in the apatite annealing zone and the interpretation of mixed ages. Earth and Planetary Science Letters 78, 245–254.

Gleadow, A.J.W., Duddy, I.R., Green, P.E., Lovering, J.F., 1986b. Confined fission track lengths in apatite: A diagnostic tool for thermal history analysis. Contributions to Mineralogy and Petrology 94, 405- 415.

Gleadow, A.J.W., Duddy, I.R., Green, P.F., Lovering, J.F., 1983. Fission track analysis: a new tool for the evaluation of thermal histories and hydrocarbon exploration. Petroleum Exploration Association Australian Journal 23, 93-102.

Gleadow, A.J.W., Fitzgerald, P.G., 1987. Uplift history and structure of the Tran Antarctic Mountains: new evidence from fission track dating of basement apatites in the Dry Valleys area, southern Victoria Land. Earth and Planetary Science Letters 82, 1-14.

Gleadow, A.J.W., MCkelvey, B.C., Ferguson, K.U., 1984. Uplift history of the transantarctic mountains in the Dry Valleys area, southern Victoria Land, Antarctica, from apatite fission track ages. New Zealand Journal of Geology and Geophysics 27, 457–464.

Gloss, M. Shreve, R.L., 1988. Subduction channel model of prism accretion, melange formation, sediment subduction and subduction erosion at convergent plate margins, 1. Background and descriptions, Pure Appl. Geophys. 128,456-500.

Green, P.F., Duddy, I.R., Gleadow, A.J.W., Tingate, P.R., Laslett, G.M., 1986. Thermal annealing of fission tracks in apatite 1. A qualitative description. Chemical Geology 59, 237–253.

Green, P.F., Durrani, S.A., 1977. Annealing studies of tracks in crystals. Nuclear track detect 1, 33-39.

Greenberg, J.K., 1981. Characteristics and origin of Egyptian younger granites. Geological Society of America Bulletin 92 (pt. 2), 749–840.

Greiling, R.O., Kriiner, A., El Ramly, M.F. and Rashwan, A.A., 1988. Structural relationships between the southern and central parts of the Eastern Desert of Egypt: details of a fold and thrust belt. In: S. El Gaby and R.O. Greiling, (Editors), The Pan-African of NE Africa and Adjacent Areas. Vieweg, Wiesbaden, pp. 121-145.

Grist, A.M., Ravenhurst, C.E., 1992a. Mineral separation techniques used at Dalhousie University. In: Zentilli M, Reynolds PH (eds). Short course handbook on low temperature thermochronology. Mineralogical Association of Canada. Short Course Handbook. 20 Append. 2: 203–209.

Grist, A.M., Ravenhurst, C.E., 1992b.A step-by-step laboratory guide to fission track.

Grobe, R. W., 2011. Long-term landscape evolution, cooling and exhumation history of Variscan rocks in the western Cantabrian Mountains (NW Spain). Doctorate Thesis Institute of Earth Sciences, University of Heidelberg, p., 168.

Guenthner, W.R., Reiners, P.W., 2010. Effects and implications of radiation damage on He diffusion in zircon. Thermo2010, 12th International Conference on Thermochronology, Glasgow, 16–20 August 2010.

Guenthner, W.R., Reiners, P.W., Ketcham, R.K., Nasdala, L., Giester, G., 2013. Helium diffusion in natural zircon: radiation damage, anisotropy, and the interpretation of zircon (U–Th)/He thermochronology. American Journal of Science 313, 145–198. doi:10.2475/03.2013.01

Guillou, H., Carracedo, F.C., Pérez Torrado, F.J., Rodríguez Badiola, E., 1996. K–Ar ages and magnetic stratigraphy of a hotspotinduced, fast grown oceanic island: El Hierro, Canary Islands. Journal of Volcanology and Geothermal Research 73, 141–155.

Guillou, H., Carracedo, J.C., Duncan, R.A., 2001. K–Ar, 40Ar–39Ar ages and magnetostratigraphy of Brunhes and Matuyama lava sequences from La Palma. Journal of Volcanology and Geothermal Research 106, 175–194.

Guiraud,R., Bosworth, W., Thierry, J., Delplanque, A., 2005. Phanerozoic geological evolution of Northern and Central Africa: an overview. Journal of African Earth Sciences 43, 83–148.

Gunnell, Y., 2000. Apatite fission track thermochronology: an overview of its potential and limitations in geomorphology. Basin Research 12, 115–132.

Hanna, G.C., Westcott, C.H., Lemmel, H.D., Leonard, B.R., Story, J.S., Attree, P.M., 1969. Revision of values for the 2200 m/s neutron constants for four fissile nuclides. G.E.C. Atomic Energy Review, 7, 3-92.

Hansen, S., Nyblade, A., Benoit, M., 2012. Mantle structure beneath Africa and Arabia from adaptively parameterized P-wave tomography: implications for the origin of Cenozoic Afro-Arabian tectonism. Earth and Planetary Science Letters 319, 23–34.

Haq, B.U., Al-qahtani, A.M., 2005. Phanerozoic cycles of sea-level change on the Arabian Platform. GeoArabia 10, 127–160.

Hasebe, N., Barbarand, J., Jarvis, K., Carter, A., Hurford, A.J., 2004. Apatite fission-track chronometry using laser ablation ICP-MS. Chemical Geology 207, 135-145.

Hashad, A.H., 1980. Present status of geochronological data on the Egyptian basement complex. Bulletin of the Institute for Applied Geology, King Abdul Aziz University, Jeddah 3(3), 31-46.

Heezen, B. C., 1960. The rift in the ocean floor. Scientific American 203 (4), 98–110. doi:10.1038/scientificamerican1060-98

Hegazi, A.M., 1995. Structural Analysis and metamorphic evolution of East Abu Zeneima area, Sinai, Egypt. Unpublished Ph. D. Thesis, Suez Canal University, Ismailia, Egypt, pp. 190.

Herman, F., Copeland, P., Avouac, J., Bollinger, L., Mahéo, G., Le Fort, P., Rai, S., Foster, D., Pêcher, A., Stüwe, K., Henry, P., 2010b. Exhumation, crustal deformation, and thermal structure of the Nepal Himalaya derived from the inversion of thermochronological and thermobarometric data and modeling of the topography. Journal of Geophysical Research115, B06407. doi:10.1029/2008JB006126

Hernández-Pacheco, A., Ibarrola, E., 1973. Geochemical variation trends between the different Canary islands in relation to their geological position. Lithos 6, 389-402.

Herold, N., Huber, M., Greenwood, D.R., Müller, R.D., Seton, M., 2011. Early to Middle Miocene monsoon climate in Australia. Geology 39, 3-6.

Herrera, R., Huertas, M.J., Ancochea, E., 2008. Edades 40Ar–39Ar del Complejo Basal de la isla de La Gomera. Geogaceta 44, 7–10.

Hess, H.H., 1962. History of ocean basins. In Petrologic Studies: a volume in honor of A.F. Buddington, pp. 599–620. Geological Society of America, New York.

Hoernle, K. , Zhang, Y. S., Graham, D., 1995. Seismic and geochemical evidence for large scale mantle upwelling beneath the eastern Atlantic and western and central Europe, Nature 374, 34–39.

Hoernle, K., Schmincke, H.U., 1993. The role of partial melting in the 15-Ma geochemical evolution of Gran Canaria: a blob model for the Canarian hotspot. Geotechnology 10, 19–32.

Hoernle, K., Tilton, G., 1991. Sr–Nd–Pb isotope data for Fuerteventura (Canary Islands) basal complex and subaerial volcanics: applications to magma genesis and evolution. Schweizerische Mineralogische und Petrographische Mitteilungen 71, 3–18.

Hoernle, K., Tilton, G., Le Bas, M.J., Duggen, S., Garbe-Schönberg, D., 2002. Geochemistry of oceanic carbonatites compared with continental carbonatites: mantle recycling of oceanic crustal carbonate. Contributions to Mineralogy and Petrology 142, 520–542.

Hoernle, K., Tilton, G., Schmincke, H. U., 1991. Sr–Nd–Pb isotopic evolution of Gran Canaria: evidence for shallow enriched mantle beneath the Canary Islands, Earth and Planetary Science Letters 106, 44– 63.

Holland, H. D., 1954. Radiation damage and its use in age determination, in Faul, H., editor, Nuclear Geology: New York, Wiley, p. 175–179.

Hourigan, J.K., Reiners, P.W., Brandon, M.T., 2005. U–Th zonation dependent alpha-ejection in (U–Th)/He chronometry. Geochimca et Cosmochim Acta 69, 3349–3365.

Hsü, K.J., Cita, M.B., Ryan, W.B.F., 1973. The origin of the Mediterranean evaporites. Init. Repts D.S.D.P. XIII, vol. 2. U.S. Government Printing Office, Washington, pp. 1203–1231.

Huerta, A., Nyblade, A., Reusch, A., 2009. Mantle transition zone structure beneath Kenya and Tanzania: more evidence for a deep-seated thermal upwelling in the mantle. Geophysical Journal International 177, 1249–1255.

Huertas, M.J., Arnaud, N.O., Ancochea, E., Cantagrel, J.M., Fúster, J. M., 2002. 40Ar/39Ar stratigraphy of pyroclastic units from the Cañadas Volcanic Edifice (Tenerife, Canary Islands) and their bearing on the structural evolution. Journal of Volcanology and Geothermal Research 115, 351–365.

Huismans, R.S., Podladchikov, Y.Y., Cloetingh, S., 2001. Transition from active to passive rifting: relative importance of asthenospheric doming and passive extension of the lithosphere. Journal of geophysical Research 106, 11271–11291.

Humphreys, E., Schmandt, B., 2011. Looking for mantle plumes. Physics Today 64(8), 34–39.

Hurford, A.J. 1990. Standardization of fission track dating calibration: recommendation by the fission track working group of the I.U.G.S. Subcommission on geochronology. Chemical Geology 80, 171– 178.

Hurford, A.J., 1986. Cooling and uplift patterns in the Lepontine Alps, South Central Switzerland and an age of vertical movement on the Insubric Fault Line. Contributions to Mineralogy and Petrology 92, 413–427.

Hurford, A.J., 1986. Standardization of fission track dating calibration: results of questionnaire distributed by international union of geological sciences subcommission on geochronology. Nuclear tracks and radiation measurements 11, 329-333.

Hurford, A.J., Green, P.F., 1982. A user's guide to fission-track dating calibration. Earth and Planetary Science Letters 59, 343–354.

Hurford, A.J., Green, P.F., 1983. The Zeta age calibration of fission-track dating. Isotope Geoscience 1, 285–317.

Hurley, P. M., 1954. The helium age method and the distribution and migration of helium in rocks, in Faul, H., editor, Nuclear Geology: New York, Wiley, p. 301–329.

Hussong, D.M., Edwards, P.B., Johnson, S.H., Campbell, J.F., Sutton, G.H., 1976. Crustal structure of the Peru-Chile trench: 8"-12"s latitude, in: G.H. Sutton, M.H. Manghani and R. Moberly, eds., The Geophysics of the Pacific Ocean Basin and its Margin, Geophysical Monograph 19, 71-85.

Ibarrola, E., 1969. Variation trends in basaltic rocks of the Canary Islands. Bulletin Volcanology 33: 729-777.

Ibarrola, E., Ancochea, E., Casquet, C., Ftister, J.M., Hernan, F., Cendrero, A., Diaz de Teran, J.R., Cantagrel, J.M. and Jamond, C., 1989b. Cronoestratigrafia de las series volcánicas postmiocenas de la Isla de Fuerteventura. E.S.F. Mtg. Canarian Volcanism. Abstract, 134-138.

Inokuchi, T., 1988. Gigantic landslides and debris avalanches on volcanoes in Japan. In: Proceedings of the Kagoshima International Conference on Volcanoes. National Institute for Research Administration, Japan, 456-459.

Ito, G., van Keken, P., 2007. Hot spots and melting anomalies. In: Schubert, G. (ed.) Treatise in Geophysics, Elsevier, New York, Vol. 7, pp. 371–435.

Iverson, R.M., 1991. Failure and runout of giant landslides on Hawaiian volcanoes: cases of enigmatic mechanics? Geological Society of America Abstracts Programs 47, A125.

Iverson, R.M., 1995. Can magma-injection and groundwater forces cause massive landslides on Hawaiian volcanoes? Journal of Volcanology and Geothermal Research 66, 295–308.

Iverson, R.M., 1996. Can magma-injection and groundwater forces cause massive landslides on Hawaiian volcanoes? Journal of Volcanology and Geothermal Research 66, 295-308.

Jakovlev, A., Rumpker, G., Schmeling, H., Koulakov, I., Lindenfeld, M., Wallner, H., 2013. Seismic images of magmatic rifting beneath the western branch of the East African rift. Geochemistry, Geophysics, Geosystems 14, 4906–4920.

Juez-Larre, A.J., 2003. Post Late Paleozoic tectonothermal evolution of the northeastern margin of Iberia, assessed by fission-track and (U-T)/He analysis: a case history from the Catalan Coastal Ranges. Ph.D. thesis, Free University of Amsterdam. 200 pp.

Kampunzu, A.B., Bonhomme, M.G., Kanika, M., 1998. Geochronology of volcanic rocks and evolution of the Cenozoic Western Branch of the East African Rift System. Journal of African Earth Sciences 26 (3), 441–461.

Karig, R.E., 1974. Tectonic erosion at trenches, Earth Planetary Science Letters 21, 209-212.

Karl, D.M., McMurtry, G. M., Malahoff, A., Garcia, M.O., 1988. Loihi Seamount, Hawaii: a mid-plate volcano with a distinctive hydrothermal system. Nature 335, 532–535.

Karner, G.D., Byamungu, B.R., Ebinger, C.J., Kampunzu, A.B., Mukasa, R.K., Nyakaana, J., Rubondo, E.N.T., Upcott, N.M., 2000. Distribution of crustal extension and regional basin architecture of the Albertine rift system, East Africa. Marine and Petroleum Geology 17, 1131–1150.

Kaufmann, G., Romanov, D., 2012. Landscape evolution and glaciation of the Rwenzori Mountains, Uganda: insights from numerical modeling. Geomorphology 138, 263–275. http://dx.doi.org/10.1016/j.geomorph.2011.09.011

Kearey, P., Klepeis, K. A., and Vine, F. J., 2009. Global Tectonics (3rd Edition), Hoboken, N.J., Wiley-Blackwell.

Kennedy, W.Q., 1964. The structural differentiation of Africa in the Pan-African (±500 m.y.) tectonic episode. Leeds University Research Institute of African Geology Annual Report 8, 48-49.

Kerdany, M.T., Cherif, O.H., 1990. The Mesozoic. In: R. Said, Editor, The Geology of Egypt, Balkema, Rotterdam, pp. 407–438.

Ketcham R.A., Donelick R.A., Carlson W.A., 1999. Variability of apatite fission-track annealing kinetics: III. Extrapolation to geological time scales. American Mineralogist 84, 1235–1255.

Ketcham, R.A., 2005. Forward and Inverse Modelling of low-temperature thermochronometry data. In: Reiners, P.W., Ehlers, T.A. (Eds.), Low-Temperature Thermochronology: Techniques, Interpretations and Applications: Reviews in Mineralogy and Geochemistry 58, pp. 275–314.

Ketcham, R.A., 2009. HeFTy version 1.6.7, Manual.

Ketcham, R.A., Carter, A., Donelick, R.A., Barbarand, J., Hurford, A.J., 2007a. Improved measurements of fission-track annealing in apatite. American Mineralogist 92, 789-798.

Ketcham, R.A., Carter, A., Donelick, R.A., Barbarand, J., Hurford, A.J., 2007b. Improved modeling of fission-track annealing in apatite. American Mineralogist 92, 799-810.

Ketcham, R.A., Donelick, R.A., Balestrieri, M.L., Zattin, M., 2009. Reproducibility of apatite fission-track length data and thermal history reconstruction. Earth and Planetary Science Letters 284, 504–515.

Ketcham, R.A., Gautheron, C., Tassan-Got, L., 2011. Accounting for long alpha-particle stopping distances in (U-Th-Sm)/He geochronology: Refinement of the baseline case: Geochimica et Cosmochimica Acta 75, 7779-7791.

Klitzsch, E., 1986. Plate tectonics and cratonal geology in Northeast Africa (Egypt, Sudan). Geologische Runchau 75, 755-768.

Klitzsch, E., 1990. Paleozoic. In: Said, R. (Ed.). The Geology of Egypt. Balkema, Rotterdam, Chapter 24, 451–486.

Koehn, D., Aanyu, K., Haines, S., Sachau, T., 2008. Rift nucleation, rift propagation and the creation of basement micro-plates within active rifts. Tectonophysics 458, 105–116.

Koehn, D., Lindenfeld, M., Rümpker, G., Aanyu, K., Haines, S., Passchier, C., 2010. Active transsection faults in rift transfer zones: evidence for rotating stress fields in the East African Rift and implications for crustal fragmentation processes. International Journal of Earth Sciences 99, 1633–1642. http://dx.doi.org/10.1007/s00531-010-0525-2

Kohn, B. P., Feinstein, S., Foster, D.A., Steckler, M. S., Eyal, M., 1997. Thermal history of the eastern the Gulf of Suez, II. Reconstruction from apatite fission track and 40Ar/39Ar K-feldspar measurements. Tectonophysics 283, 219-239.

Kohn, B.P., Eyal, M., 1981. History of uplift of the crystalline basement of Sinai and its relation to opening of the Red Sea as revealed by fission track dating of apatites. Earth and Planetary Science Letters 52, 129-141.

Kohn, B.P., Eyal, M., Feinstein, S., 1992. A major Late Devonian–Early Carboniferous (Hercynian) thermotectonic event at the NW margin of the Arabian–Nubian shield: evidence from zircon fission track dating. Tectonics 11/5, 1018–1027.

Kolodner, K., Avigad, D., McWilliams, M., Wooden, J.L., Weissbrod, T., and Feinstein, S., 2006, Provenance of north Gondwana Cambrian-Ordovician sandstone: U-Pb SHRIMP dating of detrital zircons from Israel and Jordan: Geological Magazine, doi: 10.1017/S0016756805001640.

Kröner, A., 1979. Pan-African plate tectonics and its repercussions on the crust of Northeast Africa. Geological Rundsch 68, 565–583.

Kröner, A., 1984. Late Precambrian plate tectonics and orogeny: a need to redefine the term Pan-African. In: Klerkx j. and Michit j. (eds.). African Geology, Tervuren, Belgium, 23-6.

Kröner, A., Eyal, M., Eyal, Y., 1990. Early Pan-African evolution of the basement around Elat, Israel, and Sinai Peninsula revealed by single-zircon evaporation dating, and implications for crustal accretion rates. Geology 18, 545-548.

Kröner, A., Kruger, J., Rashwan, A.A.A., 1994. Age and tectonic setting of granitoid gneisses in the Eastern Desert of Egypt and South-West Sinai. Geol Rundsch 83, 502-513.

Kusznir, N.J., Ziegler, P.A., 1992. The mechanics of continental extension and sedimentary basin formation: a simple-shear/pure-shear flexural cantilever model. Tectonophysics 215, 117–131.

Laslett, G.M., Gleadow, A.J.W., Duddy, I.R., 1984. The relationship between fission track length and density in apatite. Nuclear tracks 9, 29-38.

Le Bas, M.J., Rex, D.C., Stillman, C.J., 1986. The early magmatic chronology of Fuerteventura. Geological Magazine 123, 287–298.

Leggo, P., 1974. A geochronological study of the basement complex of Uganda. Journal of Geological Society London 130, 263–277.

Link, K., Koehn, D., Barth, M.G., Tiberindwa, J.V., Barifaijo, E., Aanyu, K., Foley, S.F., 2010. Continuous cratonic crust between the Congo and Tanzania blocks in western Uganda. International Journal of Earth Sciences. http://dx.doi.org/10.1007/s00531-010-0548-8

Lisker, F., Ventura, B., Glasmacher, U.A., 2009. Apatite thermochronology in modern geology. Geological Society of London, Special Publication 324, 1–23.

Livingstone, D.A., 1967. Postglacial vegetation of the Ruwenzori mountains in equatorial Africa. Ecological Monographs 37 (1), 25–52.

Lodge, A., Helffrich, G., 2006. Depleted swell root beneath the Cape Verde islands. Geology 34, 449–452.

Longerich, H.P., Jackson, S.E., Günter, D., 1996. Laser Ablation Inductively Coupled Plasma Mass Spectrometric transient signal data acquisition and analytic concentration calculation. Journal of Analytical Atomic Spectrometry 11, 899-904.

López Ruiz, J., 1969. Le complexe filonien de Fuerteventura (Iles Canaries. Bulltien of Volcanology 33, 1166-1185.

Lugmair, G.W., Marti, K., 1978. Lunar initial 143Nd/144Nd:Differential evolution of the lunar crust and mantle. Earth and Planetary Science Letters, 39, 349-357.

MacPhee, D., 2006. Exhumation, Rift-flank uplift, and Thermal Evolution of the Rwenzori Mountains Determined by Combined (U–Th)/He and U–Pb Thermochronometry. Master Thesis Massachusetts Institute of Technology. pp. 38.

Mansour, S., 2010. Evolution and Thermo-Tectonic Development of the Basement Complex, West-central Sinai, Egypt: Constraints from Uranium-Lead Dating and Apatite Fission Track Low-Temperature Thermochronology. Unpublished M.Sc. Thesis, Kanazawa University, Kanazawa, Japan, 173p.

Maruyama, S., 1994. Plume tectonics. Journal of Geological Society of Japan 100, 24–49.

McConnell, R., 1972. Geological development of the rift system of eastern Africa. Geological Society of America Bulletin 83, 2549–2572.

McConnell, R.B., 1959. Outline of the geology of the Ruwenzori Mountains, a preliminary account of the results of the British Ruwenzori expedition, 1951–1952. Overseas Geology and Mineral Resources 7 (3), 245–268.

McDougall, I., Brown, F.H., 2009. Timing of volcanism and evolution of the northern Kenya Rift. geology magazine 146, 34-47.

McDougall, I., Schmincke, H.U., 1976. Geochronology of Gran Canaria, Canary Islands: age of shield building volcanism and other magmatic phases. Bulletin Volcanologique 40, 1–21.

McGuire, W.J., 1996. Volcano instability: a review of contemporary themes. In: McGuire, W.J., Jones, A.P., Neuberg, J. (Eds.), Volcano Instability on the Earth and Terrestrial Planets. Geological Society of London, Special Publication 110, 1–23.

McKenzie, D., 1978. Some remarks on the development of sedimentary basins. Earth and Planet Science letters 40, 25-32.

Meert, J.G., 2003, A synopsis of events related to the assembly of eastern Gondwana: Tectonophysics 362, 1–40. doi: 10.1016/S0040-1951(02)00629-7

Menard, H.W., 1958. Development of median elevations in the ocean basins. Geological Society of America Bulletin 69, 1179–1186. http://dx.doi.org/10.1130/0016-7606(1958)69[1179:DOMEIO]2.0.CO;2

Menard, H.W., 1959. Geology of the Pacific sea floor. Experientia v. XV/G, 205-213.

Meneisy, M., 1990. Vulcanicity. In: Said, R. (Ed.), The Geology of Egypt. Balkema, Rotterdam, Netherland, pp. 157–172.

Meneisy, M.Y., 1986. Mesozoic igneous activity in Egypt. Qatar University Science Bulletin 6.

Michot, F., 1938. Etude pétrographiqueetgéologique du Ruwenzori septentrional. Mémoire-Institut Royal Colonial Belge Section des sciences naturellesetMedicales 8, 66– 271.

Missenard, Y., Zeyen, H., de Lamotte, D.F., Leturmy, P., Petit, C., Sébrier, M., and Saddiqi, O., 2006. Crustal versus asthenospheric origin of relief of the Atlas Mountains of Morocco. Journal of Geophysical Research 111, 1–13. doi: 10.1029/2005JB003708.

Mitchell, S.G., Reiners, P.W., 2003. Influence of wildfires on apatite and zircon (U–Th)/He ages. Geology 31, 1025–1028.

Moghazi, A.M., 1999. Magma source and evolution of Late Neoproterozoic granitoids in the Gabal El-Urf area, Eastern Desert, Egypt: geochemical and Sr–Nd isotopic constraints. Geological Magazine, Cambridge University Press 136:285-300.

Molnar, P., England, P., 1990. Temperatures, heat flux, and frictional stress near major thrust faults. Journal of Geophysical Research 95, 4833–4856.

Montelli, R., Nolet, G., Dahlen, F., Master, G., 2006. A catalogue of deep mantle plumes: new results from finite-frequency tomography. Geochemistry, Geophysics, Geosystems 7, Q11007.

Montgomery, D. R., 1994. Valley incision and the uplift of mountain peaks. Journal of Geophysical Research 99, 13913–13921. doi:10.1029/94JB00122

Moore, J .G., 1964. Giant submarine landslides on the Hawaiian Ridge: US. Geological Survey Professional Paper 501-D, 95—98.

Moore, M.E., Gleadow, A.J.W., Lovering, J.F., 1986. Thermal evolution of rifted continental margins: New evidence from fission tracks in basement apatites from southeastern Australia. Earth Planetary Science Letters 78, 255-270.

Morgan, E., Boulos, E.K., Hennin, S.E., EL-Sheriff, A.A., Sayed, A.A., Basta, N.Z., Melek, Y.S., 1985. Heat flow in eastern Egypt: The thermal signature of a continental breakup. Journal of Geodynamics 4, 107-131.

Morgan, W., 1971. Convection plumes in the lower mantle. Nature 230, 42–43.

Morgan, W., 1972. Deep motions and deep mantle convection. Geological Society of America Memo. 132, 7–22.

Morishta, T., Ishida, Y., Arai, S., 2005. Simultaneous determination of multiple trace element composition in thin (<30 μm) layers of BCR-2G by 193 nm ArF excimer laser ablation-ICP-MS: implications for matrix effect and elemental fractionation on quantitative analysis. Geochemical Journal 39, 327-340.

Morley, C.K., 1999. Tectonic evolution of the East African Rift System and the modifying influence of magmatism: a review. ActaVulcanologica 11 (1), 1–19.

Morley, C.K., Wescott, W.A., Stone, D.M., Harper, R.M., Wigger, S.T., and Karanja, F.M., 1992. Tectonic evolution of the northern Kenyan Rift. Journal of Geological Society of London 149, 333-348.

Morley, L.K., Ngenoh, D.K., Ego, J.K., 1999. Introduction to the East African Rift system. In: Morley, C.K. (Ed.), Geoscience of Rift Systems-Evolution of East Africa: AAPG Studies in Geology 44, 1–18.

Moustafa, A.R., Yousif, M.S.M., 1993. Structural evolution of the eastern shoulder of the Suez Rift: Um Bogma area. Neues Jahrbuch für Geologie und Paläontologie Mh. 11, 655-668.

Mulibo, G., Nyblade, A., 2013. The P and S wave velocity structure of the mantle beneath eastern Africa and the African superplume anomaly. Geochemistry, Geophysics, Geosystems 14, 2696–2715.

Muñoz, M., Sagredo, J., 2004. El Complejo Basal. In: Vera, J.A. (Ed.), Geologıa de España. SGE-IGME, Madrid, Spain, 645-649.

Muñoz, M., Sagredo, J., de Ignacio, C., 2003. Fieldtrip guide Fuerteventura, IV Eurocarbon Workshop Canary Islands. Fuerteventura, Spain.

Murry, J.B., Voight, B., 1996. Slope stability and eruption prediction on the eastern flank of Mount Etna. Geological Society of London, Special Publication 110, 111–114.

Naeser, C.W., Faul, H., 1969. Fission track annealing in apatite and sphene. Journal of Geophysical Research 74/2, 705–710.

Nasdala, L., 2009. Pb+ irradiation of synthetic zircon (ZrSiO4): Infrared spectroscopic investigation - Discussion. American Mineralogist, 94, 853-855.

Nasdala, L., Reiners, P. W., Garver, J. I., Kennedy, A. K., Stern, R. A., Balan, E., and Wirth, R., 2004a. Incomplete retention of radiation damage in zircon from Sri Lanka. American Mineralogist 89, 219–231.

Neumann, E.R., Wulff, P.E., Johnsen, K., Andersen, T., and Krogh, E., 1995. Petrogenesis of spinel harzburgite and dunite suite xenoliths from Lanzarote, eastern Canary Islands: Implications for the upper mantle. Lithos 35, 83–107. doi: 10.1016/0024-4937(95)91153-Z.

Noble, W.P., Foster, D.A. and Gleadow, A.J.W., 1997.The post-Pan-African thermal and extensional history of crystalline basement rocks in eastern Tanzania. Tectonophysics 275 (4), 331–350.

Nyblade, A., Owens, T., Gurrola, H., Ritsema, J., Langston, C., 2000. Seismic evidence for a deep upper mantle thermal anomaly beneath east Africa. Geology. 28, 599–602.

Nyblade, A.A., 2002. Crust and upper mantle structure in East Africa: implications for the origin of Cenozoic rifting and volcanism and the formation of magmatic rifted margins. Geological Society of America Special Paper 362, 15–26.

Nyblade, A.A., Brazier, R.A., 2002. Precambrian lithospheric controls on the development of the East African rift system. Geology 30 (8), 755–758.

Nyblade, A.A., Owens, T.J., Gurrola, H., Ritsema, .J, Langston, C.A., 2000. Seismic evidence for a deep upper mantle thermal anomaly beneath East Africa. Geology 28, 599–602.

Oehler, J-F., van Wyk de Vries, B., Laboratoire, P.L., 2005. Landslides and spreading of oceanic hot-spot and arc shield volcanoes on Low Strength Layers (LSLs): an analogue modeling approach. Journal of Volcanology and Geothermal Research 144, 169–189.

Ollier, C.D., Pain, C.F., 2000. The origin of mountains. Routledge, London.

Omar, G.I., Kohn, B.P., Lutz, T.M., Faul, H., 1987. The cooling history of the Silurian to Cretaceous alkaline ring complexes south Eastern Desert, Egypt, as revealed by fission track analysis. Earth and Planetary Science Letters 83, 94–108.

Omar, G.I., Steckler, M.S., 1995. Fission track evidence on the initial rifting of the Red Sea: two pulses, no propagation. Science 270, 1341-1344.

Omar, G.I., Steckler, M.S., Buck, W.R., Kohn, B.P., 1989. Fission track analysis of basement apatites at the western margin of the Gulf of Suez Rift, Egypt: evidence for synchroneity of uplift and subsidence. Earth and Planetary Science Letter 94, 316–328.

Paris, R., Guillou, H., Carracedo, J.C., Pérez-Torrado, F.J., 2005. Volcanic and morphological evolution of La Gomera (Canary Islands), based on new K-Ar ages and magnetic stratigraphy: implications for oceanic island evolution. Journal of Geological Society of London 162, 501–512.

Pearce, N.J.G., Perkins, W.T., Westage, J.A., Gorton, M.P., Jackson, S.E., Neal, C.R., Chenery, S.P., 1997. A compilation of new and published major and trace element data for NIST SRM 610 and NIST SRM 612 glass reference materials. Geostandards Newsletter: The Journal of Geostandards and Geoanalysis 21, 115-144.

Petters, S.W., 1991.Regional geology of Africa. In: Bhattacharji S, Friedmann GM, Neugebauer HJ, Seilacher A (eds) Lecture Notes Earth Sciences 40. Springer, Heidelberg.

Pickford, M., Senut, B., Hadoto, D., 1993.Geology and palaeobiology of the Albertine Rift valley in Uganda-Zaire. Vol. I. Geol. Occas. Publ., 24. Centre International pour la Formation et les Echanges Geologiques, Orléans.

Pik, R., Marty, B., Carignan, J., Lavé, J., 2003. Stability of the Upper Nile drainage network (Ethiopia) deduced from (U–Th)/He thermochronometry: implications for uplift and erosion for the Afar plume dome. Earth and Planetary Science Letters 215, 73–88.

Pik, R., Marty, B., Carignan, J., Yirgu, G., Ayalew, T., 2008. Timing of East African Rift development in southern Ethiopia: Implication for mantle plume activity and evolution of topography. Geology 36, 167–170.

Platt, J.P., England, P.C., 1993. Convective removal of lithosphere beneath mountain belts: thermal and mechanical consequences. American Journal of Science 293, 307–336.

Price, P.B., Walker, R.M., 1962. Chemical etching of charged particle tracks. Journal of Applied Physics 33, 3407-3412.

Rahn, M.K., Brandon, M.T., Batt, G.E., Garver, J.I., 2004. A zero-damage model for fission-track annealing in zircon. American Mineralogist, 89, 473-484.

Rahn, M.K.W., 2001. The Metamorphic and Exhumation History of the Helvetic Alps, Switzerland, as Revealed by Apatite and Zircon Fission Tracks. Unpublished Habilitation thesis Universität Freiburg, pp. 140.

Razzkazov, S.V., Logachev, N.A., Ivanov, A.V., Boven, A.A., Maslovskaya, M.N., Saraniana, E.V., Brandt, I.S., Brandt, S.B., 2003. A Magmatic Episode in the Western Rift of East Africa (19–17 Ma). Russian Geology and Geophysics 44 (4), 307–314.

Reiners, P.W., Brandon, M.T., 2006. Using thermochronology to understand orogenic erosion. Annual Review of Earth and Planetary Sciences 34, 419–466.

Reiners, P.W., Ehlers, T.A., 2005. Low-temperature thermochronology: techniques, interpretations and applications. Reviews in Mineralogy and Geochemistry 58, 151–176.

Reiners, P.W., Farley, K.A., 2001. Influence of crystal size on apatite (U–Th)/He thermochronology: an example from the Bighorn Mountains, Wyoming. Earth and Planetary Science Letters 188, 413–420.

Reiners, P.W., Farley, K.A., Hickes, H.J., 2002. He diffusion and (U–Th)/He thermochronometry of zircon: initial results from Fish Canyon Tuff and Gold Butte. Tectonophysics 349, 247–308.

Reiners, P.W., Nicolescu, S., 2006. Measurement of parent nuclides for (U-Th)/He chronometry by solution sector ICP-MS, ARHDL Report 1. http://www.geo.arizona.edu/~reiners/arhdl/arhdl.htm

Reiners, P.W., Shuster, D.L., 2009. Thermochronology and landscape evolution. Physics Today 62 (9), 31–36.

Reiners, P.W., Spell, T.L., Nicolescu, S., Zanetti, K.A., 2004. Zircon (U–Th)/He thermochronometry: He diffusion and comparisons with 40Ar/39Ar dating. Geochimica et Cosmochimica Acta 68, 1857–1887.

Reymer, A.P.S., 1983. Metamorphism and tectonism of Pan-African terrain in southeastern Sinai. Precambrian Research 19, 225-238.

Ries, A.C., Shackleton, R.M., Graham, R.H., Fitches, W.R., 1983. Pan African structures, ophiolites and mélange in the Eastern Desert of Egypt: a traverse at 26˚N. Journal of Geological Society London 140, 75–95.

Rimi, A., 1990. Geothermal Gradients and Heat Flow Trends in Morocco. Geothermics 19 (5), 443-454.

Ring, U., 1993.Aspects of the kinematic history and mechanisms of superposition of Proterozoic mobile belt of eastern central AFRICA (northern Malawi and southern Tanzania). Precambrian Res. 62, 207–226.

Ring, U., 1995.Lithological and kinematic constraints on the evolution of the Karoo rifts of northern Malawi (Africa). Geologische Rundschau 84, 607–625.

Ring, U., 2008. Extreme uplift of the Rwenzori Mountains in the East African Rift, Uganda: structural framework and possible role of glaciations. Tectonics 27.doi:10.1029/ 2007TC002176

Ring, U., Betzler, C., 1995. Geology of the Malawi Rift: kinematic and tectonosedimentary background to the Chiwondo Beds, northern Malawi. Journal of Human Evolution 28, 7–21.

Ring, U., Betzler, C., Delvaux, D., 1992.Normal vs. strike-slip faulting during rift development in East Africa: the Malawi rift. Geology 20, 1015–1018.

Ritsema, J., Jan der Heijst, H., Woodhouse, J., 1999. Complex shear wave velocity structure imaged beneath Africa and Iceland. Science 286, 1925–1928.

Roberts, E.M., Stevens, N.J., O’Connor, P.M., et al., 2012. Initiation of the western branch of the East African Rift coeval with the eastern branch. Nature Geoscience 5, 289–294. http://dx.doi.org/10.1038/ngeo1432

Robertson, A. H. F., Bernouilli, D., 1982. Stratigraphy, facies and significance of Late Mesozoic and early Tertiary sedimentary rocks of Fuerteventura (Canary Islands) and Maio (Cape Verde Islands), in Geology of the Northwest African Continental Margin, U. Von Rad et al. (Eds.), Springer, New York, 498 – 525.

Rodríguez-Losada, J.A., 1988. El Complejo Traquítico Fonolítico de La Gomera (Islas Canarias). PhD Thesis, Univ. Complutense, Madrid, Spain. pp. 414.

Rowley, D.B., Sahagian, D., 1986. Depth-dependent stretching: a different approach. Geology 14, 32–35.

Royden, L., Keen, C.E., 1980. Rifting process and thermal evolution of the continental margin of eastern Canada determined from subsidence curves. Earth and Planetary Science Letters 51, 343–361.

Sachau, T., Koehn, D., 2010. Faulting the lithosphere during extension and related rift-flank uplift, a numerical study. International Journal of Earth Science 99, 1619–1632. doi:10.1007/s00531-010-0513-6

Sachau, T., Koehn, D., Passchier, C., 2011. Lattice-particle simulation of stress patterns in a Rwenzori-type rift transfer zone. Journal of African Earth Sciences 61(4), 286–295. doi:10.1016/j.jafrearsci.2011.08.006

Sachau, T., Koehn, Stamps, D.S., Lindenfeld, M., 2015. Fault kinematics and stress fields in the Rwenzori Mountains. International Journal of Earth Science (GeolRundsch). doi: 10.1007/s00531-015-1162-6

Said, R., 1962. The Geology of Egypt, first ed., Elsevier, Amsterdam, pp. 377.

Said, R., 1990.The Geology of Egypt, second ed. A.A. Balkema, Rotterdam, pp. 734.

Sánchez Guzman, J., Abad, J., 1986. Sondeo geotérmico Lanzarote-1, significado geológico y geotérmico. Anales de Física serie B, 82, Special Issue, 102-109.

Schandelmeier, H., Klitzsch, E., Hendriks, F. and Wycisk, P., 1987. Structural development of northeast Africa since Precambrian times, Berliner Geowissenschaftliche Abhandlungen (A) 75.1, pp. 5-24.

Schilling, J.-G., Anderson, R.N., Vogt. P., 1976. Rare earth, Fe and Ti variations along the Galapagos spreading centre and their relationship to the Galapagos mantle plume. Nature 261, 108–13.

Schlueter, T., 1994. Zur Verbreitung, Fazies und Stratigraphie der Karoo in Uganda. Berliner Geowissenshaftliche Abhandlungen E13, 453–467.

Schlueter, T., 1997. Geology of East Africa. Gebr. Bortntraeger, Berlin, Stuttgart.

Schmincke, H.U., 1973. Magmatic evolution and tectonic regime in the Canaries, Madeira and Azores group. Geological Society of America Bulletin 84, 633–648.

Seilacher, A., 1990. Paleozoic trace fossils. In: Said, R. (eds.). The Geology of Egypt. Balkema, Rotterdam, pp. 649–670.

Sestini, G., 1984. Tectonic and sedimentary history of the NE African margin (Egypt–Libya). In: J.E. Dixon and A.H.F. Robertson, Editors, The Geological Evolution of the Eastern Mediterranean 17, Geological Society of London, pp. 161–176.

Shackleton, R., 1978. Geological map of the Ologesailie Area, Kenya. In: Geological Background to Fossil Man: Recent Research in the Gregory Rift Valley, East Africa. Toronto University Press, Buffalo, pp. 175.

Shackleton, R.M., Ries, A.C., Graham, R.H., Fitches, W.R., 1980. Late Precambrian ophiolite mélange in the Eastern Desert of Egypt. Nature 285, 472–474.

Shuster, D.L., Farley, K.A., 2009. The influence of artificial radiation damage and thermal annealing on helium diffusion kinetics in apatite. Geochimica et Cosmochimica Acta 73 (1), 183–196.

Shuster, D.L., Flowers, R.M., Farley, K.A., 2006. The influence of natural radiation damage on helium diffusion kinetics in apatite. Earth and Planetary Science Letters 249, 148–161.

Siebert, L., 1984. Large volcanic debris avalanches: characteristics of source areas, deposits, and associated eruptions. Journal of Volcanology and Geothermal Research, 22, 163-197.

Sleep, N., 2006. Mantle plumes from top to bottom. Earth Science Review 77, 231–271.

Smith, J.R., Malahoff, A., Shor, A.N., 1999. Submarine geology of the Hilina slump and morpho-structural evolution of Kilauea volcano, Hawaii. Journal of Volcanology and Geothermal Research 94, 59–88.

Spiegel, C., Kohn, B.P., Belton, D.X., Gleadow, A.J.W., 2007. Morphotectonic evolution of the central Kenya rift flanks: implications for late Cenozoic environmental change in East Africa. Geology 35 (5), 427–430.

Stampfli, G.M., Raumer, J.F., and Borel, G.D., 2002. Paleozoic evolution of pre-Variscan terranes: From Gondwana to the Variscan collision: in Martinez Catalan, J. R., Hatcher, R. D., Arenas, R., and Diaz Garcia, F., eds., Variscan-Appalachian dynamics: the building of the late Paleozoic basement. Geological Society of America Special Paper 364, 263-280.

Starz, M., 2012. Thermochronology in Eastern D. R. Congo area. Master Thesis Institute of Earth Sciences, University of Heidelberg, p., 98.

Staudigel, H., Feraud, G., Giannerini, G., 1986. The history of intrusive activity on the island of La Palma (Canary Islands). Journal of Volcanology and Geothermal Research 27, 299–322.

Steckler, M.S., Berthelot, F., Lyberis, N., Le Pichon, X., 1988. Subsidence in the Gulf of Suez: implications for rifting and plate kinematics. Tectonophysics 153, 249-270.

Steckler, M.S., Omer, G.I., 1994. Controls on erosional retreat of the uplifted rift flanks at the Gulf of Suez and northern Red Sea. Journal of Geophysical Research 99, 12159-12173.

Steckter, M.S., 1985. Uplift and extension at the Gulf of Suez-indications of induced mantle convection. Nature 317, 135-139.

Steiner, C.W., Hobson, A., Favre, P., Stampfli, G.M., Hernandez, J., 1998. Early Jurassic sea-floor spreading in the Central Atlantic-the Jurassic Sequence of Fuerteventura (Canary Islands). Geological Society of America Bulletin 110, 1304–1317.

Stern, R.J., 1994, Arc-assembly and continental collision in the Neoproterozoic East African Orogen: Implications for the consolidation of Gondwanaland: Annual Review of Earth and Planetary Sciences, v. 22, p. 319–351.

Stern, R.J., Hedge, C.E., 1985. Geochronologic and isotopic constraints on late Precambrian crustal evolution in the Eastern Desert of Egypt. American Journal of Science 285, 97–127.

Stern, R.J., Manton, W.I., 1987. Age of Feiran basement rocks, Sinai: implications for late Precambrian crustal evolution in the northern Arabian–Nubian Shield. J. Geological Society London 144, 569–575.

Stillman, C.J., 1987. A Canary Islands Dyke Swarm: Implications for the Formation of Oceanic Islands by Extensional Fissural Volcanism. In: Halls, H.C., Fahrig, W.F. (Eds.), Mafic Dyke Swarms: Geol Assoc Canada Spec Paper, pp. 34–54.

Stillman, C.J., 1999. Giant Miocene landslides and the evolution of Fuerteventura, Canary Islands. Journal of Volcanology and Geothermal Research 94, 89–104.

Stillman, C.J., Fúster, J.M., Bennell-Baker, M.J., Muñoz, M., Smewing, J.D., Sagredo, J., 1975. Basal Complex of Fuerteventura (Canary Islands) is an oceanic intrusive complex with rift-system affinities? Nature 257, 469–471.

Tanner, P.W.G., 1971. The Stanley Volcanics formation of Ruwenzori, Uganda. Fifteenth Annual Report of the Research Institute of African Geology. University of Leeds.

Taylor, R.G., Howard, K.W.F., 1998. Post-Palaeozoic evolution of weathered land surfaces in Uganda by tectonically controlled deep weathering and stripping. Geomorphology 25 (3–4),173–192.

Teixell, A., Ayarza, P., Zeyen, H., Fernàndez, M., and Arboleya, M.L., 2005. Effects of mantle upwelling in a compressional setting: The Atlas Mountains of Morocco. Terra Nova 17, 456–461. doi: 10.1111/j.1365-3121. 2005.00633.x.

Theunissen, K., Klerkx, J., Melnikov, A., Mruma, A., 1996. Mechanisms of inheritance of rift faulting in the western branch of the East African Rift, Tanzania. Tectonics 15 (4), 776–790.

Thomas, R.J., Von Veh, M.W., McCourt, S., 1993. The tectonic evolution of southern Africa: an overview. Journal of African Earth Sciences 16, 5-24.

Tugume, F.A., Nyblade, A.A., 2009. The depth distribution of seismicity at the northern end of the Rwenzori Mountains; implications for heat flow in the western branch of the East African Rift system in Uganda. South African Journal of Geology 112 (3–4), 261–276.

Upcott, N.M., Mukasa, R.K., Ebinger, C.J., 1996.Along-axis segmentation and isostasy in the Western rift, East Africa.Journal of Geophysical Research 101 (B2), 3247–3268.

Urchulutegui, J.F., Fernàndez, M., and Zeyen, H., 2006. Lithospheric structure in the Atlantic-Mediterranean transition zone (southern Spain, northern Morocco): A simple approach from regional elevation and geoid data. Comptes Rendus Geoscience 338, 140–151. doi:10.1016/j.crte.2005.11.004.

Van Damme, D., Pickford, M., 2003. The late CenozoicThiaridae (Mollusca, Gastropoda, Cerithioidea) of the Albertine Rift Valley (Uganda–Congo) and their bearing on the origin and evolution of the Tangayikanthallasoidmalacofauna. Hydrobiologia 498, 1–83.

Van der Beek, P., Mbede, E., Andriessen, P., Delvaux, D., 1998. Denudation history of the Malawi and Rukawa Rift flanks (East African Rift System) from apatite fission track thermochronology. Journal of African Earth Sciences 26, 363–385.

Van der Beek, P.A., Cloetingh, S., Andriessen, P.A.M., 1994. Mechanisms of extensional basin formation and vertical motions at rift flanks: constraints from tectonic modelling and fission track thermochronology. Earth Planetary Science Letters 121, 4 l 7-433.

van Hinsbergen, D.J.J., Kapp, P., Dupont-Nivet, G., Lippert, P.C., DeCelles, P.G., Torsvik, T.H., 2011. Restoration of Cenozoic deformation in Asia, and the size of Greater India. Tectonics 30, TC5003. http://dx.doi.org/10.1029/2011TC002908

Vermeesch, P., D. Avigad, McWilliams, M.O., 2009. 500 m.y. of thermal history elucidated by multi-method detrital thermochronology of North Gondwana Cambrian sandstone (Eilat area, Israel). Geological Society of America Bulletin 121, 1204–1216. doi:10.1130/B26473.1.

Vermeesch, P., Seward, D., Latkoczy, C., Wipf, M., Guenther, D., Baur, H., 2007. Alpha-emitting mineral inclusions in apatite, their effect on (U–Th)/He ages, and how to reduce it. Geochimica et Cosmochimca Acta 71, 1737–1746.

Von Huene, R., Lallemand, S., 1990. Tectonic erosion along the Japan and Peru convergent margins, Geol. Sot. Am. Bull. 102, 704-720.

Von Huene, R., Scholl, D.W., 1991. Observations at convergent margins concerning sediment subduction, subduction erosion and growth of continental crust, Rev. Geophys. 29, 279-3 16.

Wagner, G.A., 1972. Spaltspurenalter von Mineralen und natürlichen Gläsern: eine Übersicht. Fortschritte der Mineralogie 49, 114–145.

Wagner, G.A., 1979. Correction and interpretation of fission track ages, in: Lectures in Isotope Geology. E. JLger and J.C. Hunziker, eds., pp. 170-177.

Wagner, G.A., Van den haute, P., 1992. Fission-track Dating. Enke Publisher. pp. 285.

Wagner, M., Altherr, R. and van den Haute, P., 1992. Apatite fission-track analysis of Kenyan basement rocks: constraints on the thermotectonic evolution of the Kenya dome. A reconnaissance study. Tectonophysics 204, 93-110.

Walder, A.J., Platzner, I., Freedman, P.A., 1993. Isotope ratio measurement of lead, neodymium and neodymium-samarium mixtures, hafnium and hafnium-lutetium mixtures with a double focusing multiple collector inductively coupled plasma mass spectrometer. Journal of Analytical Atomic Spectrometry 8, 19-23.

Watts, A.B., Masson, D.G., 1995. A giant Landslide on the north flank of Tenerife, Canary Islands. Journal of Volcanology and Geothermal Research 100 (B12), 24487–24498.

Wayland, E. J., 1921. Some account of the geology of the Lake Albert rift valley. The Geographical Journal 58, 344–359.

Weissel, J.K., Karner, G.D., 1989. Flexural uplift of rift flanks due to mechanical unloading of the lithosphere during extension. Journal of Geophysical Research 94 (10), 13919–13950.

Willett, S.D., 1999. Orogeny and orography: The effects of erosion on the structure of mountain belts. Journal of Geophysical Research 104, 28957-28981.

Wilson, J.T., 1963. A possible origin of the Hawaiian Islands. Canadian Journal of Physics 41, 863-870.

Wilson, J.T., 1965. A new class of faults and their bearing on continental drift. Nature 207, 343–7.

Wilson, J.T., 1966. Did the Atlantic close and then reopen? Nature 211, 676–681.

Wipf, M., Glasmacher, U.A., Stokli, D.F., Emmerich, A., Bechstadt, T., Bauer, H., 2010. Reconstruction of the differentiated long-term exhumation history of Fuerteventura, Canary Islands, Spain, through fission-track and (U-Th-Sm)/He data. International Journal of Earth Science (Geol Rundsch) 99, 675-686.

Woelbern, I., Ruempker, G., Schumann, A., Muwanga, A., 2010. Crustal thinning beneath the Rwenzori region, Albertine rift, Uganda, from receiver-function anlysis. International Journal of Earth Sciences. http://dx.doi.org/10.1007/ s00531-009-0509-2

Wolf, R.A., Farley, K.A., Kass, D.M., 1998. Modeling of the temperature sensitivity of the apatite U–Th/He thermochronometer. Chemical Geology 148, 105–114.

Wolf, R.A., Farley, K.A., Silver, L.T., 1996. Helium diffusion and low-temperature thermochronometry of apatite. Geochimica et Cosmochimica Acta 60 (21), 4231–4240.

Wolfeden, E., Ebinger, C.J, Yirgu, G., Deino, A., Ayalew, D., 2004. Evolution of the northern Main Ethiopian Rift: Birth of a triple junction. Earth Planetary Science Letters 224, 213-228.

Wopfner, H. 1990. Rifting in Tanzanian Karoo basins and its economic implications In: Etudes Recentes sur la Geologie de l'Afrique, 15e colloque de Geologie Africaine, Nancy 1990 (Edited by Rocci, G. and Deschamps, M.) CIFEG Occasional Publications 1990/22, 217-220.

Wopfner, H. 1993. Structural development of Tanzanian Karoo basins and the break-up of Gondwana. In: Gondwana Eight; Assembly, Evolution and Dispersal {Edited by Findlay, R. H., Unrug, R., Banks, M. R. and Veevers. J..L) pp531-540. Balkema, Rotterdam.

Yamada, R., Tagami, T, Nishimura, S, Ito, H., 1995. Annealing kinetics of fission tracks in zircon: an experimental study. Chemical Geology (Isotope Geoscience Section) 122, 249-258.

Zachos, J., Pagani, M., Sloan, L., Thomas, E., Billups, K., 2001. Trends, rhythms, and aberrations in global climate 65 Ma to present. Science 292, 686–693.

Zachos, J.C., Dickens, G.R., Zeebe, R.E., 2008. An early Cenozoic perspective on greenhouse warming and carbon-cycle dynamics. Nature 451/17, 279-283. doi:10.1038/nature06588

Zeitler, P.K., Meltzer, A.S., Koons, P.O., Craw, D., Hallet, B., Chamberlain, C.P., Kidd, W.S.F., Park, S.K., Seeber, L., Bishop, M., Shroder, J., 2001. Erosion, Himalayan geodynamics, and the geomorphology of metamorphism. Geological Society of America Today 11, 4-9.

Zhang, M., Boatner, L., Salje, E.K.H., Honda, S., Ewing, R.C., 2008a. Pb+ irradiation of synthetic zircon (ZrSiO4): infrared spectroscopic investigation. American Mineralogist 93, 1418–1423.

Zhao, D., 2001b. Seismic structure and origin of hotspots and mantle plumes. Earth and Planetary Science Letters 192, 251–265.

Zhao, D., 2004. Global tomographic images of mantle plumes and subducting slabs: Insight into deep Earth dynamics. Physics of the Earth and Planetary Interiors 146, 3–34.

Zhao, D., 2007. Seismic images under 60 hotspots: search for mantle plumes. Gondwana Research 12, 335–355.

Zhao, D., 2015. Multiscale Seismic Tomography. Springer Geophysics, p. 304.

Zhao, D., Yamamoto, Y., Yanada, T., 2013. Global mantle heterogeneity and its influence on teleseismic regional tomography. Gondwana Research 23, 595–616.

Ziegler, P.A., 1989. Evolution of Laurussia. In: A Study in Late Paleozoic Plate Tectonics. Kluwer Academic, Dordrecht, p. 102.

Ziegler, P. A., 1992. Geodynamics of rifting and implications for hydrocarbon habitat. Tectonophysics 215 (1-2), 221–253.

Ziegler, P.A., 1990. Geological Atlas of Western and Central Europe. Shell International Petroleum Mij, Geological Society Publishing House (Bath), 239 pp. 56 encl.

Ziegler, P.A., Cloetingh, S., 2004. Dynamic processes controlling evolution of rifted basins. Earth-Science Reviews 64, 1 –50.

11

APPENDIX

CONTENTS

11.1 RIFT WITH HIGH ELEVATED FLANKS (THE RWENZORI MOUNTAINS) - AFT DATA SHEETS

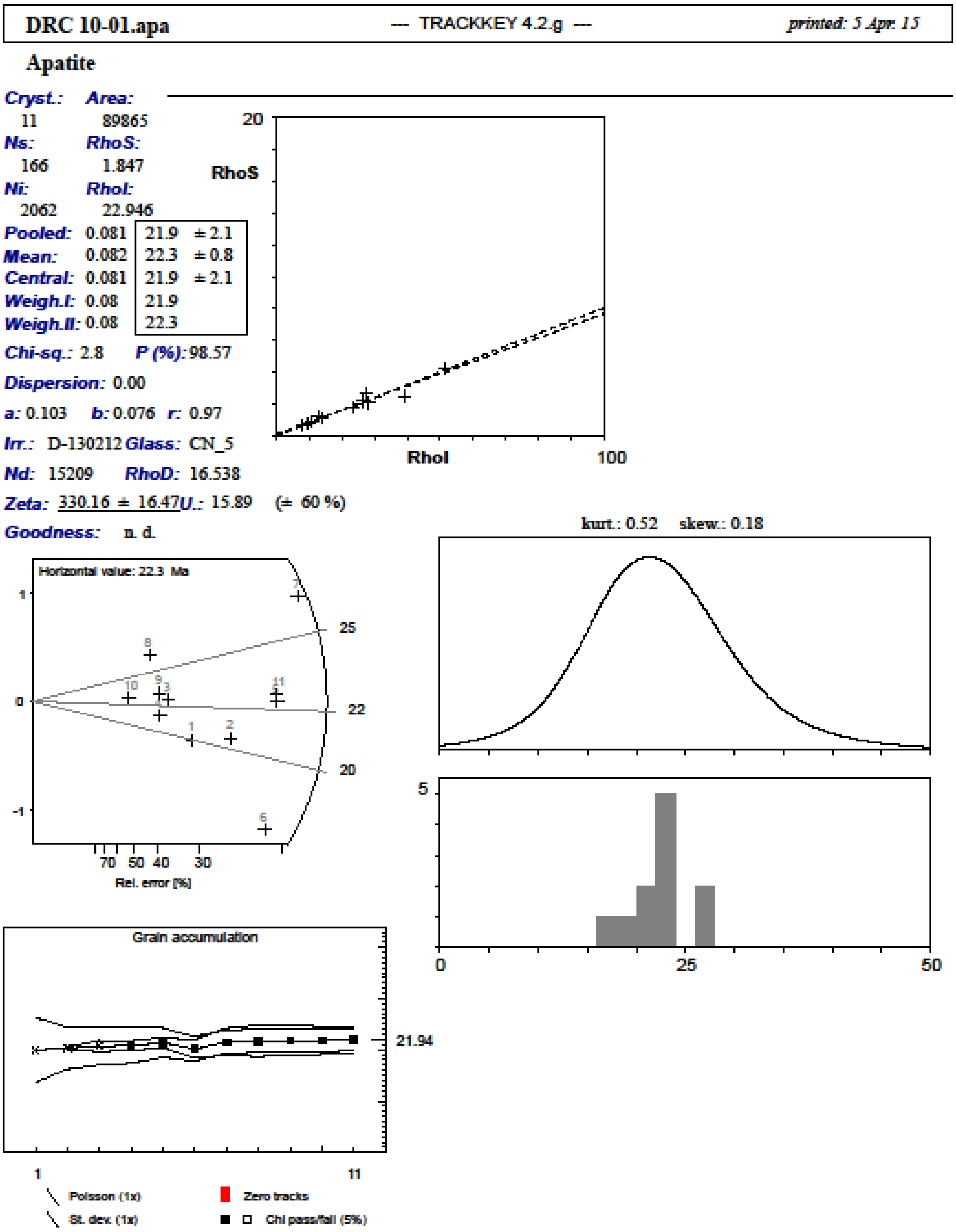

DRC 10-01.apa — TRACKKEY 4.2.g — *printed: 5 Apr. 15*

Apatite

Cryst.: 11 *Area:* 89865

Ns: 166 *RhoS:* 1.847

Ni: 2062 *RhoI:* 22.946

Pooled:	0.081	21.9	±2.1
Mean:	0.082	22.3	±0.8
Central:	0.081	21.9	±2.1
Weigh.I:	0.08	21.9	
Weigh.II:	0.08	22.3	

Chi-sq.: 2.8 *P (%):* 98.57

Dispersion: 0.00

a: 0.103 *b:* 0.076 *r:* 0.97

Irr.: D-130212 *Glass:* CN_5

Nd: 15209 *RhoD:* 16.538

Zeta: 330.16 ± 16.47 *U.:* 15.89 (± 60 %)

Goodness: n. d.

kurt.: 0.52 skew.: 0.18

DRC 10-03.apa — TRACKKEY 4.2.g — *printed: 5 Apr. 15*

Apatite

Cryst.: 18 ***Area:*** 147525

Ns: 258 ***RhoS:*** 1.749

Ni: 2301 ***RhoI:*** 15.597

Pooled:	0.112	29.9	± 2.5
Mean:	0.117	31.3	± 2.0
Central:	0.112	29.9	± 2.5
Weigh.I:	0.114	30.4	
Weigh.II:	0.12	31.3	

Chi-sq.: 13.49 ***P (%):*** 70.32

Dispersion: 0.01

a: 0.24 ***b:*** 0.097 ***r:*** 0.84

Irr.: D-130505 ***Glass:*** CN_5

Nd: 15167 ***RhoD:*** 16.179333

Zeta: 330.16 ± 16.47 ***U.:*** 10.86 (± 44 %)

Goodness: n. d.

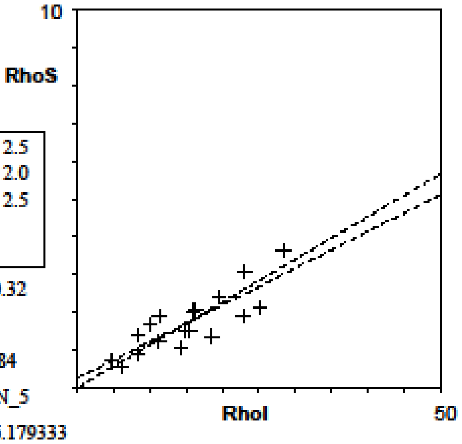

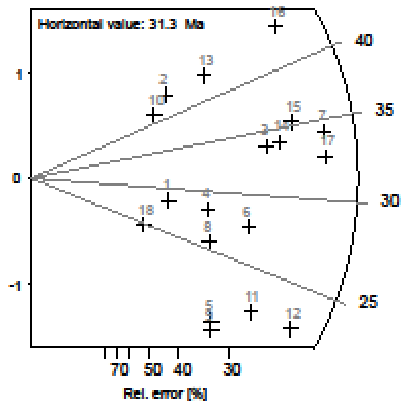

kurt.: -1.05 skew.: 0.30

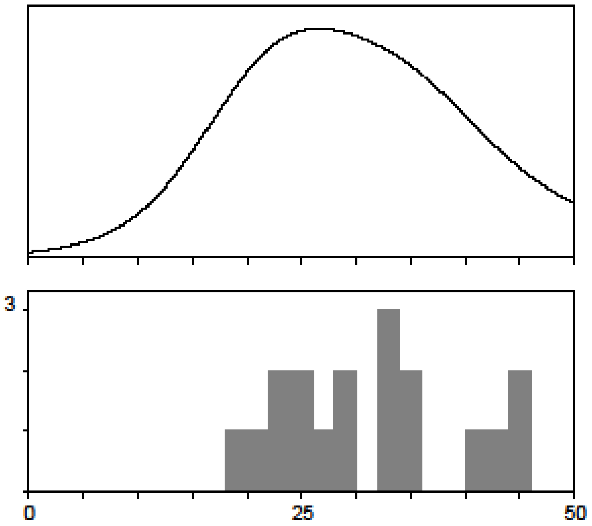

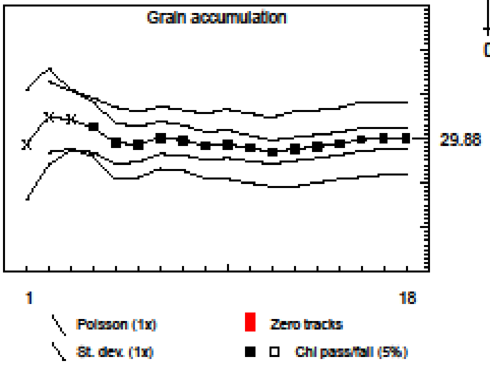

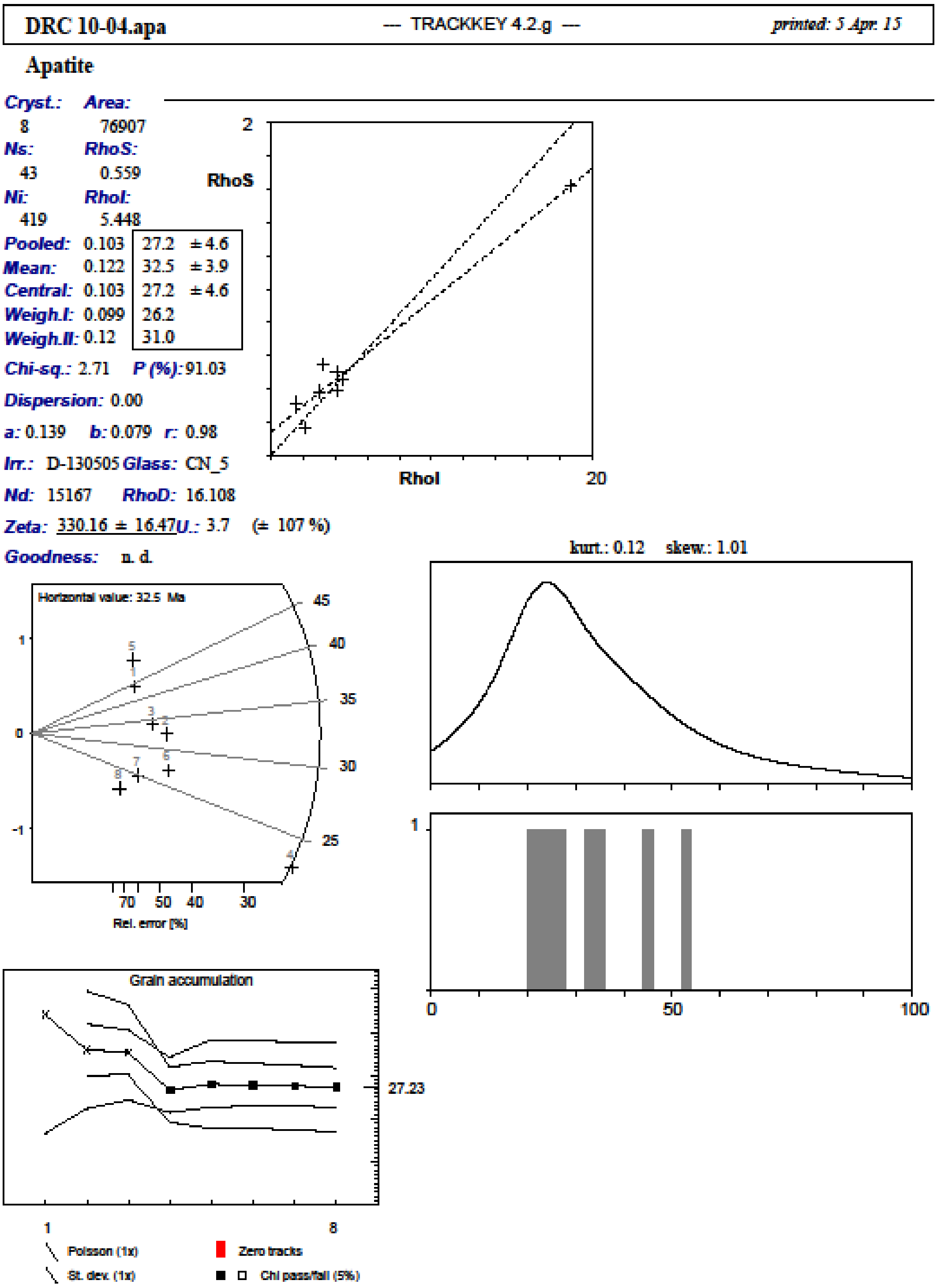

DRC 10-04.apa — TRACKKEY 4.2.g — *printed: 5 Apr. 15*

Apatite

Cryst.:	***Area:***		
8	76907		
Ns:	***RhoS:***		
43	0.559		
Ni:	***RhoI:***		
419	5.448		
Pooled:	0.103	27.2	±4.6
Mean:	0.122	32.5	±3.9
Central:	0.103	27.2	±4.6
Weigh.I:	0.099	26.2	
Weigh.II:	0.12	31.0	

Chi-sq.: 2.71 ***P (%):*** 91.03

Dispersion: 0.00

a: 0.139 ***b:*** 0.079 ***r:*** 0.98

Irr.: D-130505 ***Glass:*** CN_5

Nd: 15167 ***RhoD:*** 16.108

Zeta: 330.16 ± 16.47 ***U.:*** 3.7 (± 107 %)

Goodness: n. d.

kurt.: 0.12 skew.: 1.01

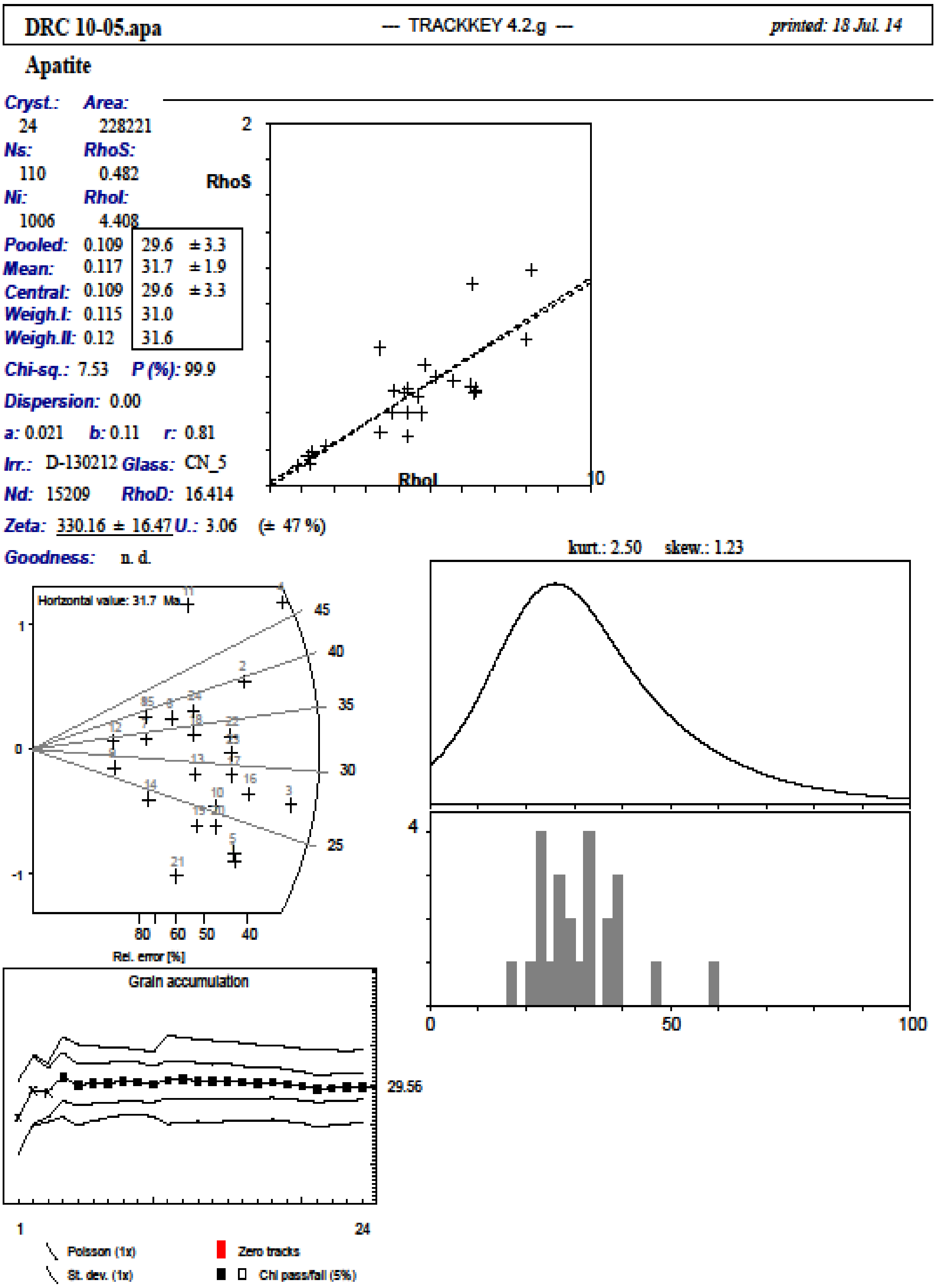

DRC 10-05.apa — TRACKKEY 4.2.g — *printed: 18 Jul. 14*

Apatite

Cryst.: 24 *Area:* 228221
Ns: 110 *RhoS:* 0.482
Ni: 1006 *RhoI:* 4.408
Pooled: 0.109 29.6 ± 3.3
Mean: 0.117 31.7 ± 1.9
Central: 0.109 29.6 ± 3.3
Weigh.I: 0.115 31.0
Weigh.II: 0.12 31.6
Chi-sq.: 7.53 *P (%):* 99.9
Dispersion: 0.00
a: 0.021 *b:* 0.11 *r:* 0.81
Irr.: D-130212 *Glass:* CN_5
Nd: 15209 *RhoD:* 16.414
Zeta: 330.16 ± 16.47 *U.:* 3.06 (± 47 %)
Goodness: n. d.

DRC 10-06.apa — TRACKKEY 4.2.g — *printed: 5 Apr. 15*

Apatite

Cryst.: 7 ***Area:*** 24404

Ns: 14 ***RhoS:*** 0.574

Ni: 94 ***RhoI:*** 3.852

Pooled:	0.149	39.3	± 11.4
Mean:	0.21	55.3	± 12.7
Central:	0.149	39.3	± 11.4
Weigh.I:	0.153	40.4	
Weigh.II:	0.20	53.8	

Chi-sq.: 4.48 ***P (%):*** 61.18

Dispersion: 0.00

a: 0.424 ***b:*** 0.062 ***r:*** 0.62

Irr.: D-130505 ***Glass:*** CN_5

Nd: 15167 ***RhoD:*** 16.036667

Zeta: 330.16 ± 16.47 ***U.:*** 3.2 (± 82 %)

Goodness: n. d.

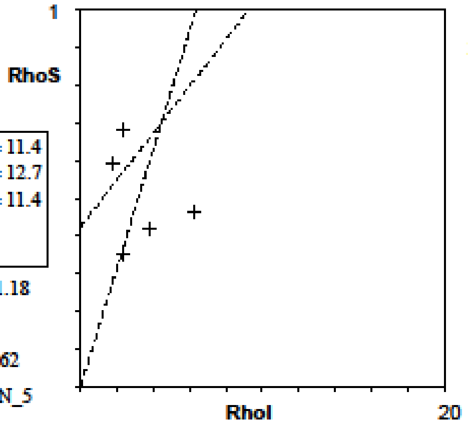

2 crystals outside the plot !

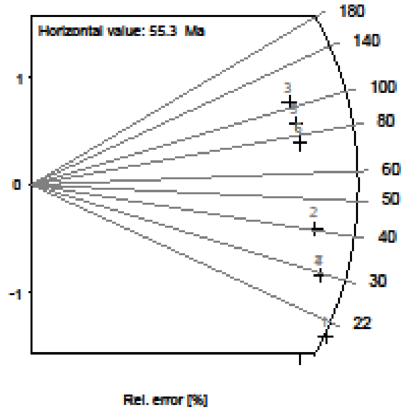

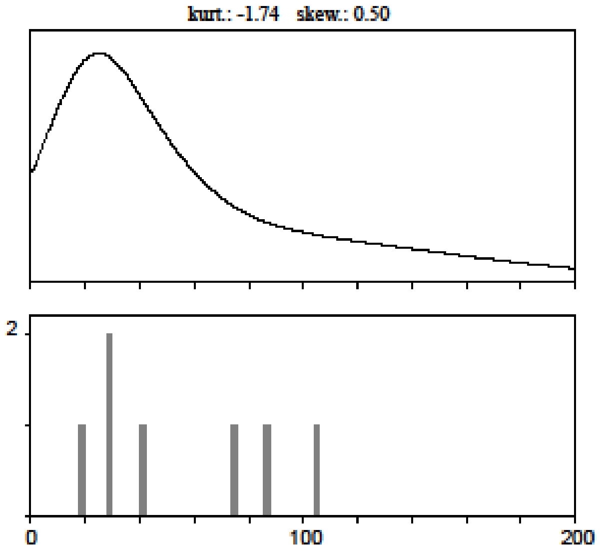

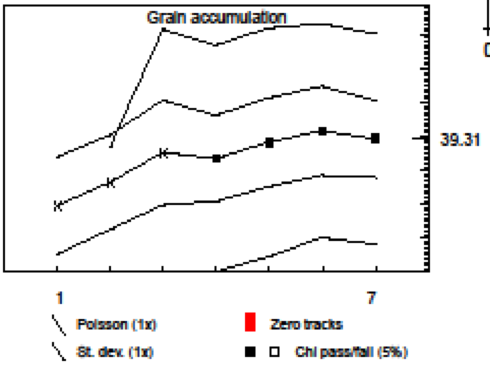

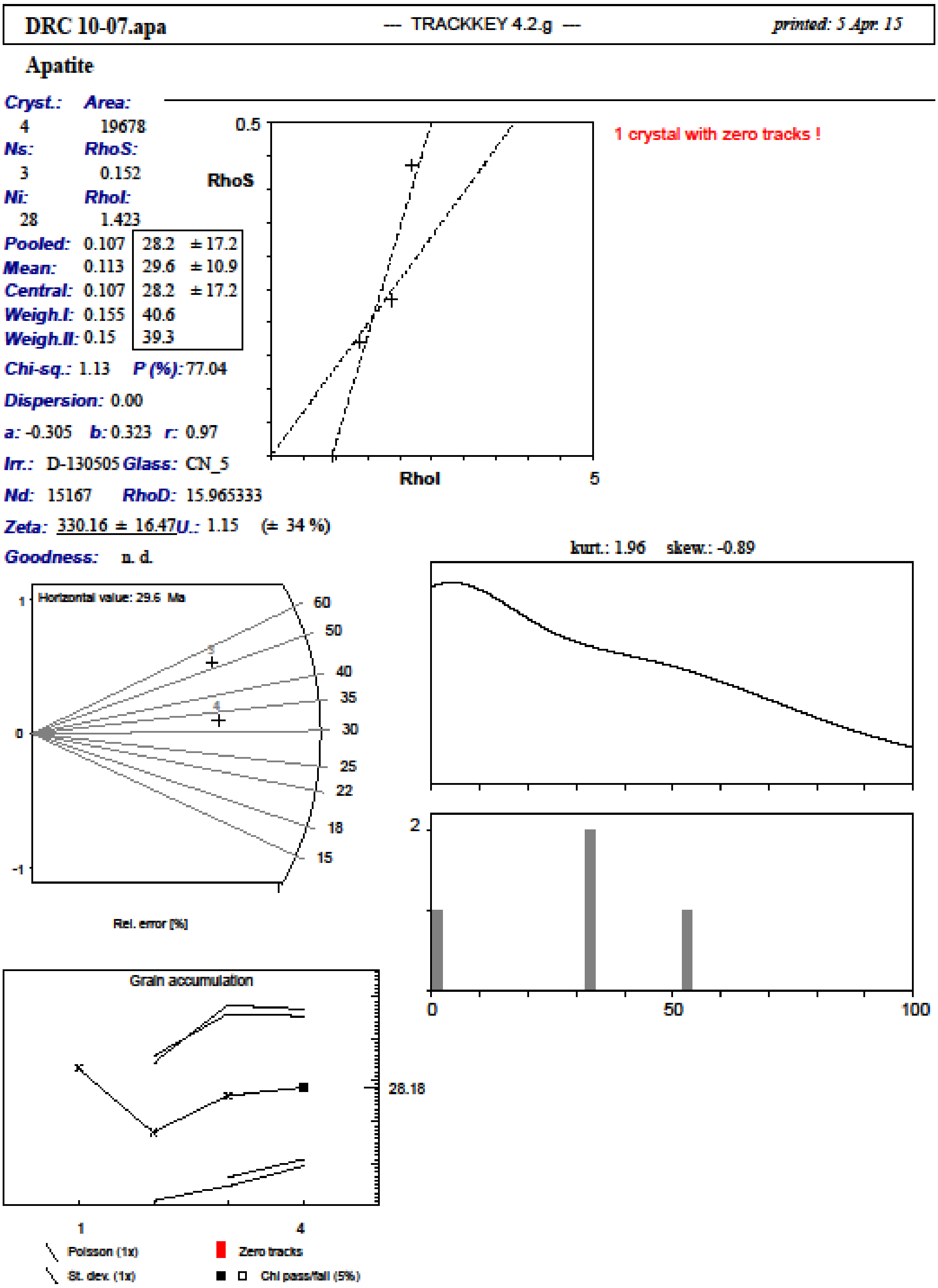

DRC 10-07.apa — TRACKKEY 4.2.g — *printed: 5 Apr. 15*

Apatite

Cryst.:	Area:
4	19678
Ns:	**RhoS:**
3	0.152
Ni:	**RhoI:**
28	1.423

Pooled:	0.107	28.2	± 17.2
Mean:	0.113	29.6	± 10.9
Central:	0.107	28.2	± 17.2
Weigh.I:	0.155	40.6	
Weigh.II:	0.15	39.3	

Chi-sq.: 1.13 **P (%):** 77.04

Dispersion: 0.00

a: -0.305 **b:** 0.323 **r:** 0.97

Irr.: D-130505 **Glass:** CN_5

Nd: 15167 **RhoD:** 15.965333

Zeta: 330.16 ± 16.47 **U.:** 1.15 (± 34 %)

Goodness: n. d.

1 crystal with zero tracks !

DRC 10-08.apa — TRACKKEY 4.2.g — *printed: 5 Apr. 15*

Apatite

Cryst.:	***Area:***
12	68193
Ns:	***RhoS:***
35	0.513
Ni:	***RhoI:***
395	5.792

Pooled:	0.089	23.2	± 4.3
Mean:	0.112	29.3	± 2.5
Central:	0.091	23.8	± 4.5
Weigh.I:	0.081	21.2	
Weigh.II:	0.11	28.5	

Chi-sq.: 5.27 ***P (%):*** 91.72

Dispersion: 0.12

a: 0.251 ***b:*** 0.054 ***r:*** 0.9

Irr.: D-130505 ***Glass:*** CN_5

Nd: 15167 ***RhoD:*** 15.894

Zeta: 330.16 ± 16.47 ***U.:*** 4.89 (± 152 %)

Goodness: n. d.

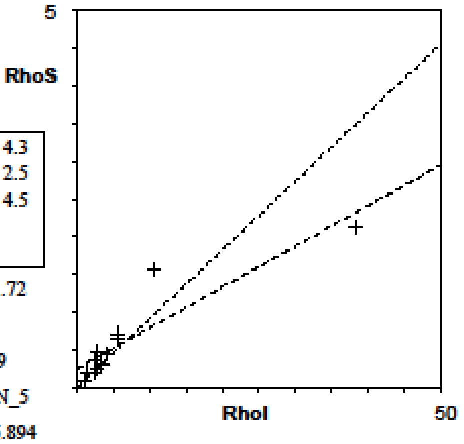

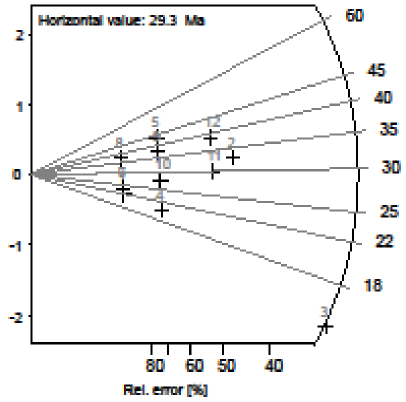

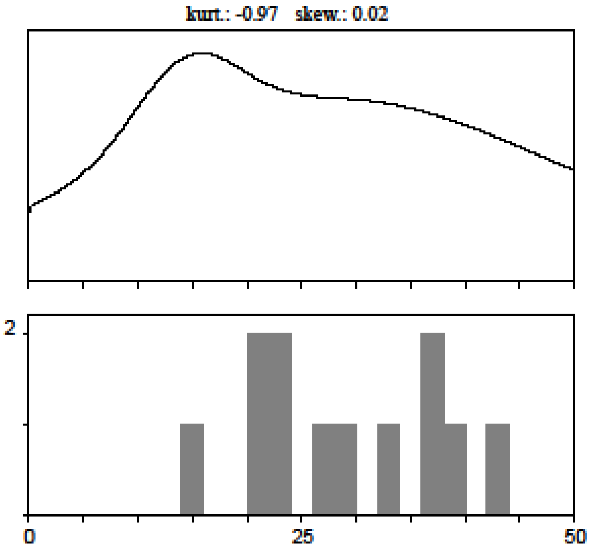

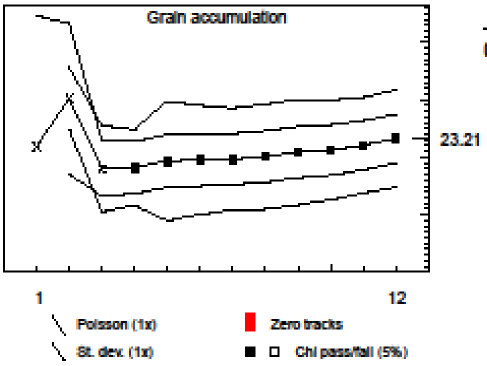

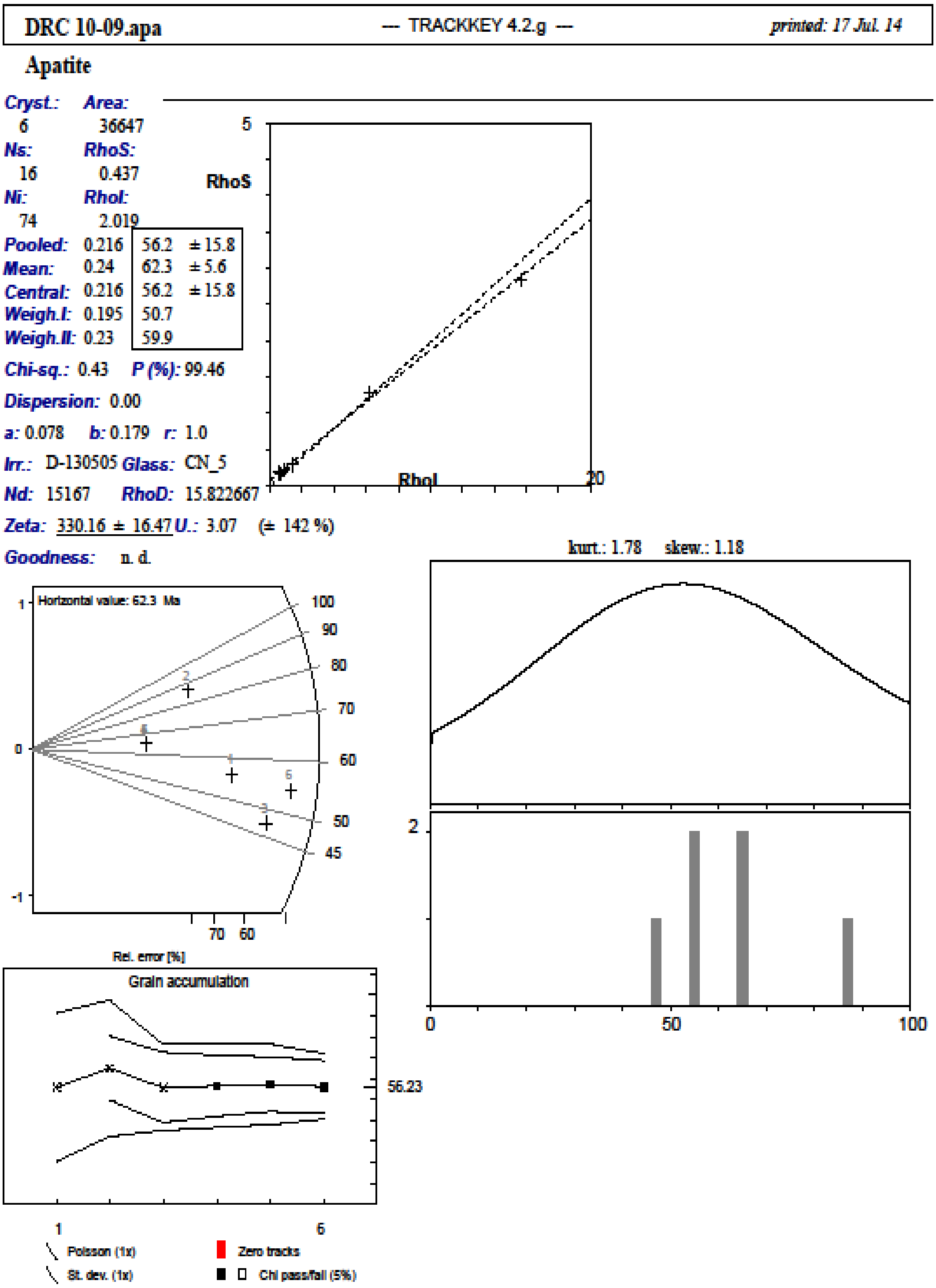

DRC 10-09.apa — TRACKKEY 4.2.g — *printed: 17 Jul. 14*

Apatite

Cryst.: 6	**Area:** 36647		
Ns: 16	**RhoS:** 0.437		
Ni: 74	**RhoI:** 2.019		
Pooled:	0.216	56.2	± 15.8
Mean:	0.24	62.3	± 5.6
Central:	0.216	56.2	± 15.8
Weigh.I:	0.195	50.7	
Weigh.II:	0.23	59.9	

Chi-sq.: 0.43 **P (%):** 99.46

Dispersion: 0.00

a: 0.078 **b:** 0.179 **r:** 1.0

Irr.: D-130505 **Glass:** CN_5

Nd: 15167 **RhoD:** 15.822667

Zeta: 330.16 ± 16.47 **U.:** 3.07 (± 142 %)

Goodness: n. d.

DRC 10-10.apa — TRACKKEY 4.2.g — *printed: 5 Apr. 15*

Apatite

Cryst.: 22 ***Area:*** 89974

Ns: 66 ***RhoS:*** 0.734

Ni: 336 ***RhoI:*** 3.734

Pooled:	0.196	50.9	± 7.3
Mean:	0.194	50.2	± 2.9
Central:	0.196	50.9	± 7.3
Weigh.I:	0.2	51.8	
Weigh.II:	0.20	52.1	

Chi-sq.: 3.81 ***P (%):*** 100.0

Dispersion: 0.00

a: 0.119 ***b:*** 0.163 ***r:*** 0.73

Irr.: D-130505 ***Glass:*** CN_5

Nd: 15167 ***RhoD:*** 15.751333

Zeta: 330.16 ± 16.47 ***U.:*** 2.88 (± 37 %)

Goodness: n. d.

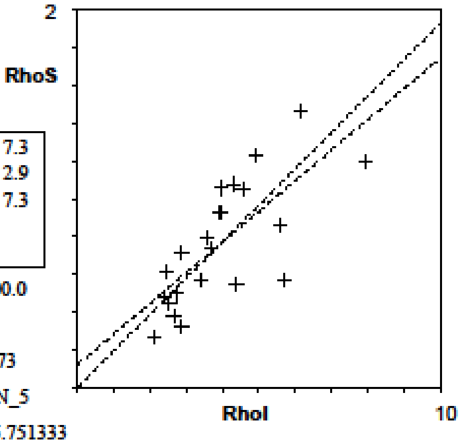

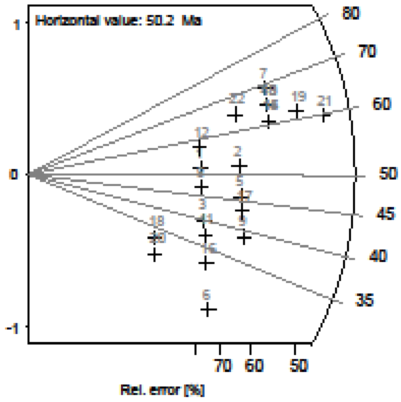

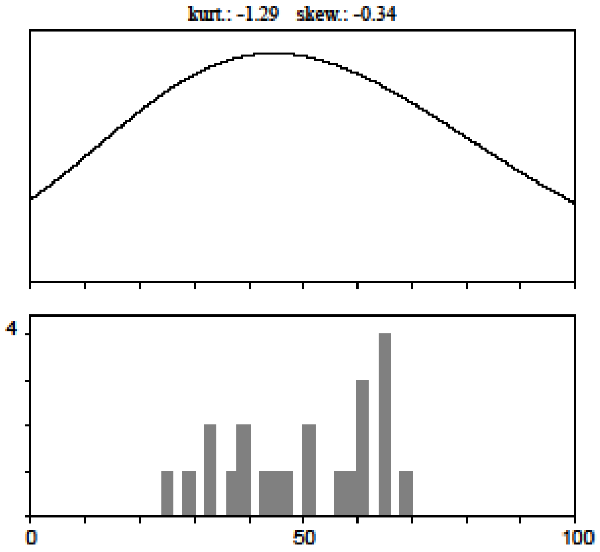

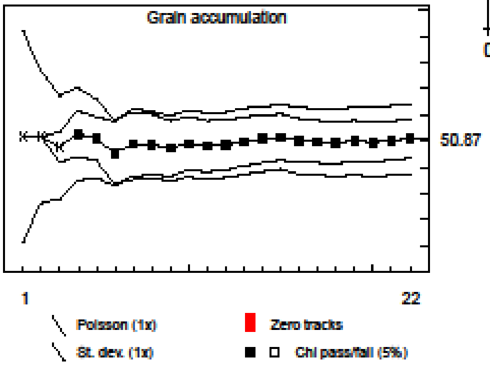

DRC 10-11.apa — TRACKKEY 4.2.g — *printed: 17 Jul. 14*

Apatite

Cryst.: 10 **Area:** 36164

Ns: 24 **RhoS:** 0.664

Ni: 118 **RhoI:** 3.263

Pooled:	0.203	52.3	± 12.0
Mean:	0.21	54.1	± 5.0
Central:	0.203	52.3	± 12.0
Weigh.I:	0.204	52.3	
Weigh.II:	0.21	54.2	

Chi-sq.: 1.01 **P (%):** 99.94

Dispersion: 0.00

a: 0.102 **b:** 0.174 **r:** 0.9

Irr.: D-130505 **Glass:** CN_5

Nd: 15167 **RhoD:** 15.636316

Zeta: 330.16 ± 16.47 **U.:** 2.76 (± 57 %)

Goodness: n. d.

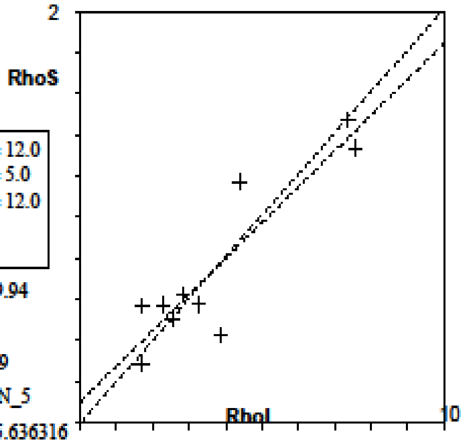

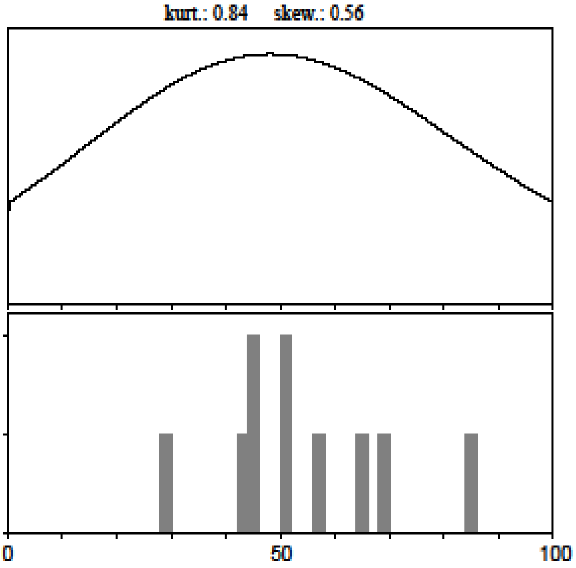

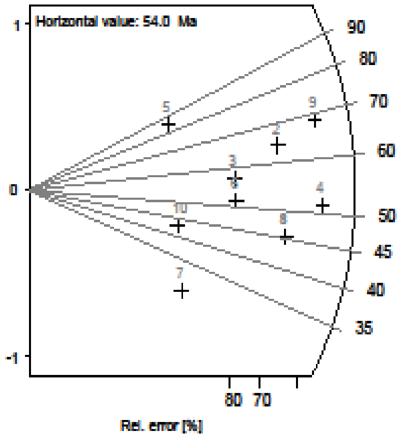

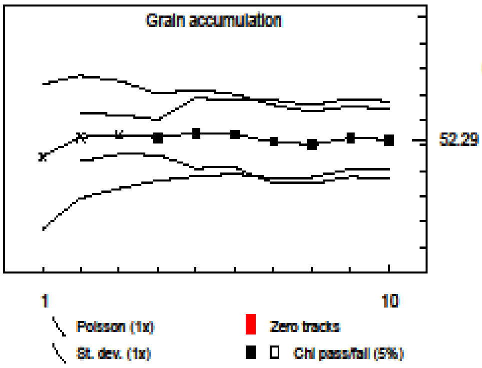

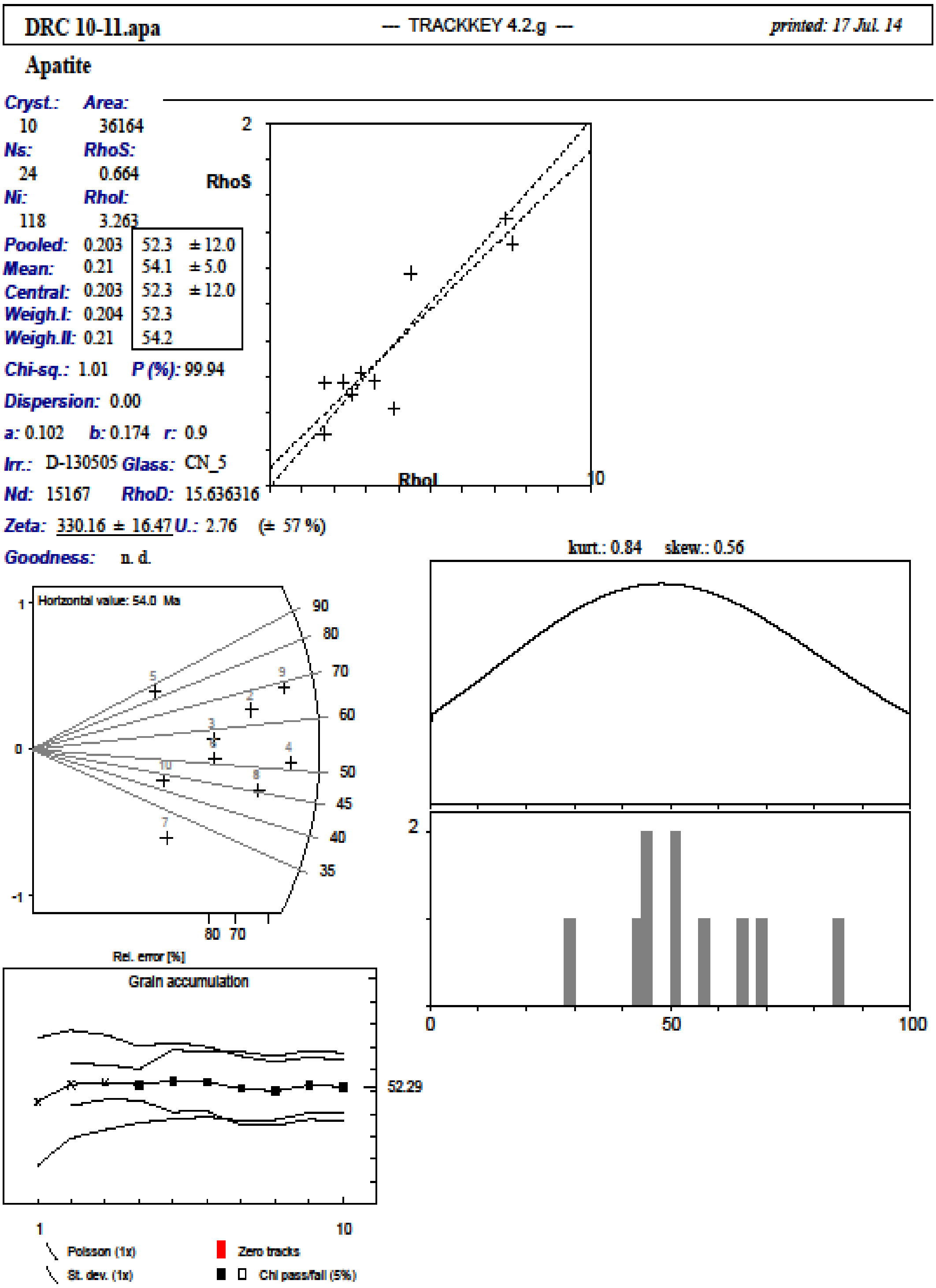

DRC 10-11.apa — TRACKKEY 4.2.g — *printed: 17 Jul. 14*

Apatite

Cryst.: 10 **Area:** 36164

Ns: 24 **RhoS:** 0.664

Ni: 118 **RhoI:** 3.263

Pooled:	0.203	52.3	± 12.0
Mean:	0.21	54.1	± 5.0
Central:	0.203	52.3	± 12.0
Weigh.I:	0.204	52.3	
Weigh.II:	0.21	54.2	

Chi-sq.: 1.01 **P (%):** 99.94

Dispersion: 0.00

a: 0.102 **b:** 0.174 **r:** 0.9

Irr.: D-130505 **Glass:** CN_5

Nd: 15167 **RhoD:** 15.636316

Zeta: 330.16 ± 16.47 **U.:** 2.76 (± 57 %)

Goodness: n. d.

DRC 10-14.apa — TRACKKEY 4.2.g — *printed: 5 Apr. 15*

Apatite

Cryst.:	**Area:**
13	71788
Ns:	**RhoS:**
39	0.543
Ni:	**RhoI:**
206	2.87

Pooled:	0.189	48.4	± 8.8
Mean:	0.205	52.5	± 4.9
Central:	0.189	48.4	± 8.8
Weigh.I:	0.161	41.1	
Weigh.II:	0.21	52.7	

Chi-sq.: 3.77 **P (%):** 98.72

Dispersion: 0.00

a: 0.226 **b:** 0.106 **r:** 0.97

Irr.: D-130505 **Glass:** CN_5

Nd: 15167 **RhoD:** 15.548947

Zeta: 330.16 ± 16.47 **U.:** 2.78 (± 136 %)

Goodness: n. d.

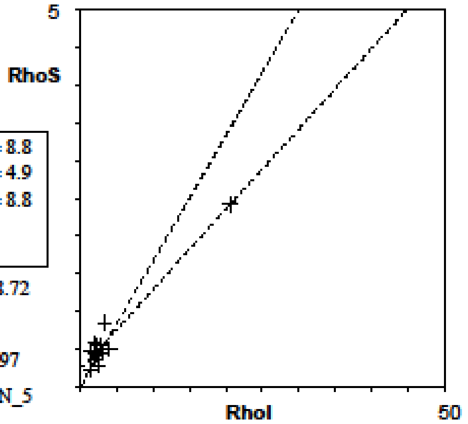

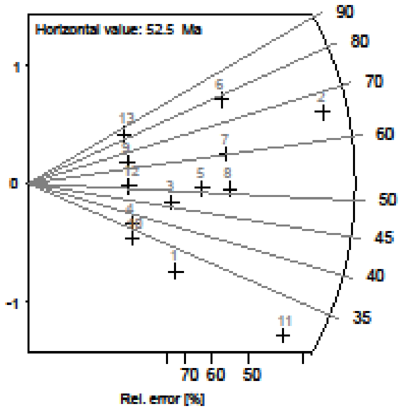

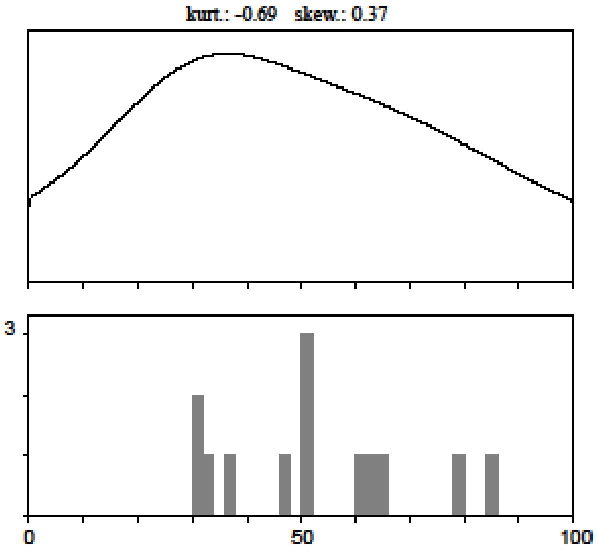

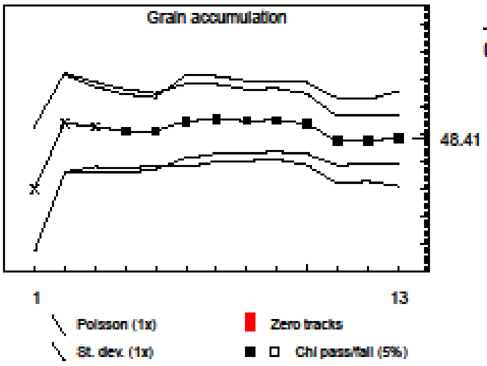

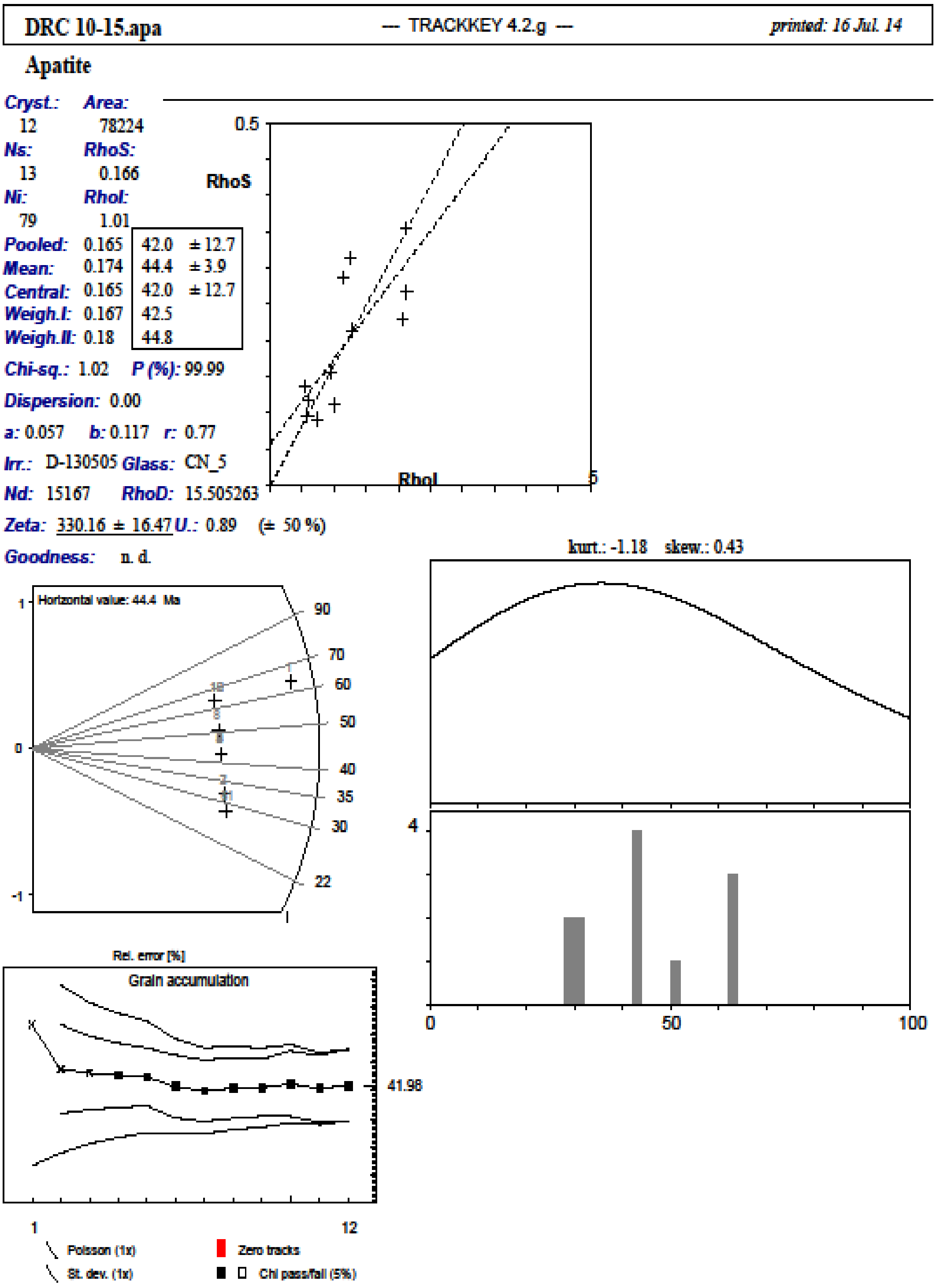

DRC 10-15.apa — TRACKKEY 4.2.g — *printed: 16 Jul. 14*

Apatite

Cryst.: 12 *Area:* 78224

Ns: 13 *RhoS:* 0.166

Ni: 79 *RhoI:* 1.01

Pooled:	0.165	42.0	± 12.7
Mean:	0.174	44.4	± 3.9
Central:	0.165	42.0	± 12.7
Weigh.I:	0.167	42.5	
Weigh.II:	0.18	44.8	

Chi-sq.: 1.02 *P (%):* 99.99

Dispersion: 0.00

a: 0.057 *b:* 0.117 *r:* 0.77

Irr.: D-130505 *Glass:* CN_5

Nd: 15167 *RhoD:* 15.505263

Zeta: 330.16 ± 16.47 *U.:* 0.89 (± 50 %)

Goodness: n. d.

kurt.: -1.18 skew.: 0.43

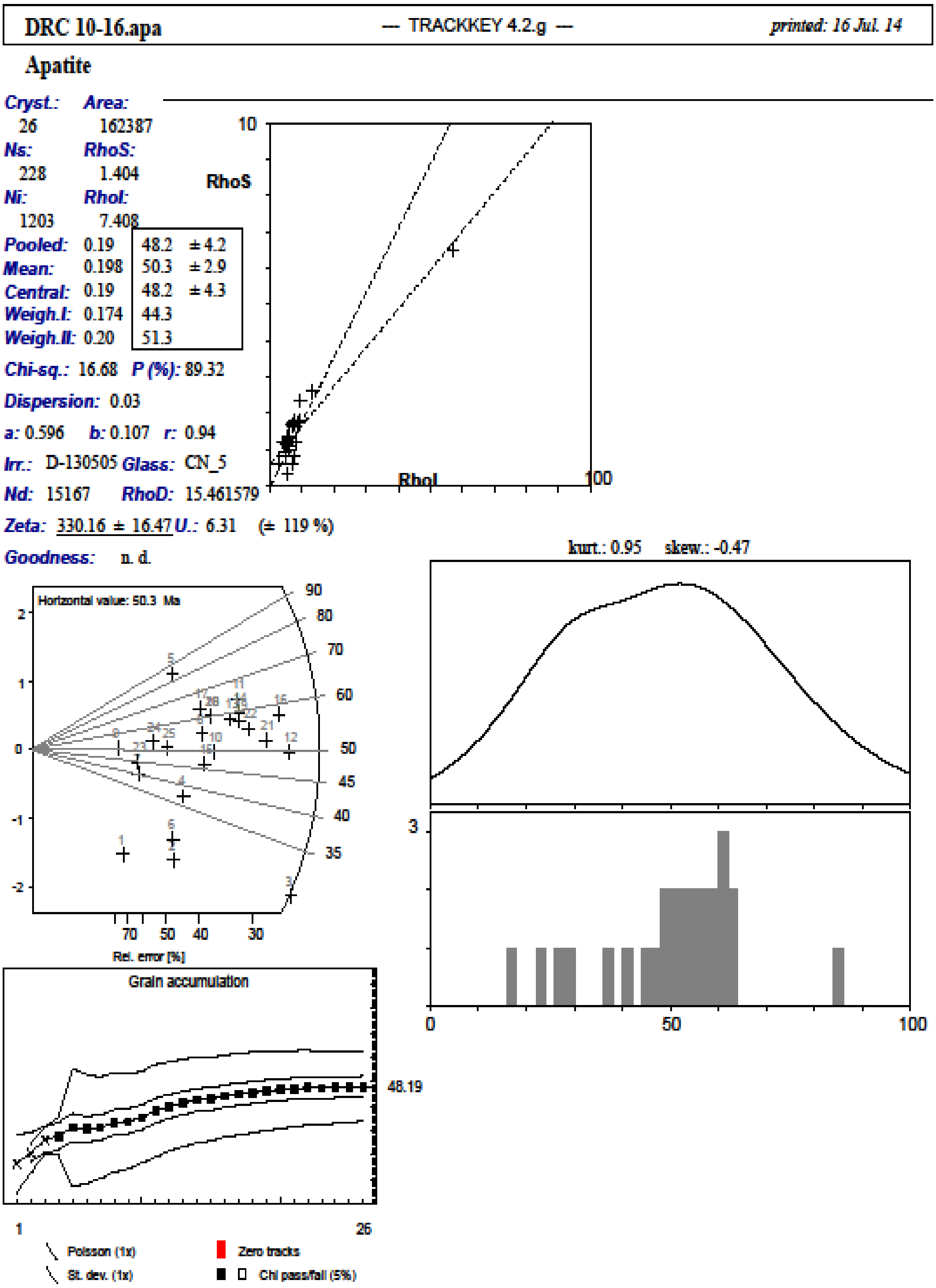

DRC 10-16.apa — TRACKKEY 4.2.g — *printed: 16 Jul. 14*

Apatite

Cryst.:	*Area:*
26	162387
Ns:	***RhoS:***
228	1.404
Ni:	***RhoI:***
1203	7.408

Pooled:	0.19	48.2	± 4.2
Mean:	0.198	50.3	± 2.9
Central:	0.19	48.2	± 4.3
Weigh.I:	0.174	44.3	
Weigh.II:	0.20	51.3	

Chi-sq.: 16.68 ***P (%):*** 89.32

Dispersion: 0.03

a: 0.596 ***b:*** 0.107 ***r:*** 0.94

Irr.: D-130505 ***Glass:*** CN_5

Nd: 15167 ***RhoD:*** 15.461579

Zeta: 330.16 ± 16.47 ***U.:*** 6.31 (± 119 %)

Goodness: n. d.

DRC 10-17.apa — TRACKKEY 4.2.g — *printed: 16 Jul. 14*

Apatite

Cryst.: 14 *Area:* 76937

Ns: 30 *RhoS:* 0.39

Ni: 161 *RhoI:* 2.093

Pooled:	0.186	47.3	± 9.7
Mean:	0.185	47.0	± 4.2
Central:	0.186	47.3	± 9.7
Weigh.I:	0.19	48.3	
Weigh.II:	0.19	49.2	

Chi-sq.: 2.5 *P (%):* 99.92

Dispersion: 0.00

a: 0.168 *b:* 0.106 *r:* 0.47

Irr.: D-130505 *Glass:* CN_5

Nd: 15167 *RhoD:* 15.417895

Zeta: 330.16 ± 16.47 *U.:* 1.66 (± 30 %)

Goodness: n. d.

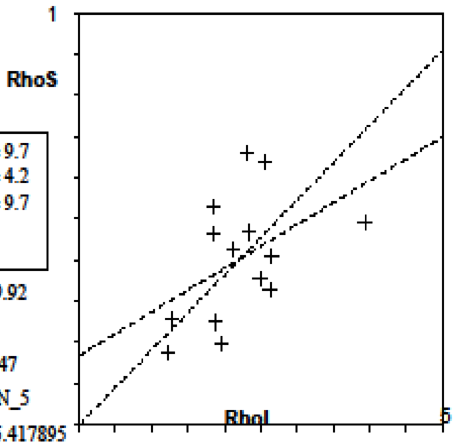

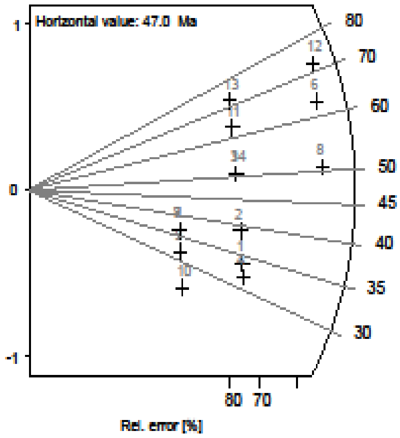

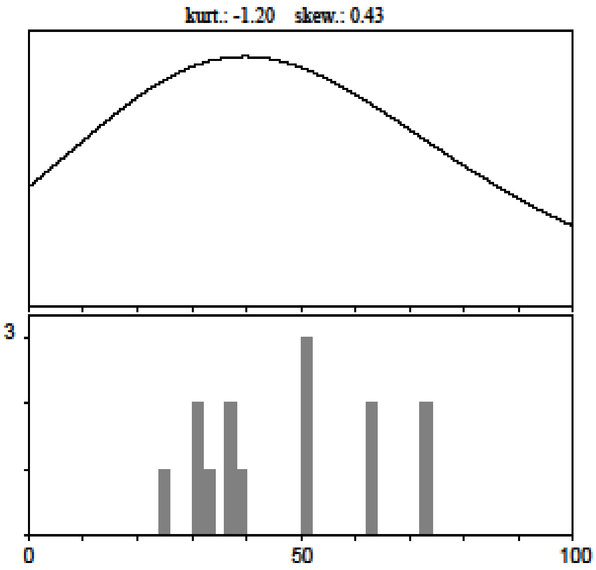

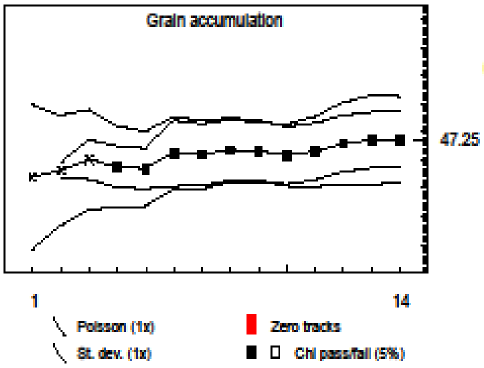

DRC 10-18.apa — TRACKKEY 4.2.g — *printed: 5 Apr. 15*

Apatite

Cryst.: 14 **Area:** 85793

Ns: 52 **RhoS:** 0.606

Ni: 248 **RhoI:** 2.891

Pooled: 0.21 53.0 ± 8.5

Mean: 0.209 52.7 ± 2.8

Central: 0.21 53.0 ± 8.5

Weigh.I: 0.212 53.7

Weigh.II: 0.21 53.6

Chi-sq.: 1.12 **P (%):** 100.0

Dispersion: 0.00

a: 0.008 **b:** 0.207 **r:** 0.86

Irr.: D-130505 **Glass:** CN_5

Nd: 15167 **RhoD:** 15.374211

Zeta: 330.16 ± 16.47 **U.:** 2.15 (± 30 %)

Goodness: n. d.

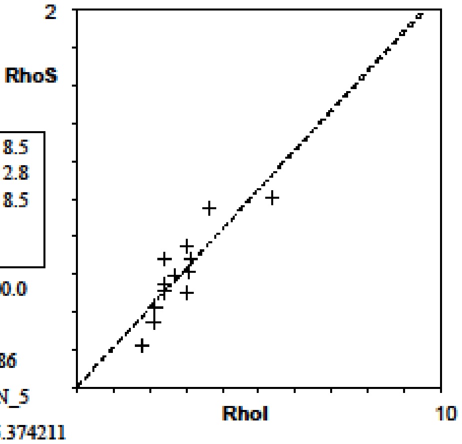

kurt.: 0.41 skew.: -0.08

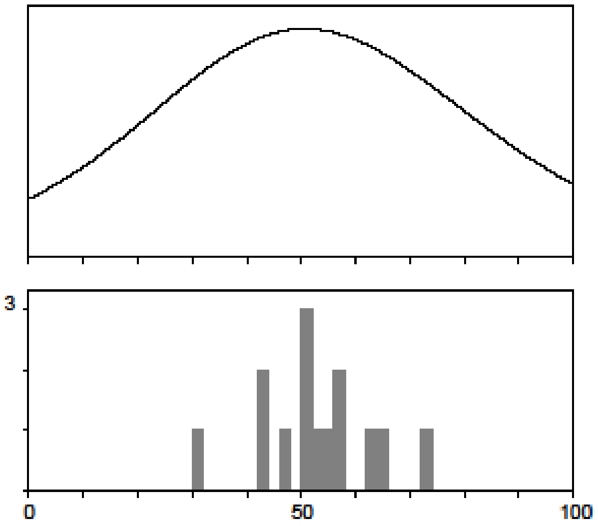

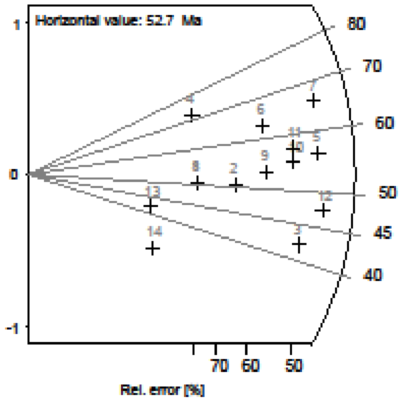

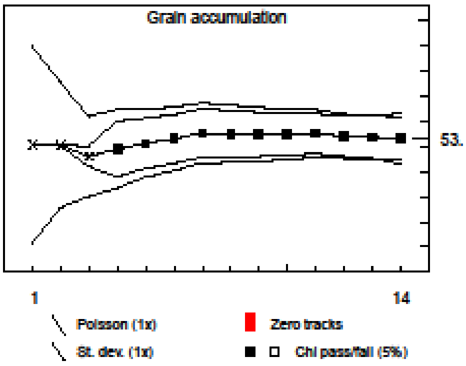

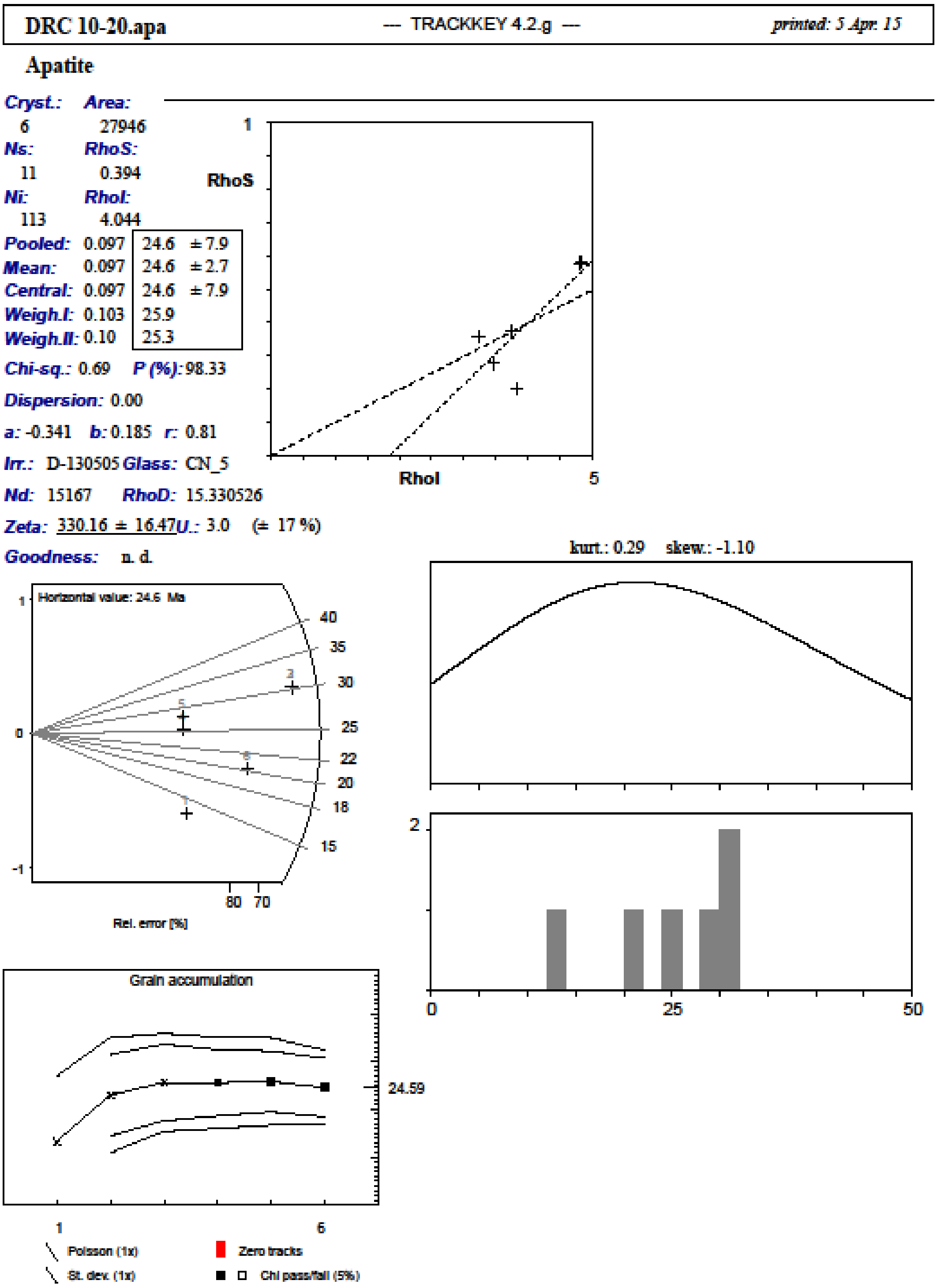

DRC 10-20.apa — TRACKKEY 4.2.g — *printed: 5 Apr. 15*

Apatite

Cryst.: 6 *Area:* 27946

Ns: 11 *RhoS:* 0.394

Ni: 113 *RhoI:* 4.044

Pooled: 0.097 24.6 ± 7.9
Mean: 0.097 24.6 ± 2.7
Central: 0.097 24.6 ± 7.9
Weigh.I: 0.103 25.9
Weigh.II: 0.10 25.3

Chi-sq.: 0.69 *P (%):* 98.33

Dispersion: 0.00

a: -0.341 *b:* 0.185 *r:* 0.81

Irr.: D-130505 *Glass:* CN_5

Nd: 15167 *RhoD:* 15.330526

Zeta: 330.16 ± 16.47 *U.:* 3.0 (± 17 %)

Goodness: n. d.

DRC 10-21.apa — TRACKKEY 4.2.g — *printed: 5 Apr. 15*

Apatite

Cryst.: 8 **Area:** 20654

Ns: 10 **RhoS:** 0.484

Ni: 59 **RhoI:** 2.857

Pooled:	0.169	42.6	± 14.7
Mean:	0.168	42.3	± 4.2
Central:	0.169	42.6	± 14.7
Weigh.I:	0.169	42.4	
Weigh.II:	0.17	43.7	

Chi-sq.: 0.74 **P (%):** 99.8

Dispersion: 0.00

a: 0.033 b: 0.156 r: 0.84

Irr.: D-130505 **Glass:** CN_5

Nd: 15167 **RhoD:** 15.286842

Zeta: 330.16 ± 16.47 **U.:** 2.63 (± 50 %)

Goodness: n. d.

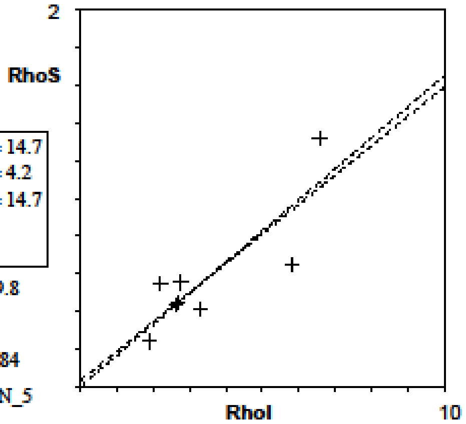

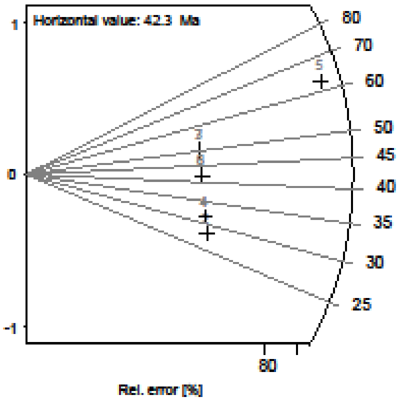

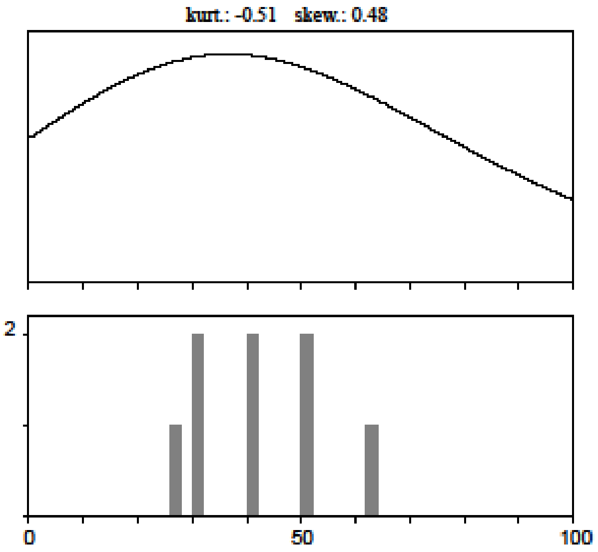

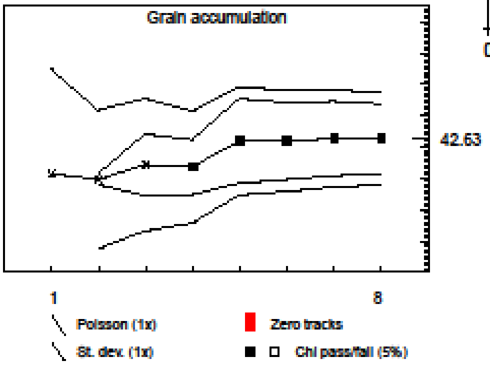

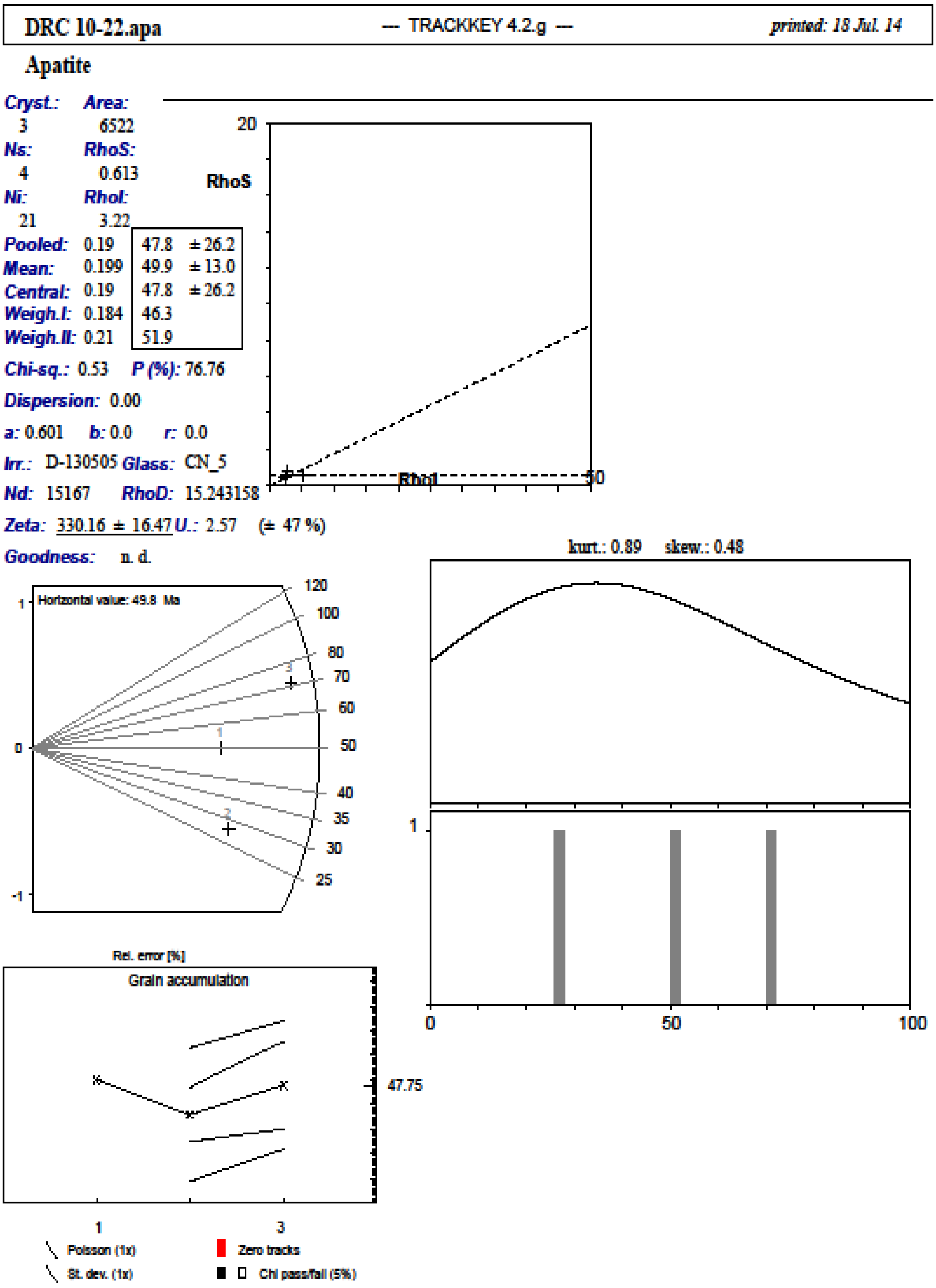

DRC 10-22.apa — TRACKKEY 4.2.g — *printed: 18 Jul. 14*

Apatite

Cryst.:	Area:
3	6522
Ns:	**RhoS:**
4	0.613
Ni:	**RhoI:**
21	3.22

Pooled:	0.19	47.8	± 26.2
Mean:	0.199	49.9	± 13.0
Central:	0.19	47.8	± 26.2
Weigh.I:	0.184	46.3	
Weigh.II:	0.21	51.9	

Chi-sq.: 0.53 **P (%):** 76.76

Dispersion: 0.00

a: 0.601 **b:** 0.0 **r:** 0.0

Irr.: D-130505 **Glass:** CN_5

Nd: 15167 **RhoD:** 15.243158

Zeta: 330.16 ± 16.47 **U.:** 2.57 (± 47 %)

Goodness: n. d.

DRC 10-23.apa — TRACKKEY 4.2.g — *printed: 5 Apr. 15*

Apatite

Cryst.:	**Area:**
9	41621
Ns:	**RhoS:**
266	6.391
Ni:	**RhoI:**
1384	33.252

Pooled:	0.192	48.0	± 4.0
Mean:	0.189	47.2	± 2.2
Central:	0.192	48.0	± 4.0
Weigh.I:	0.187	46.7	
Weigh.II:	0.19	48.0	

Chi-sq.: 4.2 **P (%):** 83.88

Dispersion: 0.00

a: 1.357 **b:** 0.148 **r:** 0.96

Irr.: D-130505 **Glass:** CN_5

Nd: 15167 **RhoD:** 15.199474

Zeta: 330.16 ± 16.47 **U.:** 28.12 (± 54 %)

Goodness: n. d.

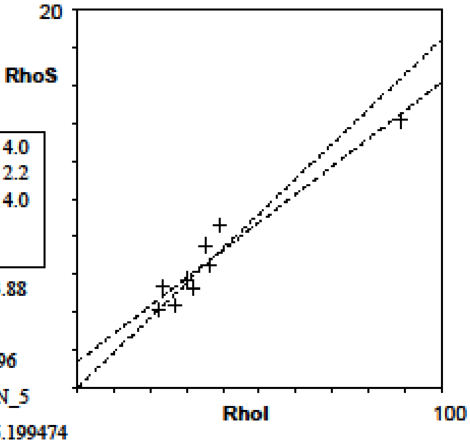

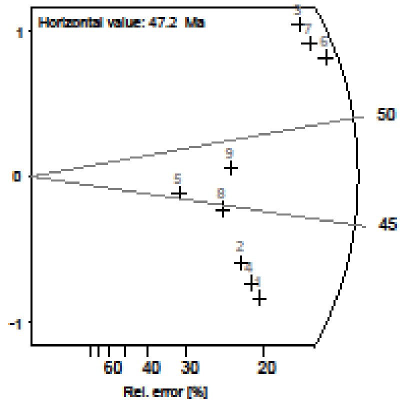

kurt.: -1.60 skew.: 0.37

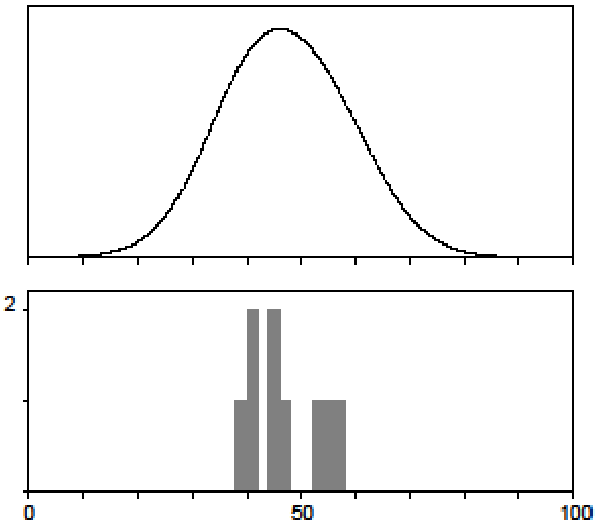

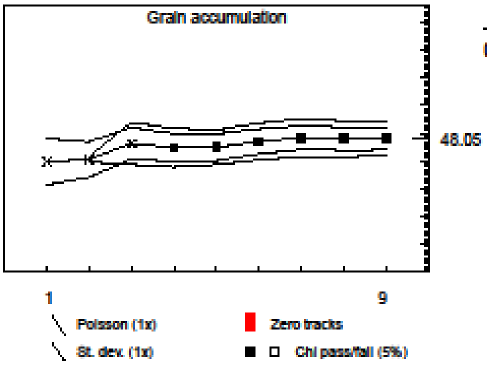

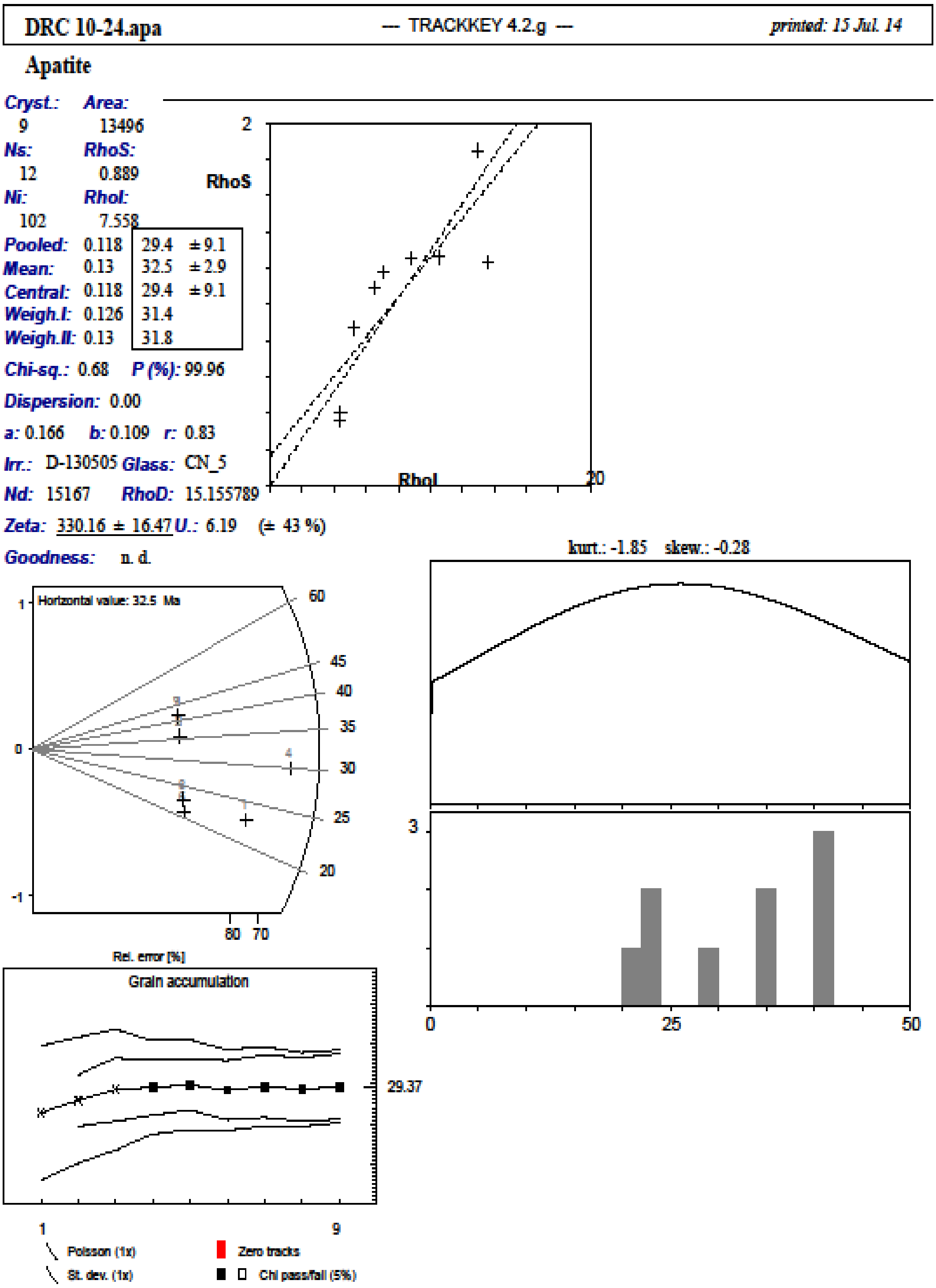

DRC 10-24.apa — TRACKKEY 4.2.g — *printed: 15 Jul. 14*

Apatite

Cryst.: 9	*Area:* 13496			
Ns: 12	*RhoS:* 0.889			
Ni: 102	*RhoI:* 7.558			
Pooled:	0.118	29.4	± 9.1	
Mean:	0.13	32.5	± 2.9	
Central:	0.118	29.4	± 9.1	
Weigh.I:	0.126	31.4		
Weigh.II:	0.13	31.8		

Chi-sq.: 0.68 *P (%):* 99.96

Dispersion: 0.00

a: 0.166 *b:* 0.109 *r:* 0.83

Irr.: D-130505 *Glass:* CN_5

Nd: 15167 *RhoD:* 15.155789

Zeta: 330.16 ± 16.47 *U.:* 6.19 (± 43 %)

Goodness: n. d.

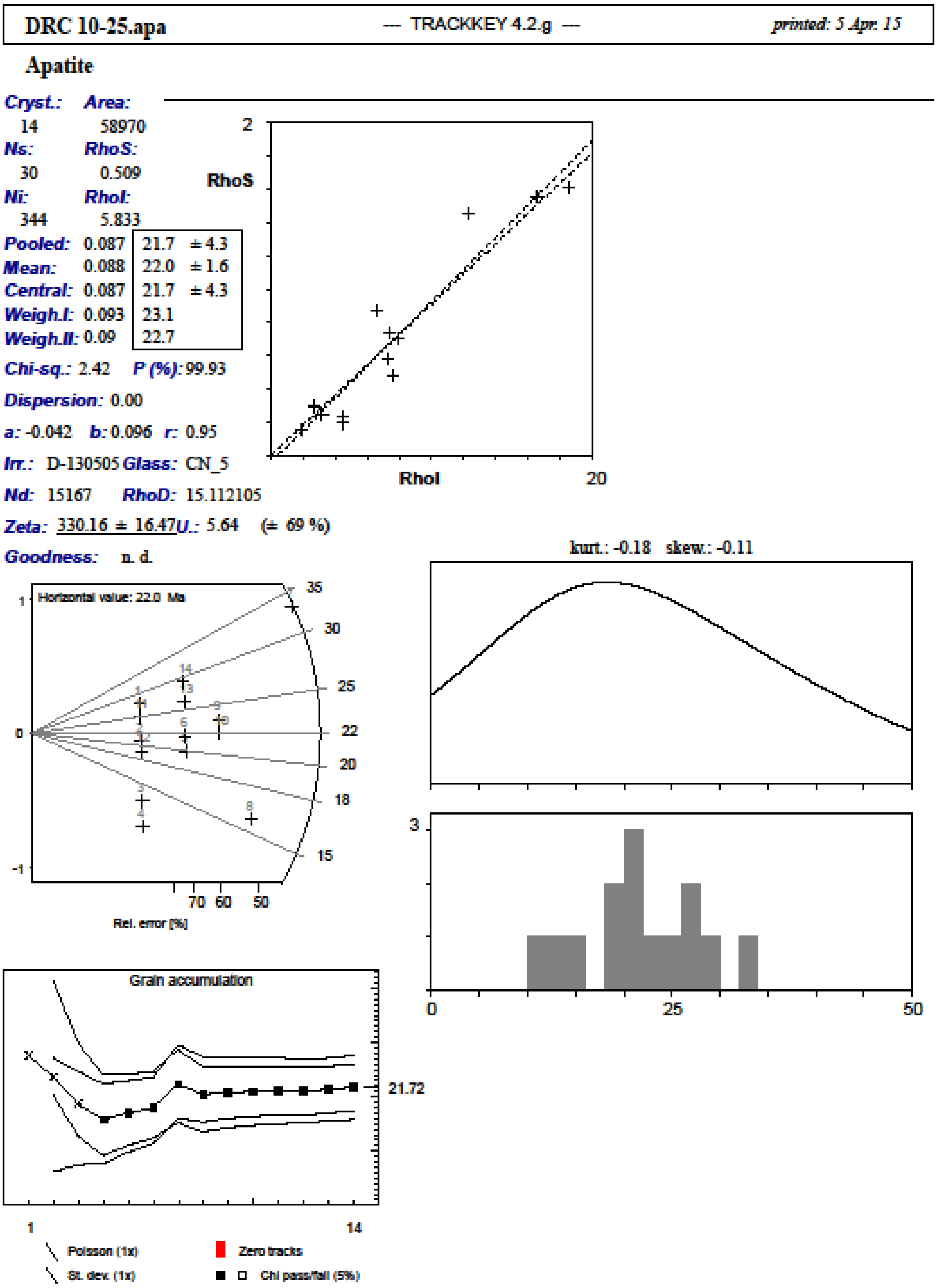

DRC 10-25.apa — TRACKKEY 4.2.g — *printed: 5 Apr. 15*

Apatite

Cryst.: 14 **Area:** 58970
Ns: 30 **RhoS:** 0.509
Ni: 344 **RhoI:** 5.833

Pooled:	0.087	21.7	± 4.3
Mean:	0.088	22.0	± 1.6
Central:	0.087	21.7	± 4.3
Weigh.I:	0.093	23.1	
Weigh.II:	0.09	22.7	

Chi-sq.: 2.42 **P (%):** 99.93
Dispersion: 0.00
a: -0.042 **b:** 0.096 **r:** 0.95
Irr.: D-130505 **Glass:** CN_5
Nd: 15167 **RhoD:** 15.112105
Zeta: 330.16 ± 16.47 **U.:** 5.64 (± 69 %)
Goodness: n. d.

DRC 10-26.apa — TRACKKEY 4.2.g — *printed: 5 Apr. 15*

Apatite

Cryst.: **Area:**
27 186385
Ns: **RhoS:**
260 1.395
Ni: **RhoI:**
2842 15.248

Pooled:	0.091	24.6	± 2.0
Mean:	0.094	25.3	± 1.0
Central:	0.091	24.6	± 2.0
Weigh.I:	0.093	24.9	
Weigh.II:	0.09	25.2	

Chi-sq.: 9.06 **P (%):** 99.91

Dispersion: 0.00

a: 0.146 **b:** 0.083 **r:** 0.8

Irr.: D-130212 **Glass:** CN_5

Nd: 15209 **RhoD:** 16.29

Zeta: 330.16 ± 16.47 **U.:** 10.7 (± 29 %)

Goodness: n. d.

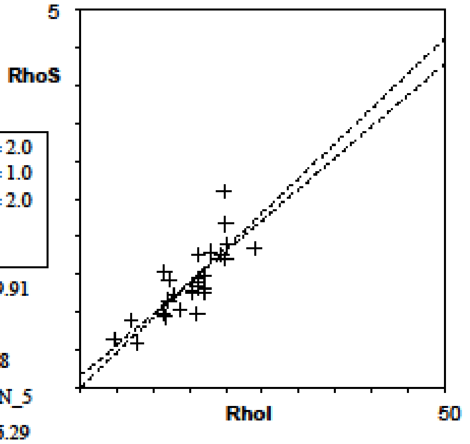

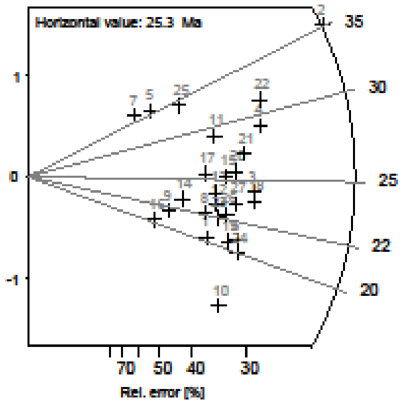

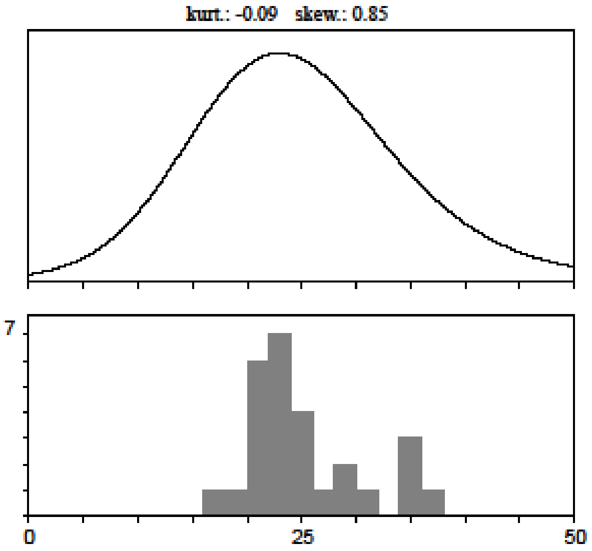

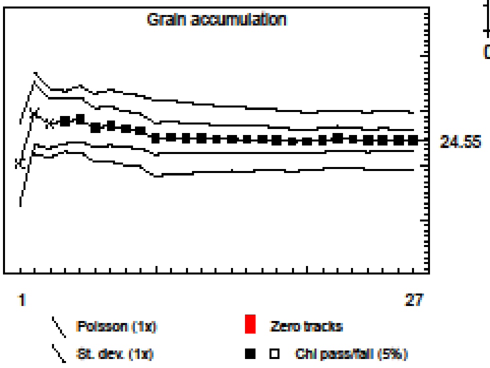

DRC 10-27.apa — TRACKKEY 4.2.g — *printed: 5 Apr. 15*

Apatite

Cryst.: 24 ***Area:*** 164873

Ns: 258 ***RhoS:*** 1.565

Ni: 2763 ***RhoI:*** 16.758

Pooled:	0.093	23.1	± 1.9
Mean:	0.094	23.2	± 0.7
Central:	0.093	23.1	± 1.9
Weigh.I:	0.095	23.5	
Weigh.II:	0.09	23.3	

Chi-sq.: 3.65 ***P (%):*** 100.0

Dispersion: 0.00

a: -0.099 ***b:*** 0.101 ***r:*** 0.9

Irr.: D-130505 ***Glass:*** CN_5

Nd: 15167 ***RhoD:*** 15.024737

Zeta: 330.16 ± 16.47 ***U.:*** 12.75 (± 27 %)

Goodness: n. d.

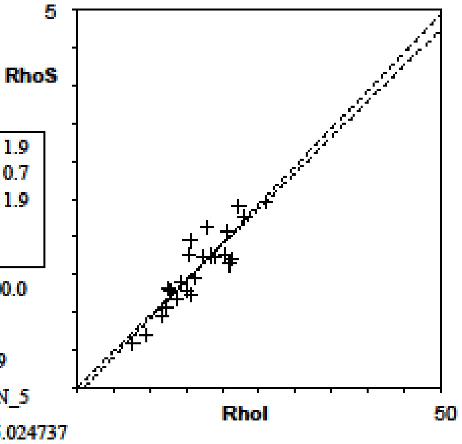

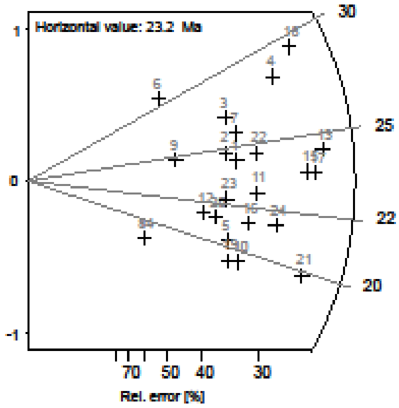

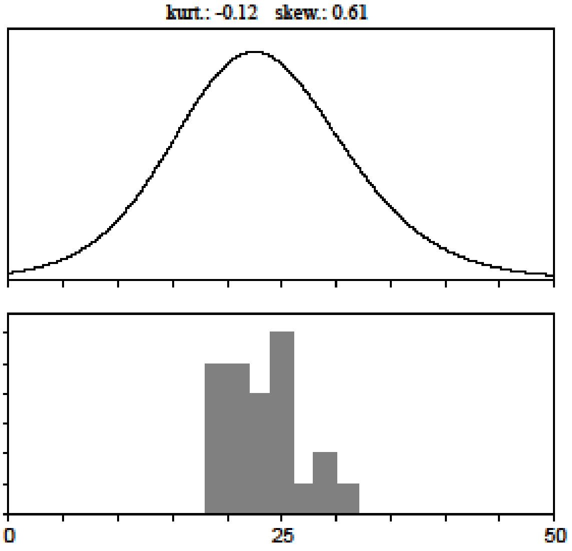

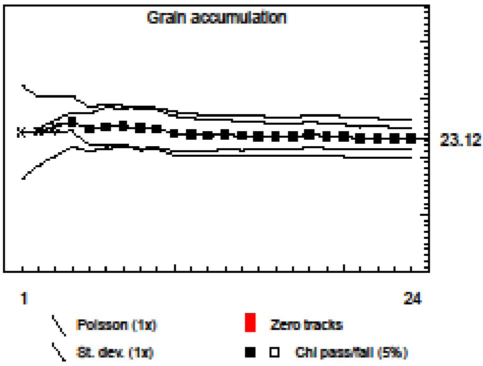

DRC 10-28.apa — TRACKKEY 4.2.g — *printed: 5 Apr. 15*

Apatite

Cryst.: 25 ***Area:*** 71426

Ns: 250 ***RhoS:*** 3.5

Ni: 2381 ***RhoI:*** 33.335

Pooled:	0.105	25.9	± 2.2
Mean:	0.113	27.9	± 1.3
Central:	0.105	25.9	± 2.2
Weigh.I:	0.11	27.2	
Weigh.II:	0.11	27.4	

Chi-sq.: 10.64 ***P (%):*** 99.14

Dispersion: 0.00

a: 0.262 ***b:*** 0.104 ***r:*** 0.83

Irr.: D-130505 ***Glass:*** CN_5

Nd: 15167 ***RhoD:*** 14.981053

Zeta: 330.16 ± 16.47 ***U.:*** 26.31 (± 36 %)

Goodness: n. d.

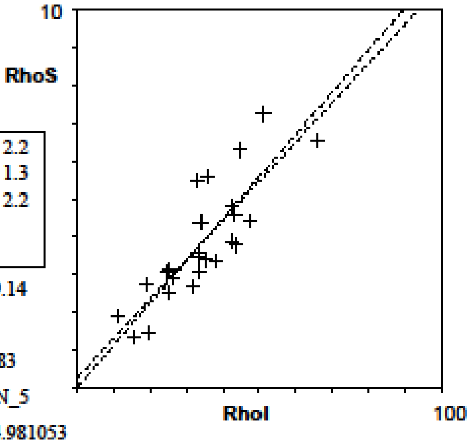

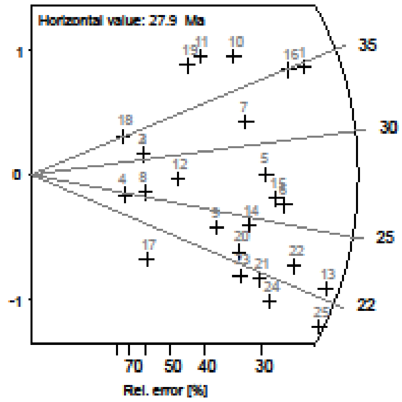

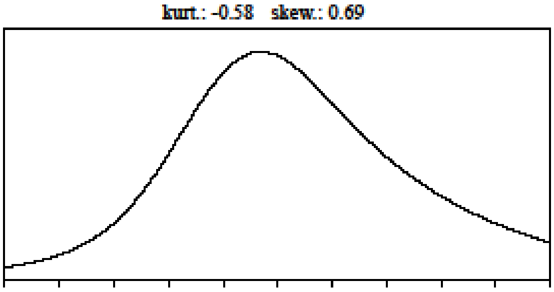

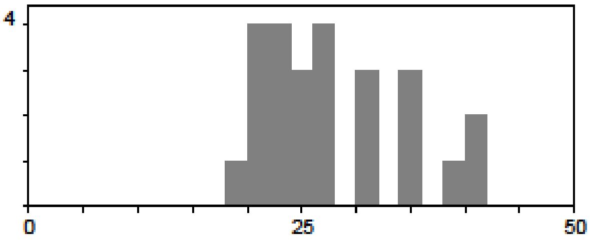

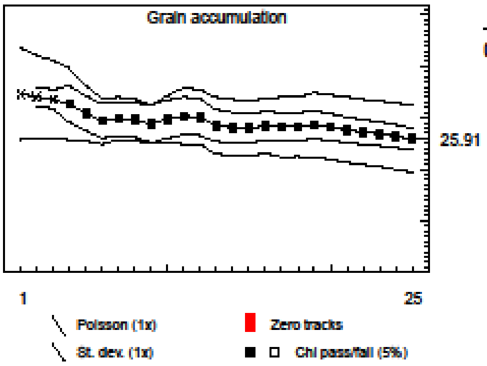

DRC 10-29.apa — TRACKKEY 4.2.g — *printed: 5 Apr. 15*

Apatite

Cryst.: ***Area:***
10 67949
Ns: ***RhoS:***
22 0.324
Ni: ***RhoI:***
245 3.606

Pooled:	0.09	23.7	± 5.4
Mean:	0.108	28.6	± 2.8
Central:	0.09	23.7	± 5.4
Weigh.I:	0.08	21.1	
Weigh.II:	0.10	27.2	

Chi-sq.: 1.71 ***P (%):*** 99.53

Dispersion: 0.00

a: 0.062 ***b:*** 0.075 ***r:*** 1.0

Irr.: D-130813 ***Glass:*** CN_5

Nd: 15285 ***RhoD:*** 16.01

Zeta: 330.16 ± 16.47 ***U.:*** 5.33 (± 205 %)

Goodness: n. d.

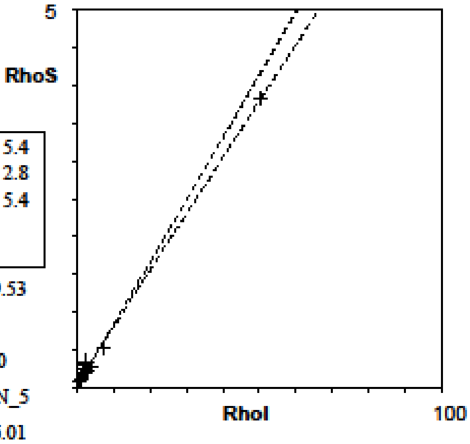

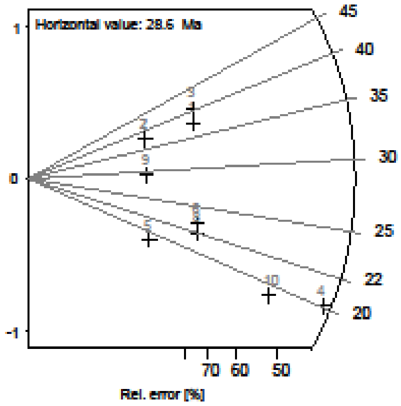

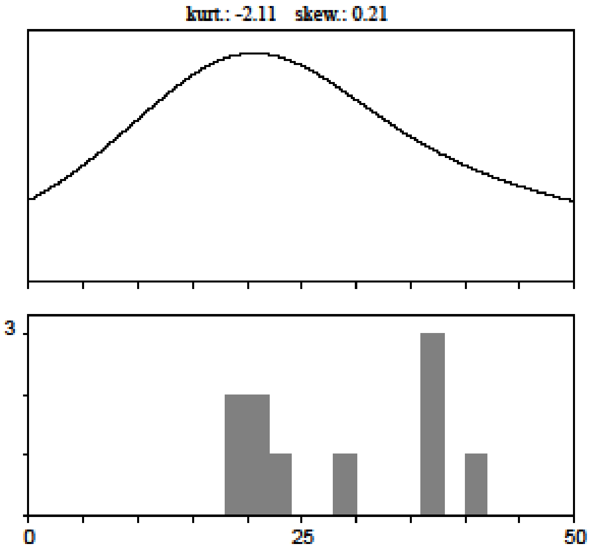

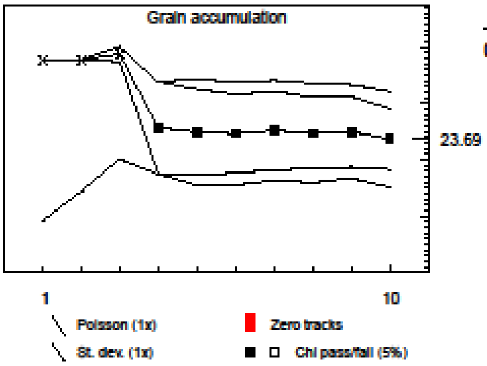

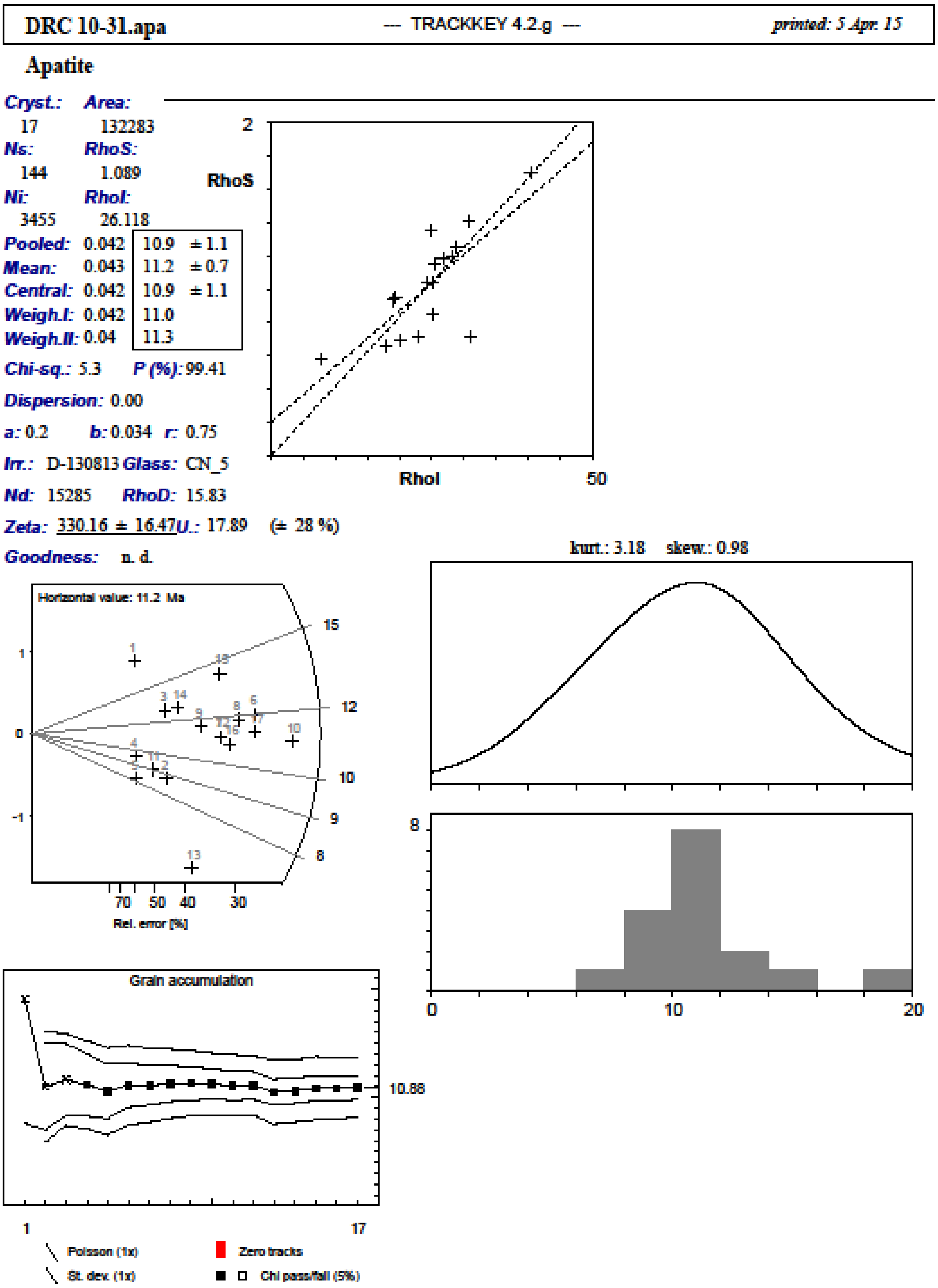

DRC 10-31.apa — TRACKKEY 4.2.g — *printed: 5 Apr. 15*

Apatite

Cryst.: 17 ***Area:*** 132283

Ns: 144 ***RhoS:*** 1.089

Ni: 3455 ***RhoI:*** 26.118

Pooled: 0.042 10.9 ± 1.1

Mean: 0.043 11.2 ± 0.7

Central: 0.042 10.9 ± 1.1

Weigh.I: 0.042 11.0

Weigh.II: 0.04 11.3

Chi-sq.: 5.3 ***P (%):*** 99.41

Dispersion: 0.00

a: 0.2 ***b:*** 0.034 ***r:*** 0.75

Irr.: D-130813 ***Glass:*** CN_5

Nd: 15285 ***RhoD:*** 15.83

Zeta: 330.16 ± 16.47 ***U.:*** 17.89 (± 28 %)

Goodness: n. d.

DRC 10-32.apa — TRACKKEY 4.2.g — *printed: 5 Apr. 15*

Apatite

Cryst.: 18 *Area:* 138639

Ns: 43 *RhoS:* 0.31

Ni: 878 *RhoI:* 6.333

Pooled:	0.049	12.6	± 2.1
Mean:	0.045	11.5	± 1.1
Central:	0.049	12.6	± 2.1
Weigh.I:	0.051	13.1	
Weigh.II:	0.05	13.0	

Chi-sq.: 3.26 *P (%):* 99.99

Dispersion: 0.00

a: -0.114 *b:* 0.065 *r:* 0.85

Irr.: D-130813 *Glass:* CN_5

Nd: 15285 *RhoD:* 15.65

Zeta: 330.16 ± 16.47 *U.:* 4.47 (± 34 %)

Goodness: n. d.

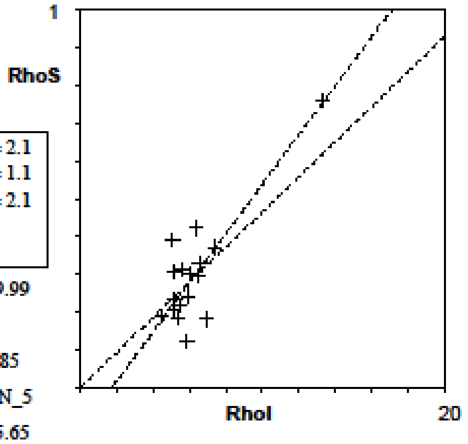

1 crystal with zero tracks !

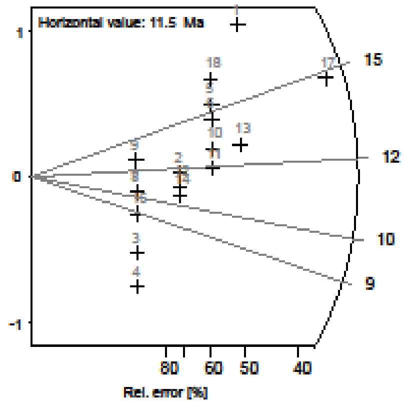

kurt.: 1.61 skew.: -0.72

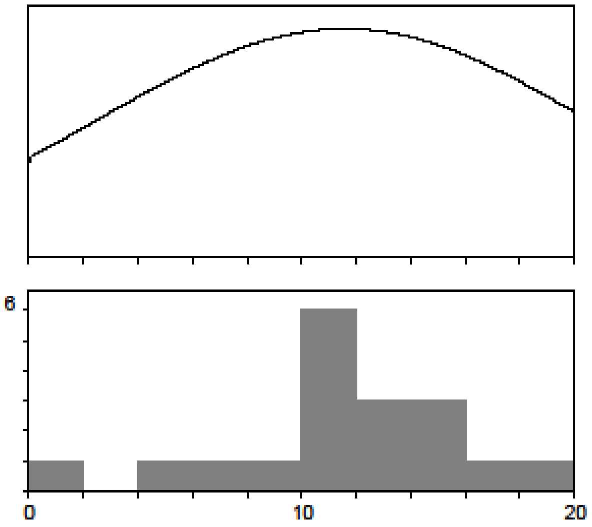

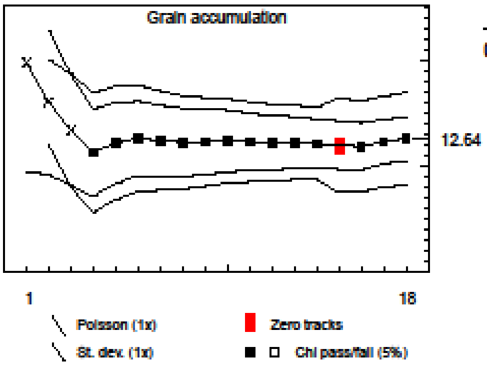

11.2 RIFT WITH LOW ELEVATED FLANKS (THE SAMRA MOUNTAIN AREA)-ZFT DATA SHEETS

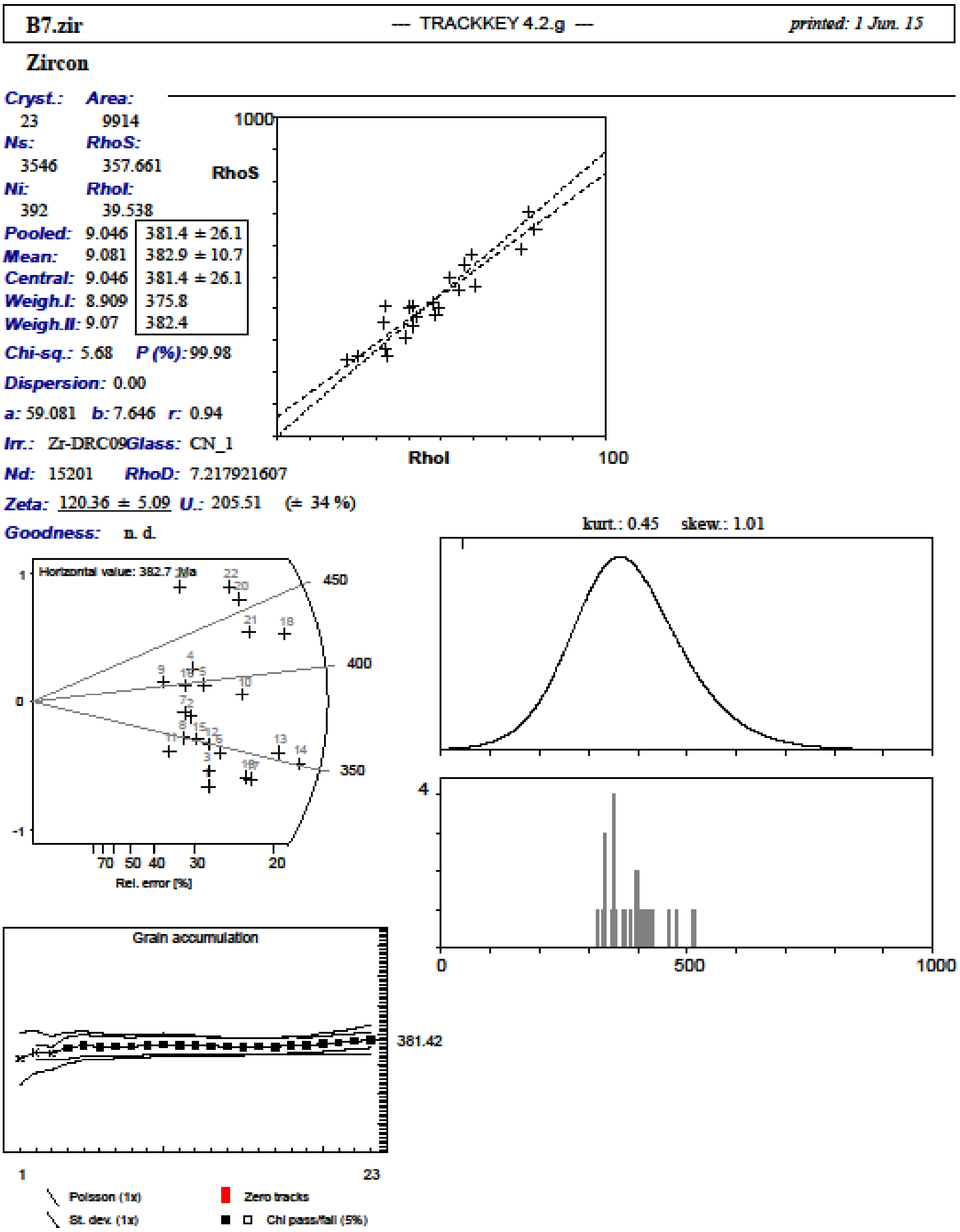

B7.zir — TRACKKEY 4.2.g — *printed: 1 Jun. 15*

Zircon

Cryst.:	Area:
23	9914
Ns:	**RhoS:**
3546	357.661
Ni:	**RhoI:**
392	39.538

Pooled:	9.046	381.4 ± 26.1
Mean:	9.081	382.9 ± 10.7
Central:	9.046	381.4 ± 26.1
Weigh.I:	8.909	375.8
Weigh.II:	9.07	382.4

Chi-sq.: 5.68 **P (%):** 99.98

Dispersion: 0.00

a: 59.081 **b:** 7.646 **r:** 0.94

Irr.: Zr-DRC09 **Glass:** CN_1

Nd: 15201 **RhoD:** 7.217921607

Zeta: 120.36 ± 5.09 **U.:** 205.51 (± 34 %)

Goodness: n. d.

Polsson (1x) 🟥 Zero tracks

St. dev. (1x) ■ □ Chi pass/fail (5%)

B11.zir — TRACKKEY 4.2.g — *printed: 27 Aug. 15*

Zircon

Cryst.:	***Area:***
12	4679
Ns:	***RhoS:***
1823	389.588
Ni:	***RhoI:***
176	37.612

Pooled:	10.358	442.2 ± 39.8
Mean:	10.224	436.6 ± 8.7
Central:	10.358	442.2 ± 39.8
Weigh.I:	10.212	436.2
Weigh.II:	10.30	439.8

Chi-sq.: 0.6 ***P (%):*** 100.0

Dispersion: 0.00

a: 72.858 ***b:*** 8.383 ***r:*** 0.95

Irr.: Zr-DRC09 ***Glass:*** CN_1

Nd: 15201 ***RhoD:*** 7.342583992

Zeta: 120.36 ± 5.09 ***U.:*** 179.67 (± 23 %)

Goodness: n. d.

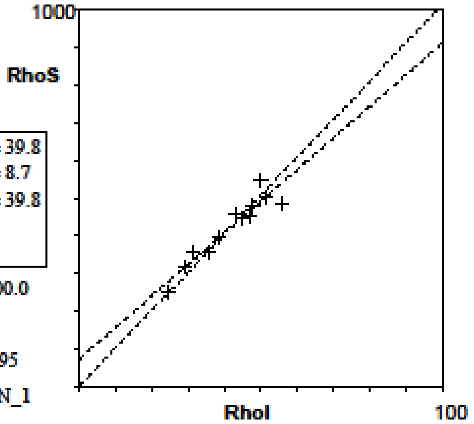

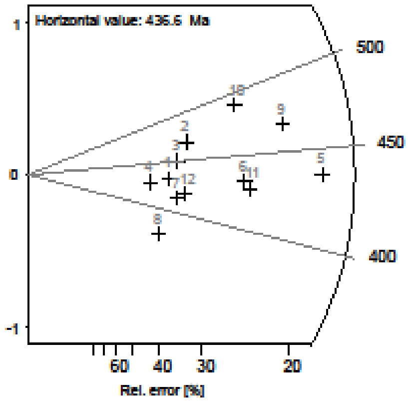

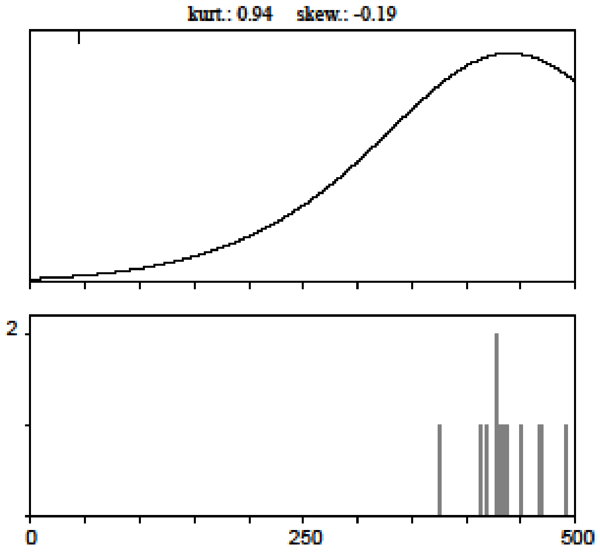

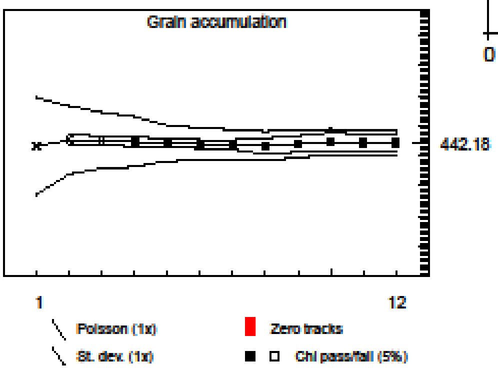

D4.zir — TRACKKEY 4.2.g — *printed: 1 Jun. 15*

Zircon

Cryst.: 22 ***Area:*** 9855

Ns: 3875 ***RhoS:*** 393.192

Ni: 355 ***RhoI:*** 36.021

Pooled: 10.915 452.4 ± 31.8

Mean: 10.982 455.1 ± 5.9

Central: 10.915 452.4 ± 31.8

Weigh.I: 10.945 453.6

Weigh.II: 10.95 453.9

Chi-sq.: 0.88 ***P (%):*** 100.0

Dispersion: 0.00

a: 10.112 ***b:*** 10.707 ***r:*** 0.96

Irr.: Zr-DRC09 ***Glass:*** CN_1

Nd: 15201 ***RhoD:*** 7.134813351

Zeta: 120.36 ± 5.09 ***U.:*** 163.8 (± 21 %)

Goodness: n. d.

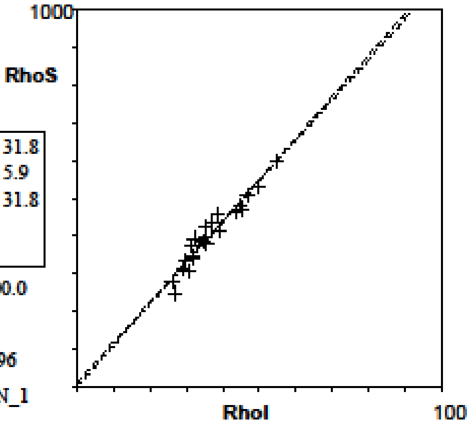

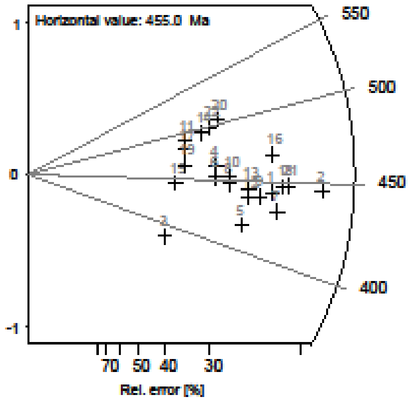

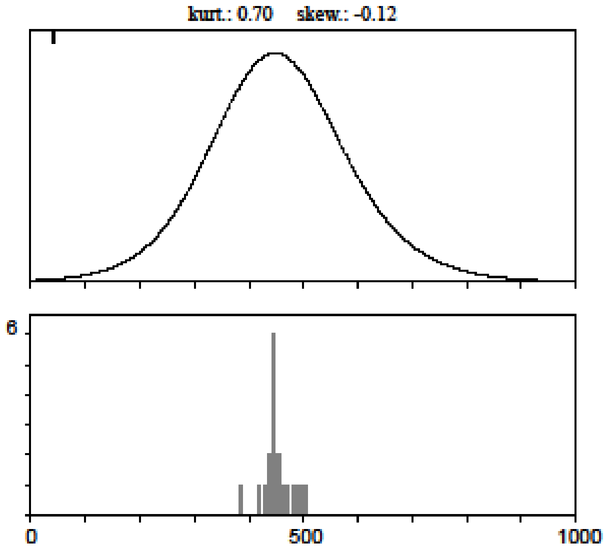

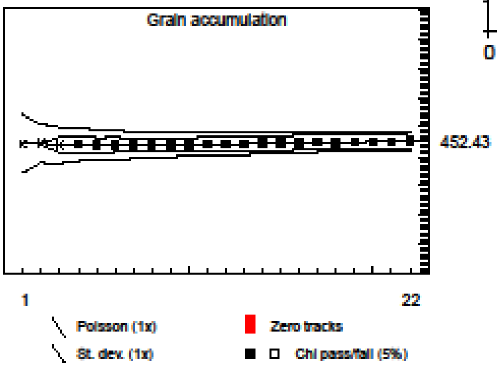

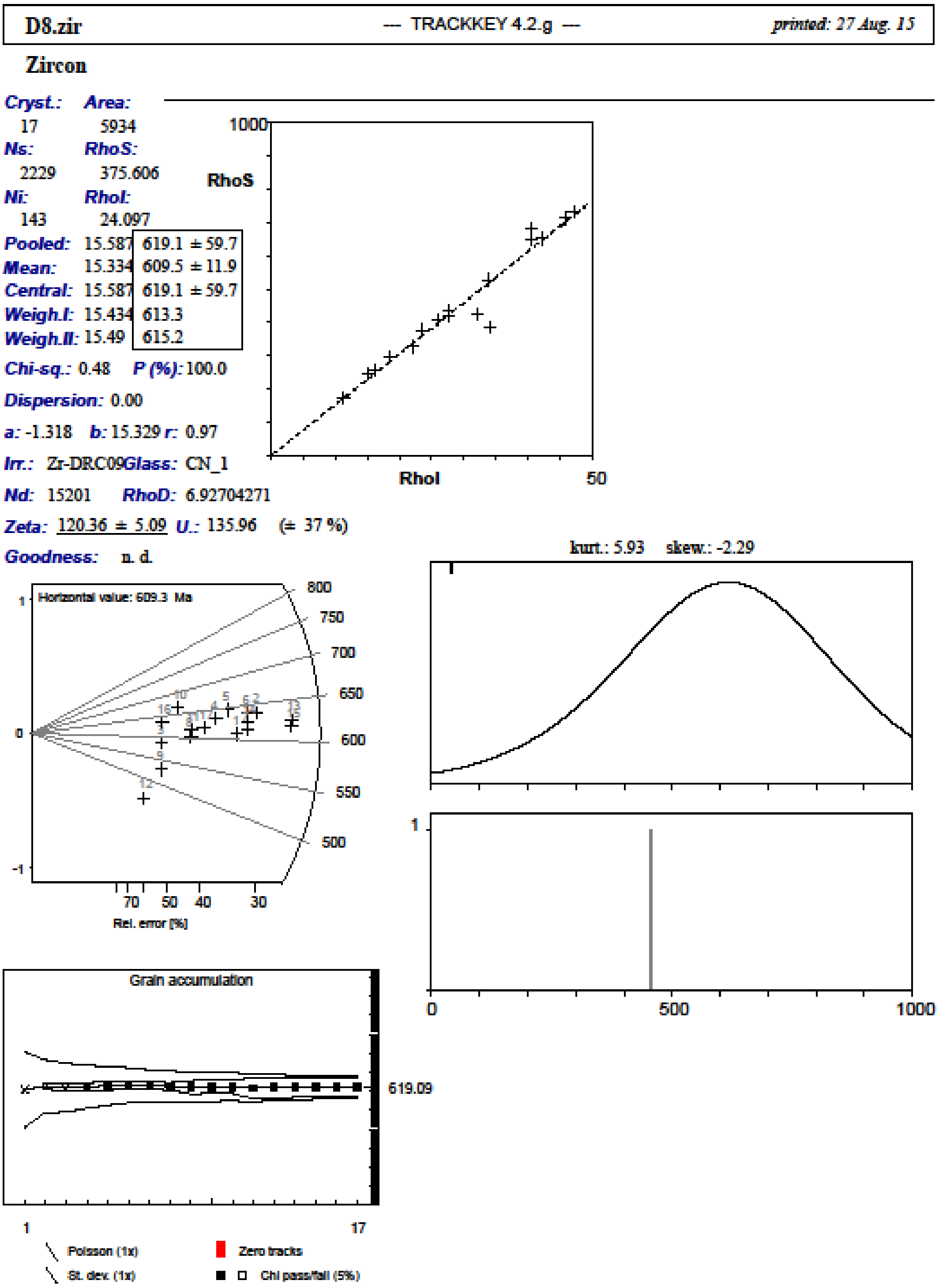

D8.zir — TRACKKEY 4.2.g — *printed: 27 Aug. 15*

Zircon

Cryst.: 17 ***Area:*** 5934

Ns: 2229 ***RhoS:*** 375.606

Ni: 143 ***RhoI:*** 24.097

Pooled:	15.587	619.1 ± 59.7
Mean:	15.334	609.5 ± 11.9
Central:	15.587	619.1 ± 59.7
Weigh.I:	15.434	613.3
Weigh.II:	15.49	615.2

Chi-sq.: 0.48 ***P (%):*** 100.0

Dispersion: 0.00

a: -1.318 *b:* 15.329 *r:* 0.97

Irr.: Zr-DRC09 ***Glass:*** CN_1

Nd: 15201 ***RhoD:*** 6.92704271

Zeta: 120.36 ± 5.09 ***U.:*** 135.96 (± 37 %)

Goodness: n. d.

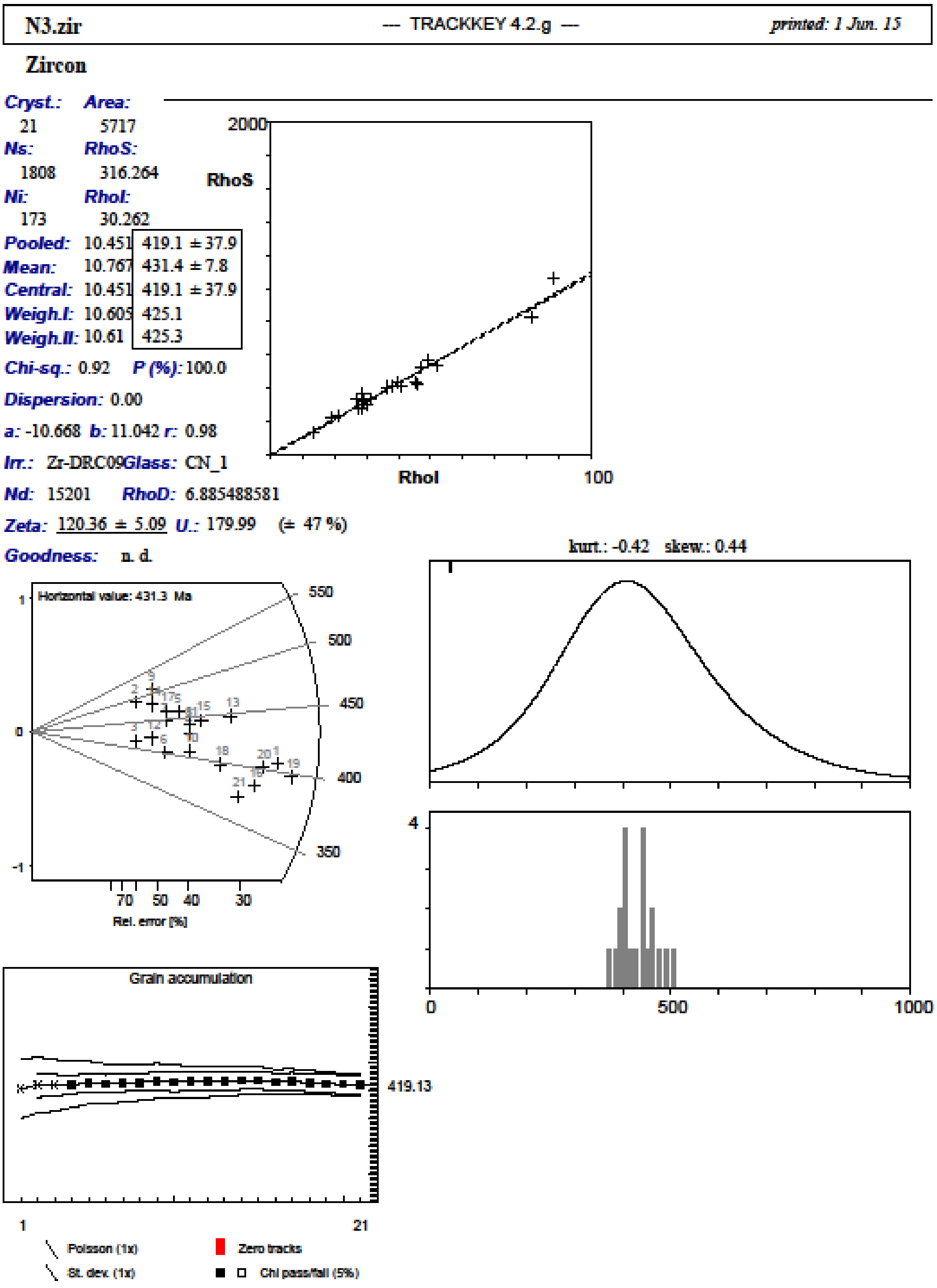

N3.zir — TRACKKEY 4.2.g — *printed: 1 Jun. 15*

Zircon

Cryst.: 21 **Area:** 5717

Ns: 1808 **RhoS:** 316.264

Ni: 173 **RhoI:** 30.262

Pooled: 10.451 419.1 ± 37.9

Mean: 10.767 431.4 ± 7.8

Central: 10.451 419.1 ± 37.9

Weigh.I: 10.605 425.1

Weigh.II: 10.61 425.3

Chi-sq.: 0.92 **P (%):** 100.0

Dispersion: 0.00

a: -10.668 **b:** 11.042 **r:** 0.98

Irr.: Zr-DRC09 **Glass:** CN_1

Nd: 15201 **RhoD:** 6.885488581

Zeta: 120.36 ± 5.09 **U.:** 179.99 (± 47 %)

Goodness: n. d.

S4.zir — TRACKKEY 4.2.g — *printed: 1 Jun. 15*

Zircon

Cryst.: **Area:**
13 2512
Ns: **RhoS:**
1581 629.447
Ni: **RhoI:**
95 37.823
Pooled: 16.642 673.9 ± 76.9
Mean: 16.526 669.5 ± 11.1
Central: 16.642 673.9 ± 76.9
Weigh.I: 16.589 671.9
Weigh.II: 16.59 671.8
Chi-sq.: 0.27 **P (%):** 100.0
Dispersion: 0.00
a: -3.339 **b:** 16.616 **r:** 0.98
Irr.: Zr-DRC09 **Glass:** CN_1
Nd: 15201 **RhoD:** 7.093259223
Zeta: 120.36 ± 5.09 **U.:** 177.02 (± 28 %)
Goodness: n. d.

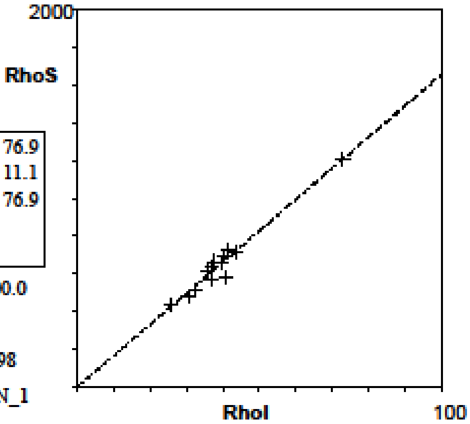

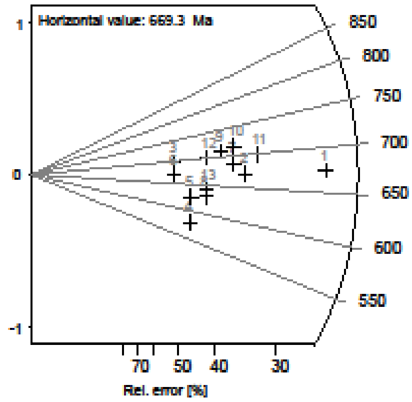

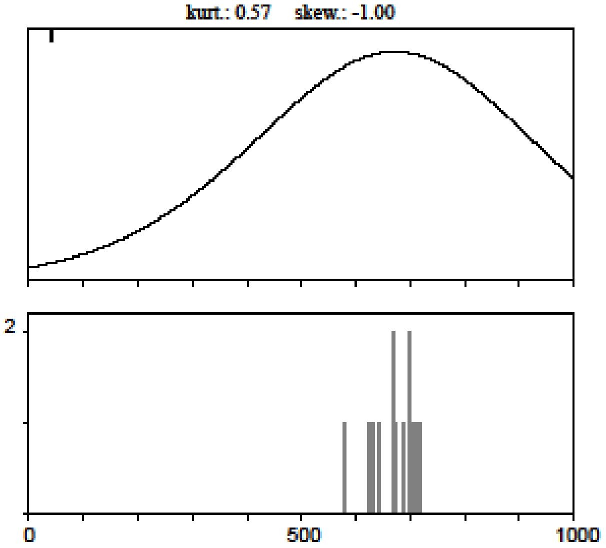

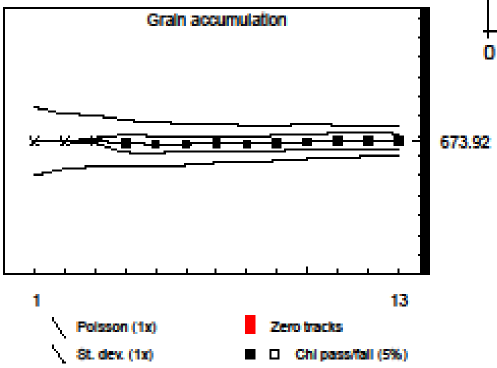

S10.zir — TRACKKEY 4.2.g — *printed: 1 Jun. 15*

Zircon

Cryst.:	***Area:***
21	9369
Ns:	***RhoS:***
2981	318.172
Ni:	***RhoI:***
186	19.852

Pooled:	16.027	668.3 ± 58.1
Mean:	16.078	670.3 ± 6.9
Central:	16.027	668.3 ± 58.1
Weigh.I:	16.049	669.2
Weigh.II:	16.05	669.3

Chi-sq.: 0.31 ***P (%):*** 100.0

Dispersion: 0.00

a: -4.706 ***b:*** 16.297 ***r:*** 0.99

Irr.: Zr-DRC09 ***Glass:*** CN_1

Nd: 15201 ***RhoD:*** 7.301029864

Zeta: 120.36 ± 5.09 ***U.:*** 95.42 (± 33 %)

Goodness: n. d.

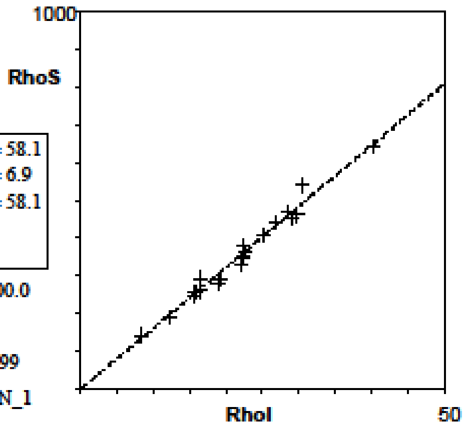

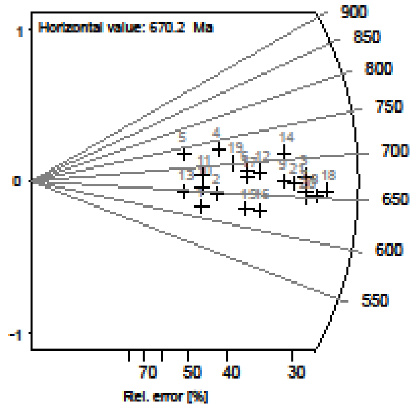

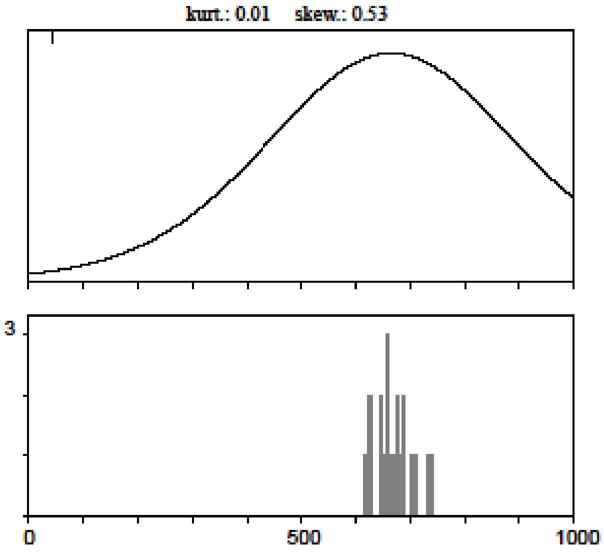

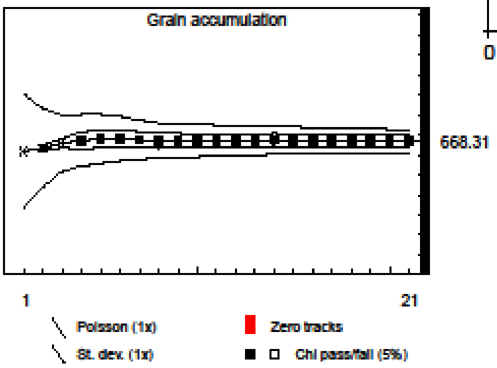

Z3zir.zir — TRACKKEY 4.2.g — *printed: 27 Aug. 15*

Zircon

Cryst.: 24 ***Area:*** 10715

Ns: 4112 ***RhoS:*** 383.761

Ni: 371 ***RhoI:*** 34.624

Pooled:	11.084	461.7 ± 32.0
Mean:	11.08	461.6 ± 2.3
Central:	11.084	461.7 ± 32.0
Weigh.I:	11.066	461.0
Weigh.II:	11.08	461.6

Chi-sq.: 0.21 ***P (%):*** 100.0

Dispersion: 0.00

a: 10.397 ***b:*** 10.795 ***r:*** 0.99

Irr.: Zr-DRC09***Glass:*** CN_1

Nd: 15201 ***RhoD:*** 7.176367479

Zeta: 120.36 ± 5.09 ***U.:*** 168.92 (± 25 %)

Goodness: n. d.

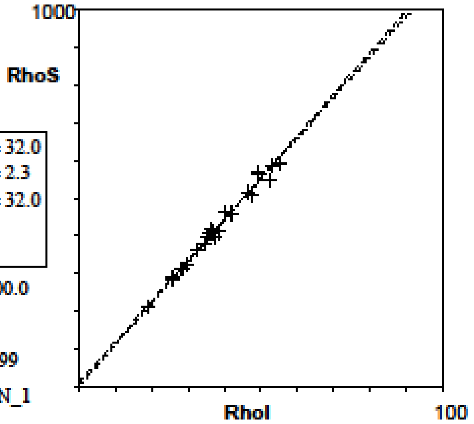

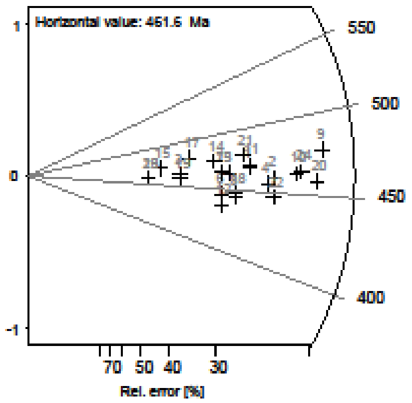

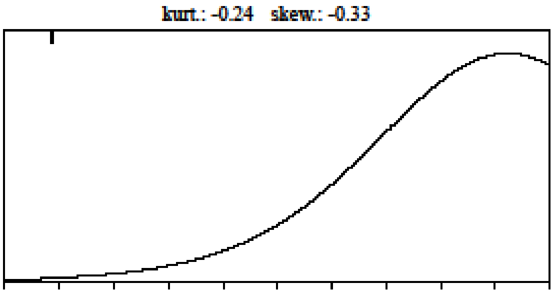

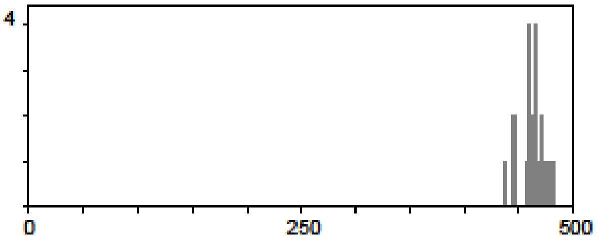

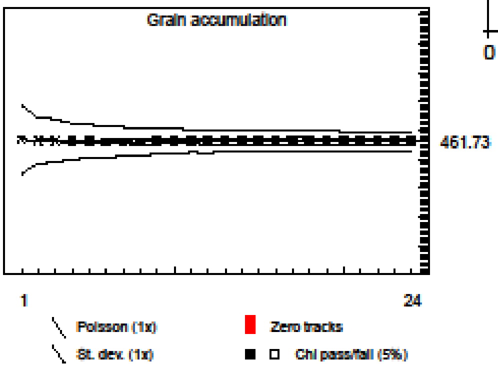

11.3 CANARY ISLANDS (FUERTEVENTURA) - DATA SHEETS

11.3.1 Fuerteventura ZFT

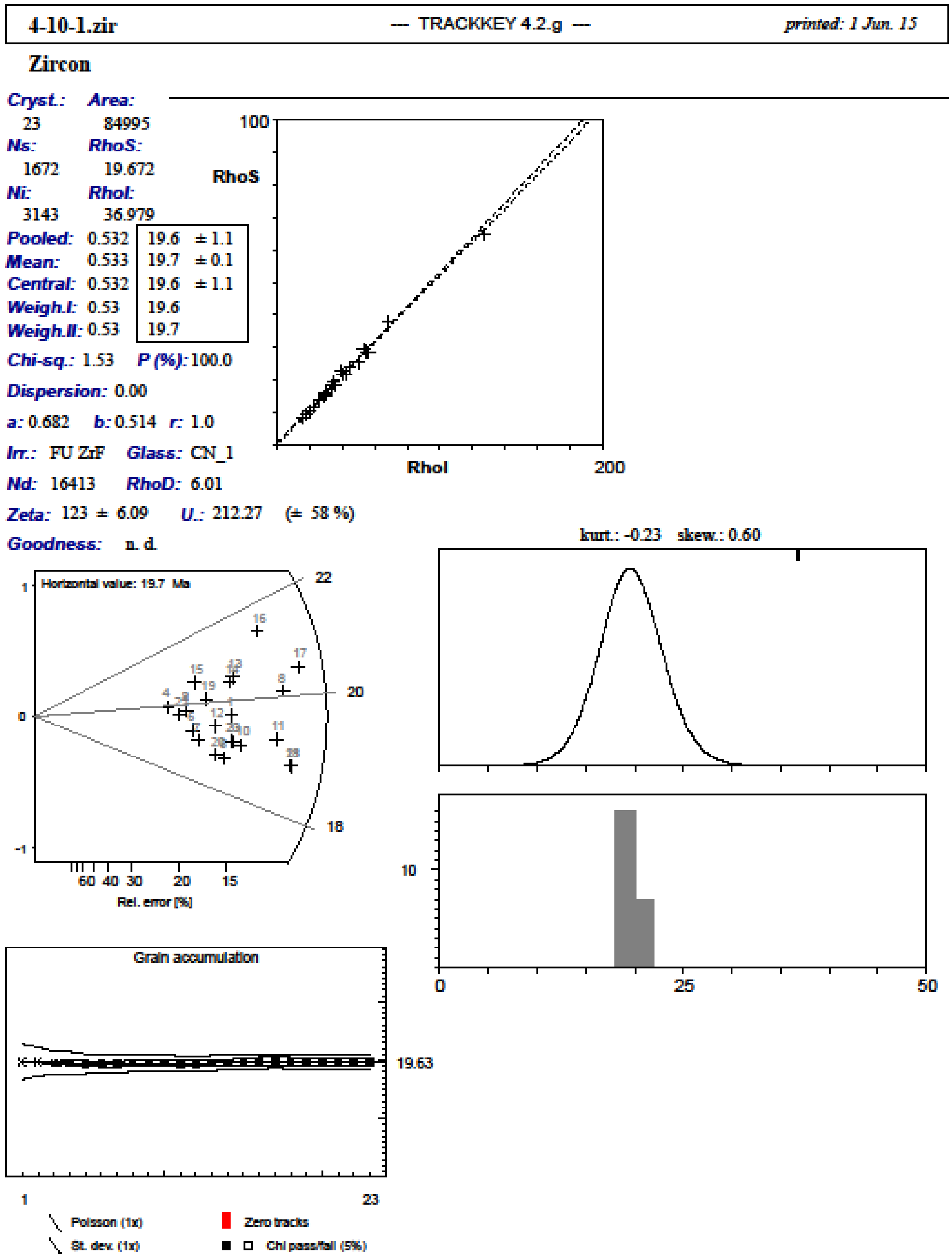

4-10-1.zir — TRACKKEY 4.2.g — *printed: 1 Jun. 15*

Zircon

Cryst.: 23 **Area:** 84995
Ns: 1672 **RhoS:** 19.672
Ni: 3143 **RhoI:** 36.979

Pooled:	0.532	19.6	± 1.1
Mean:	0.533	19.7	± 0.1
Central:	0.532	19.6	± 1.1
Weigh.I:	0.53	19.6	
Weigh.II:	0.53	19.7	

Chi-sq.: 1.53 **P (%):** 100.0
Dispersion: 0.00
a: 0.682 **b:** 0.514 **r:** 1.0
Irr.: FU ZrF **Glass:** CN_1
Nd: 16413 **RhoD:** 6.01
Zeta: 123 ± 6.09 **U.:** 212.27 (± 58 %)
Goodness: n. d.

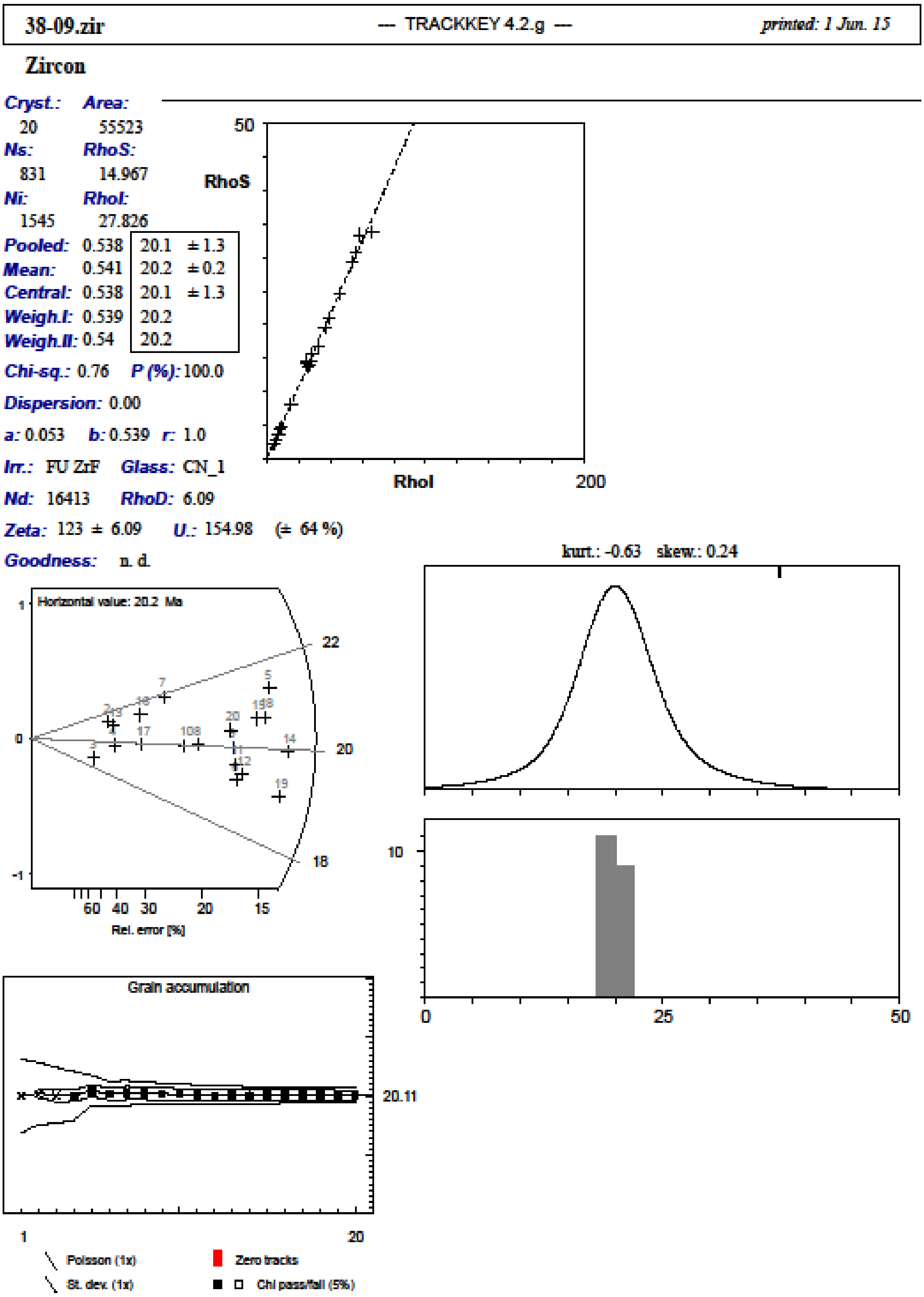

38-09.zir — TRACKKEY 4.2.g — *printed: 1 Jun. 15*

Zircon

Cryst.: 20 **Area:** 55523
Ns: 831 **RhoS:** 14.967
Ni: 1545 **RhoI:** 27.826

Pooled:	0.538	20.1	± 1.3
Mean:	0.541	20.2	± 0.2
Central:	0.538	20.1	± 1.3
Weigh.I:	0.539	20.2	
Weigh.II:	0.54	20.2	

Chi-sq.: 0.76 **P (%):** 100.0
Dispersion: 0.00
a: 0.053 **b:** 0.539 **r:** 1.0
Irr.: FU ZrF **Glass:** CN_1
Nd: 16413 **RhoD:** 6.09
Zeta: 123 ± 6.09 **U.:** 154.98 (± 64 %)
Goodness: n. d.

40-09.zir — TRACKKEY 4.2.g — *printed: 1 Jun. 15*

Zircon

Cryst.: 8 ***Area:*** 18016

Ns: 171 ***RhoS:*** 9.492

Ni: 311 ***RhoI:*** 17.262

Pooled:	0.55	20.5	± 2.2
Mean:	0.553	20.6	± 0.2
Central:	0.55	20.5	± 2.2
Weigh.I:	0.551	20.5	
Weigh.II:	0.55	20.5	

Chi-sq.: 0.09 ***P (%):*** 100.0

Dispersion: 0.00

a: 0.055 ***b:*** 0.549 ***r:*** 1.0

Irr.: FU ZrF ***Glass:*** CN_1

Nd: 16413 ***RhoD:*** 6.06

Zeta: 123 ± 6.09 ***U.:*** 86.8 (± 71 %)

Goodness: n. d.

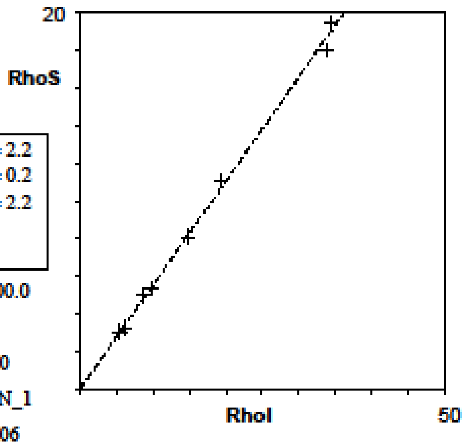

kurt.: -2.02 skew.: -0.16

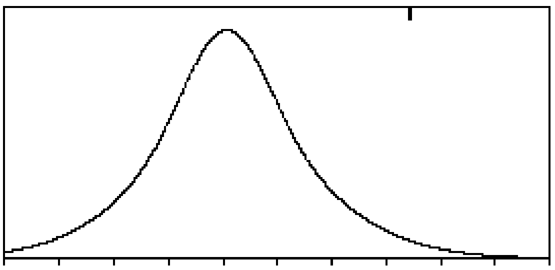

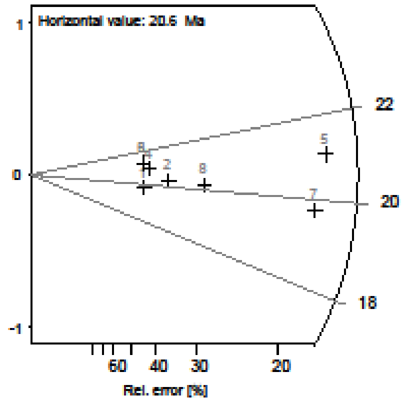

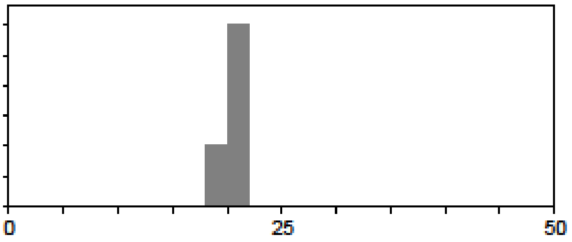

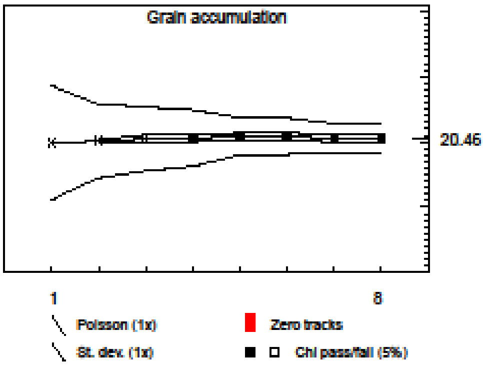

43-2.zir — TRACKKEY 4.2.g — *printed: 1 Jun. 15*

Zircon

Cryst.: **Area:**
8 12318
Ns: **RhoS:**
257 20.864
Ni: **RhoI:**
482 39.13

Pooled:	0.533	20.0	± 1.8
Mean:	0.55	20.7	± 0.5
Central:	0.533	20.0	± 1.8
Weigh.I:	0.523	19.7	
Weigh.II:	0.54	20.5	

Chi-sq.: 0.96 **P (%):** 99.55

Dispersion: 0.00

a: 2.274 **b:** 0.486 **r:** 1.0

Irr.: FU ZrF **Glass:** CN_1

Nd: 16413 **RhoD:** 6.12

Zeta: 123 ± 6.09 **U.:** 243.47 (± 90 %)

Goodness: n. d.

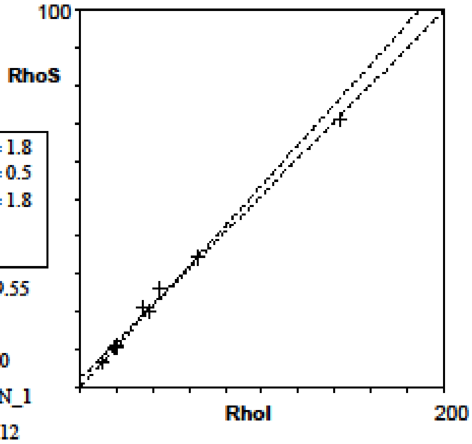

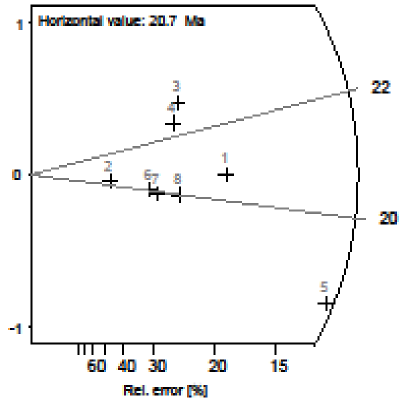

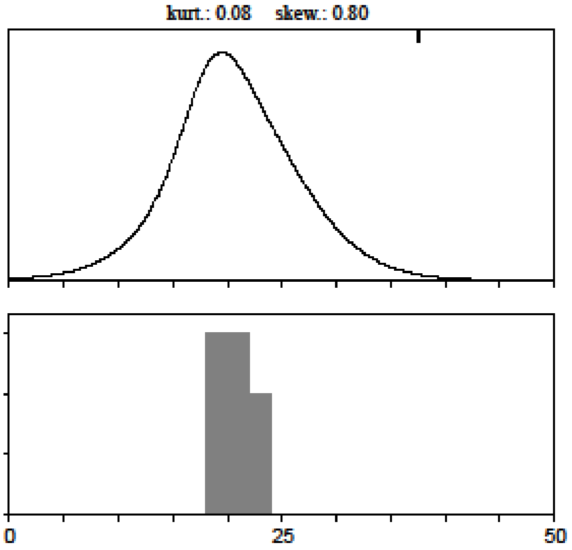

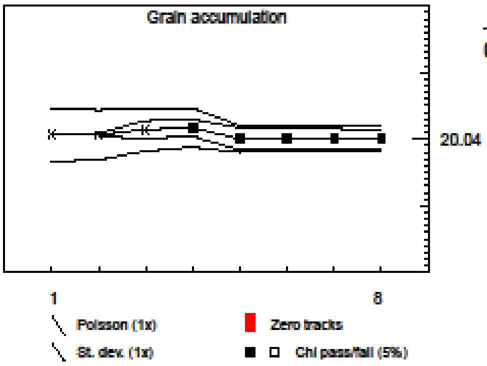

11.3.2 Fuerteventura AFT

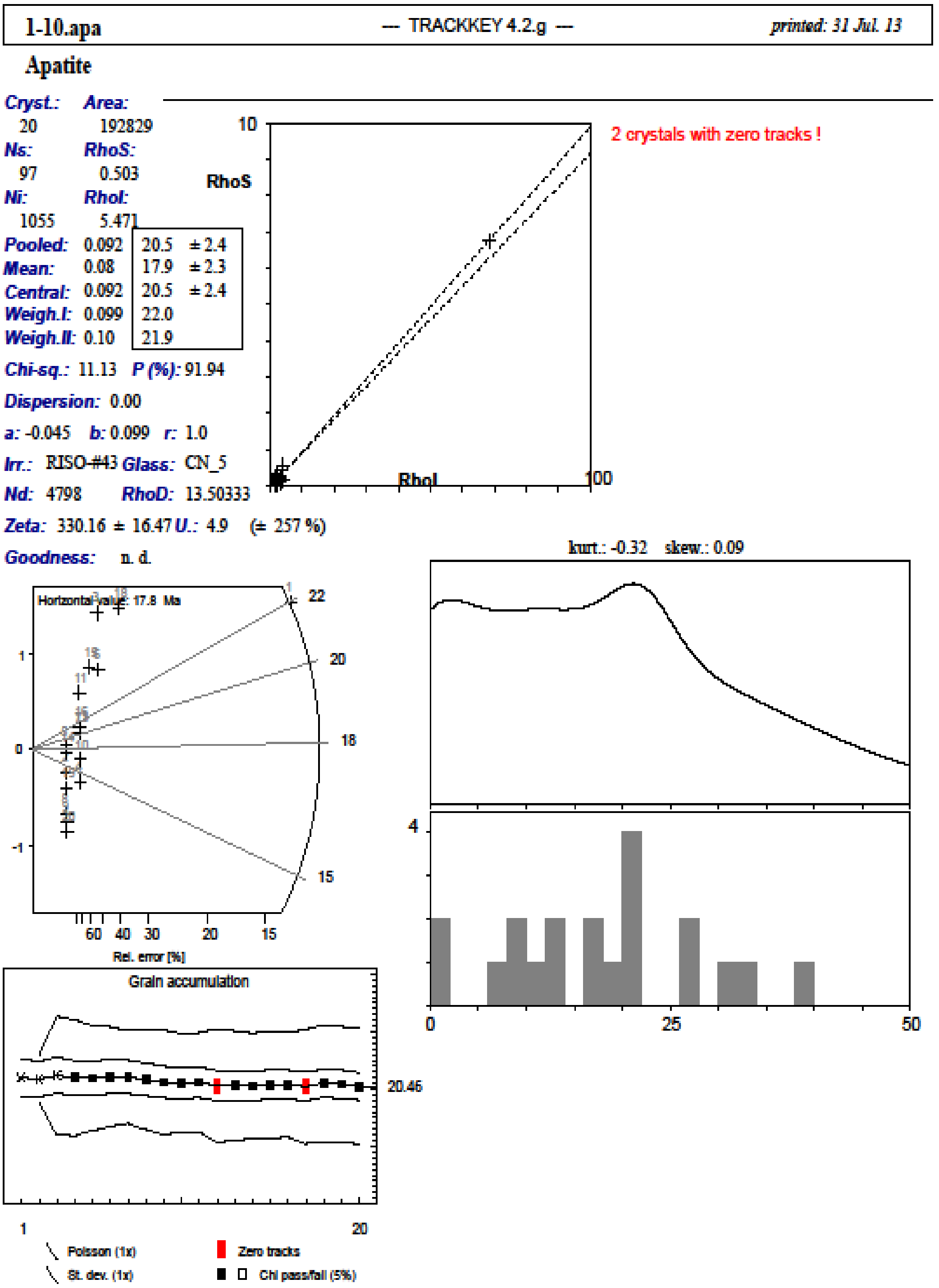

1-10.apa — TRACKKEY 4.2.g — *printed: 31 Jul. 13*

Apatite

Cryst.: 20 *Area:* 192829

Ns: 97 *RhoS:* 0.503

Ni: 1055 *RhoI:* 5.471

Pooled:	0.092	20.5	± 2.4
Mean:	0.08	17.9	± 2.3
Central:	0.092	20.5	± 2.4
Weigh.I:	0.099	22.0	
Weigh.II:	0.10	21.9	

Chi-sq.: 11.13 *P (%):* 91.94

Dispersion: 0.00

a: -0.045 *b:* 0.099 *r:* 1.0

Irr.: RISO-#43 *Glass:* CN_5

Nd: 4798 *RhoD:* 13.50333

Zeta: 330.16 ± 16.47 *U.:* 4.9 (± 257 %)

Goodness: n. d.

2 crystals with zero tracks !

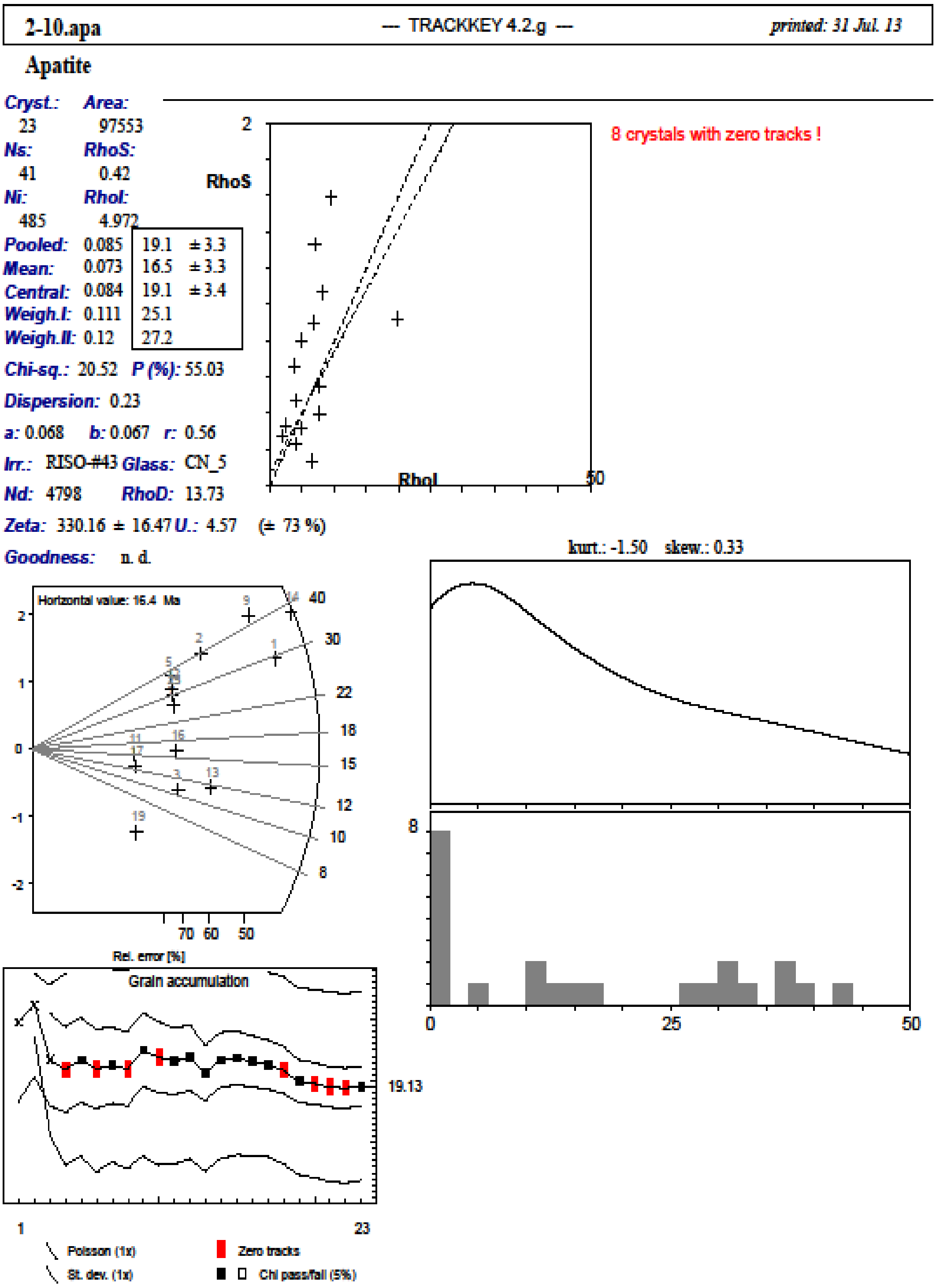

2-10.apa — TRACKKEY 4.2.g — *printed: 31 Jul. 13*

Apatite

Cryst.: 23 ***Area:*** 97553

Ns: 41 ***RhoS:*** 0.42

Ni: 485 ***RhoI:*** 4.972

Pooled:	0.085	19.1	± 3.3
Mean:	0.073	16.5	± 3.3
Central:	0.084	19.1	± 3.4
Weigh.I:	0.111	25.1	
Weigh.II:	0.12	27.2	

Chi-sq.: 20.52 ***P (%):*** 55.03

Dispersion: 0.23

a: 0.068 ***b:*** 0.067 ***r:*** 0.56

Irr.: RISO-#43 ***Glass:*** CN_5

Nd: 4798 ***RhoD:*** 13.73

Zeta: 330.16 ± 16.47 ***U.:*** 4.57 (± 73 %)

Goodness: n. d.

8 crystals with zero tracks !

kurt.: -1.50 skew.: 0.33

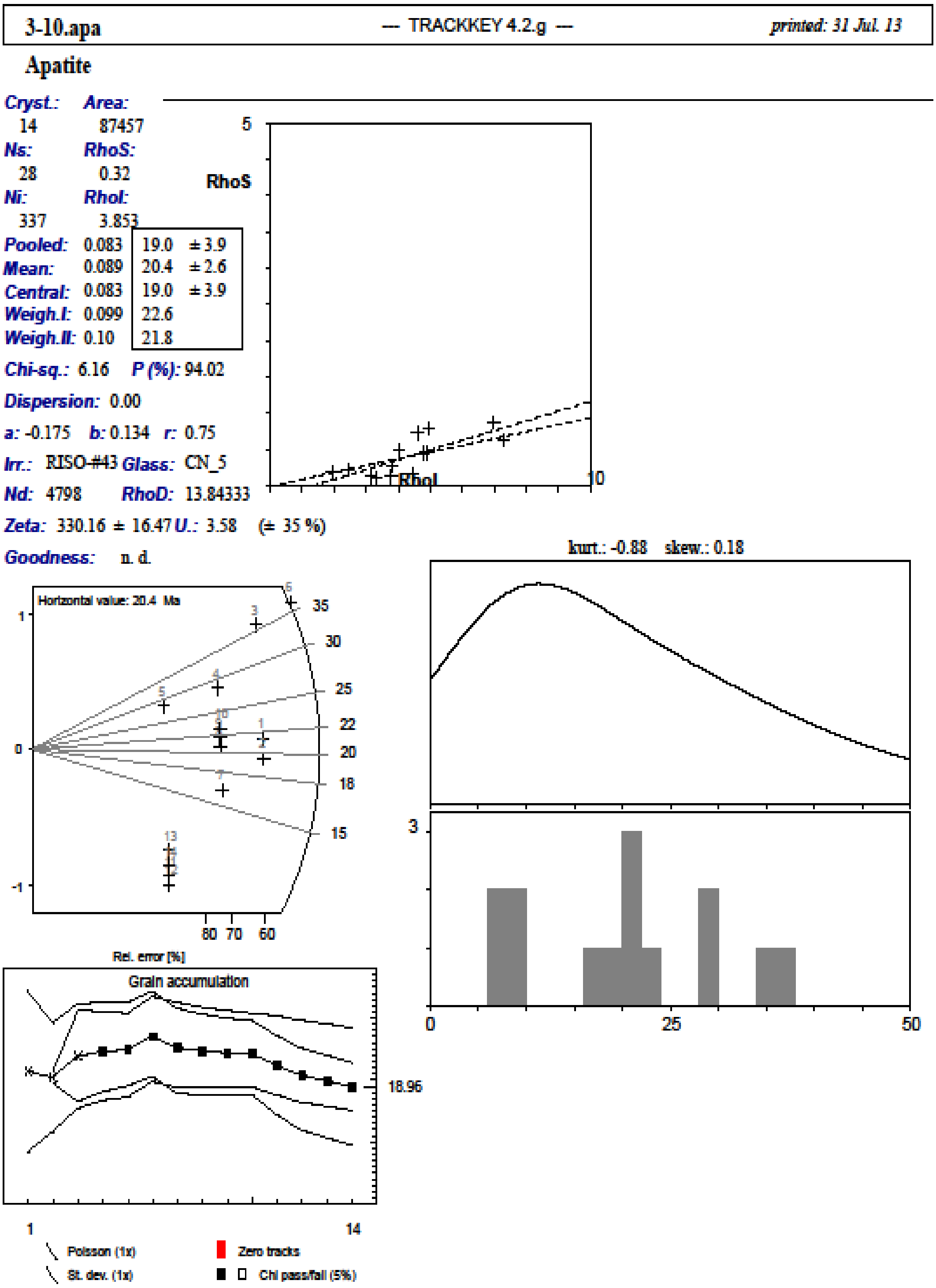

3-10.apa — TRACKKEY 4.2.g — *printed: 31 Jul. 13*

Apatite

Cryst.: 14 *Area:* 87457

Ns: 28 *RhoS:* 0.32

Ni: 337 *RhoI:* 3.853

Pooled:	0.083	19.0	± 3.9
Mean:	0.089	20.4	± 2.6
Central:	0.083	19.0	± 3.9
Weigh.I:	0.099	22.6	
Weigh.II:	0.10	21.8	

Chi-sq.: 6.16 *P (%):* 94.02

Dispersion: 0.00

a: -0.175 *b:* 0.134 *r:* 0.75

Irr.: RISO-#43 *Glass:* CN_5

Nd: 4798 *RhoD:* 13.84333

Zeta: 330.16 ± 16.47 *U.:* 3.58 (± 35 %)

Goodness: n. d.

4-10.apa — TRACKKEY 4.2.g — *printed: 31 Jul. 13*

Apatite

Cryst.:	***Area:***
22	134685
Ns:	***RhoS:***
99	0.735
Ni:	***RhoI:***
1575	11.694

Pooled:	0.063	14.5	± 1.7
Mean:	0.065	15.0	± 1.2
Central:	0.063	14.5	± 1.7
Weigh.I:	0.065	15.0	
Weigh.II:	0.07	15.5	

Chi-sq.: 9.83 ***P (%):*** 98.11

Dispersion: 0.00

a: 0.041 ***b:*** 0.061 ***r:*** 0.93

Irr.: RISO-#43 ***Glass:*** CN_5

Nd: 4798 ***RhoD:*** 13.95667

Zeta: 330.16 ± 16.47 ***U.:*** 9.05 (± 83 %)

Goodness: n. d.

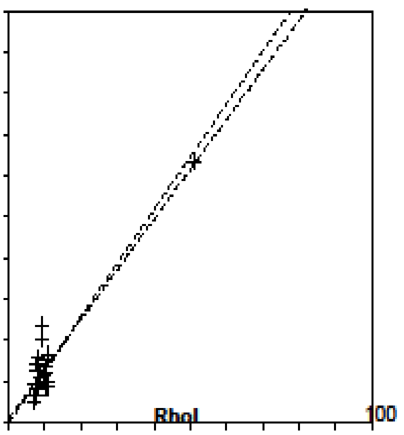

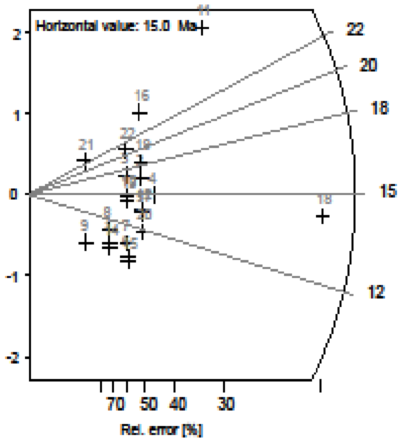

kurt.: 1.04 skew.: 1.17

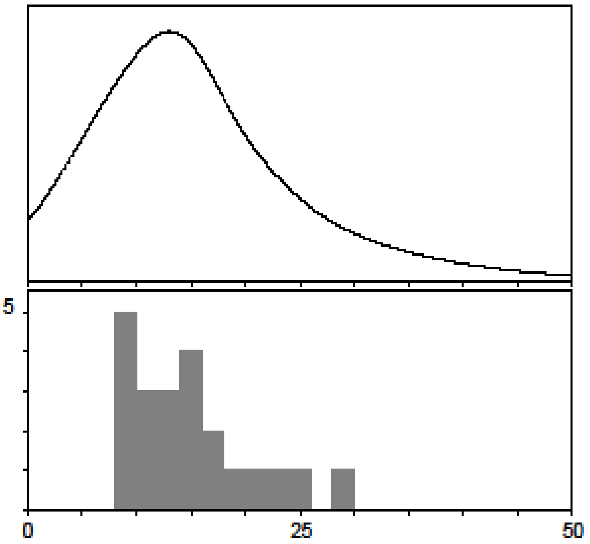

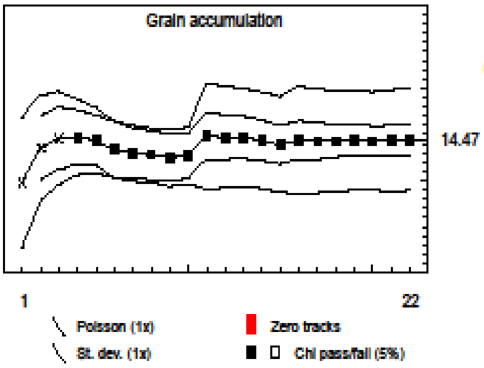

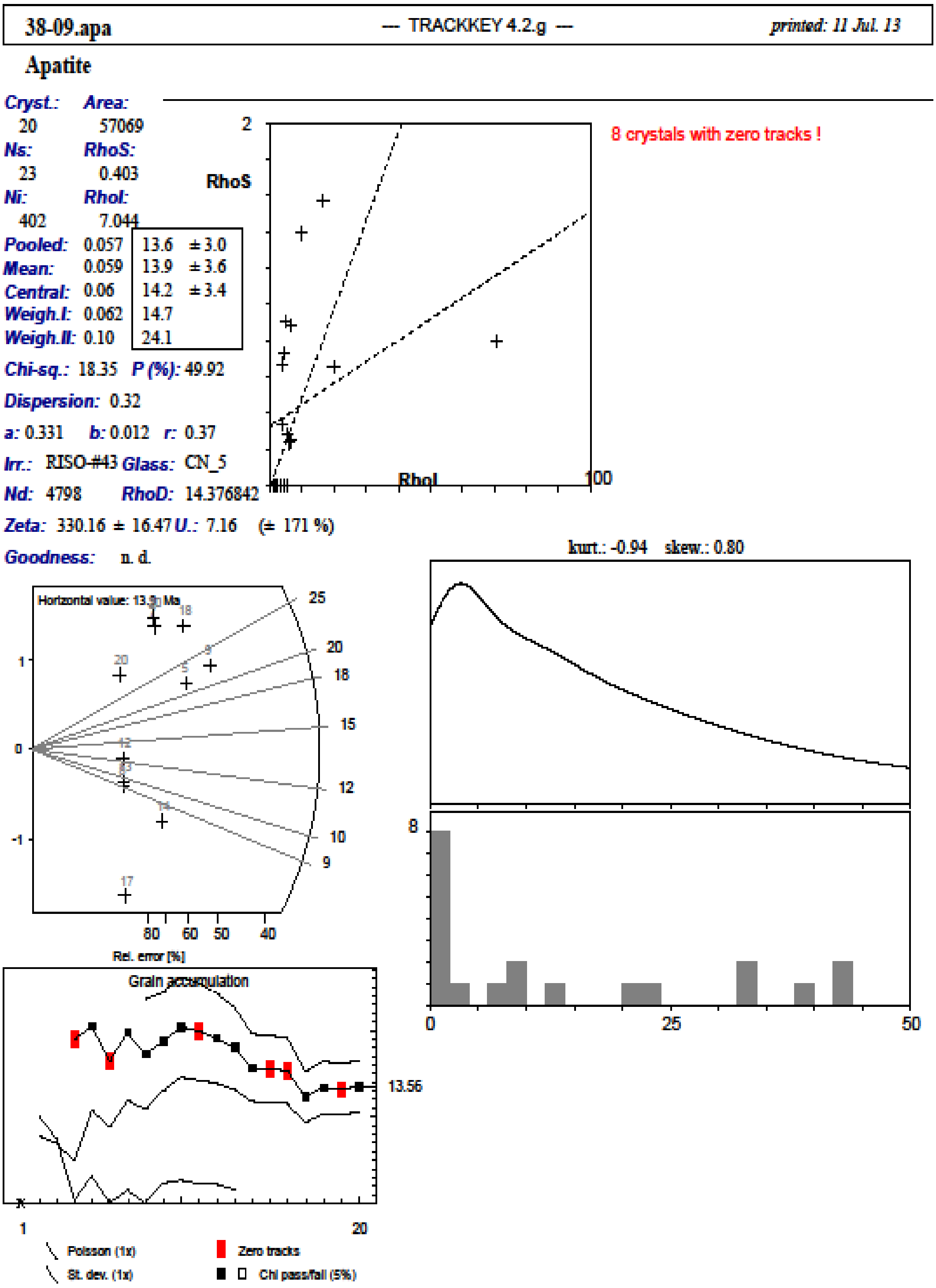

38-09.apa — TRACKKEY 4.2.g — *printed: 11 Jul. 13*

Apatite

Cryst.: 20 ***Area:*** 57069

Ns: 23 ***RhoS:*** 0.403

Ni: 402 ***RhoI:*** 7.044

Pooled:	0.057	13.6	± 3.0
Mean:	0.059	13.9	± 3.6
Central:	0.06	14.2	± 3.4
Weigh.I:	0.062	14.7	
Weigh.II:	0.10	24.1	

Chi-sq.: 18.35 ***P (%):*** 49.92

Dispersion: 0.32

a: 0.331 ***b:*** 0.012 ***r:*** 0.37

Irr.: RISO-#43 ***Glass:*** CN_5

Nd: 4798 ***RhoD:*** 14.376842

Zeta: 330.16 ± 16.47 ***U.:*** 7.16 (± 171 %)

Goodness: n. d.

8 crystals with zero tracks !

kurt.: -0.94 skew.: 0.80

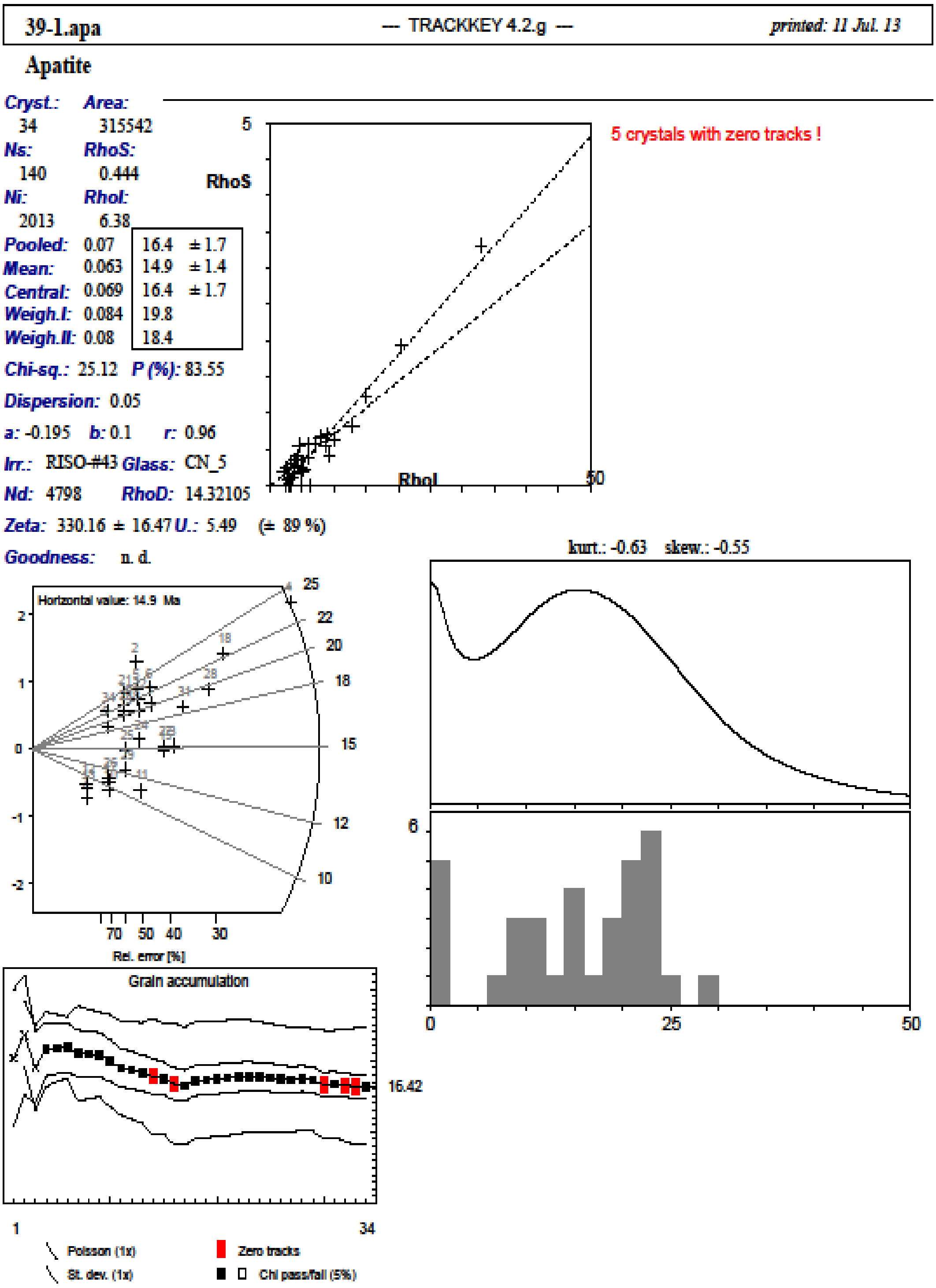

39-1.apa — TRACKKEY 4.2.g — *printed: 11 Jul. 13*

Apatite

Cryst.:	**Area:**
34	315542
Ns:	**RhoS:**
140	0.444
Ni:	**RhoI:**
2013	6.38

Pooled:	0.07	16.4	± 1.7
Mean:	0.063	14.9	± 1.4
Central:	0.069	16.4	± 1.7
Weigh.I:	0.084	19.8	
Weigh.II:	0.08	18.4	

Chi-sq.: 25.12 **P (%):** 83.55

Dispersion: 0.05

a: -0.195 **b:** 0.1 **r:** 0.96

Irr.: RISO-#43 **Glass:** CN_5

Nd: 4798 **RhoD:** 14.32105

Zeta: 330.16 ± 16.47 **U.:** 5.49 (± 89 %)

Goodness: n. d.

5 crystals with zero tracks !

kurt.: -0.63 skew.: -0.55

40-09-01.apa — TRACKKEY 4.2.g — *printed: 31 Jul. 13*

Apatite

Cryst.:	***Area:***		
29	214052		
Ns:	***RhoS:***		
37	0.173		
Ni:	***RhoI:***		
622	2.906		
Pooled:	0.059	13.9	± 2.5
Mean:	0.066	15.4	± 2.5
Central:	0.06	14.0	± 2.5
Weigh.I:	0.079	18.4	
Weigh.II:	0.09	21.4	

Chi-sq.: 22.37 ***P (%):*** 76.39

Dispersion: 0.13

a: 0.096 ***b:*** 0.027 ***r:*** 0.32

Irr.: RISO-#43 ***Glass:*** CN_5

Nd: 4798 ***RhoD:*** 14.15

Zeta: 330.16 ± 16.47 ***U.:*** 2.33 (± 63 %)

Goodness: n. d.

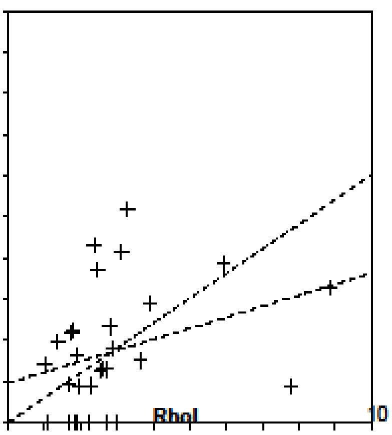

7 crystals with zero tracks !

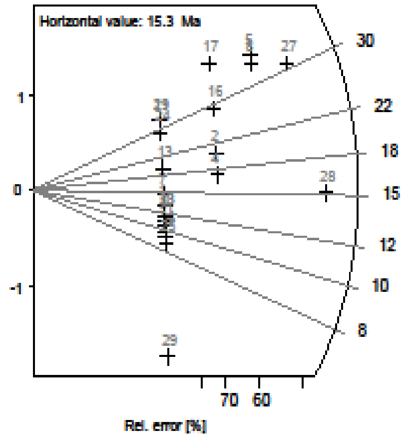

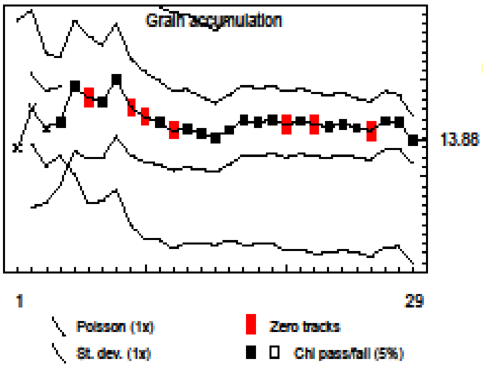

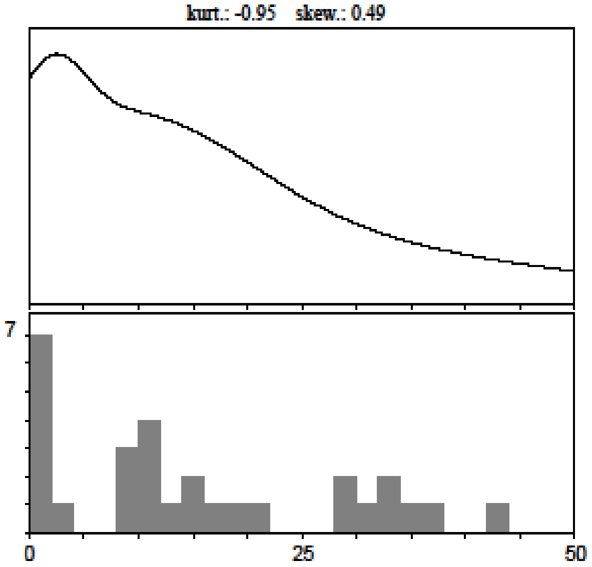

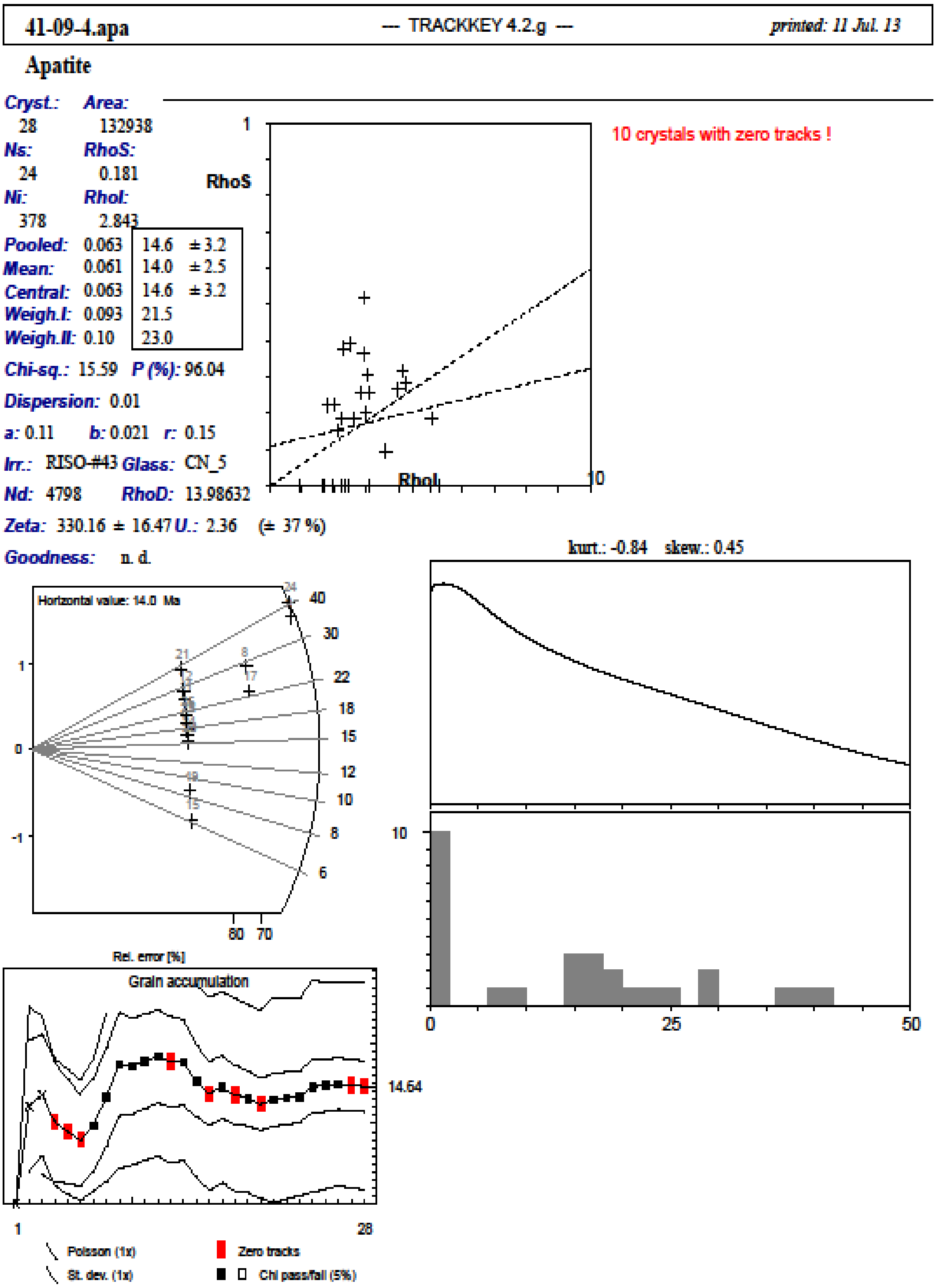

41-09-4.apa — TRACKKEY 4.2.g — *printed: 11 Jul. 13*

Apatite

Cryst.:	*Area:*
28	132938
Ns:	*RhoS:*
24	0.181
Ni:	*RhoI:*
378	2.843

Pooled:	0.063	14.6	± 3.2
Mean:	0.061	14.0	± 2.5
Central:	0.063	14.6	± 3.2
Weigh.I:	0.093	21.5	
Weigh.II:	0.10	23.0	

Chi-sq.: 15.59 *P (%):* 96.04

Dispersion: 0.01

a: 0.11 *b:* 0.021 *r:* 0.15

Irr.: RISO-#43 *Glass:* CN_5

Nd: 4798 *RhoD:* 13.98632

Zeta: 330.16 ± 16.47 *U.:* 2.36 (± 37 %)

Goodness: n. d.

10 crystals with zero tracks !

kurt.: -0.84 skew.: 0.45

42-II.apa — TRACKKEY 4.2.g — *printed: 31 Jul. 13*

Apatite

Cryst.: 20 ***Area:*** 66405

Ns: 10 ***RhoS:*** 0.151

Ni: 184 ***RhoI:*** 2.771

Pooled:	0.054	12.5	± 4.1
Mean:	0.051	11.7	± 3.5
Central:	0.054	12.5	± 4.1
Weigh.I:	0.096	22.0	
Weigh.II:	0.11	25.3	

Chi-sq.: 9.3 ***P (%):*** 96.83

Dispersion: 0.00

a: -0.059 ***b:*** 0.076 ***r:*** 0.57

Irr.: RISO-#43 ***Glass:*** CN_5

Nd: 4798 ***RhoD:*** 13.930536

Zeta: 330.16 ± 16.47 ***U.:*** 2.36 (± 60 %)

Goodness: n. d.

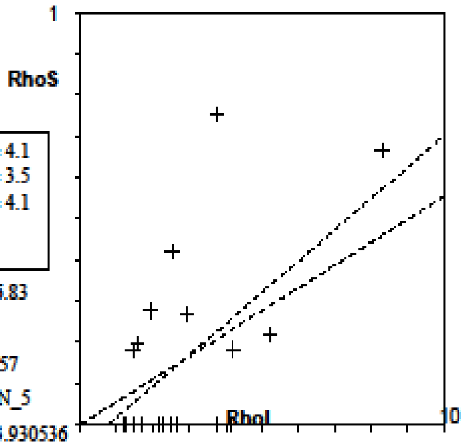

11 crystals with zero tracks !

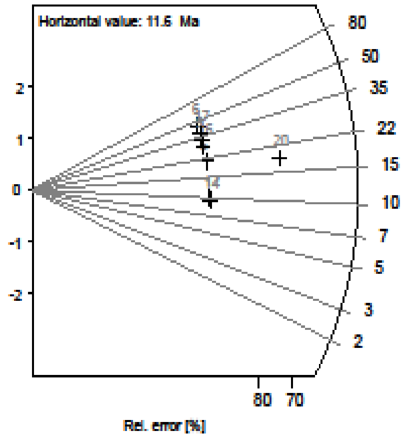

kurt.: -0.44 skew.: 0.98

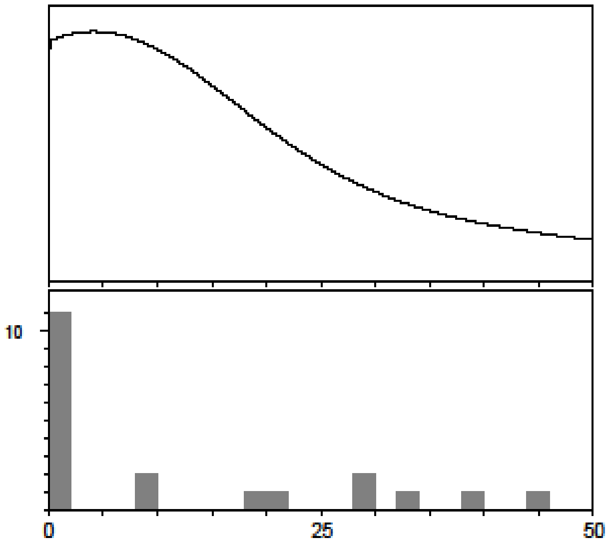

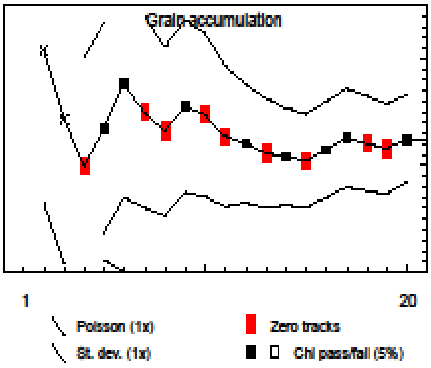

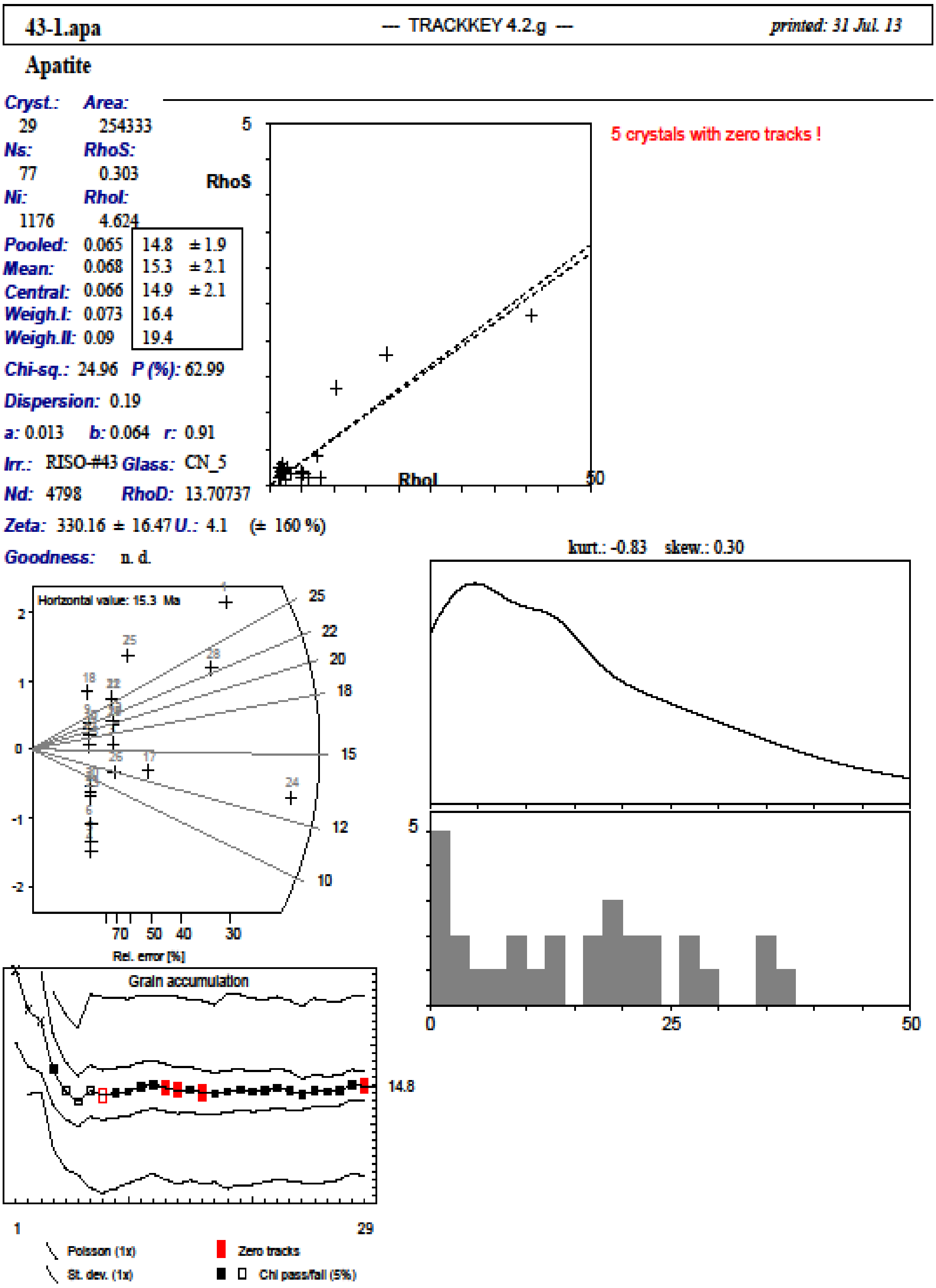

43-1.apa — TRACKKEY 4.2.g — *printed: 31 Jul. 13*

Apatite

Cryst.:	*Area:*
29	254333
Ns:	*RhoS:*
77	0.303
Ni:	*RhoI:*
1176	4.624

Pooled:	0.065	14.8	± 1.9
Mean:	0.068	15.3	± 2.1
Central:	0.066	14.9	± 2.1
Weigh.I:	0.073	16.4	
Weigh.II:	0.09	19.4	

Chi-sq.: 24.96 *P (%):* 62.99

Dispersion: 0.19

a: 0.013 *b:* 0.064 *r:* 0.91

Irr.: RISO-#43 *Glass:* CN_5

Nd: 4798 *RhoD:* 13.70737

Zeta: 330.16 ± 16.47 *U.:* 4.1 (± 160 %)

Goodness: n. d.

5 crystals with zero tracks !

kurt.: -0.83 skew.: 0.30

44-1.apa — TRACKKEY 4.2.g — *printed: 31 Jul. 13*

Apatite

Cryst.: 20	**Area:** 143891		
Ns: 32	**RhoS:** 0.222		
Ni: 462	**RhoI:** 3.211		
Pooled:	0.069	15.6	± 3.0
Mean:	0.074	16.7	± 2.8
Central:	0.069	15.6	± 3.0
Weigh.I:	0.091	20.4	
Weigh.II:	0.10	22.6	

Chi-sq.: 14.16 **P (%):** 77.44

Dispersion: 0.00

a: 0.008 **b:** 0.07 **r:** 0.66

Irr.: RISO-#43 **Glass:** CN_5

Nd: 4798 **RhoD:** 13.65158

Zeta: 330.16 ± 16.47 **U.:** 2.9 (± 68 %)

Goodness: n. d.

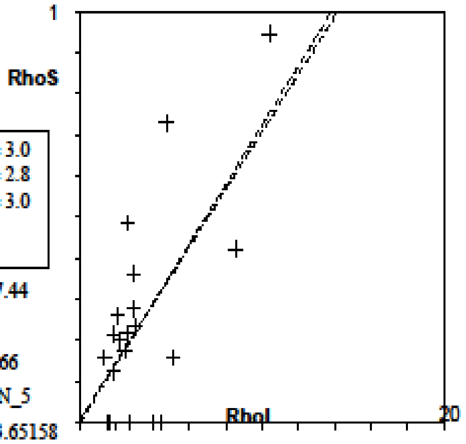

5 crystals with zero tracks !

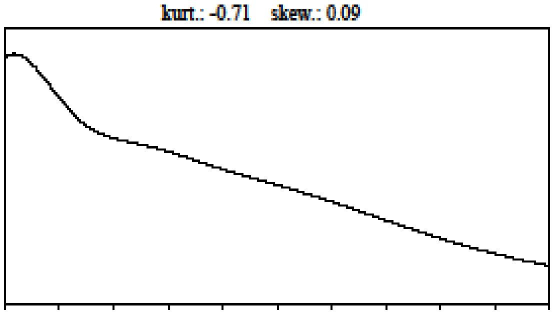

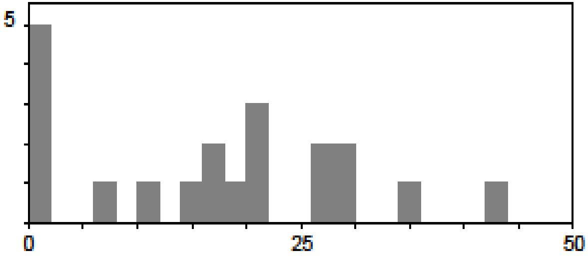

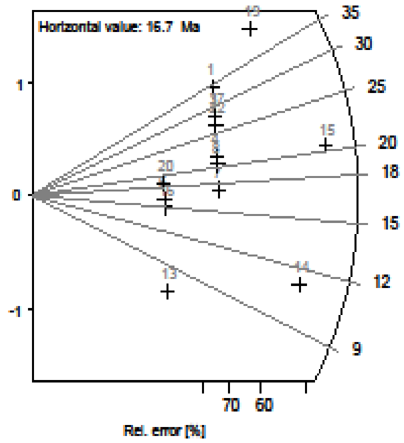

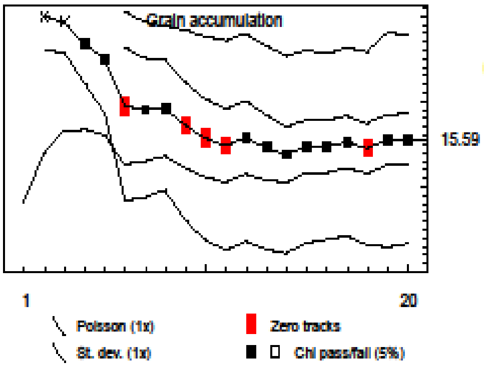

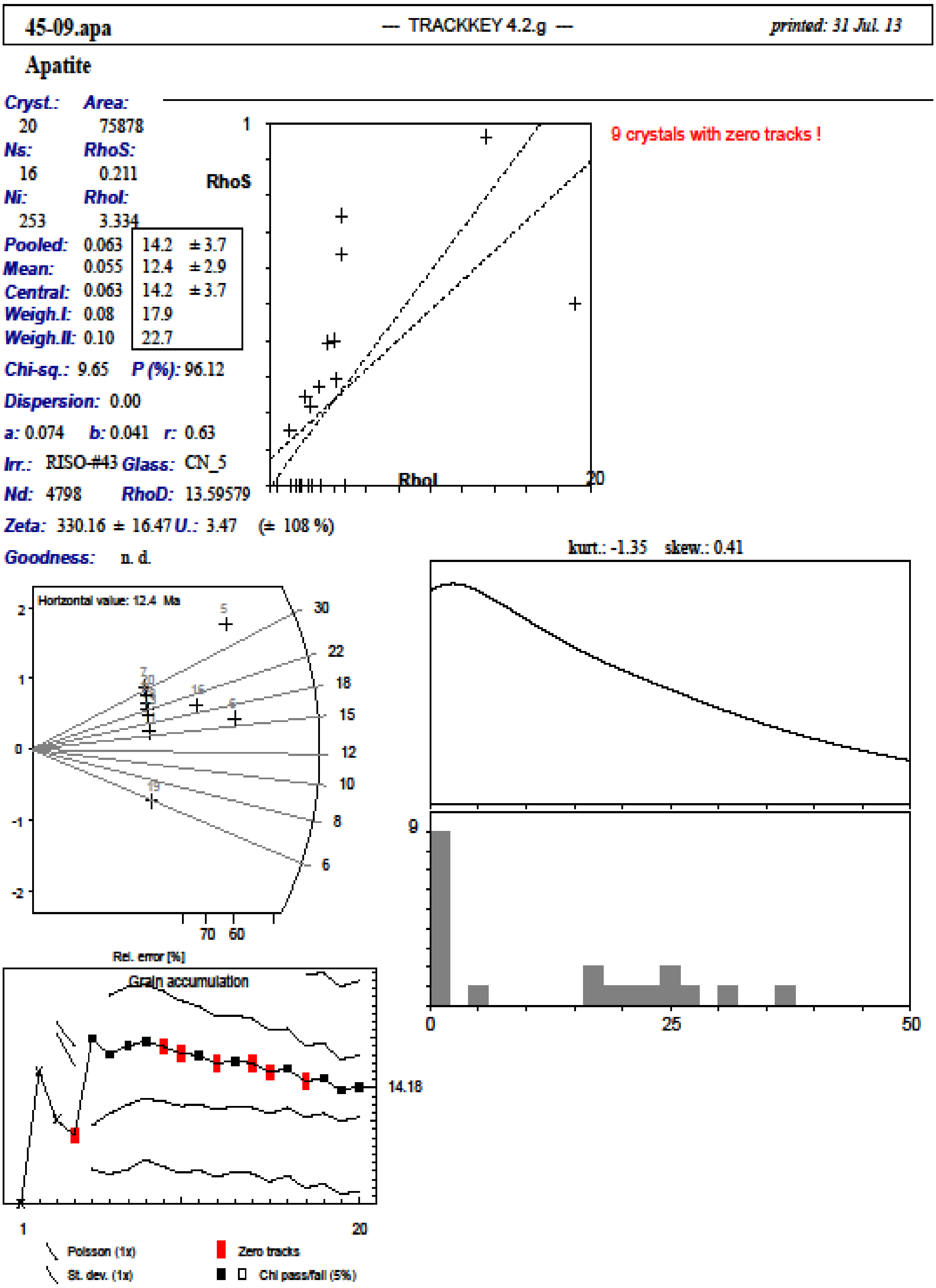

45-09.apa — TRACKKEY 4.2.g — *printed: 31 Jul. 13*

Apatite

Cryst.: 20 **Area:** 75878

Ns: 16 **RhoS:** 0.211

Ni: 253 **RhoI:** 3.334

Pooled: 0.063 14.2 ± 3.7

Mean: 0.055 12.4 ± 2.9

Central: 0.063 14.2 ± 3.7

Weigh.I: 0.08 17.9

Weigh.II: 0.10 22.7

Chi-sq.: 9.65 **P (%):** 96.12

Dispersion: 0.00

a: 0.074 **b:** 0.041 **r:** 0.63

Irr.: RISO-#43 **Glass:** CN_5

Nd: 4798 **RhoD:** 13.59579

Zeta: 330.16 ± 16.47 **U.:** 3.47 (± 108 %)

Goodness: n. d.

9 crystals with zero tracks !

kurt.: -1.35 skew.: 0.41

11.4 CANARY ISLANDS (LA GOMERA) - DATA SHEETS

11.4.1 La Gomera ZFT

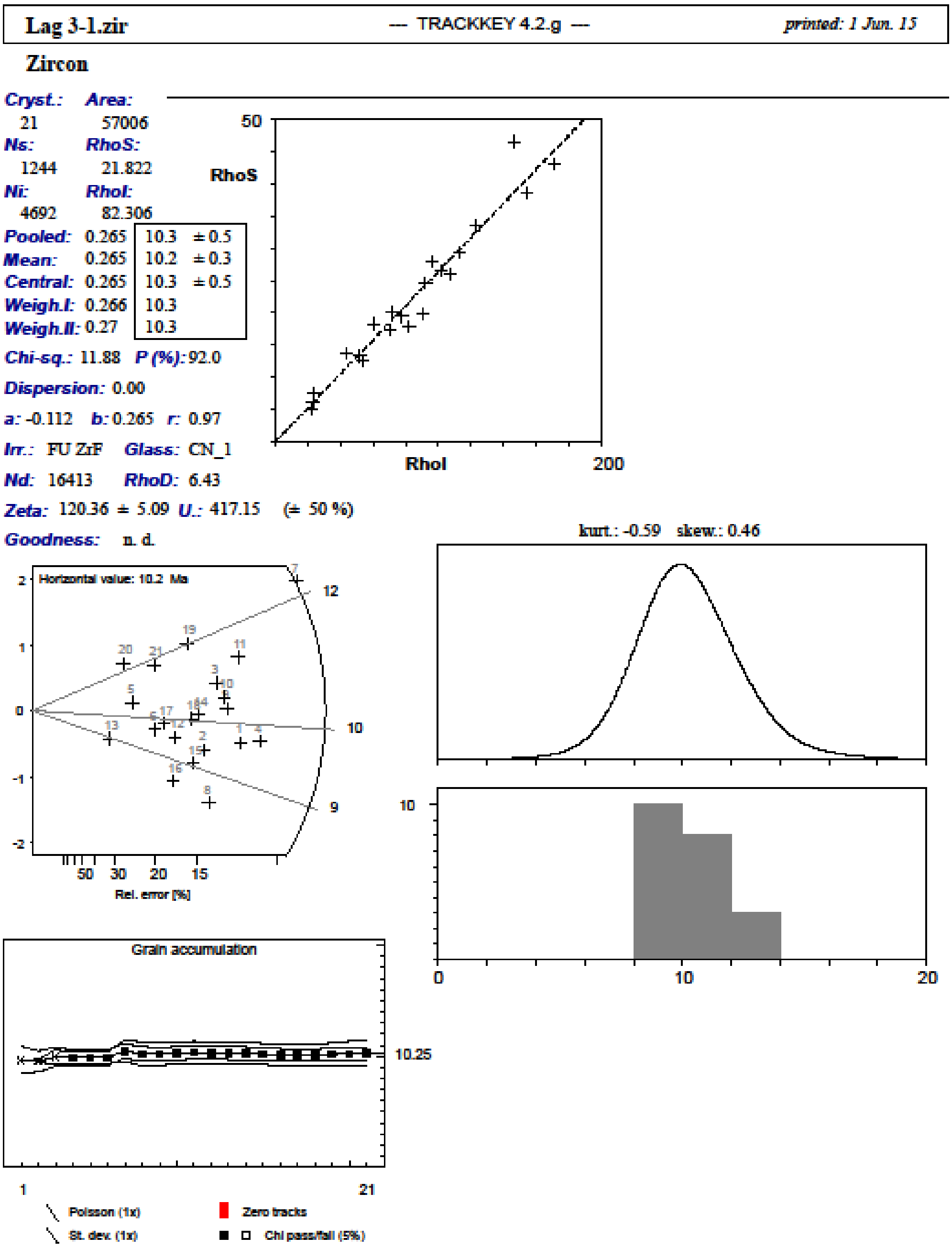

Lag 3-1.zir — TRACKKEY 4.2.g — *printed: 1 Jun. 15*

Zircon

Cryst.: 21 *Area:* 57006
Ns: 1244 *RhoS:* 21.822
Ni: 4692 *RhoI:* 82.306
Pooled: 0.265 10.3 ±0.5
Mean: 0.265 10.2 ±0.3
Central: 0.265 10.3 ±0.5
Weigh.I: 0.266 10.3
Weigh.II: 0.27 10.3
Chi-sq.: 11.88 *P (%):* 92.0
Dispersion: 0.00
a: -0.112 *b:* 0.265 *r:* 0.97
Irr.: FU ZrF *Glass:* CN_1
Nd: 16413 *RhoD:* 6.43
Zeta: 120.36 ± 5.09 *U.:* 417.15 (± 50 %)
Goodness: n. d.

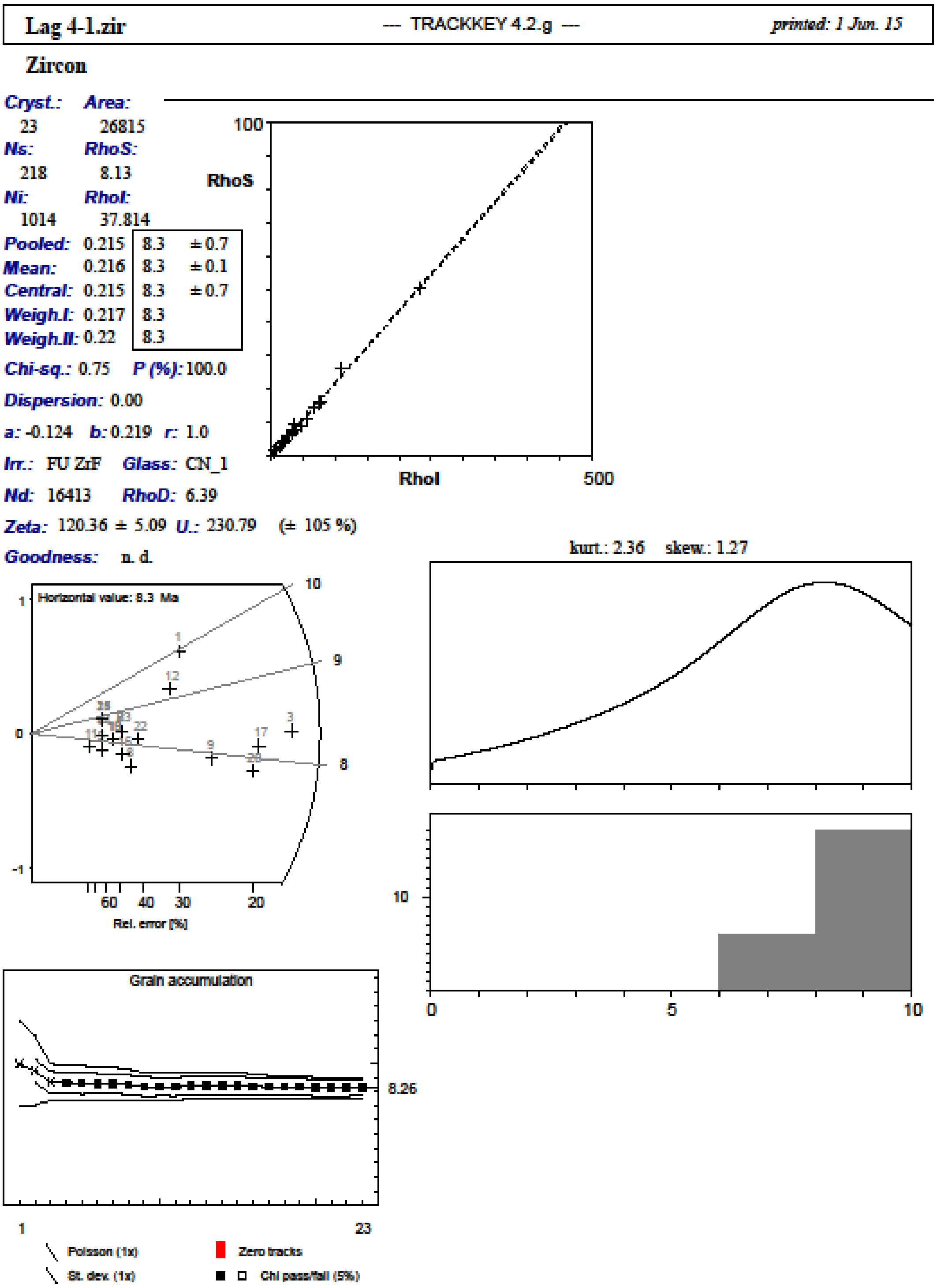

Lag 4-1.zir — TRACKKEY 4.2.g — *printed: 1 Jun. 15*

Zircon

Cryst.:	**Area:**
23	26815
Ns:	**RhoS:**
218	8.13
Ni:	**RhoI:**
1014	37.814

Pooled:	0.215	8.3	± 0.7
Mean:	0.216	8.3	± 0.1
Central:	0.215	8.3	± 0.7
Weigh.I:	0.217	8.3	
Weigh.II:	0.22	8.3	

Chi-sq.: 0.75 **P (%):** 100.0

Dispersion: 0.00

a: -0.124 **b:** 0.219 **r:** 1.0

Irr.: FU ZrF **Glass:** CN_1

Nd: 16413 **RhoD:** 6.39

Zeta: 120.36 ± 5.09 **U.:** 230.79 (± 105 %)

Goodness: n. d.

kurt.: 2.36 skew.: 1.27

Lag 5-1.zir — TRACKKEY 4.2.g — *printed: 1 Jun. 15*

Zircon

Cryst.:	**Area:**
25	53259
Ns:	**RhoS:**
624	11.716
Ni:	**RhoI:**
2790	52.385

Pooled:	0.224	8.6	± 0.5
Mean:	0.223	8.5	± 0.3
Central:	0.224	8.6	± 0.5
Weigh.I:	0.226	8.6	
Weigh.II:	0.23	8.7	

Chi-sq.: 16.64 **P (%):** 86.35

Dispersion: 0.01

a: 0.278 **b:** 0.218 **r:** 0.9

Irr.: FU ZrF **Glass:** CN_1

Nd: 16413 **RhoD:** 6.36

Zeta: 120.36 ± 5.09 **U.:** 258.24 (± 45 %)

Goodness: n. d.

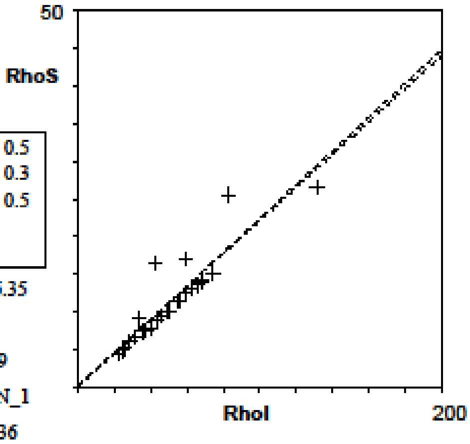

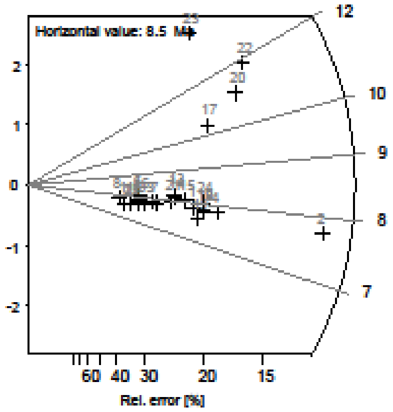

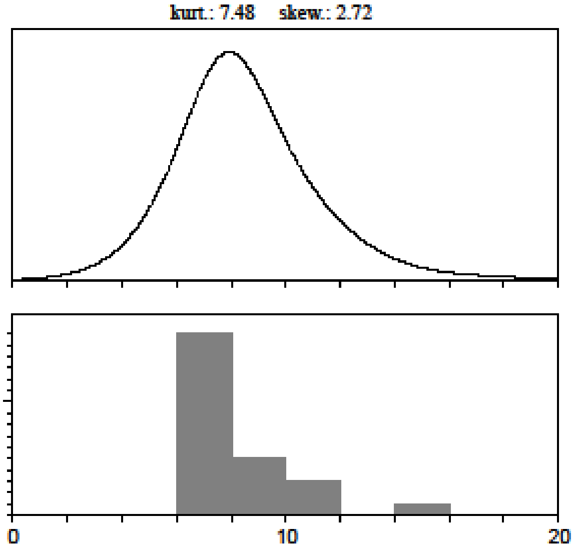

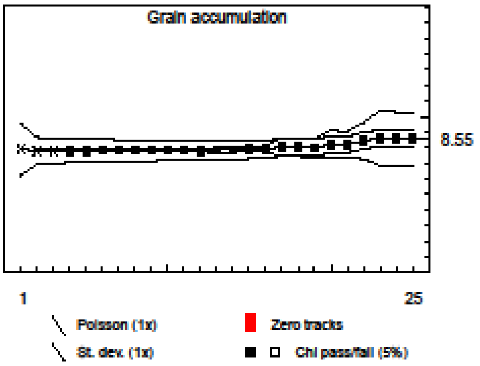

Lag 7-1.zir — TRACKKEY 4.2.g — *printed: 1 Jun. 15*

Zircon

Cryst.:	*Area:*
22	45687
Ns:	*RhoS:*
996	21.8
Ni:	*RhoI:*
4209	92.127

Pooled:	0.237	9.0	± 0.5
Mean:	0.239	9.1	± 0.1
Central:	0.237	9.0	± 0.5
Weigh.I:	0.236	9.0	
Weigh.II:	0.24	9.0	

Chi-sq.: 0.88 *P (%):* 100.0

Dispersion: 0.00

a: 0.5 *b:* 0.232 *r:* 1.0

Irr.: FU ZrF *Glass:* CN_1

Nd: 16413 *RhoD:* 6.33

Zeta: 120.36 ± 5.09 *U.:* 524.2 (± 74 %)

Goodness: n. d.

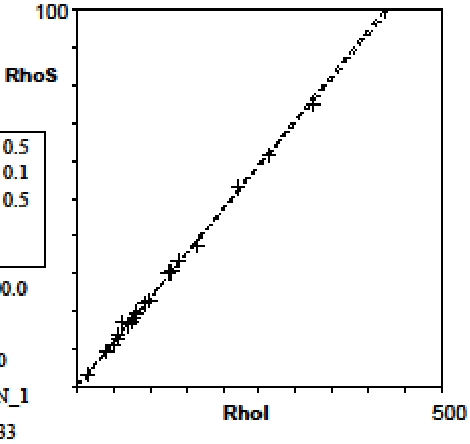

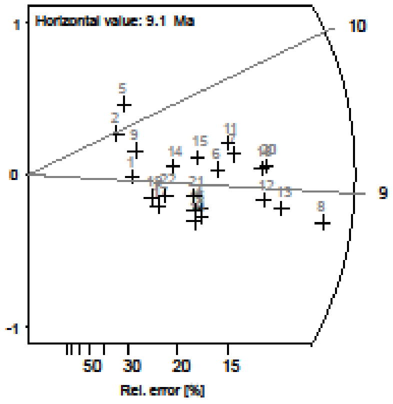

kurt.: 3.66 skew.: 1.74

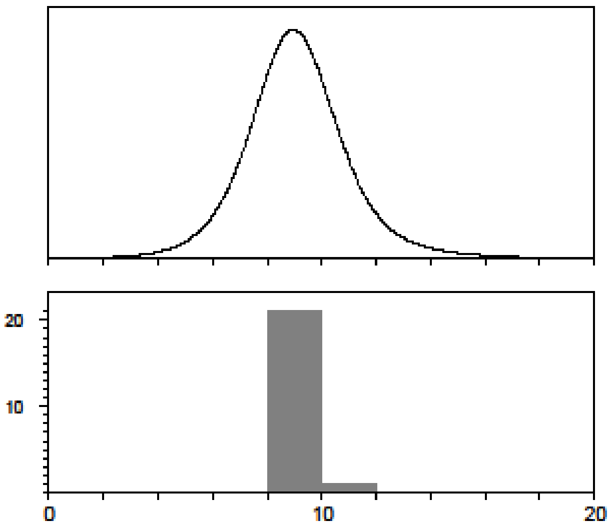

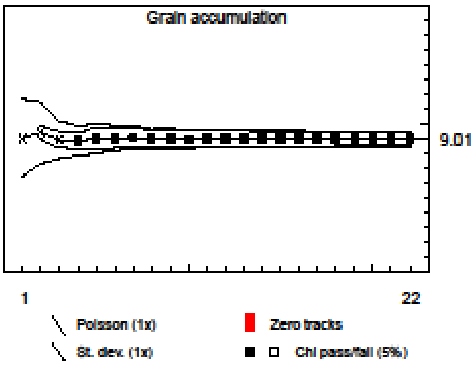

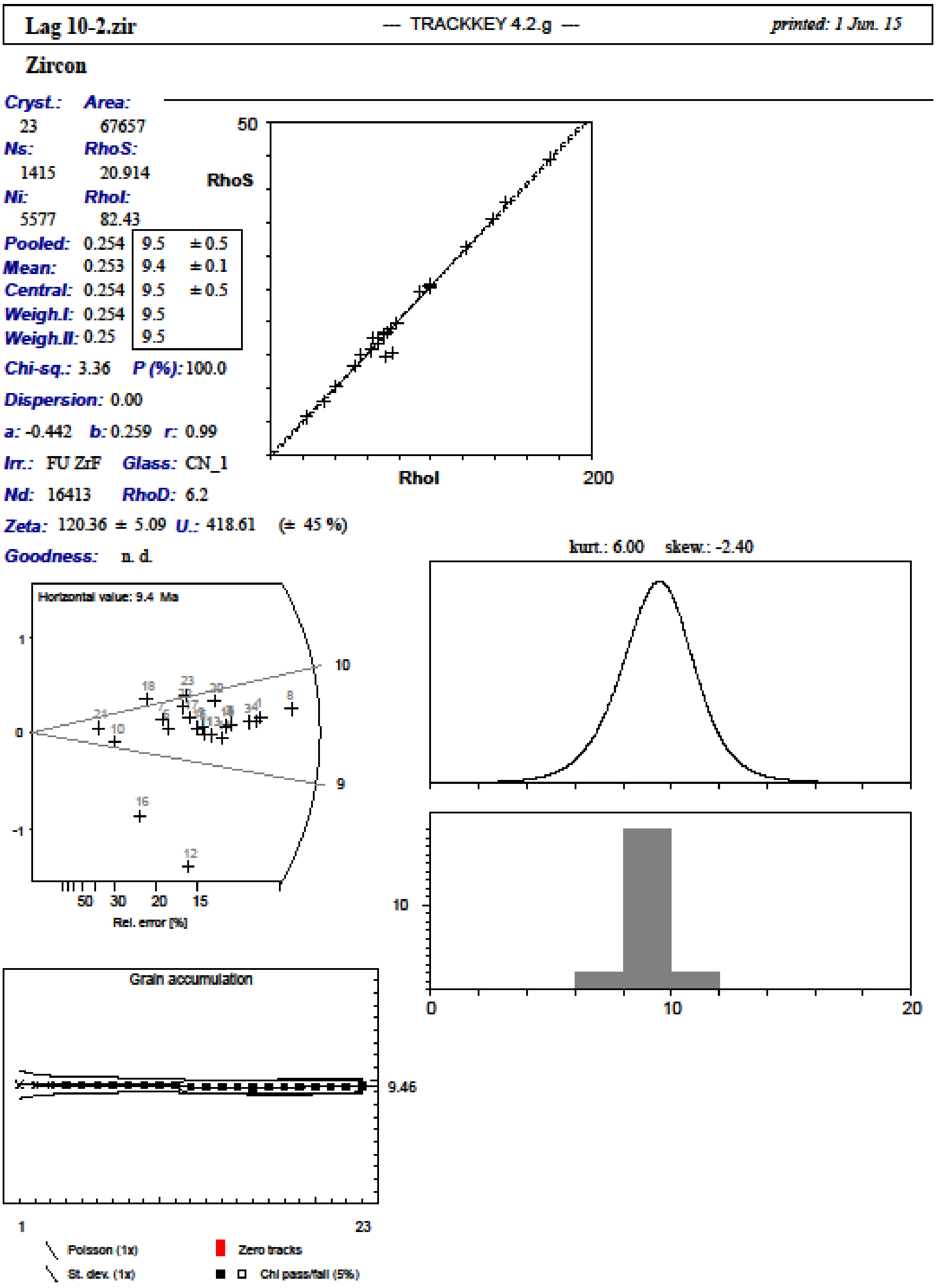

Lag 10-2.zir — TRACKKEY 4.2.g — *printed: 1 Jun. 15*

Zircon

Cryst.:	**Area:**
23	67657
Ns:	**RhoS:**
1415	20.914
Ni:	**RhoI:**
5577	82.43

Pooled:	0.254	9.5	± 0.5
Mean:	0.253	9.4	± 0.1
Central:	0.254	9.5	± 0.5
Weigh.I:	0.254	9.5	
Weigh.II:	0.25	9.5	

Chi-sq.: 3.36 **P (%):** 100.0

Dispersion: 0.00

a: -0.442 **b:** 0.259 **r:** 0.99

Irr.: FU ZrF **Glass:** CN_1

Nd: 16413 **RhoD:** 6.2

Zeta: 120.36 ± 5.09 **U.:** 418.61 (± 45 %)

Goodness: n. d.

kurt.: 6.00 skew.: -2.40

Lag 11-1.zir — TRACKKEY 4.2.g — *printed: 1 Jun. 15*

Zircon

Cryst.: 21 **Area:** 40013
Ns: 544 **RhoS:** 13.596
Ni: 2199 **RhoI:** 54.957

Pooled:	0.247	9.2	± 0.6
Mean:	0.25	9.3	± 0.1
Central:	0.247	9.2	± 0.6
Weigh.I:	0.247	9.2	
Weigh.II:	0.25	9.3	

Chi-sq.: 1.54 **P (%):** 100.0
Dispersion: 0.00
a: 0.768 **b:** 0.234 **r:** 0.98
Irr.: FU ZrF **Glass:** CN_1
Nd: 16413 **RhoD:** 6.18
Zeta: 120.36 ± 5.09 **U.:** 277.21 (± 33 %)
Goodness: n. d.

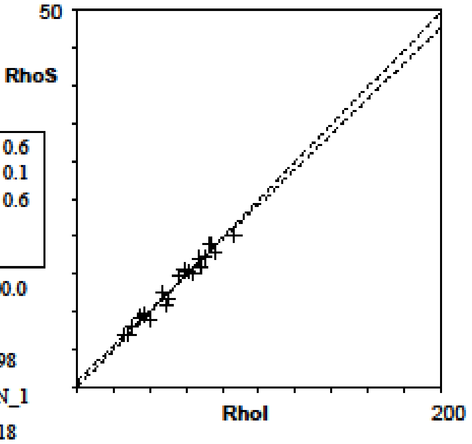

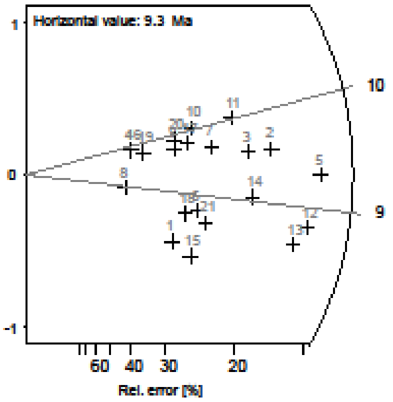

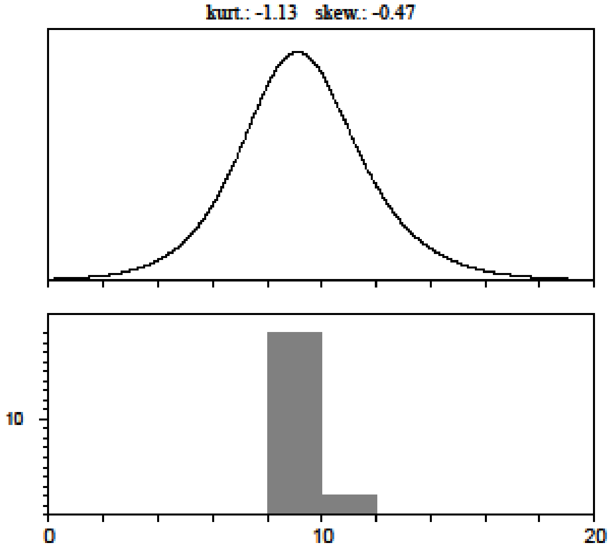

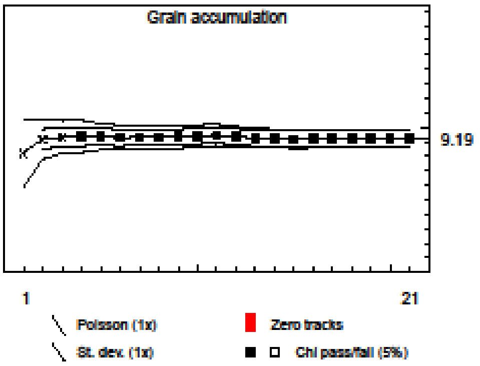

11.4.2 La Gomera AFT

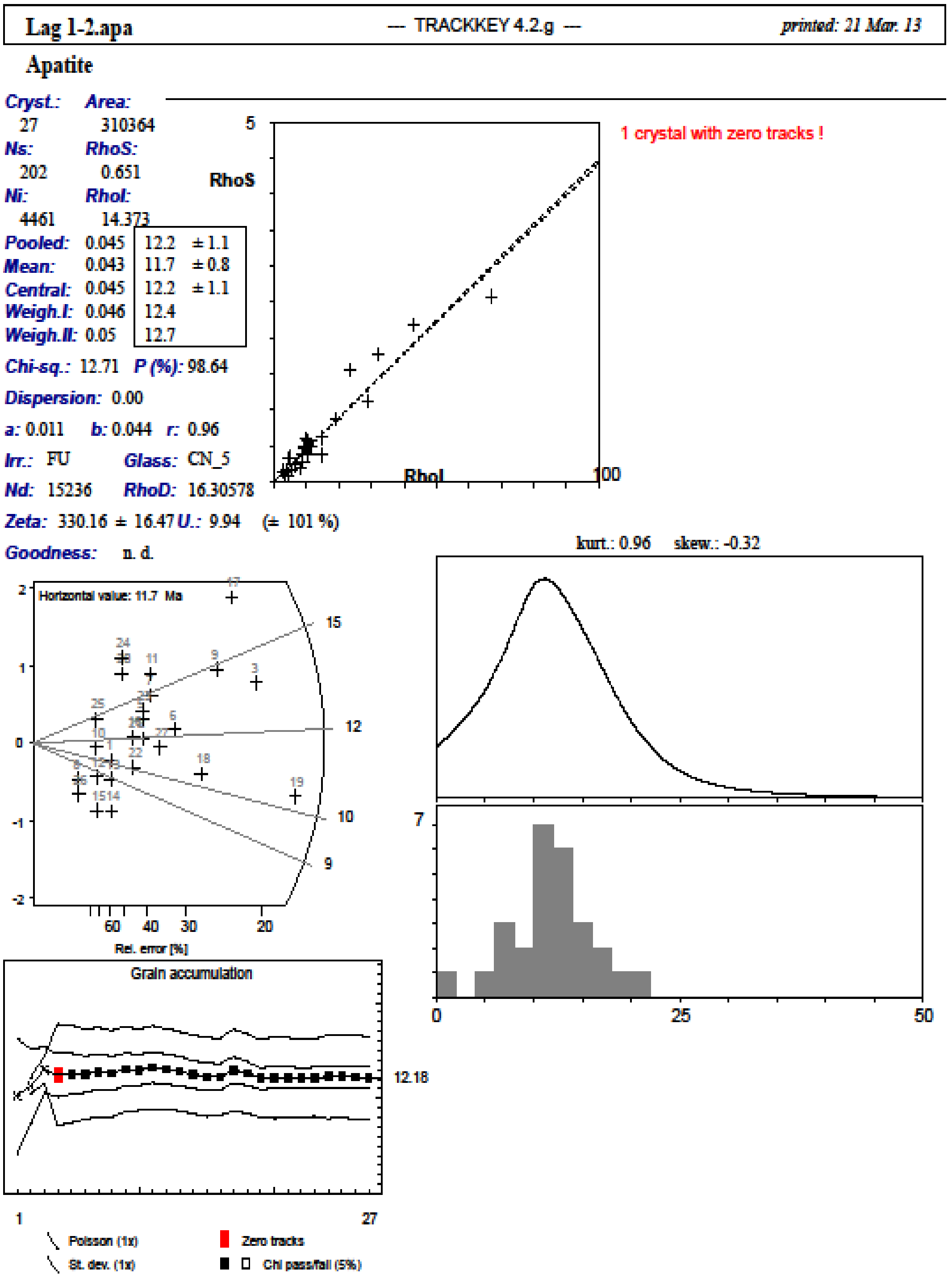

Lag 1-2.apa — TRACKKEY 4.2.g — *printed: 21 Mar. 13*

Apatite

Cryst.: 27	*Area:* 310364			
Ns: 202	*RhoS:* 0.651			
Ni: 4461	*RhoI:* 14.373			
Pooled:	0.045	12.2	± 1.1	
Mean:	0.043	11.7	± 0.8	
Central:	0.045	12.2	± 1.1	
Weigh.I:	0.046	12.4		
Weigh.II:	0.05	12.7		

Chi-sq.: 12.71 *P (%):* 98.64

Dispersion: 0.00

a: 0.011 *b:* 0.044 *r:* 0.96

Irr.: FU *Glass:* CN_5

Nd: 15236 *RhoD:* 16.30578

Zeta: 330.16 ± 16.47 *U.:* 9.94 (± 101 %)

Goodness: n. d.

1 crystal with zero tracks !

kurt.: 0.96 skew.: -0.32

Grain accumulation

12.18

Poisson (1x)

St. dev. (1x)

🟥 Zero tracks

■ ☐ Chi pass/fail (5%)

Lag 2.apa — TRACKKEY 4.2.g — *printed: 21 Mar. 13*

Apatite

Cryst.:	*Area:*		
14	87612		
Ns:	*RhoS:*		
65	0.742		
Ni:	*RhoI:*		
1959	22.36		
Pooled:	0.033	8.9	± 1.2
Mean:	0.032	8.6	± 0.8
Central:	0.033	8.9	± 1.2
Weigh.I:	0.034	9.2	
Weigh.II:	0.03	9.2	

Chi-sq.: 6.36 *P (%):* 93.19

Dispersion: 0.00

a: 0.033 *b:* 0.031 *r:* 0.69

Irr.: FU *Glass:* CN_5

Nd: 15236 *RhoD:* 16.23075

Zeta: 330.16 ± 16.47 *U.:* 15.54 (± 37 %)

Goodness: n. d.

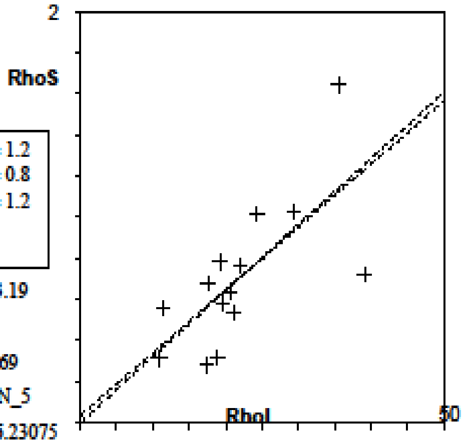

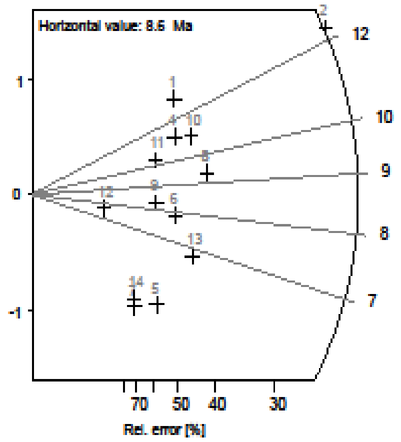

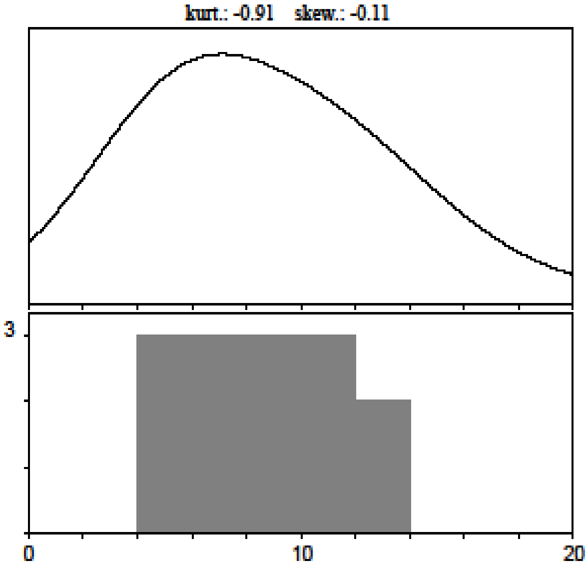

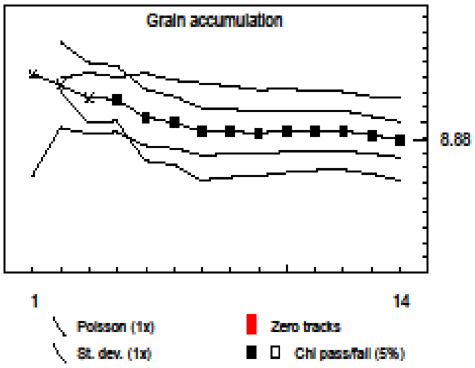

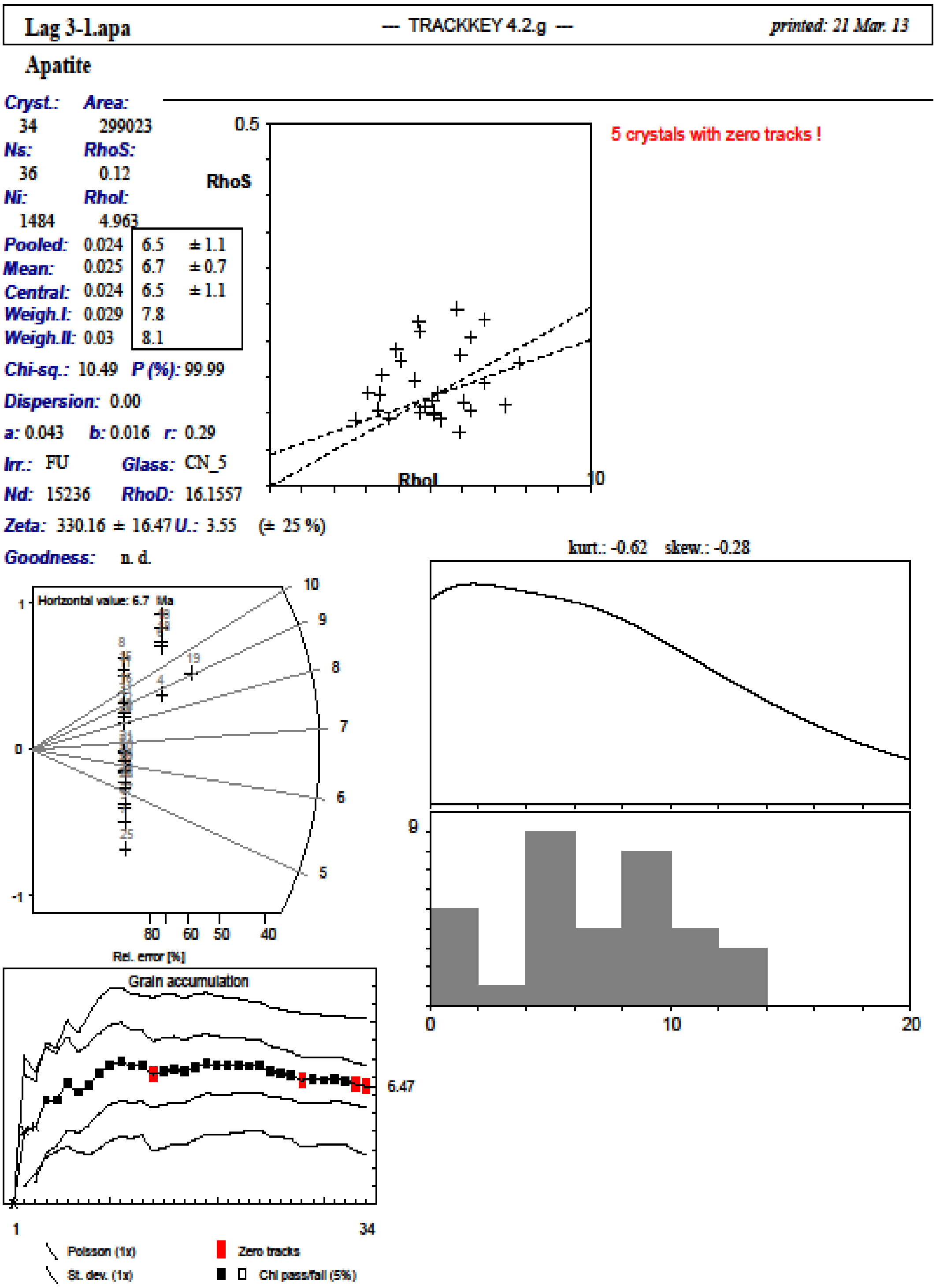

Lag 3-1.apa — TRACKKEY 4.2.g — *printed: 21 Mar. 13*

Apatite

Cryst.:	**Area:**		
34	299023		
Ns:	**RhoS:**		
36	0.12		
Ni:	**RhoI:**		
1484	4.963		
Pooled:	0.024	6.5	± 1.1
Mean:	0.025	6.7	± 0.7
Central:	0.024	6.5	± 1.1
Weigh.I:	0.029	7.8	
Weigh.II:	0.03	8.1	

Chi-sq.: 10.49 **P (%):** 99.99

Dispersion: 0.00

a: 0.043 **b:** 0.016 **r:** 0.29

Irr.: FU **Glass:** CN_5

Nd: 15236 **RhoD:** 16.1557

Zeta: 330.16 ± 16.47 **U.:** 3.55 (± 25 %)

Goodness: n. d.

5 crystals with zero tracks !

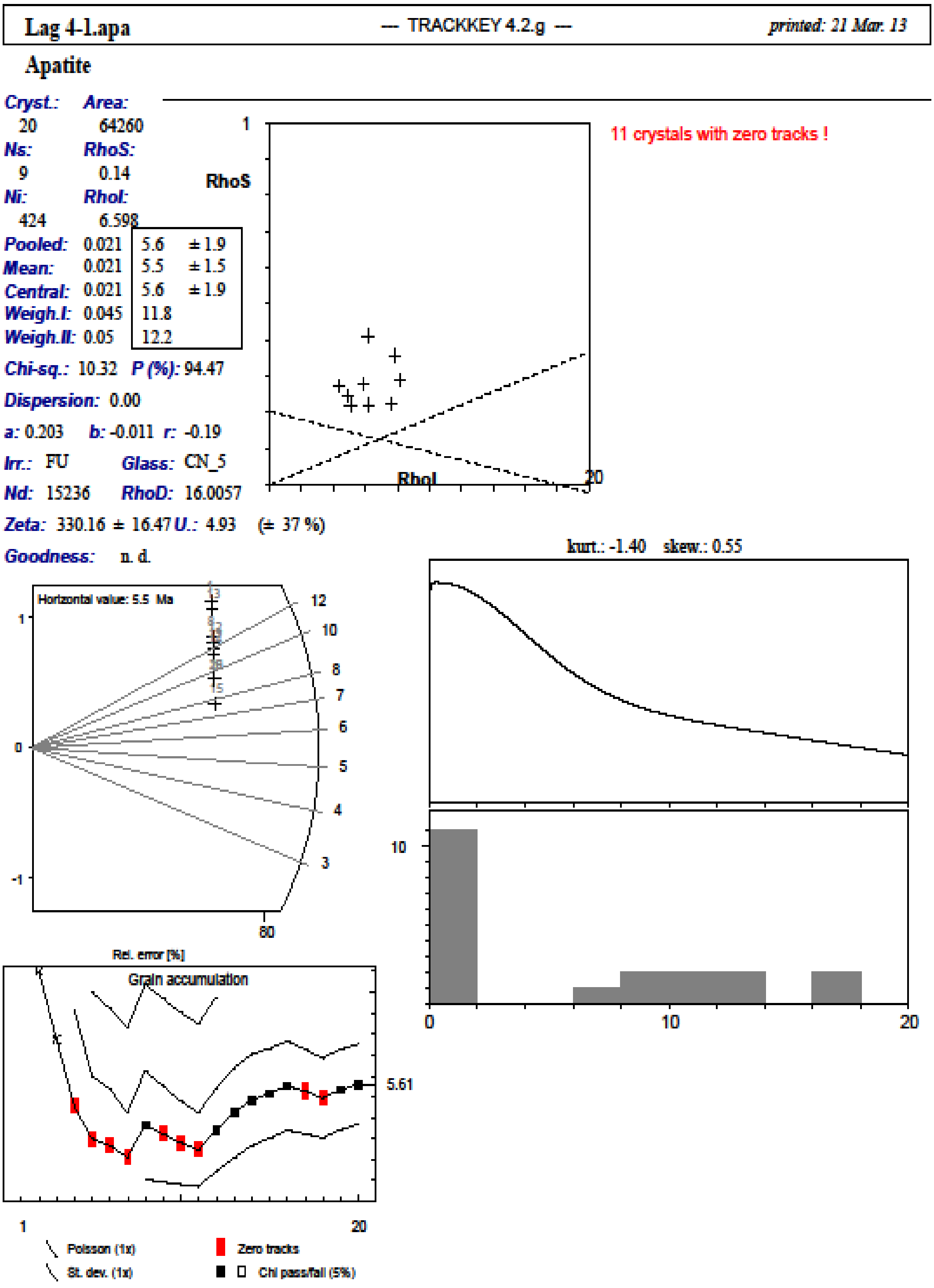

Lag 4-1.apa — TRACKKEY 4.2.g — *printed: 21 Mar. 13*

Apatite

Cryst.:	*Area:*
20	64260
Ns:	***RhoS:***
9	0.14
Ni:	***RhoI:***
424	6.598

Pooled:	0.021	5.6	± 1.9
Mean:	0.021	5.5	± 1.5
Central:	0.021	5.6	± 1.9
Weigh.I:	0.045	11.8	
Weigh.II:	0.05	12.2	

Chi-sq.: 10.32 ***P (%):*** 94.47

Dispersion: 0.00

a: 0.203 ***b:*** -0.011 ***r:*** -0.19

Irr.: FU ***Glass:*** CN_5

Nd: 15236 ***RhoD:*** 16.0057

Zeta: 330.16 ± 16.47 ***U.:*** 4.93 (± 37 %)

Goodness: n. d.

11 crystals with zero tracks !

kurt.: -1.40 skew.: 0.55

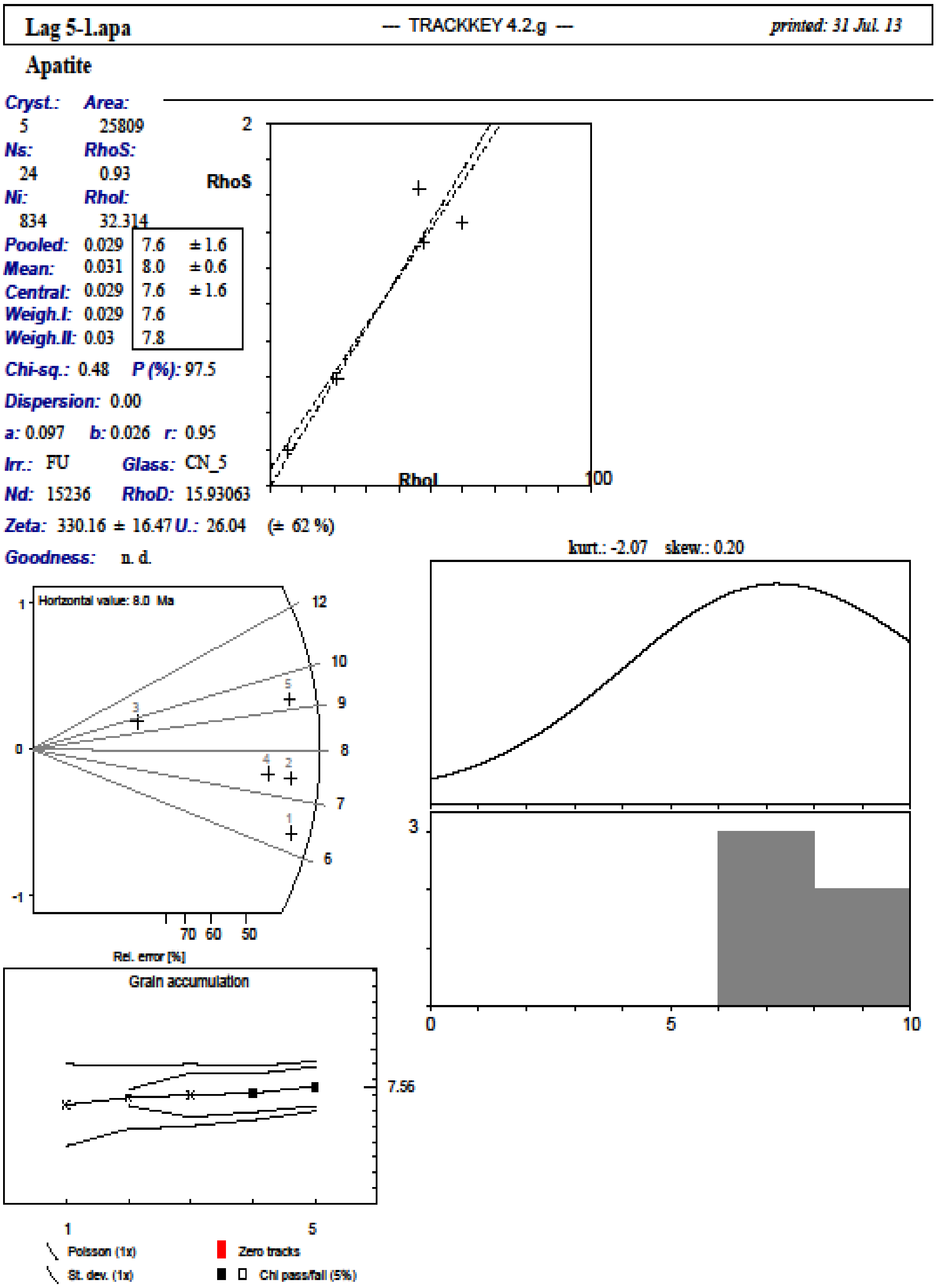

Lag 5-1.apa — TRACKKEY 4.2.g — *printed: 31 Jul. 13*

Apatite

Cryst.: 5 *Area:* 25809

Ns: 24 *RhoS:* 0.93

Ni: 834 *RhoI:* 32.314

Pooled: 0.029 7.6 ± 1.6

Mean: 0.031 8.0 ± 0.6

Central: 0.029 7.6 ± 1.6

Weigh.I: 0.029 7.6

Weigh.II: 0.03 7.8

Chi-sq.: 0.48 *P (%):* 97.5

Dispersion: 0.00

a: 0.097 *b:* 0.026 *r:* 0.95

Irr.: FU *Glass:* CN_5

Nd: 15236 *RhoD:* 15.93063

Zeta: 330.16 ± 16.47 *U.:* 26.04 (± 62 %)

Goodness: n. d.

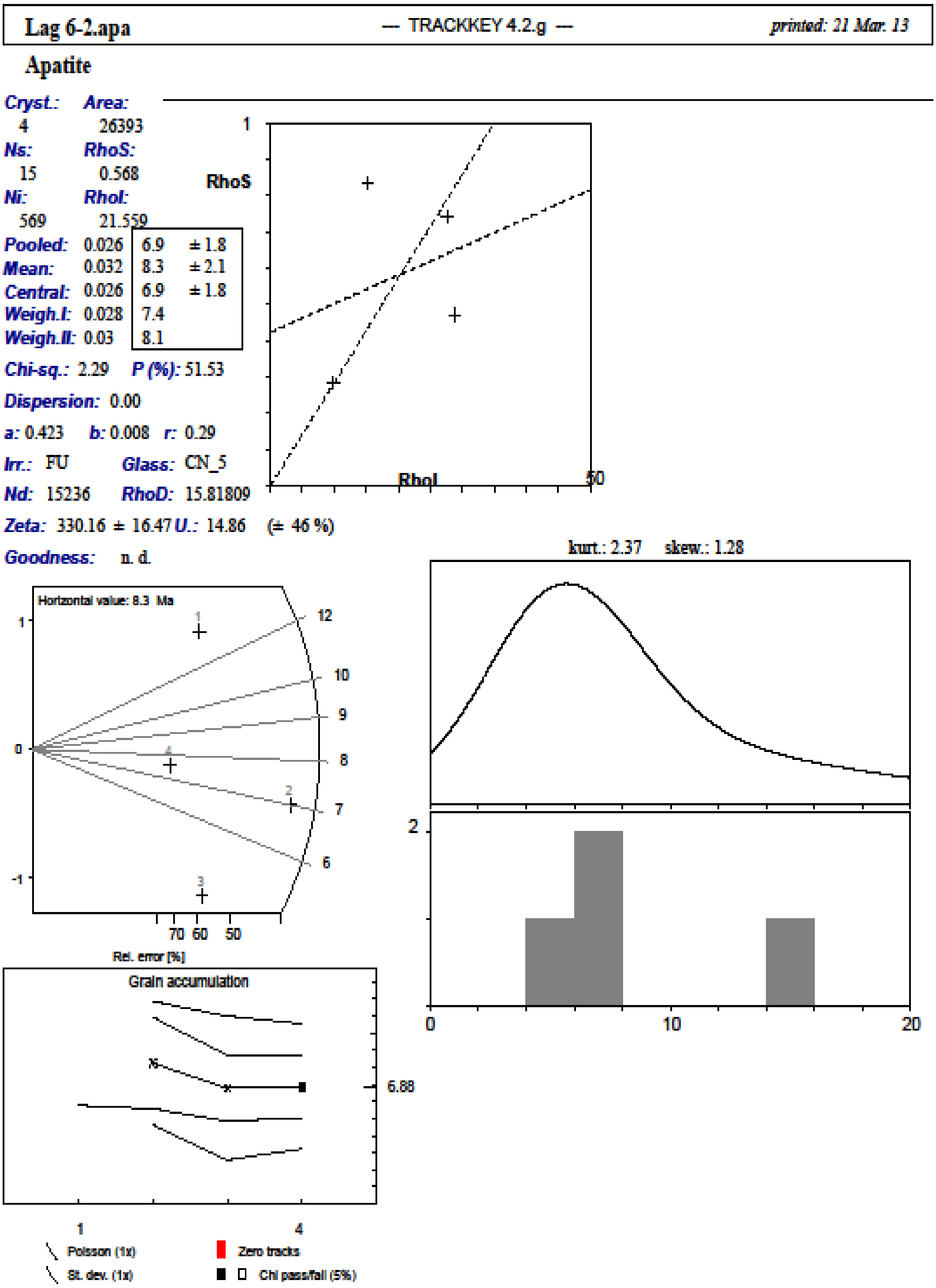

Lag 6-2.apa — TRACKKEY 4.2.g — *printed: 21 Mar. 13*

Apatite

Cryst.: 4	*Area:* 26393		
Ns: 15	*RhoS:* 0.568		
Ni: 569	*RhoI:* 21.559		
Pooled:	0.026	6.9	± 1.8
Mean:	0.032	8.3	± 2.1
Central:	0.026	6.9	± 1.8
Weigh.I:	0.028	7.4	
Weigh.II:	0.03	8.1	

Chi-sq.: 2.29 *P (%):* 51.53

Dispersion: 0.00

a: 0.423 *b:* 0.008 *r:* 0.29

Irr.: FU *Glass:* CN_5

Nd: 15236 *RhoD:* 15.81809

Zeta: 330.16 ± 16.47 *U.:* 14.86 (± 46 %)

Goodness: n. d.

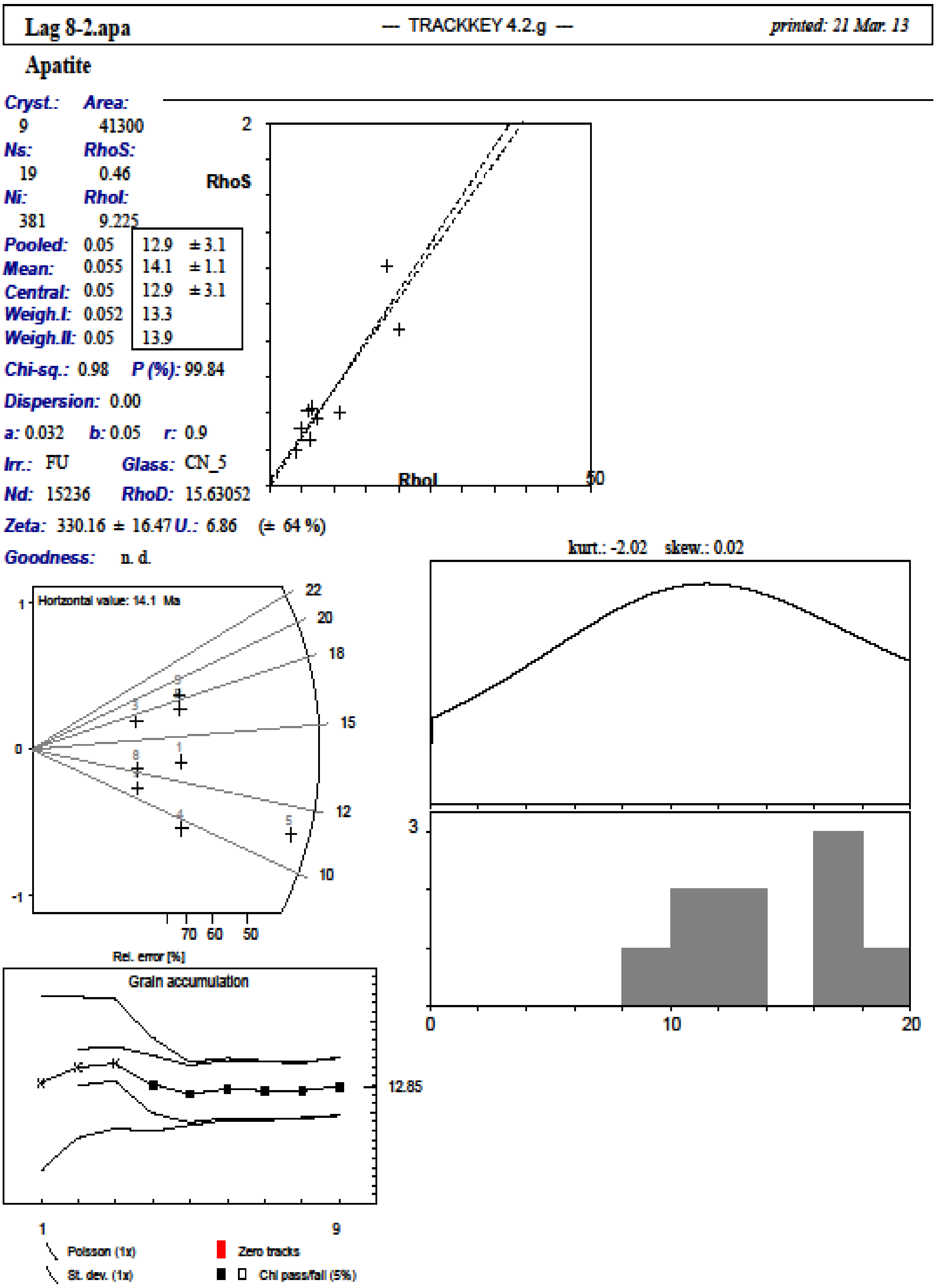

Lag 8-2.apa — TRACKKEY 4.2.g — *printed: 21 Mar. 13*

Apatite

Cryst.:	*Area:*
9	41300
Ns:	*RhoS:*
19	0.46
Ni:	*RhoI:*
381	9.225

Pooled:	0.05	12.9	± 3.1
Mean:	0.055	14.1	± 1.1
Central:	0.05	12.9	± 3.1
Weigh.I:	0.052	13.3	
Weigh.II:	0.05	13.9	

Chi-sq.: 0.98 *P (%):* 99.84

Dispersion: 0.00

a: 0.032 *b:* 0.05 *r:* 0.9

Irr.: FU *Glass:* CN_5

Nd: 15236 *RhoD:* 15.63052

Zeta: 330.16 ± 16.47 *U.:* 6.86 (± 64 %)

Goodness: n. d.

kurt.: -2.02 skew.: 0.02

Lag 9-1.apa — TRACKKEY 4.2.g — *printed: 21 Mar. 13*

Apatite

Cryst.: 24 **Area:** 209883

Ns: 60 **RhoS:** 0.286

Ni: 3205 **RhoI:** 15.27

Pooled:	0.019	4.8	± 0.7
Mean:	0.019	4.9	± 0.4
Central:	0.019	4.8	± 0.7
Weigh.I:	0.02	5.1	
Weigh.II:	0.02	5.3	

Chi-sq.: 8.21 **P (%):** 99.8

Dispersion: 0.00

a: 0.073 **b:** 0.014 **r:** 0.61

Irr.: FU **Glass:** CN_5

Nd: 15236 **RhoD:** 15.55549

Zeta: 330.16 ± 16.47 **U.:** 12.24 (± 38 %)

Goodness: n. d.

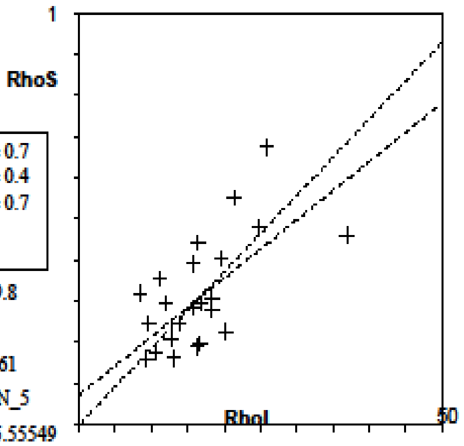

1 crystal with zero tracks !

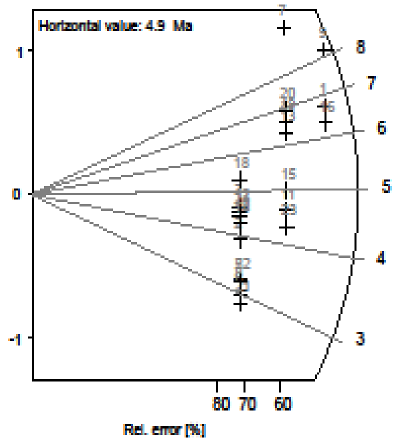

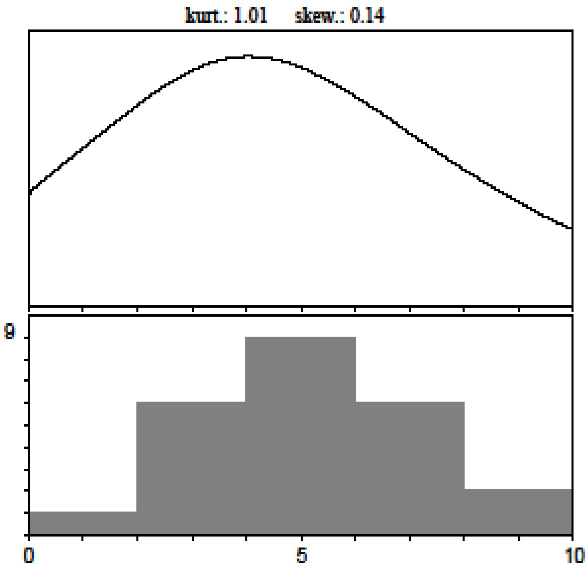

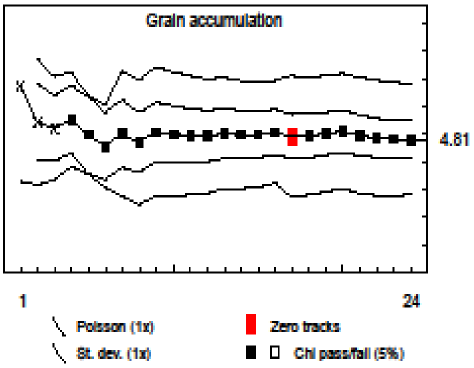

11.5 CONFERENCE CONTRIBUTIONS

EGU General Assembly 2013

April 22th to April 27th, 2013

Vienna, Austria Poster-presentation

Evaluating the thermal history and causes for long-term landscape evolution of Volcanic Islands in the Atlantic Ocean using Low Temperature Thermochronology; Fuerteventura and La Gomera, Canary Islands

[1]Sherif Mansour, [1]Ulrich Anton Glasmacher, [1]Marie Albinger, [2]Danny Fritz Stoeckli

[1]Institute of Earth Sciences, Heidelberg University, Germany
[2]Jackson school of Geosciences, University of Texas at Austin, USA

The Canary archipelago comprises seven main volcanic islands off the northwestern African coast which have been formed by multiple volcanic episodes. Among them Fuerteventura is the oldest, easternmost and nearest to the African continent. Fuerteventura shows exceptional features within the Canary Islands; it is the oldest, eastern-most and nearest to the African continent, the occurrence of wide exposures of submarine seamount stage rocks on its western side, it's unclear erosional history, and its longer time span volcanic activity. Fuerteventura has formed by three different adjacent large volcanic complexes: Southern (SVC), Central (CVC) and Northern (NVC) (Ancochea, 1996). In the Western Fuerteventura, by 17.5 Ma huge landslides have removed about 3500 km3 of lavas and volcanoclastics of the shield stage to expose more than 300 km2 of submarine rocks of the Basal Complex (Stillman, 1999). On the other hand, La Gomera is the smallest and lesser known among all the Canary Islands. La Gomera consists volcano-stratigraphically from Submarine Edifice (SE) or Basal Complex (BC), Old Edifice (OE) felsic rocks, and Young Edifice felsic domes and lava flows with >15 Ma, 10.5 to 6.4 Ma, and 5.7 to 2.8 Ma formation ages, respectively. During the OE time several lateral collapse events/landslides which caused for the removal of large part of the island northern sector (Ancochea et al., 2006).

Three Jurassic to Cretaceous sandstone samples of marine origin, which represent the seamount stage of Fuerteventura gave zircon fission-track (ZFT) ages of 58.5±7.3 to 50.0±9.3 Ma, zircon (U-Th-Sm)/He (ZHe) ages of 20.6±1.6 to 18.5±1.4 Ma, and apatite fission-track (AFT) ages of 46.3±30.0 to 14.5 ±4.0 Ma, respectively (Wipf et al., 2010). Another three samples from the Miocene intrusions gave ZFT age of 15.6±3.6 to 21.5±4.3 Ma and ZHe age of 13.4±0.5 to 15.0±1.2 Ma and AFT ages of 12.0±2.1, to 14.1±4.9 Ma, respectively.

The aim of the ongoing study is to reconstruct the long-term landscape evolution of Fuerteventura and La Gomera islands and to unravel the process that causes the giant landslides. Therefore, different thermochronometric techniques were applied on samples representing the main rocks units from the studied islands. 18 samples from the CVC and NVC were dated in the western part of Fuerteventura. Resetting ZFT ages at ~50 Ma may document starting the doming in the Basal Complex since the Early Eocene. Then, this region was cooled slowly from ZFT closure temperature to ZHe closure temperature in ~30 Ma with cooling rate of 1.5–3°C/Myr (Wipf et al., 2010). Afterward, rapid exhumation has started ~20 Ma to cool the samples from depths equivalent to depths of AFT closure temperature in <5 Ma with cooling rate of 50–70°C/Myr. The Lower Miocene intruded samples show a rapid cooling from depths equivalent to ZFT closure temperature to AFT closure temperature in ~3.6-7.4 Myr with cooling rate of 13–27°C/Myr. The rapid cooling could have been caused by the occurrences of giant landslides. Interesting enough the timing of the rapid cooling is close to major climate changes in the region. Eleven samples were dated from the North and Northwestern sectors of the island La Gomera. The collected samples cover all main volcano-stratigraphic units.

References

Ancochea, E., Brandle, J.L., Cubas, C.R., Hernan, F., Huertas, M.J., 1996. Volcanic complexes in the eastern ridge of the Canary Islands: the Miocene activity of the island of Fuerteventura. J. Volcanol. Geotherm. Res. 70, 183–204. doi:10.1016/0377-0273(95)00051-8
Ancochea, E., Hernán, F., Huertas, M.J., Brändle, J.L., Herrera, R., 2006. A new chronostratigraphical and evolutionary model for La Gomera: Implications for the overall evolution of the Canarian Archipelago. J. Volcanol. Geotherm. Res. 157, 271–293.
Stillman C.J., 1999. Giant Miocene landslides and the evolution of Fuerteventura, Canary Islands. J Volcanol Geotherm Res 94:89–104. doi:10.1016/S0377-0273(99)00099-2
Wipf M., Glasmacher U. A., Stockli D. F., Emmerich A., Bechstädt T., Heinrich Baur H., 2010. Reconstruction of the differentiated long-term exhumation history of Fuerteventura, Canary Islands, Spain, through fission-track and (U-Th–Sm)/He data. Int J Earth Sci (Geol Rundsch) 99, 675-686. Doi: 10.1007/s00531-008-0415-z

Sample SPP 2013

August 11th to August 14th, 2013

Heidelberg, Germany Poster-presentation

Evaluating the thermal history and causes for long-term landscape evolution of Volcanic Islands in the Atlantic Ocean using Low Temperature Thermochronology; Fuerteventura and La Gomera, Canary Islands

[1]Sherif Mansour, [1]Ulrich Anton Glasmacher, [1]Marie Albinger, [2]Danny Fritz Stoeckli

[1]Institute of Earth Sciences, Heidelberg University, Germany
[2]Jackson school of Geosciences, University of Texas at Austin, USA

The Canary archipelago comprises seven main volcanic islands off the northwestern African coast which have been formed by multiple volcanic episodes. Among them Fuerteventura is the oldest, easternmost and nearest to the African continent. Fuerteventura shows exceptional features within the Canary Islands; it is the oldest, eastern-most and nearest to the African continent, the occurrence of wide exposures of submarine seamount stage rocks on its western side, it's unclear erosional history, and its longer time span volcanic activity. Fuerteventura has formed by three different adjacent large volcanic complexes: Southern (SVC), Central (CVC) and Northern (NVC) (Ancochea, 1996). In the Western Fuerteventura, by 17.5 Ma huge landslides have removed about 3500 km3 of lavas and volcanoclastics of the shield stage to expose more than 300 km2 of submarine rocks of the Basal Complex (Stillman, 1999). On the other hand, La Gomera is the smallest and lesser known among all the Canary Islands. La Gomera consists volcano-stratigraphically from Submarine Edifice (SE) or Basal Complex (BC), Old Edifice (OE) felsic rocks, and Young Edifice felsic domes and lava flows with >15 Ma, 10.5 to 6.4 Ma, and 5.7 to 2.8 Ma formation ages, respectively. During the OE time several lateral collapse events/landslides which caused for the removal of large part of the island northern sector (Ancochea et al., 2006).

Three Jurassic to Cretaceous sandstone samples of marine origin, which represent the seamount stage of Fuerteventura gave zircon fission-track (ZFT) ages of 58.5±7.3 to 50.0±9.3 Ma, zircon (U-Th-Sm)/He (ZHe) ages of 20.6±1.6 to 18.5±1.4 Ma, and apatite fission-track (AFT) ages of 46.3±30.0 to 14.5 ±4.0 Ma, respectively (Wipf et al., 2010). Another three samples from the Miocene intrusions gave ZFT age of 15.6±3.6 to 21.5±4.3 Ma and ZHe age of 13.4±0.5 to 15.0±1.2 Ma and AFT ages of 12.0±2.1, to 14.1±4.9 Ma, respectively.

The aim of the ongoing study is to reconstruct the long-term landscape evolution of Fuerteventura and La Gomera islands and to unravel the process that causes the giant landslides. Therefore, different thermochronometric techniques were applied on samples representing the main rocks units from the studied islands. 18 samples from the CVC and NVC were dated in the western part of Fuerteventura. Resetting ZFT ages at ~50 Ma may document starting the doming in the Basal Complex since the Early Eocene. Then, this region was cooled slowly from ZFT closure temperature to ZHe closure temperature in ~30 Ma with cooling rate of 1.5–3°C/Myr (Wipf et al., 2010). Afterward, rapid exhumation has started ~20 Ma to cool the samples from depths equivalent to depths of AFT closure temperature in <5 Ma with cooling rate of 50–70°C/Myr. The Lower Miocene intruded samples show a rapid cooling from depths equivalent to ZFT closure temperature to AFT closure temperature in ~3.6-7.4 Myr with cooling rate of 13–27°C/Myr. The rapid cooling could have been caused by the occurrences of giant landslides. Interesting enough the timing of the rapid cooling is close to major climate changes in the region. Eleven samples were dated from the North and Northwestern sectors of the island La Gomera. The collected samples cover all main volcano-stratigraphic units.

References

Ancochea, E., Brandle, J.L., Cubas, C.R., Hernan, F., Huertas, M.J., 1996. Volcanic complexes in the eastern ridge of the Canary Islands: the Miocene activity of the island of Fuerteventura. J. Volcanol. Geotherm. Res. 70, 183–204. doi:10.1016/0377-0273(95)00051-8

Ancochea, E., Hernán, F., Huertas, M.J., Brändle, J.L., Herrera, R., 2006. A new chronostratigraphical and evolutionary model for La Gomera: Implications for the overall evolution of the Canarian Archipelago. J. Volcanol. Geotherm. Res. 157, 271–293.

Stillman C.J., 1999. Giant Miocene landslides and the evolution of Fuerteventura, Canary Islands. J Volcanol Geotherm Res 94:89–104. doi:10.1016/S0377-0273(99)00099-2

Wipf M., Glasmacher U. A., Stockli D. F., Emmerich A., Bechstädt T., Heinrich Baur H., 2010. Reconstruction of the differentiated long-term exhumation history of Fuerteventura, Canary Islands, Spain, through fission-track and (U-Th–Sm)/He data. Int J Earth Sci (Geol Rundsch) 99, 675-686. Doi: 10.1007/s00531-008-0415-z

6th Deutsch-Brasilianisches Symposium zu „Nachhaltiger Entwicklung“

September 29th to October 04th, 2013

Santarem, Brazil Poster-presentation

Climate Change - Landslide Formation on Volcanic Islands: Fuerteventura and La Gomera, Canary Islands

[1]Sherif Mansour, [1]Ulrich Anton Glasmacher, [1]Marie Albinger, [2]Danny Fritz Stoeckli

[1]Institute of Earth Sciences, Heidelberg University, Germany
[2]Jackson school of Geosciences, University of Texas at Austin, USA

The Canary archipelago comprises seven main volcanic islands off the northwestern African coast which have been formed by multiple volcanic episodes. Among them Fuerteventura is the oldest, easternmost and nearest to the African continent. In the Western Fuerteventura, by 17.5 Ma huge landslides have removed about 3500 km3 of lavas and volcanoclastics (Stillman, 1999). On the other hand, La Gomera is the smallest and lesser known among all the Canary Islands. During the Old Edifice time several lateral collapse events/landslides which caused for the removal of large part of the island northern sector (Ancochea et al., 2006).

Different thermochronometric techniques were applied on samples representing the main rocks units from the studied islands. Rapid exhumation has started ~20 Ma synchronously with giant landslides. Interestingly enough the timing of the rapid cooling/landslide is close to major climate changes termed the Miocene climatic optimum. Relative warmth during Miocene is well documented in marine and terrestrial records (Zachos et al. 2008; Herold et al. 2011). In fact, rainfall is the most relevant factor for the generating of landslides. Particularly, the Miocene warmth exhibits broad increases in mean annual precipitation over central and northern Africa (Herold et al. 2011). These facts recommend being the climate change/increases precipitation rate is the main reason in the giant landslides.

References

Ancochea, E., Brandle, J.L., Cubas, C.R., Hernan, F., Huertas, M.J., 1996. Volcanic complexes in the eastern ridge of the Canary Islands: the Miocene activity of the island of Fuerteventura. J. Volcanol. Geotherm. Res. 70, 183–204. doi:10.1016/0377-0273(95)00051-8
Ancochea, E., Hernán, F., Huertas, M.J., Brändle, J.L., Herrera, R., 2006. A new chronostratigraphical and evolutionary model for La Gomera: Implications for the overall evolution of the Canarian Archipelago. J. Volcanol. Geotherm. Res. 157, 271–293.
Stillman C.J., 1999. Giant Miocene landslides and the evolution of Fuerteventura, Canary Islands. J Volcanol Geotherm Res 94:89–104. doi:10.1016/S0377-0273(99)00099-2
Wipf M., Glasmacher U. A., Stockli D. F., Emmerich A., Bechstädt T., Heinrich Baur H., 2010. Reconstruction of the differentiated long-term exhumation history of Fuerteventura, Canary Islands, Spain, through fission-track and (U-Th–Sm)/He data. Int J Earth Sci (Geol Rundsch) 99, 675-686. Doi: 10.1007/s00531-008-0415-z
Zachos, J. C., G. R. Dickens, and R. E. Zeebe, 2008: An early Cenozoic perspective on greenhouse warming and carbon-cycle dynamics. Nature, 451, 279–283.

EGU General Assembly 2014

April 27th to May 2nd, 2014

Vienna, Austria Poster-presentation

Long-term landscape evolution of the Basal Complexes of Fuerteventura and La Gomera Islands, Canary Archipelago

[1]Sherif Mansour, [1]Ulrich Anton Glasmacher, [1]Marie Albinger, [2]Daniel Fritz Stoeckli

[1]Institute of Geology and Palaeontology, Heidelberg University, Germany
[2]Jackson school of Geosciences, University of Texas at Austin, USA

The Canarias archipelago consists from seven volcanic islands located at the northwestern African margin. Among them only Fuerteventura and La Gomera islands show distinctive wide exposures of the basal complex (BC) that is characteristic with complex geological history. The basal complex was exposed on the western part of Fuerteventura and northwestern sector of La Gomera because of giant landslide(s) which have removed most of the shield stage volcanic rocks (Ancochea et al., 1996; 2006; Stillman, 1999). Generally, landslides are a common feature in the earlier constructive stages of the entire archipelago and many other volcanic islands (McGuire, 1996).

Integration of low temperature thermochronological data, and time-Temperature (t-T) numerical modelling have proven to be a powerful tool for reconstructing the thermal and tectonic history, defining and quantifying long-term landscape evolution in variety of geological settings. Therefore, zircon and apatite fission-track techniques and t-T paths modelling were applied to 36 samples representing the main rock units of the BC on both islands. Fuerteventura BC has experienced two very rapid cooling/exhumation events. While, La Gomera BC shows one long-lived very fast cooling/exhumation event. Interestingly, these very rapid cooling/exhumation events are synchronous with these major landslides. There are many reasons for the major landslides on such a volcanic island (see e.g., McGuire, 1996). The most recommended triggers for these huge mass wasting/landslides events on Fuerteventura and La Gomera are recommended to be the continuous igneous intrusions and dikes which have the potential to decrease the edifice stability, igneous extrusions which add new materials at the surface leading to over-steeping and overloading, and major climatic changes of the Middle Miocene Climatic Optimum which controlled the see level changes and the precipitation rate (McGuire, 1996, Herold et al., 2011).

References

Ancochea, E., Brändle, J.L., Cubas, C.R.,Hernán, F.,Huertas, M.J., 1996. Volcanic complexes in the eastern ridge of the Canary Islands: the Miocene activity of the Island of Fuerteventura. Journal of Volcanology and Geothermal Research 70, 183–204.

Ancochea, E., Hernán, F., Huertas, M.J., Brändle, J.L., Herrera, R., 2006. A new chronostratigraphical and evolutionary model for La Gomera: implications for the overall evolution of the Canarian Archipelago. Journal of Volcanology and Geothermal Research 157, 271–293.

Herold, N., Huber, M., Greenwood, D.R., Müller, R.D., Seton, M., 2011. Early to Middle Miocene monsoon climate in Australia. Geology 39, 3-6.

McGuire, W.J., 1996. Volcano instability: a review of contemporary themes. In: McGuire, W.J., Jones, A.P., Neuberg, J. (Eds.), Volcano Instability on the Earth and Terrestrial Planets. Geological Society of London, Special Publication 110, 1–23.

Stillman, C.J., 1999. Giant Miocene landslides and the evolution of Fuerteventura, Canary Islands. Journal of Volcanology and Geothermal Research 94, 89–104.

14th International Conference on Thermochronology (Thermo 2014)

September 8th to September 12th, 2014

Chamonix, France Poster-presentation

Long-term landscape evolution of the Basal Complexes of Fuerteventura and La Gomera Islands, Canary Archipelago

[1]Sherif Mansour, [1]Ulrich Anton Glasmacher, [1]Marie Albinger, [2]Daniel Fritz Stoeckli

[1]Earth Sciences Institute, Heidelberg University, Germany
[2]Jackson school of Geosciences, University of Texas at Austin, USA

The Canarias archipelago consists from seven volcanic islands located at the northwestern African margin. Among them only Fuerteventura and La Gomera islands show distinctive wide exposures of the basal complex (BC) that is characteristic with complex geological history. The basal complex was exposed on the western part of Fuerteventura and northwestern sector of La Gomera because of giant landslide(s) which have removed most of the shield stage volcanic rocks1-3. Generally, landslides are a common feature in the earlier constructive stages of the entire archipelago and many other volcanic islands4.

Integration of low temperature thermochronological data, and time-Temperature (t-T) numerical modelling have proven to be a powerful tool for reconstructing the thermal and tectonic history, defining and quantifying long-term landscape evolution in variety of geological settings. Therefore, zircon and apatite fission-track techniques and t-T paths modelling were applied to 36 samples representing the main rock units of the BC on both islands. Fuerteventura BC has experienced two very rapid cooling/exhumation events. While, La Gomera BC shows one long-lived very fast cooling/exhumation event. Interestingly, these very rapid cooling/exhumation events are synchronous with these major landslides. There are many reasons for the major landslides on such a volcanic island4. The most recommended triggers for these huge mass wasting/landslides events on Fuerteventura and La Gomera are recommended to be the continuous igneous intrusions and dikes which have the potential to decrease the edifice stability, igneous extrusions which add new materials at the surface leading to over-steeping and overloading, and major climatic changes of the Middle Miocene Climatic Optimum which controls the sea level changes and the precipitation rate4-5.

References

1. Ancochea, E., Brändle, J.L., Cubas, C.R.,Hernán, F.,Huertas, M.J., 1996. Volcanic complexes in the eastern ridge of the Canary Islands: the Miocene activity of the Island of Fuerteventura. Journal of Volcanology and Geothermal Research 70, 183–204.
2. Ancochea, E., Hernán, F., Huertas, M.J., Brändle, J.L., Herrera, R., 2006. A new chronostratigraphical and evolutionary model for La Gomera: implications for the overall evolution of the Canarian Archipelago. Journal of Volcanology and Geothermal Research 157, 271–293.
3. Stillman, C.J., 1999. Giant Miocene landslides and the evolution of Fuerteventura, Canary Islands. Journal of Volcanology and Geothermal Research 94, 89–104.
4. McGuire, W.J., 1996. Volcano instability: a review of contemporary themes. In: McGuire, W.J., Jones, A.P., Neuberg, J. (Eds.), Volcano Instability on the Earth and Terrestrial Planets. Geological Society of London, Special Publication 110, 1–23.
5. Herold, N., Huber, M., Greenwood, D.R., Müller, R.D., Seton, M., 2011. Early to Middle Miocene monsoon climate in Australia. Geology 39, 3-6.

GeoFrankfurt - Earth System Dynamics

September 21th to September 24th, 2014

Frankfurt, Germany Poster-presentation

Volcanic Island from Emerge to post-Shield stage: Implications from Low Temperature Thermochronology applications on the Basal Complexes of Fuerteventura and La Gomera Islands, Canary Archipelago

[1]Sherif Mansour, [1]Ulrich Anton Glasmacher, [1]Marie Albinger, [2]Daniel Fritz Stoeckli

[1]Institute of Earth Sciences, Heidelberg University, INF 234, 69120 Heidelberg, Germany, sherif.mansour@geow.uni-heidelberg.de, ulrich.a.glasmacher@geow.uni-heidelberg.de, marie.albinger@ geow.uni-heidelberg.de
[2]Jackson school of Geosciences, University of Texas at Austin, USA, 23rd, Austin, TX 78759, United States, stockli@jsg.utexas.edu

The Canarias archipelago consists from seven volcanic islands located at the northwestern African margin. Among them only Fuerteventura and La Gomera islands show distinctive wide exposures of the basal complex (BC) that is characteristic with complex geological history. The basal complex was exposed on the western part of Fuerteventura and northwestern sector of La Gomera because of giant landslide(s) which have removed most of the shield stage volcanic rocks (Ancochea et al., 1996; 2006; Stillman, 1999). Generally, landslides are a common feature in the earlier constructive stages of the entire archipelago and many other volcanic islands (McGuire, 1996).

Integration of low temperature thermo-chronological data, and time-Temperature (t-T) numerical modelling have proven to be a powerful tool for reconstructing the thermal and tectonic history, defining and quantifying long-term landscape evolution in variety of geological settings. Therefore, zircon and apatite fission-track techniques and t-T paths modelling were applied to 36 samples representing the main rock units of the BC on both islands. Fuerteventura BC has experienced two very rapid cooling/exhumation events. While, La Gomera BC shows one long-lived very fast cooling/ exhumation event. Interestingly, these very rapid cooling/ exhumation events are synchronous with these major landslides. There are many reasons for the major landslides on such a volcanic island (see e.g., McGuire, 1996)., But, the most sufficient triggers for these huge mass wasting/landslides events on Fuerteventura and La Gomera are recommended to be the continuous igneous intrusions and dikes which have the potential to decrease the edifice stability, igneous extrusions which add new materials at the surface leading to over-steeping and overloading (McGuire, 1996), and major climatic changes of the Middle Miocene Climatic Optimum (Herold et al., 2011).

References

Ancochea, E., Brändle, J.L., Cubas, C.R.,Hernán, F.,Huertas, M.J. (1996): Volcanic complexes in the eastern ridge of the Canary Islands: the Miocene activity of the Island of Fuerteventura. Journal of Volcanology and Geothermal Research 70, 183–204.

Ancochea, E., Hernán, F., Huertas, M.J., Brändle, J.L., Herrera, R. (2006): A new chronostratigraphical and evolutionary model for La Gomera: implications for the overall evolution of the Canarian Archipelago. Journal of Volcanology and Geothermal Research 157, 271–293.

Herold, N., Huber, M., Greenwood, D.R., Müller, R.D., Seton, M. (2011): Early to Middle Miocene monsoon climate in Australia. Geology 39, 3-6.

McGuire, W.J. (1996): Volcano instability: a review of contemporary themes. In: McGuire, W.J., Jones,

A.P., Neuberg, J. (Eds.), Volcano Instability on the Earth and Terrestrial Planets. Geological Society of London, Special Publication 110, 1–23.
Stillman, C.J. (1999): Giant Miocene landslides and the evolution of Fuerteventura, Canary Islands. Journal of Volcanology and Geothermal Research 94,89–104.

GeoFrankfurt - Earth System Dynamics

September 21th to September 24th, 2014

Frankfurt, Germany Poster-presentation

Thermo-tectonic history of the Rwenzori Mountains, D. R. Congo

[1]Sherif Mansour, [2]Friederike U. Bauer, [1]Ulrich Anton Glasmacher, [3]René W. Grobe, [1]Matthias Starz

[1]Institute of Earth Sciences, Heidelberg University, INF 234, 69120 Heidelberg, Germany, sherif.mansour@geow.uni-heidelberg.de, ulrich.a.glasmacher@geow.uni-heidelberg.de
[2]Department of Earth Science, University of Bergen, Allégaten 41, 5007 Bergen, Norway, friederike.bauer@geo.uib.no
[3]GeoThermal Engineering GmbH, DE-76133 Karlsruhe

The Albertine Rift forms the northern section of the western Rift of the East African Rift System (EARS) which was developed during the Neogene time. The Rwenzori Mtns evolved along the eastern rift shoulder of the Albertine Rift, rising up to form a striking feature within the rift valley. The Rwenzori Mtns represent the horst block in the Albertine Rift, with elevations reaching 5109 m a.s.l. (Margherita Peak). The main lithologies of the Rwenzori Mtns are gneiss, schist and amphibolite, subordinate intrusive rocks with various metamorphic overprint, and quart-zite of Precambrian age (Tanner, 1971). All these units are intensively truncated by N–S, NW–SE, NE–SW and E–W trending normal faults, locally with a significant strike-slip component (Ring, 2008). The slope Rwenzori Mtns western flank is much steeper than the eastern one. This asymmetry is most striking in the central part where the western flank rises from about 1000 m a.s.l. to more than 5000 m a.s.l. in less than 15 km while, the eastern flank plunges to 1000 m a.s.l. again along a distance of more than 30 km (Bauer et al., 2013).

The scarcity of volcanic activity in the Western Rift has raised questions about the Rwenzori Mtns origin and evolution and how this fits into the general evolution of the Albertine Rift and the EARS.

Detailed thermochronologic study of Bauer et al., (2010, 2013) on the eastern (Uganda) side of central Rwenzori differentiated it into northern and southern blocks. Samples from the northern block cooled faster, with an initial cooling/exhumation event to ~120 °C in Carboniferous to Permian times. Followed by a period slow cooling until another period of accelerated cooling occurred in Mesozoic times to ~70 °C. Followed again by slow cooling in Mesozoic and Palaeogene times to 50–40 °C, and more rapid cooling to surface temperature in the Neogene. With exhumation rates over time vary between 0.325 and 0.006 km/Ma. While, the southern block shows an earlier onset of cooling (>400 Ma). Temperatures of about 70 °C were reached in Silurian to Devonian times. A long period of constant and very slow cooling lasted more than 200 Ma. In Cretaceous to Palaeogene times differentiated cooling to surface temperatures occurred. Resulting exhumation rates are between 2.5 and 0.003 km/Ma.

During this study, 33 samples were collected from the western side of central Rwenzori (Congo side). Fission track and (U/Th)-He techniques are applied on both apatite and zircons from these samples. The sofar acheived results reveal the difference in thermo-tectonic history between the eastern and western flanks of Rwenzori Mtns which is clearly presented by the topographic asymetry.

References

Bauer, F.U., Glasmacher, U.A., Ring, U., Karl, M., Schumann, A., Nagudi, B. (2013). Tracing the exhumation history of the Rwenzori Mountains, Albertine Rift, Uganda, using low-temperature thermochronology, Tectonophysics, 599, 8-28. http://dx.doi.org/10.1016/j.tecto.2013.03.032.
Ring, U., 2008. Extreme uplift of the Rwenzori Mountains in the East African Rift, Uganda: structural framework and possible role of glaciations. Tectonics 27 (TC4018). http://dx.doi.org/10.1029/2007TC002176.
Tanner, P.W.G., 1971. The Stanley Volcanics formation of Ruwenzori, Uganda. Fifteenth Annual Report of the Research Institute of African Geology. University of Leeds.

AGU Fall Meeting 2014

December 15th to December 19th, 2014

San Francisco, USA Poster-presentation

Reconstructing the Thermo-tectonic history of the Rwenzori Mountains, D. R. Congo

1Sherif Mansour, [2]Friederike U. Bauer, [1]Ulrich A. Glasmacher, [3]René W. Grobe, [1]Matthias Starz

[1]Institute of Earth Sciences, Heidelberg University, Germany
[2]Department of Earth Science, University of Bergen, Norway
[3]GeoThermal Engineering GmbH, DE-76133 Karlsruhe, Germany

The Albertine Rift forms the northern section of the western Rift of the East African Rift System (EARS). The Rwenzori Mtns evolved along the eastern rift shoulder of the Albertine Rift, rising up to form a striking feature within the rift valley with elevations reaching 5109 m a.s.l. While, the scarcity of volcanic activity in the Western Rift has raised questions about the Rwenzori Mtns origin and how this fits into the general evolution of the Albertine Rift and the EARS.

Detailed thermochronologic study of Bauer et al., (2013) on the eastern side on Rwenzori Mtns, differentiated it into northern and southern blocks. The northern block cooled faster to ~120 °C in Carboniferous to Permian times. The second cooling event to ~70 °C occurred in Mesozoic time. The third cooling event to surface temperature occurred in the Neogene. While, the southern block shows an earlier onset of cooling at >400 Ma. Temperatures of about 70 °C were reached in Silurian to Devonian times.

During this study, 33 samples were collected from the western side of central Rwenzori. Zircon and apatite fission track and (U/Th)-He techniques were applied on these samples. The apatite fission track data could be divided into three age groups; ~45±11, ~25±5, ~12±2 Ma. These results reveal the difference in thermo-tectonic history between the eastern and western flanks of Rwenzori Mtns and support the tilt uplift geometry hypotheses (e.g., Pickford et al., 1993).

References

Bauer, F.U., Glasmacher, U.A., Ring, U., Karl, M., Schumann, A., Nagudi, B., 2013. Tracing the exhumation history of the Rwenzori Mountains, Albertine Rift, Uganda, using low-temperature thermochronology, Tectonophysics, 599, 8-28. http://dx.doi.org/10.1016/j.tecto.2013.03.032.

Pickford, M., Senut, B., Hadoto, D., 1993. Geology and Palaeobiology of the Albertine Rift Valley Uganda-Zaire, vol. 1. Geology. CIFEG Occas, Orleans. Publication, vol. 24, pp. 1–190.

Eidesstattliche Versicherung gemäß § 8 der Promotionsordnung der Naturwissenschaftlich-Mathematischen Gesamtfakultät der Universität Heidelberg

1. Bei der eingereichten Dissertation zu dem Thema

Long-term topographic evolution of the African plate, causes and

consequences for surrounding lithospheric plates

handelt es sich um meine eigenständig erbrachte Leistung.

2. Ich habe nur die angegebenen Quellen und Hilfsmittel benutzt und mich keiner unzulässigen Hilfe Dritter bedient. Insbesondere habe ich wörtlich oder sinngemäß aus anderen Werken übernommene Inhalte als solche kenntlich gemacht.

3. Die Arbeit oder Teile davon habe ich wie folgt/bislang nicht[1] an einer Hochschule des In- oder Auslands als Bestandteil einer Prüfungs- oder Qualifikationsleistung vorgelegt.

Titel der Arbeit: ____________________

Hochschule und Jahr: ____________________

Art der Prüfungs- oder Qualifikationsleistung: ____________________

4. Die Richtigkeit der vorstehenden Erklärungen bestätige ich.

5. Die Bedeutung der eidesstattlichen Versicherung und die strafrechtlichen Folgen einer unrichtigen oder unvollständigen eidesstattlichen Versicherung sind mir bekannt.

Ich versichere an Eides statt, dass ich nach bestem Wissen die reine Wahrheit erklärt und nichts verschwiegen habe.

Ort und Datum	Unterschrift

---

[1] Nicht Zutreffendes streichen. Bei Bejahung sind anzugeben: der Titel der andernorts vorgelegten Arbeit, die Hochschule, das Jahr der Vorlage und die Art der Prüfungs- oder Qualifikationsleistung.

12/2012